Electromechanics and Electrorheology of Fluid Flow with Internal Micro-particle Electrorotation

by

Hsin-Fu Huang

2005, M.S., Fluid Mechanics Division, Department of Mechanical Engineering
National Taiwan University, Taipei, Taiwan
2004, B.S., Department of Mechanical Engineering
National Taiwan University, Taipei, Taiwan

Submitted to the Department of Mechanical Engineering
in partial fulfillment of the requirements for the degree of

DOCTOR OF PHILOSOPHY

at the

MASSACHUSETTS INSTITUTE OF TECHNOLOGY

JUNE 2010

Signature of Author_____
Department of Mechanical Engineering
April 30, 2010

Certified by_____
Markus Zahn
Thomas and Gerd Perkins Professor of Electrical Engineering
Thesis Supervisor

Certified by_____
Gareth H. McKinley
SoE Professor of Teaching Innovation, Professor of Mechanical Engineering
Thesis Committee Chairman

Accepted by_____
David E. Hardt
Ralph E. and Eloise F. Cross Professor of Mechanical Engineering
Chairman, Department Committee on Graduate Studies

Electromechanics and Electrorheology of Fluid Flow with Internal Micro-particle Electrorotation

by

Hsin-Fu Huang

Submitted to the Department of Mechanical Engineering on
April 30, 2010 in partial fulfillment of the requirements for
the degree of Doctor of Philosophy

ABSTRACT

The negative electrorheological responses of two dimensional Couette and Poiseuille flows with internal micro-particle electrorotation are modeled and analyzed via a set of "fully continuum mechanical modeling field equations" formulated in this thesis. By combining the theories of particle electromechanics and continuum anti-symmetric/couple stresses, general governing equations are presented to describe the physical aspects of mass conservation, linear momentum balance, angular momentum balance, and electro-quasi-static field of the negative electro-rheological fluid flow. A "rotating coffee cup model" is also developed for the first time to derive the retarding polarization relaxation equation with its accompanying equilibrium retarding polarization in order to characterize the non-equilibrium motion effects of the continuum spin velocity, $\overline{\omega}$, continuum linear velocity, $\overline{v}$, and micro-particle rotation speed, $\overline{\Omega}$, on the polarization responses as well as the electrical body torque inputs in the negative electrorheological flow field. Using the general assumptions of steady, incompressible, fully developed, and two dimensional flows, we reduce and simplify the full general governing equations in the zero spin viscosity and the finite spin viscosity small spin velocity limits for both Couette and Poiseuille flow geometries.

In the zero spin viscosity limit, expressions for the spin velocity and effective viscosity of Couette flow as well as the spin velocity, linear velocity, and two dimensional volume flow rate of Poiseuille flow are derived in terms of the applied direct current electric field strength, shear rate (for Couette flow), driving pressure gradient (for Poiseuille flow), and spatial coordinate by solving the simplified continuum linear and angular momentum equations with the linear flow velocity being subjected to the no-slip boundary condition. As for the finite spin viscosity small spin velocity limit, analytical solutions to the spin velocity, linear velocity, and effective viscosity of Couette flow as well as solutions to the spin velocity, linear velocity, and two dimensional volume flow rate of Poiseuille flow are obtained and expressed in terms of the applied direct current electric field strength, boundary condition selection parameter (β), spin viscosity, and driving shear rate (for Couette flow) or pressure gradient (for Poiseuille flow) by solving a set of differential equations coupling the linear and angular momentum balances of the negative electrorheological fluid flow subjected to the no-slip and $\overline{\omega} = 0.5\beta\nabla\times\overline{v}$ (with $0 \le \beta \le 1$) boundary conditions. After obtaining the solutions in the respective zero spin viscosity and finite spin viscosity small spin velocity limits, series of parametric studies are then performed on these solutions via varying the pertinent physical parameters involved in several

parametric regimes of interest so as to illustrate the negative electrorheological behavior and fluid flow response due to internal micro-particle electrorotation.

Modeling results in the two limits generally show that with a direct current electric field applied perpendicularly to the flow direction, the spin velocity is increased and the effective viscosity is decreased as compared to the zero electric field values of the electrorheological fluid flow in Couette geometries at a given driving shear rate. It is also found that with a constant driving pressure gradient, the internal micro-particle electrorotation induces increased continuum fluid spin velocity, linear flow velocity, and two-dimensional volume flow rate on the macroscopic level in Poiseuille flow geometries when a direct current electric field perpendicular to the direction of flow is applied. Results of the Couette effective viscosity and Poiseuille volume flow rate obtained from our present continuum mechanical formulation are further compared to the experimental measurements as well as modeling results from single particle dynamics based two-phase volume averaged effective medium analysis found in current literature. With the "rotating coffee cup" fluid polarization model, the present zero spin viscosity continuum solutions to the effective viscosity and volume flow rate agree with the theoretical solutions obtained from single particle dynamics analysis. The zero spin viscosity solutions to the Couette effective viscosity also fall closer to the experimental measurements reported in current literature for low to moderate direct current electric field strengths. Moreover, the present continuum mechanical formulation in the finite spin viscosity small spin velocity limit is more capable of accurately capturing the negative electrorheological flow responses in the low shear rate and low driving pressure gradient flow regimes characterized by the respective Couette effective viscosity and Poiseuille volume flow rate. These finite spin viscosity small spin velocity results agree better with previous experimental measurements reported in the literature and bring the theoretical modeling of the negative electrorheological flow phenomenon due to internal micro-particle electrorotation closer to physical reality—both of which were generally not possible in previous literature. This important improvement in modeling the negative electrorheological response considered in this thesis is due to our proposed "rotating coffee cup model," which is likely the first model to treat the continuum spin velocity and the micro-particle rotation speed as separate physical variables. Using the finite spin viscosity small spin velocity analysis, we also derive for the first time a characteristic length scale determined by the balances between the electrical body torque input and the angular momentum conversion between the linear and spin velocity fields, which can be used to explain why the present continuum zero spin viscosity solutions are very much similar to those obtained from single particle dynamics based two-phase volume averaged effective medium analysis found in current literature.

Future work includes a more advanced modeling of the polarization relaxation processes in the negative electrorheological fluid flow, the full non-linear analysis of finite spin viscosity effects on the angular momentum balances within the electrorheological flow field without the restriction of the small spin velocity limit, and the search of possible applications of our proposed continuum mechanical modeling field equations theory in the research areas of micro/nano-fluidics, biofluid dynamics, and engineering torque-shear rate control systems.

Thesis Supervisor: Markus Zahn
Title: Thomas and Gerd Perkins Professor of Electrical Engineering

Thesis Committee Chairman: Gareth H. McKinley
Title: SoE Professor of Teaching Innovation, Professor of Mechanical Engineering

Acknowledgements

First and foremost, I'd like to express my sincere gratitude to my thesis and research advisor, Prof. Markus Zahn, for being a great teacher, advisor, friend, and mentor during my time at MIT. This thesis and research work would never have been possible nor reached its final stage of completion without Mark's time, efforts, patience, and understanding. Through Mark's guidance and expertise, I got the rare yet great opportunity as well as experience to delve into the research fields of electrohydrodynamics, ferrohydrodynamics, and continuum electromechanics. With Mark's help in offering funds, equipment, and the High Voltage Research Laboratory (HVRL) lab space, I also had the opportunity to gain practical hands-on lab/experimental experiences additional to the theoretical work presented in this thesis. My trip to Israel with Prof. Zahn for collaborative research has also proven to be an invaluable experience on both professional and personal levels.

I'd like to greatly thank my superb thesis committee, Profs. Gareth McKinley, Alan Grodzinsky, and Martin Bazant, for their input and help in perfecting my thesis work and in identifying my research contributions to the field. I'd like to thank Martin for sharing his expertise in non-linear electrokinetics and for the numerous insightful suggestions and comments during our research discussions. I have also greatly benefited from Gareth's pivotal role as my "lighthouse" giving me pointers and directions to what comes up next in each stage of my Ph.D. program and to what are the relevant fluid mechanical aspects and details when comparing and interpreting experimental and theoretical results. Since my very first day at MIT, Al has been my constant source of inspiration and encouragement. My MIT journey wouldn't be much the same without Al's guidance and participation during each phase of my MIT life. I am truly grateful to have the friendship, understanding, and continuous support of my thesis committee.

I would especially like to acknowledge Profs. Elisabeth Lemaire and Francois Peters, principle investigators of our collaborating group at the Universite de Nice in France, for their help and discussions on the experimental work and for generously offering the original experimental data points published in Lemaire *et al.* (2006, 2008) and Peters *et al.* (2010) to facilitate the comparisons between the continuum mechanical theory presented in this thesis and the experimental results found in current literature. Research discussions with Prof. Mark Shliomis at the Ben-Gurion University of the Negev in Israel have also been remarkably fruitful and invaluable, and given me all the confidence I need to pursue my beliefs in the theoretical modeling of this electrorotation topic.

On both professional and personal levels, I'd like to thank Dr. Chathan Cooke, our great research scientist in HVRL, for sharing his expertise and experiences in high voltage research as well as several of his experimental equipment that facilitated my impedance measurements and energized my experimental apparatuses. I would also like to thank Prof. Chiang C. Mei for offering great classes in theoretical hydrodynamics (in which I had a really great time) and for inspiring and encouraging my continuing interests in theoretical hydrodynamics as well as applied mathematics and asymptotic analyses.

Thanks also goes to my labmates: Zach Thomas, Uzoma Orji, Clint Lawler, Padraig Cantillon Murphy, Frank O'Sullivan, Tony He, Shahriar Khushrushahi, Georege Hwang, Ben Cannon, and Xuewei Zhang, colleagues and visiting professors: Prof. Yuanxiang Zhou of Beijing Tsinghua University, Prof. Ying Yang of Beijing Tsinghua University, Prof. Gwan Soo Park of Pusan National University, and Prof. Qing Yang of Chongqing University, and directors and staff of the Laboratory for Electromagnetic and Electronic Systems and Research Laboratory of Electronics (LEES/RLE): Prof. John Kassakian, Prof. Joel Schindall, Wayne Ryan, Gary DesGroseilliers, Al McGurl, Miwa Suzuki, Dimonika Bizi, Makiko Wada, and to the memory of Vivian Mizuno, for all of their great help, warm friendship, continuous support, and wonderful company along the course of my research work and life at MIT.

I'd especially like to thank Profs. Ying Yang and Qing Yang as well as Xuewei Zhang for teaching me everything I know about high voltage experiments and for helping out the details and safety during my experimental work. Also for my experimental work, I'd like to acknowledge Clarke Low, Vivian Chuang, Chia-Ling Pai, Chun-Hao Tseng, Shahriar Khushrushahi, Wayne Ryan, Steve Vincent, Sidney Tsai, Cheng-Hsun Wu, Jason Sen, Wu-Jung Lee, Kerri Keng, Hank Chu, and Xiao Rong for their input and suggestions on material selection, equipment fabrication, technical details, equipment wiring, and LabVIEW details. Video recording assistance and several photo shots taken for the experimental section of this thesis are the courtesies of Yu-Chih Ko.

I am very grateful to Leslie, Joan, and the whole MechE grad office administrative staff for taking great care of us (MechE grad students) and "watching us grow up" all along from the admission letter, to quals, to the submission of thesis, and even job hunting! I can't imagine what sort of chaos grad school would be like without their great help and support. Leslie, Joan, and the whole MechE grad office administrative staff are definitely the best!!

The best study group a MechE Ph.D. could possibly ever have: Thor Eusner, Wayne Staats, Chris MacMinn, Dave Henann, Shawn Chester, Kimin Jun, Tae Yoon Kim, Kevin Xueyan Zhang, and Haijie Chen. Thanks to all the resourcefulness, friendship, and support during the great times that we spent on studying, brainstorming, solving problems, and gossiping (☺) together!!

From the very beginning till the very end, Sheng Shen has been my guardian angel during my time at MIT. From course work, quals preparation, residence relocations, to future plan discussions, Sheng not only provided me with all the help I needed, but also supported me with all the friendship, encouragement, and strength to move on. Also from the very beginning till the very end, Jacky Chen has been like a "big brother" not only to me, but also to many of the

Taiwanese students around the greater Boston area. I am very grateful to have Jacky's friendship and company over the past few years, which balanced me between work and fun as well as reminded me that there is still a "true life" out there for me to enjoy apart from this professional life we're now after. Thanks also goes to my ROCSA friends for their friendship, help in daily life and research, and all the fun times together. They are Long-Hua, Aithne, Andrew, Cheng-Wei, Jones, Chiao-Lun, Chien-Jen, Chih-Yu, Dah-Yoh, Dai-Yin, Hsiang-Chieh, Hsien-Chung, Hsu-Yi, Hueihan, Hung-An, Hung-Wen, Wei-Chuan & Iris, Michael, Paul, Podo, Scott, Shih-Chi, Tien-Yun, Tsung-Han, Yen-Jie, Yi, Ying-Chih, Sam, Shih-Yu, and many others (sorry it's difficult to include everyone ☹, please add yourself if I shouldn't have missed your name ☺).

On behalf of my parents and family, I'd like to thank Candy and Bonnie, Dr. Wei-Chuan Sun, and Prof. Chin-Pao Huang of the University of Delaware for keeping an eye on me and for the great and warm hospitality while I'm away from home here in Boston. It is also great to have my sister Yu-Ju's company near Boston to share all the bitterness and happiness that shape an international student's life. I am in great debt to my dad, Jenn-Wen, and all his colleagues and friends at his university for "staying tuned" to the progresses of my grad school life. The support and belief in me from you guys have always given me the momentum to move on and to press on towards the final goal of my doctoral studies. Finally, I am also in great debt to my MOM, Chiu-Yueh, for constantly visiting me and taking care of me here, half way around the globe, in Boston despite of her suffering medical conditions. I know I should have spent more time enjoying what life has given me as well as spent more time with you instead of always using my work as "the excuse." Nevertheless, MOM, this thesis is dedicated to you ☺.

The financial support for my doctoral studies at MIT is jointly sponsored by the Ministry of Education, the Council for Economic Planning and Development, and the National Science Council (Taipei, Taiwan) through the Taiwan Merit Scholarships (TMS) program under grant no. TMS-094-2-A-029. Experimental research work is partially supported by the United States-Israel Binational Science Foundation (BSF) through grant no. 2004081.

H.-F. H.
Cambridge, MA
Spring, 2010

Parts of this thesis have been presented in:

Hsin-Fu Huang, Markus Zahn, Elisabeth Lemaire, and Mark I. Shliomis, Continuum modeling of micro-particle electrorotation in Couette and Poiseuille flows—the zero spin viscosity limit, 2009 Electrostatics Joint Conference (ESA/IEEE-IAS/IEJ/SFE/IEA), June 16-18, 2009, Boston University, Boston, MA, U.S.A.

Contents

List of Tables

method and the data were taken at 1 kHz and 17-21°C. Note that in our third liquid conductivity test, the carrier liquid conductivity of Oil blend & AOT #3, *i.e.*, DIALA® : DC 200 = 0.526 : 0.474 base oil with [AOT] = 0.09053 (M), was measured to be 1.93E-08. This result is probably due to the cold temperature around 17°C the day the measurement was made.

Table A.5. Summary of the measured and standard viscosity values of the liquids employed in the calibration test of the viscometer. The standard values of the liquid viscosities were obtained from manufacturer material data sheets (Shell material data sheet, 2005; Sigma-Aldrich material data sheet, 2009) and literature (Elborai, 2006; Khushrushahi, 2010). The measured viscosities were all obtained at a spindle rotation speed of 60 rpm.

Table A.6. Summary of viscosity results of the base pure oil blend respectively measured at spindle rotation velocities of 50 and 60 rpm.

Table A.7. Summary of measured viscosity results for the liquid phase of the proposed ER fluid. Measurements were performed at spindle rotation speeds of 50 and 60 rpm, respectively.

Table A.8. Comparison between the theoretically predicted and experimentally measured values of the proposed ER fluid viscosity, η, *i.e.*, the zero electric field viscosity of the ER fluid.

Table A.9. Summary of the final formula and material properties of the proposed ER fluid considered in this appendix.

List of Figures

Figure 3.5. Cartoon illustrating a state of dynamic equilibrium for the equilibrium retarding polarization of an ER fluid parcel with the suspended micro-particles rotating in complete random directions within the ER fluid parcel. This dynamic equilibrium state best represents the condition of micro-particles rotating in random directions in a quiescent carrier liquid.

Chapter 4

Figure 4.1. The schematic diagram illustrating the geometry, dimensions, and physical parameters for Couette flow with internal micro-particle electrorotation.

Figure 4.2. The dimensionless Couette spin velocity, ω^*, plotted with respect to the average shear rate, γ^*, evaluated at $E^* = 0$, 0.4, 0.8, 1.0, 2.0, and 3.0. For $E^* \geq 1.0$, the spin velocity is given by Eq. (4.16), *i.e.*, $\omega^* = \omega^*_{C2}$ (negative valued Ω from Eq. (2.57) used in Eqs. (4.5)-(4.7)), whereas for the cases of $E^* \leq 0.8$, ω^* is given by Eq. (4.15), $\omega^* = \omega^*_{C1}$, with the micro-particle rotation speed, Ω, set to zero in Eqs. (4.5)-(4.7). The gray line denotes the zero electric field spin velocity, namely, half of the fluid vorticity, $\omega^*_0 = -\gamma^*/2$.

Figure 4.3. The effective viscosity, η^*, found for Couette flow plotted with respect to the average shear rate, γ^*, evaluated at $E^* = 0$, 0.4, 0.8, 1.0, 2.0, and 3.0. For $E^* \geq 1.0$, the spin velocity given by Eq. (4.16), *i.e.*, $\omega^* = \omega^*_{C2}$, is used in the evaluation of Eqs. (4.23) and (4.24), whereas for $E^* \leq 0.8$, $\omega^* = \omega^*_{C1}$ given by Eq. (4.15) is employed in Eqs. (4.23) and (4.24). The gray line denotes the zero electric field value of the effective viscosity, *i.e.*, $\eta^* = \eta_{eff}/\eta = 1$, with the value of η given in Table 4.1.

Figure 4.4. The spatial variations of the total spin velocity profiles, ω^*, given by Eq. (4.36) evaluated for (a) $E^* \geq 1$ and (b) $E^* \leq 1$ with $\beta = 1$, $\eta^*_p = 1$, and $U_0 = 0.01$ (m/s) (or $\gamma^* \approx 0.01$) kept constant. The gray line in Fig. 4.4(b) denotes the zero electric field solution of $\omega^*_0 = -\gamma^*/2$ when the applied DC electric field is reduced to zero.

Figure 4.5. The spatial variations of the total spin velocity profiles, ω^* (in (a) and (b)), and the normalized spin velocity profiles, $\widetilde{\omega^*}$ (in (c) and (d)), evaluated at distinct values of the Couette boundary driving velocity, *i.e.*, $U_0 = 0.01$, 0.05, and 0.1 (m/s) (or equivalently,

in both (a) and (b) because the micro-particle rotation speed equals to zero, $\Omega = 0$, when $E^* = 1$ as calculated via Eq. (2.57) for (a), which is equivalent to setting $\Omega = 0$ in (b).

Figure 4.13. Variations of the effective viscosity, η^*, plotted with respect to the applied shear rate, γ^*, evaluated at $\eta_p^* = 1$ and $\beta = 0$, 0.25, 0.5, 0.75, and 1 for (a) $E^* = 2 \geq 1$ and (b) $E^* = 0.6 < 1$.

Figure 4.14. Variations of the effective viscosity, η^*, plotted with respect to the shear rate, γ^*, evaluated at $\beta = 1$ and $\eta_p^* = 0.5$, 0.65, 1, 2, and 10 for (a) $E^* = 2 \geq 1$ and (b) $E^* = 0.6 < 1$.

Chapter 5

Figure 5.1. The schematic diagram illustrating the geometry, dimensions, and physical parameters for Poiseuille flow with internal micro-particle electrorotation.

Figure 5.2. The three roots, ω_{P1}^*, ω_{P2}^*, and ω_{P3}^* (given respectively in Eqs. (5.7), (5.8), and (5.9)), of the dimensionless Poiseuille spin velocity, ω^*, to the angular momentum equation, Eq. (5.6). The spin velocity profiles are plotted with respect to the spatial coordinate, z^*, at $\Gamma = 2 \times 10^4$ (Pa/m) and $E^* = E_0/E_c$ =1.0, 1.01, and 1.05 for both Figs. 5.2(a) and 5.2(b), and $E^* = 0.7$, 0.8, 0.9, 0.95, and 0.99 for Fig. 5.2(c) with $E_c = 1.3 \times 10^6$ (V/m). The dash-dash curves denote ω_{P1}^* (Eq. (5.7)), the dash-dot-dash curves denote ω_{P2}^* (Eq.(5.8)), and the solid gray curves denote ω_{P3}^* (Eq. (5.9)). In Fig. 5.2(a), we have substituted the positive valued particle rotation speed, Ω, of Eq. (2.57) or (5.12) into Eqs. (4.5)-(4.7) in evaluating the spin velocity profiles. Therefore, the profiles shown in Fig. 5.2(a) are only valid within the spatial region of $0.5 < z^* \leq 1$. Similarly, a negative valued Ω from Eq. (2.57) or (5.12) has been used in Eqs. (4.5)-(4.7), and thus, the spin velocity profiles shown in Fig. 5.2(b) are only valid within $0 \leq z^* < 0.5$. As for Fig. 5.2(c), the particle rotation speed is set to zero, $\Omega = 0$, in Eqs. (4.5)-(4.7). It can be seen that the spin velocity profiles evaluated at electric fields strengths of $E^* = 0.95 \sim 1$ become multi-valued in space near the middle of the flow channel (note that Ω goes to zero for $E^* = 1$ in Eq. (2.57) or (5.12)).

Figure 5.3. The normalized Poiseuille spin velocity profile, $\widetilde{\omega^*}$, plotted with respect to the spatial coordinate, z^*, evaluated at $E^* = 0$, 0.4, 0.8, 1.0, 2.0, and 3.0, with $\Gamma^* = 1$. The gray

curve denotes the zero electric field value for the spin velocity, *i.e.*, the vorticity of ordinary Poiseuille flow. Note that Eqs. (5.7) and (5.8), with the proper selection of the micro-particle rotation speeds in Eq. (2.57) or (5.12), are used in the evaluation of the spin velocity for $E^* \geq 1$, whereas for $E^* \leq 0.9$, Eq. (5.7) (with $\Omega = 0$ in Eqs. (4.5)-(4.7)) is used throughout the spatial domain of interest.

Figure 5.4. The normalized Poiseuille spin velocity profile, $\widetilde{\omega^*}$, plotted with respect to the spatial coordinate, z^*, evaluated at $\Gamma^* = 1$, 2, and 5, with $E^* = 2$. The gray curve denotes the zero electric field value for the spin velocity, *i.e.*, the vorticity of ordinary viscous Poiseuille flow. Note that Eqs. (5.7) and (5.8), with the proper selection of the micro-particle rotation speeds in Eq. (2.57) or (5.12), are employed in the evaluation of the spin velocity shown in this figure.

Figure 5.5. The normalized linear velocity profile, u^*, of Poiseuille flow with internal micro-particle electrorotation plotted with respect to the spatial coordinate, z^*, evaluated at $E^* = 0$, 0.4, 0.8, 1.0, 2.0, and 3.0, with $\Gamma^* = 1$. The gray curve denotes the zero electric field velocity profile, which is the original Poiseuille parabolic profile. Equations (5.7) (*use positive* Ω *from Eq. (2.57) or (5.12) in Eqs. (4.5)-(4.7)*) and (5.8) (*use negative* Ω *from Eq. (2.57) or (5.12) in Eqs. (4.5)-(4.7)*) are respectively employed in the integrals of Eqs. (5.15) and (5.16) for $E^* \geq 1$. The evaluation of u^* for $E^* \leq 0.9$ is done by employing Eq. (5.7) in both Eqs. (5.15) and (5.16) with $\Omega = 0$ in Eqs. (4.5)-(4.7).

Figure 5.6. The normalized linear velocity profile, u^*, of Poiseuille flow with internal micro-particle electrorotation plotted with respect to the spatial coordinate, z^*, evaluated at $\Gamma^* = 1$, 2, and 5, with $E^* = 2$. The gray curve denotes the zero electric field velocity profile, which is the original Poiseuille parabolic profile. Equations (5.7) (*use positive* Ω *from Eq. (2.57) or (5.12) in Eqs. (4.5)-(4.7)*) and (5.8) (*use negative* Ω *from Eq. (2.57) or (5.12) in Eqs. (4.5)-(4.7)*) are respectively employed in the integrals of Eqs. (5.15) and (5.16) for the linear velocity profiles shown herein.

Figure 5.7. The two dimensional Poiseuille volume flow rate, Q (m^2/s), plotted with respect to the applied pressure gradient, Γ^*, evaluated at $E^* = 0$, 0.4, 0.8, 1.0, 2.0, and 3.0. The gray curve represents the zero electric field volume flow rate given by $Q_0 = \Gamma h^3/12\eta$.

Figure 5.8. The schematic diagram illustrating the new coordinate system employed for analyzing Poiseuille flow with internal micro-particle electrorotation in the finite spin viscosity small spin velocity limit.

Figure. 5.9. (a) Spatial variations of the total spin velocity profile evaluated at $E^* = 1$, 1.5, 2, 2.5, and 3 with $\beta = 1$, $\eta_p^* = 1$, and $\Gamma^* = 0.125$ (or $\Gamma = 2500$ (Pa/m)) kept constant. (b) Spatial variations of the differences in total spin velocity, $\Delta\omega^*$ as defined in Eq. (5.49), evaluated at $E^* = 0$, 0.2, 0.4, 0.6, 0.8, and 1 with $\beta = 1$, $\eta_p^* = 1$, and $\Gamma^* = 0.125$ (or $\Gamma = 2500$ (Pa/m)) kept constant.

Figure 5.10. (a) and (b) show the spatial variations of the total spin velocity, ω^*, evaluated at $\Gamma = 1500$, 2000, 2500, 3000, and 3500 (Pa/m) (or $\Gamma^* = 0.075$, 0.1, 0.125, 0.15, and 0.175, respectively) while $\beta = 1$, $\eta_p^* = 1$ and the respective electric field strengths of $E^* = 2$ (Fig. 5.10(a)) and $E^* = 0.6$ (Fig. 5.10(b)) are maintained constant. (c) Spatial variations of the normalized spin velocity, $\widetilde{\omega}^*$ as defined in Eq. (5.50), evaluated at $\Gamma = 1500$, 2000, 2500, 3000, and 3500 (Pa/m) while $\beta = 1$, $\eta_p^* = 1$ and $E^* = 2$ are kept constant. The solid gray line in Fig. 5.10(c) denotes the zero electric field solution of $\widetilde{\omega}_0^* = z^*$ as given in Eq. (5.51). (d) The spatial variations of the differences in the normalized spin velocity, $\Delta\widetilde{\omega}^*$ as defined in Eq. (5.52), evaluated at $\Gamma = 1500$, 2000, 2500, 3000, and 3500 (Pa/m) while $\beta = 1$, $\eta_p^* = 1$ and $E^* = 0.6$ are kept constant. Note that all five profiles have merged into one curve at this electric field strength of interest.

Figure 5.11. The spatial variations of the total spin velocity evaluated at $\beta = 0$, 0.25, 0.5, 0.75, and 1 while $\Gamma^* = 0.125$, $\eta_p^* = 1$, and the electric field strengths of $E^* = 2$ for Fig. 5.11(a) and $E^* = 0.6$ for Fig. 5.11(b) are kept constant.

Figure 5.12. (a) Spatial variations of the total spin velocity evaluated at $\eta_p^* = 0.5$, 0.65, 1, 2, and 10 with $E^* = 2$, $\beta = 1$, and $\Gamma^* = 0.125$ kept constant. (b) Spatial variations of the differences in the total spin velocity, $\Delta\omega^*$ as defined in Eq. (5.53), evaluated at $\eta_p^* = 0.5$, 0.65, 1, 2, and 10 with $E^* = 0.6$, $\beta = 1$, and $\Gamma^* = 0.125$ kept constant.

Chapter 6

Figure 6.1. Comparison of the two Couette effective viscosity solutions respectively obtained in the zero spin viscosity, $\eta' = 0$, and finite spin viscosity small spin velocity, $\eta' \neq 0$, $\tau_{MW}^2 \omega_x^2 \ll 1$, limits. For both curves, we have employed a DC electric field strength of $E^* = 2$. Also, we have used $\beta = 1$ and $\eta_p^* = 1$ for the $\eta' \neq 0$, $\tau_{MW}^2 \omega_x^2 \ll 1$ solution.

Figure 6.2. Comparison of the two total volume flow rate solutions obtained in the zero spin viscosity, $\eta' = 0$, and the finite spin viscosity small spin velocity, $\eta' \neq 0$, $\tau_{MW}^2 \omega_x^2 \ll 1$, limits, respectively. The solid back line represents the $\eta' = 0$ solution evaluated at $E^* = 2$, whereas the solid gray line represents the $\eta' \neq 0$, $\tau_{MW}^2 \omega_x^2 \ll 1$ solution evaluated at $E^* = 2$, $\beta = 1$, and $\eta_p^* = 1$. The dash-dash line denotes the zero electric field solution, *i.e.*, the total 2D flow rate of purely viscous Poiseuille flows, $Q_0 = \Gamma h^3 / 12\eta$.

Figure 6.3. Comparison of the Couette effective viscosity results among the present continuum zero spin viscosity modeling predictions (HT, solid curve), the experimental measurements (LE, dotted curve) reported in Fig. 7a of Lemaire *et al.* (2008), and the combined single particle dynamics two-phase volume averaged effective medium theory predictions (LT, dashed-dashed curve) employed in Fig. 7a of Lemaire *et al.* (2008). In this figure, the ER fluid solid volume fraction is $\phi = 0.05$, and the solutions or measurements are obtained at DC electric field strengths of (a) $E_0 = 1$ (kV/mm), (b) $E_0 = 2$ (kV/mm), and (c) $E_0 = 3$ (kV/mm). No fitting parameters or procedures are used in evaluating the zero spin viscosity HT solutions.

Figure 6.4. Comparison of the Couette effective viscosity results among the present continuum zero spin viscosity modeling predictions (HT, solid curve), the experimental measurements (LE, dotted curve) reported in Fig. 7b of Lemaire *et al.* (2008), and the combined single particle dynamics two-phase volume averaged effective medium theory predictions (LT, dashed-dashed curve) employed in Fig. 7b of Lemaire *et al.* (2008). In this figure, the ER fluid solid volume fraction is $\phi = 0.1$, and the solutions or measurements are obtained at DC electric field strengths of (a) $E_0 = 1$ (kV/mm), (b) $E_0 = 2$ (kV/mm), and (c) $E_0 = 3$

Figure 6.7. Comparison of the 2D Poiseuille volume flow rate results among the present zero spin viscosity HT (solid curve) predictions, the experimental measurements, LE (dotted curve), found in Fig. 5 of Lemaire *et al.* (2006), and the single particle dynamics based predictions (dashed-dashed curve) found in Fig. 5 of Lemaire *et al.* (2006). In this figure, the gray solid lines denote the zero electric field Poiseuille volume flow rate and the ER fluid solid volume fraction is $\phi = 0.05$. The HT and LT solutions and the LE measurements are obtained at DC electric field strength of $E_0 = 2.7$ (kV/mm) in Fig. 6.7(a) and of $E_0 = 3.3$ (kV/mm) in Fig. 6.7(b). No fitting parameters or procedures are used in the evaluation of the HT results.

Figure 6.8. Comparison of the 2D Poiseuille volume flow rate results among the present zero spin viscosity HT (solid curve) predictions, the experimental measurements, LE (dotted curve), found in Fig. 6 of Lemaire *et al.* (2006), and the single particle dynamics based predictions (dashed-dashed curve) found in Fig. 6 of Lemaire *et al.* (2006). In this figure, the gray solid lines denote the zero electric field Poiseuille volume flow rate and the ER fluid solid volume fraction is $\phi = 0.1$. The HT and LT solutions and the LE measurements are obtained at DC electric field strength of $E_0 = 2.7$ (kV/mm) in Fig. 6.8(a) and of $E_0 = 3.3$ (kV/mm) in Fig. 6.8(b). No fitting parameters or procedures are used in the evaluation of the HT results.

Figure 6.9. Comparison of the 2D Poiseuille volume flow rate results in the low pressure gradient regime among the present finite spin viscosity small spin velocity HT (solid curve) predictions, the experimental measurements, LE (dotted curve), found in Fig. 5 of Lemaire *et al.* (2006), and the single particle dynamics based predictions (dashed-dashed curve) found in Fig. 5 of Lemaire *et al.* (2006). In this figure, the ER fluid solid volume fraction is $\phi = 0.05$. The HT and LT solutions and the LE measurements are obtained at DC electric field strength of $E_0 = 2.7$ (kV/mm) in Fig. 6.9(a) and of $E_0 = 3.3$ (kV/mm) in Fig. 6.9(b). In the evaluations of the HT predictions, $\beta = 1$ and $\eta' = h^2\eta$ are chosen by physical arguments discussed in Chapters 4 and 5. No *ad hoc* fitting parameters or procedures are used in the evaluation of the HT results.

Figure 6.10. Comparison of the 2D Poiseuille volume flow rate results in the low pressure gradient regime among the present finite spin viscosity small spin velocity HT (solid curve)

Figure A.5. The experimental setup for measuring the viscosity of the proposed ER fluid and other related liquid samples. The basic components of the experimental setup are a standard 600 (mL) beaker and a Brookfield Model DV-1+ viscometer along with an accompanying Brookfield Model LV-1 spindle (Brookfield Engineering Laboratories, Middleboro, MA).

Figure A.6. The Poiseuille electrorheological fluid flow and electrorotation testing channel.

Figure A.7. Zoom-in view of the Poiseuille flow channel testing section of the whole completed electrorotation testing apparatus. The dimension of channel height, h, of Poiseuille flow channel is restrained by plastic C-clamps as shown holding the test cell in the figure.

Figure A.8. Global view of the whole completed Poiseuille flow electrorotation testing apparatus and equipment.

Figure A.9. Simple LabVIEW program used for monitoring the driving pressure gradient within the Poiseuille flow channel. (a) Front panel. (b) Block diagram.

Figure A.10. (a) Experimental setup of the Poiseuille flow electrorotation testing apparatus when the apparatus is energized with high voltage by the Hipotronics R10B high voltage DC power supply. (b) A Fluke 80k-40 high voltage probe (connected to a Fluke 45 dual display multimeter) with a voltage division ratio of 1000:1 is used to measure the actual voltage stressed within the ITO glass Poiseuille flow test cell.

Figure A.11. Mass flow rate of the suspension fluid (or ER fluid) measured with respect to the driving pressure gradient at applied DC electric field strengths of $E_0 = 0.018$ (box), 0.7 (star), 1.43 (triangle), and 2.06 (diamond) (kV/mm). Each data point shown in the figure is the averaged result of 2-3 measurements.

Nomenclature

Abbreviations

Two-dimensional	2D
Three-dimensional	3D
Alternating current	AC
Docusate sodium salt, Aerosol OT	AOT
Direct current	DC
Silicone oil DC 200	DC 200
Silicone oil DC 561	DC 561
Shell DIALA® AX oil	DIALA®
Sub-/super-script denoting for the lower half of the Poiseuille flow channel in Chap. 5	DW
Electro-quasi-static	EQS
Electrorheological	ER
Particle-liquid mixture	ER fluid
Huang theory presented in this thesis	HT
Indium tin oxide	ITO
Lemaire *et al.* (2006, 2008) experimental measurements	LE
Left hand side	LHS
Lemaire *et al.* (2006, 2008) theoretical predictions	LT
Maxwell-Wagner	MW
Negative electrorheological effect of the first kind	nER1
Negative electrorheological effect of the second kind	nER2
Order of magnitude	$O(\bullet)$
Polychlorinated biphenyl	PCB

Polyethylene	PE
Poly(methyl methacrylate)	PMMA
Polytetrafluoroethylene, Teflon®	PTFE
Right hand side	RHS
Revolutions per minute	RPM/rpm
Superscript of "$'$" denoting transpose of matrix	^{t}
Tetrachlorobenzyltoluenes	Ugilec®
Sub-/super-script denoting for the upper half of the Poiseuille flow channel in Chap. 5	UP
Concentration of AOT salt	[AOT]
Superscript "*" denoting dimensionless variables	*
Multiplication or vector cross product	×
Tilde "$\tilde{}$" denoting normalized variables	$\tilde{}$
Hat "$\hat{}$" denoting dummy indices of integration	$\hat{}$

.

Alphabets

Outer diameter of the middle rod of the coaxial cylindrical electrode	a
Variable defined in Eq. (2.35)	a_3
Variable defined in Eq. (2.36)	a_6
Eigen parameter defined in Eqs. (4.34) and (5.26)	A
The inner diameter of the outer ring of the coaxial cylinder electrode	b
Parameter defined in Eqs. (4.35) and (5.27)	B
Measured capacitance	C
Integration constant in Eq. (4.10)	C_c
Integration constant in Eq. (5.2)	C_p
Diameter of the micro-particles	d
The differential area element (scalar)	dA
The differential area element (vector)	$d\overline{A}$

The microscopic differential electrical force	$\overline{dF^{\dagger}}$
The electric displacement field (vector)	$\overline{D}$
The microscopic electric displacement field (vector)	$\overline{D^{\dagger}}$
Coefficients of correction to the macroscopic electric field in Eq. (4.8), $i = 1, 2, \ldots$etc.	e_i
The applied electric field strength	E_0
Critical electric field strength for the onset of micro-particle Quincke rotation	E_c
y-component of the macroscopic applied electric field	E_y
z-component of the macroscopic applied electric field	E_z
Dimensionless applied electric field strength	E^*
r-component of the microscopic electric field	$E_r^{\dagger}$
z-component of the microscopic electric field	$E_z^{\dagger}$
θ-component of the microscopic electric field	$E_{\theta}^{\dagger}$
ϕ-component of the microscopic electric field	$E_{\phi}^{\dagger}$
Macroscopically applied electric field vector	$\overline{E}$
The microscopic molecular electric field vector	$\overline{E_m}$
Microscopically applied electric field vector	$\overline{E^{\dagger}}$
Volume fraction of Shell DIALA® Oil AX	f_r
Measured conductance	G
Channel height of Couette and Poiseuille flow channels	h
Macroscopically applied (rotating) magnetic field vector	$\overline{H}$
The imaginary number, $i = \sqrt{-1}$	i
Unit vector in the x-direction in Cartesian coordinates	$\overline{i_x}$
Unit vector in the y-direction in Cartesian coordinates	$\overline{i_y}$
Unit vector in the z-direction in Cartesian coordinates	$\overline{i_z}$
Unit vector in the r-direction in spherical coordinates	$\overline{i_r}$
Unit vector in the θ-direction in spherical coordinates	$\overline{i_{\theta}}$

Unit vector in the ϕ-direction in spherical coordinates	$\overline{i_\phi}$
Unit vector in the y"-direction defined in Fig. 3.2	$\overline{i_y}$"
Unit vector in the z"-direction defined in Fig. 3.2	$\overline{i_z}$"
Averaged moment-of-inertia per unit volume (scalar)	I
Sum of the moment-of-inertia of the micro-particles per unit volume	I_{vdp}
Moment-of-inertia density tensor	$\overline{\overline{I}}$
The unit identity tensor	$\overline{\overline{I_0}}$
Constants in Eqs. (2.17), (2.18), and (2.20), j_i, $i = 1, 2, 3, 4, \ldots$etc.	j_i
Ohmic current per unit area (microscopic variable)	$\overline{J_f^\dagger}$
Surface current density (microscopic variable)	$\overline{K_f^\dagger}$
Characteristic length scale defined by Eq. (6.3)	ℓ
Separation constant in Eq. (2.14)	l
Characteristic diffusion length for angular momentum	l_D
Modified Mason number defined in Eq. (5.5)	m^*
Internal angular momentum (vector) of a continuum fluid particle or parcel, Eq. (1.2)	$\overline{m}$
Mason number based on vortex viscosity as in Eq. (4.13)	M^*
Macroscopic magnetization (vector) of the ferrofluid	$\overline{M}$
The equilibrium magnetization of ferrofluid	$\overline{M_{eq}}$
Number density of micro-particles	n
Normal vector of surfaces	$\overline{n}$
Hydrodynamic pressure	p
y-component of the molecular dipole moment	p_{my}
z-component of the molecular dipole moment	p_{mz}
x-component of the total dipole moment of the micro-particle	$p_x^\dagger$
y-component of the total dipole moment of the micro-particle	$p_y^\dagger$
z-component of the total dipole moment of the micro-particle	$p_z^\dagger$

Molecular dipole moment	$\overline{p^m}$
The retarding dipole moment of the micro-particle	$\overline{p^\dagger}$
The microscopic molecular dipole moment	$\overline{p_t^m}$
Equilibrium retarding dipole moment	$\overline{p_{eq}^\dagger}$
Total dipole moment of the micro-particle	$\overline{p_t^\dagger}$
Dipole moment of micro-particle at infinite frequency response	$\overline{p_\infty^\dagger}$
y-component of the equilibrium retarding polarization defined in Eq. (3.33)	P_{eq}^y
z-component of the equilibrium retarding polarization defined in Eq. (3.33)	P_{eq}^z
y-component of the total polarization	P_{ty}
y-component of the retarding polarization	P_y
z-component of the retarding polarization	P_z
Macroscopic retarding polarization (vector) of the ER fluid	$\overline{P}$
Polarization contribution from the carrier liquid phase	$\overline{P_l}$
Total polarization (vector) of the ER fluid	$\overline{P_t}$
Polarization due to the infinite frequency response of the rotating micro-particles	$\overline{P_\infty}$
Equilibrium polarization of the rotating coffee cup model defined in Eqs. (3.32) and (3.33)	$\overline{P_{eq}}$
The equilibrium retarding polarization defined in Eq. (3.14)	$\overline{P_{eq}^0}$
Equilibrium retarding polarization as observed in frame rotating with spin velocity	$\overline{P_{eq}^\omega}$
The two-dimensional Poiseuille volume flow rate	Q
Zero electric field (purely viscous) 2D Poiseuille volume flow rate, $Q_0 = \Gamma h^3/12\eta$	Q_0
Quincke rotation induced 2D Poiseuille volume flow rate	Q_q
r-coordinate in spherical coordinates	r
Radius of spherical micro-particle	R
Internal angular momentum (vector) defined in Eq. (1.3)	$\bar{s}$
Time or time coordinate	t

Electrical torque exerted on the micro-particle	$\overline{T_e^{\dagger}}$
Viscous torque exerted on the micro-particle	$\overline{T_v^{\dagger}}$
Total stress tensor	$\overline{\overline{T}}$
Anti-symmetric part of the total stress tensor	$\overline{\overline{T_a}}$
Symmetric part of the total stress tensor	$\overline{\overline{T_s}}$
y-component of the continuum linear velocity, $\bar{v} = u_y \bar{i}_y + u_z \bar{i}_z$	u_y
z-component of the continuum linear velocity, $\bar{v} = u_y \bar{i}_y + u_z \bar{i}_z$	u_z
Dimensionless linear velocity	u^*
Zero electric field (purely viscous) total linear velocity (dimensionless)	u_0^*
Quincke rotation induced linear velocity (dimensionless)	u_q^*
The Couette boundary driving velocity	U_0
Continuum linear flow velocity vector	$\bar{v}$
Microscopic liquid convection velocity	$\overline{v^{\dagger}}$
Characteristic velocity defined by Eq. (5.29) for Poiseuille flow	V_0
Dimensionless parameter defined in Eq. (5.5)	V^*
Linear velocity on the surface of the rotating micro-particle	$\overline{V}$
x-coordinate in Cartesian coordinates	x
y-coordinate in Cartesian coordinates	y
y-coordinate defined in Fig. 3.2	y''
The associated Legendre function, $Y_l^{\kappa}(\cos\theta)$	Y_l^{κ}
z-coordinate in Cartesian coordinates	z
Dimensionless z-coordinate	z^*
z-coordinate defined in Fig. 3.2	z''

.

Greek Alphabets

The elements of the polarizability tensor (i and j are indices)	α_{ij}
y-component of polarizability defined in Eq. (4.7)	α_y
z-component of polarizability defined in Eq. (4.7)	α_z
Ratio of the polarizabilities, $\alpha^* = \alpha_y / \alpha_z = -\tau_{MW}\Omega$	α^*
The (microscopic) polarizability tensor	$\overline{\overline{\alpha}}$
The boundary condition selection parameter	β
Shear rate in Couette flow (dimensionless)	γ^*
The Poiseuille flow driving pressure gradient, $\Gamma = -dp/dy$	Γ
Reference pressure gradient, $\Gamma_r = 2\times10^4 \ (Pa/m)$	Γ_r
Dimensionless pressure gradient	Γ^*
Small perturbation of micro-particle rotation	$\delta\Omega$
The Kronecker delta, ($\delta_{i=j}=1$, $\delta_{i\neq j}=0$)	δ_{ij}
Effective shear rate defined in Eq. (5.23) for Poiseuille flow	δ^*
Permittivity of free space, $\varepsilon_0 = 8.854\times10^{-12} \ (C^2/N\cdot m^2)$	ε_0
Permittivity of the liquid phase of the ER fluid	ε_1
Permittivity of the solid phase (micro-particle) of the ER fluid	ε_2
Permittivity of air	ε_{air}
The scalar macroscopic effective permittivity defined in Eq. (3.25)	ε_{eff}
Elements of the effective permittivity tensor (i and j are indices)	ε_{ij}
The macroscopic effective permittivity tensor	$\overline{\overline{\varepsilon}}_{eff}$
The permutation tensor	$\overline{\overline{\varepsilon}}$
Solid volume fraction of the suspended micro-particles	ϕ
ϕ-coordinate in spherical coordinates (mostly in Chapters 2 and 3)	ϕ
The microscopic electric potential	$\Phi^\dagger$
Zero electric field viscosity of ER fluid, $\eta \sim \eta_0(1+2.5\phi)$	η

Viscosity of the liquid phase, or carrier liquid, of the ER fluid	η_0
Viscosity when anti-symmetric stresses are present, $\eta_e = \eta + \zeta$	η_e
Effective viscosity of ER fluid	η_{eff}
Spin viscosity	η'
Dimensionless effective viscosity	η^*
Reference value of spin viscosity, $\eta'_0 = 1.53 \times 10^{-8}$ $(N \cdot s)$	η'_0
Dimensionless spin viscosity	η_p^*
Function defined in Eq. (4.18)	φ_{C1}
Function defined in Eq. (4.19)	φ_{C2}
Angle of rotation of coordinate transformation defined in Fig. 3.2 (i and j being indices)	φ_{ij}
Function defined in Eq. (5.10)	φ_{P1}
Function defined in Eq. (5.11)	φ_{P2}
Separation constant in Eq. (2.15)	κ
The second coefficient of viscosity	λ
The second coefficient of spin viscosity	λ'
Parameter defined in Eq. (5.28)	Λ
Magnetic permeability of free space, $\mu_0 = 4\pi \times 10^{-7}$ (N/A^2)	μ_0
Coefficients or constants in solutions shown in Section 4.4, i=1, 2, …etc.	μ_i
The modified bulk compressibility viscosity, $\nu = \lambda + \eta - \zeta$	ν
Sum of the spin viscosity and the second coefficient of spin viscosity, $\nu' = \eta' + \lambda'$	ν'
Coefficients or constants in solutions shown in Section 5.4, $i = 1, 2, 3, \ldots$etc.	Π_i
θ-coordinate in spherical coordinates	θ
Separation function for the θ-variable in Eq. (2.13)	Θ
Density of ER fluid	ρ
Density of Shell DIALA® AX oil	ρ_{AX}
Density of Silicone oil DC 200	ρ_{DC}
Free space charge density	ρ_f

Density of micro-particles	ρ_p
Density of PE micro-particles	ρ_{PE}
Conductivity of the liquid phase of the ER fluid	σ_1
Conductivity of the solid phase (micro-particle) of the ER fluid	σ_2
Surface charge density	σ_f
Charge relaxation time of the liquid phase of the ER fluid, $\tau_1 = \varepsilon_1/\sigma_1$	τ_1
Charge relaxation time of the solid phase (micro-particle) of the ER fluid, $\tau_2 = \varepsilon_2/\sigma_2$	τ_2
The magnetization relaxation time	τ_M
The Maxwell-Wagner charge relaxation time defined in Eq. (2.39)	τ_{MW}
Wall shear stress	τ_s
Elements of the Maxwell stress tensor (i and j being indices)	$\tau_{ij}^{\dagger}$
The traction vector	$\overline{\tau_t^{\dagger}}$
The Maxwell stress tensor (microscopic)	$\overline{\overline{\tau^{\dagger}}}$
x-component of the continuum spin velocity (scalar)	ω_x
Dimensionless spin velocity	ω^*
Zero electric field solution to spin velocity	ω_0^*
First root to Couette flow spin velocity in the zero spin viscosity limit	ω_{C1}^*
Second root to Couette flow spin velocity in the zero spin viscosity limit	ω_{C2}^*
Third root to Couette flow spin velocity in the zero spin viscosity limit	ω_{C3}^*
First root to Poiseuille flow spin velocity in the zero spin viscosity limit	ω_{P1}^*
Second root to Poiseuille flow spin velocity in the zero spin viscosity limit	ω_{P2}^*
Third root to Poiseuille flow spin velocity in the zero spin viscosity limit	ω_{P3}^*
Normalized (dimensionless) spin velocity	$\widetilde{\omega^*}$
Normalized (dimensionless) zero electric field spin velocity	$\widetilde{\omega_0^*}$
Differences in dimensionless spin velocity	$\Delta\omega^*$

Differences in normalized dimensionless spin velocity	$\Delta\widetilde{\omega^*}$
Continuum spin velocity vector	$\overline{\omega}$
Micro-particle (averaged) rotation speed (scalar)	Ω
Micro-particle (averaged) rotation speed (vector)	$\overline{\Omega}$
Averaged micro-particle rotation speed as observed from particle rotation frame	$\overline{\Omega^{\Omega}}$
Immersion depth of the electrode (inside)	ξ
Externally observed immersion depth of the electrode	ξ_{out}
Separation function for the r-variable in Eq. (2.13)	Ξ
Separation function for the ϕ-variable in Eq. (2.13)	Ψ
Vortex viscosity, $\zeta \sim 1.5\phi\eta_0$	ζ

.

Chapter 1
Introduction

1.1 Electrorheology

Electrorheological (ER) fluids are a class of fluids that consist of conducting or insulating dielectric solid micro-particles suspended within a continuous dielectric liquid medium. Due to the electrical property (*i.e.*, conductivity or permittivity) mismatch between the solid and liquid phases, one can control the formation of different microscopic structures formed by the micro-particles and subsequently the macroscopic material properties of the ER fluid such as the apparent or effective viscosity of the suspension via the application of external direct current (DC) or alternating current (AC) electric fields. This phenomenon is termed the "electro-rheological effect" first defined by W.M. Winslow in the year 1949 (Winslow, 1949). Further research in the field and literature have then categorized ER phenomena, based on the flow or rheological responses, into either positive ER or negative ER effects when the ER fluid is subjected to different forms or combinations of electric field excitations (Winslow, 1949; Klingenberg & Zukoski, 1990; Halsey, 1992; Foulc *et al.*, 1994; Boissy *et al.*, 1995; Wu & Conrad, 1997).

Upon the application of DC electric fields, Foulc *et al.* (1994) discussed the important role of electrical conductivities of the respective solid and liquid phases in determining the inter-particle electrical force interactions in ER fluids. Boissy *et al.* (1995) then further characterized and made distinctions of macroscopic positive and negative ER responses based on different ratios or relative magnitudes of the respective conductivities of the two phases. For ER fluids consisting

of micro-particles with a conductivity, σ_2, larger than that, σ_1, of the carrier liquid, stable particle chains are formed in the direction of the electric field so that the macroscopic fluid resistance against externally applied shear perpendicular to the electric field is enhanced and result in an increased measured effective viscosity—the positive ER effect (Winslow, 1949; Klingenberg & Zukoski, 1990; Halsey, 1992). On the other hand, when the conductivity of the carrier liquid is larger than that of the micro-particles, *i.e.*, $\sigma_1 > \sigma_2$, laminated layers (perpendicular to the electric field) of packed particles resulting from electromigration are formed adjacent to one of the two electrodes leaving a portion of the ER fluid relatively clear of particles and hence leading to a reduction in the resistance against externally applied shear forces perpendicular to the electric field; a decrease in the effective viscosity is thus measured—the negative ER effect (Boissy *et al.*, 1995; Wu & Conrad, 1997).

Despite the relatively sparse reports on negative ER effects over the past 60 years of ER research development, recent experimental observations have found that: (i) with a given constant shear rate or equivalently the Couette flow boundary driving velocity, the measured shear stress required to drive the Couette ER fluid flow is reduced (an effectively decreased viscosity) and (ii) at a given constant pressure gradient, the Poiseuille flow rate of the ER fluid can be increased both by applying a uniform DC electric field perpendicular to the direction of the flows (Lobry & Lemaire, 1999; Cebers *et al.*, 2000; Cebers *et al.*, 2002; Lemaire *et al.*, 2006; Pannacci *et al.*, 2007*a*; Lemaire *et al.*, 2008). The mechanism responsible for the observed apparent increased flow rate and decreased effective viscosity was attributed to the spontaneous electrorotation of the dielectric insulating micro-particles suspended within the more conducting carrier liquid, which is a mechanism different from the traditional electromigration or particle electrophoresis explanation as mentioned in previous negative ER literature (Boissy *et al.*, 1995; Wu & Conrad, 1997). This spontaneous particle electrorotation under the action of a uniform DC electric field is also often called "Quincke rotation" for G. Quincke's systematic study done in 1896 (Quincke, 1896; Melcher & Taylor, 1969; Melcher, 1974; Melcher, 1981; Jones, 1984; Jones, 1995). Here, for short hand notation purposes, we shall term the particle electromigration or electrophoresis induced negative ER effect as the negative ER effect of the first kind (nER1) and the spontaneous micro-particle electrorotation induced negative ER effect as the negative ER effect of the second kind (nER2).

1.2 Particle Electromechanics and Negative Electrorheology

The origin and the operating principles of Quincke rotation can be qualitatively illustrated by considering an insulating dielectric spherical micro-particle with permittivity ε_2 and conductivity σ_2 suspended in a slightly conducting carrier liquid having a permittivity of ε_1 and a conductivity of σ_1. The material property combination is chosen so that $\tau_2 > \tau_1$ where $\tau_1 = \varepsilon_1/\sigma_1$ and $\tau_2 = \varepsilon_2/\sigma_2$ are the charge relaxation time constants of the carrier liquid and the micro-particle, respectively. As the carrier liquid and the suspended micro-particle altogether are subjected to a uniform DC electric field, charge relaxation follows the Maxwell-Wagner (MW) polarization at the solid-liquid interface, and the suspended particle acquires a final equilibrium dipole moment in the opposite direction to that of the applied DC field for the condition of $\tau_2 > \tau_1$. This, however, is an unstable equilibrium, and as the applied DC electric field strength reaches a critical value (Jones, 1984; Jones 1995), namely,

$$E_c \equiv \left(1+\frac{\sigma_2}{2\sigma_1}\right)\sqrt{\frac{8\eta_0\sigma_1}{3\varepsilon_1\sigma_2(\tau_2-\tau_1)}}, \tag{1.1}$$

where η_0 is the viscosity of the carrier liquid, the liquid viscous dampening can no longer withstand any small perturbations misaligning the particle dipole moment and the applied DC field. The electrical torque resulting from the misalignment of the particle dipole moment and the electric field exceeds the liquid viscous torque exerted on the micro-particle giving rise to spontaneous, self-sustained particle rotation either clockwise or counter clockwise with the rotation axis being perpendicular to the planes defined by the electric field, *i.e.*, no *a priori* preferential direction for rotation.

The above physical picture can be further generalized and applied to a dilute collection of dielectric insulating micro-particles suspended in a slightly conducting carrier liquid medium, that is, a dilute particle-liquid suspension. Since there is no *a priori* preferential direction for Quincke rotation when the micro-particle suspension is subjected to a DC electric field strength greater than the critical electric field, E_c, we can expect that the rotation direction of the micro-particles suspended in a quiescent liquid being completely random except the constraint of the particle axis of rotation being perpendicular to the planes defined by the electric field. Note however that when the particle-liquid suspension, or ER fluid, is driven by a boundary shear

stress (for Couette flows) or a pressure gradient (for Poiseuille flows), the macroscopic background flow vorticity gives the suspended micro-particles, instead of by random chance, preferable directions for rotation via viscous interactions once an external DC electric field (generally larger than the critical field, E_c) is applied. It is this combined effect of microscopic particle electrorotation and macroscopic flow vorticity that gives rise to the newly observed nER2 phenomenon as described above (Lobry & Lemaire, 1999; Cebers *et al.*, 2000; Cebers *et al.*, 2002; Lemaire *et al.*, 2006; Pannacci *et al.*, 2007*a*; Lemaire *et al.*, 2008). Up to this point, no experimental evidence has observed an nER2 effect without initial background flow or vorticity when a DC electric field with strengths generally greater than E_c is applied (Lobry & Lemaire, 1999)—both initial vorticity and micro-particle Quincke rotation are required for nER2.

Additional to the experimental observations, scientists and engineers are always interested in the theoretical modeling of ER effects such that the ER responses can be predicted mathematically or computationally, and that commercial products such as electrically actuated dampers, clutches, or smart materials can be designed and realized. However, ER fluid flow modeling has also been very challenging due to its inherent solid-liquid two phase nature and the complexities involved at the microscopic level such as particle-particle interactions, particle-liquid interactions, electric and flow field interactions, and so on. Nonetheless, with the initial macroscopic flow vorticity and the micro-particle Quincke rotation identified as fundamental mechanisms responsible for the nER2 effect, we would like to take a step further and ask how to theoretically and mathematically model and describe this nER2 phenomenon, that is, how to model and describe the negative electrorheological responses of a particle-liquid suspension with the suspended micro-particles undergoing spontaneous electrorotation or Quincke rotation when the suspension is subjected to a uniform DC electric field and to an initial flow vorticity.

Although models are available in current literature for describing the new nER2 phenomenon, they are focused on first analyzing the dynamics of a single micro-particle in a shear flow subjected to a DC electric field and then substituting the micro-particle rotation speed solved from single particle dynamics into a two-phase volume averaged, effective continuum description of the suspension effective viscosity proposed by Brenner in the 1970s (Brenner, 1970; Lobry & Lemaire, 1999; Cebers *et al.*, 2000; Cebers *et al.*, 2002; Lemaire *et al.*, 2006; Pannacci *et al.*, 2007*a*; Lemaire *et al.*, 2008). Very little has been done in developing a continuum mechanical model from a more classical field theory based perspective or starting

point for predicting the dynamical behavior of fluids consisting of micro-particles undergoing spontaneous electrorotation. To the best of the author's knowledge, the ferrofluid spin-up flow is the most representative flow phenomenon arising from external field induced internal particle rotation in current rheology research (Moskowitz & Rosensweig, 1967; Rosensweig *et al.*, 1990; Rosensweig, 1997; Chaves *et al.*, 2006; Elborai, 2006; He, 2006; Chaves *et al.*, 2007, 2008).

1.3 The Ferrofluid Spin-up Flow and the Theory of Continuum Anti-symmetric/Couple Stresses

Ferrofluids consist of colloidally stabilized magnetic nanoparticles, typically magnetite, suspended in a non-magnetizable liquid. Spin-up flow phenomenon of ferrofluids was first observed by Moskowitz and Rosensweig in 1967 when a swirling flow pattern was found on the fluid surface by applying a rotating magnetic field to a beaker of ferrofluid (Moskowitz & Rosensweig, 1967; Rosensweig, 1997). Though current literature is more inclined to the theory of the origin and the direction of the swirling flow being respectively dependent on the surface stresses and the surface curvature conditions of the ferrofluid (Rosensweig *et al.*, 1990; Rinaldi, 2002), the introduction of magnetic body torque into the ferrofluid is still considered as one of the fundamental mechanisms or principles in understanding, describing, and analyzing the dynamical behavior of ferrofluid spin-up flows (Rosensweig, 1997; Rinaldi, 2002; Rinaldi & Zahn, 2002; Elborai, 2006; He, 2006; Chaves *et al.*, 2007, 2008).

In a ferrofluid spin-up flow, magnetic torque is introduced into the ferrofluid through the misalignment of the ferrofluid nanoparticle's permanent magnetization and the applied rotating magnetic field. The internal angular momentum of a continuum ferrofluid "parcel," $\overline{m}$, most likely containing a representative collection of carrier liquid molecules and rotating magnetic nanoparticles, becomes significant and the continuum stress tensor becomes anti-symmetric for strong enough magnetic body torques introduced at the microscopic level. A moment-of-inertia density, $\overline{\overline{I}}$, is defined for the ferrofluid parcel based on the mass distributions of the carrier liquid molecules and magnetic particles in the parcel. A continuum spin velocity, $\overline{\omega}$, (column vector) is then defined by the product of the internal angular momentum density (column vector) with the inverse of the moment-of-inertia density (tensor), *i.e.*,

$$\overline{\omega} \equiv \overline{\overline{I}}^{-1} \cdot \overline{m}, \tag{1.2}$$

(Dahler & Scriven, 1961; Dahler & Scriven, 1963; Condiff & Dahler, 1964). Since a ferrofluid continuum contains an enormous amount of these parcels, the spin velocity, $\overline{\omega}$, is defined as a continuous field quantity which in general, can be a function of space and time, *i.e.*, $\overline{\omega} = \overline{\omega}(x, y, z, t)$. In order to macroscopically model the internal microscopic particle rotation effects on the continuum fluid flow motion, a continuum angular momentum conservation equation is added and coupled with the linear momentum equation so that, in general, the externally applied magnetic body couple, angular momentum conversion between linear and spin velocity fields, and the diffusive transport of angular momentum are incorporated into the description of the flow momentum balances (Dahler & Scriven, 1961; Dahler & Scriven, 1963; Condiff & Dahler, 1964; Eringen, 1966; Rosensweig, 1997).

A fundamental issue in the current development of ferrofluid spin-up flow is whether the diffusive angular momentum transport or couple stress has a finite contribution in the angular momentum balances of the flow. The current consensus is that the couple stress contribution is vanishingly small, *i.e.*, zero spin viscosity or diffusive transport conditions, as discussed in Rosensweig (1997), Schumacher *et al.* (2003), Chaves *et al.* (2007, 2008), and so on. In a most recent work by Feng *et al.* (2006), scaling and numerical analyses were presented to show that in the limit of an effective continuum, the angular momentum equation is to be couple stress free and the value of the spin viscosity should be identically zero. However, spin-up velocity profiles measured by ultrasound velocimetry reported by Elborai (2006), He (2006), and Chaves *et al.* (2007, 2008) were compared with the numerical simulations of the full spin-up flow governing equations and found that the experimental and numerical results would agree only if the spin viscosity assumes some finite value instead of being vanishingly small or identically zero.

Another issue perhaps related to the debate over zero or finite spin viscosities (or couple stresses) is about the exact definition of the flow kinematic variable of spin velocity, $\overline{\omega} = \overline{\omega}(x, y, z, t)$, when modeling ferrofluid spin-up flows with the continuum anti-symmetric/ couple stress tensor theories and the continuum linear and angular momentum governing equations. By extensive literature review, it can be found that the continuum spin velocity field, $\overline{\omega}$, is seemly often defined as the averaged micro-particle rotation speed, $\overline{\Omega}$, or vice versa.

The continuum angular momentum theory for structured continua of Dahler and Scriven (1961, 1963) and Condiff and Dahler (1964) was originally applied for modeling flow motion of fluids consisting of polar molecules. Both phenomenological and statistical approaches were utilized in deriving the governing linear and angular momentum equations and the definition of the spin velocity, $\bar{\omega}$, is more likely a continuum kinematic field variable that characterizes the rate of internal rotation of continuum fluid particles or "parcels" defined under the framework of the continuum hypothesis (Fox & McDonald, 1998). Eringen (1964, 1966) also derived a similar set of continuum linear and angular momentum equations for micro-polar fluent media from a purely mathematical tensorial approach without reference to a detailed description of the microscopic picture. The equivalent kinematic variable to the spin velocity field was termed "micro-rotation" in Eringen's model. Without a detailed description of the microscopic picture, it seems that the "micro-rotation" kinematic variable can only be a field or continuum mechanical quantity. Kaloni (1992) pointed out the similarities found between the governing continuum linear and angular momentum equations for polar continua developed by Dahler and Scriven (1961, 1963) and Condiff and Dahler (1964), and by Eringen (1964, 1966).

With the invention of ferrofluids and the observation of ferrofluid spin-up flows in the 1960s, Zaitsev and Shliomis (1969) gave a first analysis of the ferrofluid spin-up problem including the effects of diffusion of particle rotation angular momentum. Their original definition of internal angular momentum, $\bar{s}$, includes the total angular momentum of the suspended particles within a given volume and that of the carrier liquid entrained by rotation of the particles. Shliomis (1972) further proposed a constitutive relation relating the internal angular momentum, $\bar{s}$, and the averaged micro or nano particle rotation velocity, $\bar{\Omega}$, through

$$\bar{s} = I_{vdp}\bar{\Omega}, \tag{1.3}$$

where I_{vdp} is the volume density of the sum of the particles' moment of inertia and is given explicitly in a very recent work by Shliomis (2002) for a suspension of spherical particles as

$$I_{vdp} = \frac{\rho_p \phi d^2}{10}, \tag{1.4}$$

where ρ_p, d, and ϕ are respectively the solid particle density, particle diameter, and solid volume fraction of the particles. The kinematic variable representing the internal rotation and related to the internal angular momentum of the ferrofluid was then based on the averaged nano

(or micro) particle rotation speed, $\overline{\Omega}$. In order to account for the non-equilibrium effects of flow motion on the macroscopic magnetization during the ferrofluid spin-up phenomenon, a first magnetization relaxation equation was also presented by Shliomis in 1972 (Shliomis, 1972; Shliomis, 2002) with the averaged particle rotation speed, $\overline{\Omega}$, being the non-equilibrium variable.

Rosensweig *et al.* (1990) pointed out the similarity or equivalence between the governing linear and angular momentum equations used by Zaitsev and Shliomis (1969) and by Dahler and Scriven (1961, 1963) and Condiff and Dahler (1964) for modeling fluid flows with internal angular momentum. By examining Eqs. (1.2) and (1.3), we can also find the very similar functional forms of the two constitutive relations. Note however that the respective physical meanings or definitions of the spin velocity field, $\overline{\omega}$, and the averaged particle rotation speed, $\overline{\Omega}$, as well as those of Eq. (1.2) and Eq. (1.3) should still be carefully distinguished. The formulation by Dahler and Scriven (1961, 1963) and Condiff and Dahler (1964) was then extensively employed in modeling ferrofluid spin-up flows as in Rosensweig *et al.* (1990), Rosensweig (1997, 2002), Rinaldi (2002), Rinaldi & Zahn (2002), Elborai (2006), He (2006), and Chaves *et al.* (2007, 2008).

In 1970, Brenner (1970) considered the macroscopic effective stress tensor and effective viscosity arising from the dynamic influences of a dilute collection of rotating spherical solid micro-particles suspended in a carrier viscous liquid at the microscopic level. An elegant two scale analysis was performed by first finding the microscopic local flow field near a translating and rotating micro-particle with Lamb's general spherical harmonics solution (Lamb, 1945) and then by averaging the dynamic and kinematic variables involved, *e.g.*, microscopic pressure and velocity fields, over a representative volume of the particle-liquid suspension (a procedure similar to modern homogenization methods) to obtain an "effective continuum" stress tensor. This two-phase effective continuum stress tensor is anti-symmetric, is dependent upon the averaged micro-particle rotation speed, $\overline{\Omega}$, and has a functional form similar to those found in Condiff and Dahler (1964) and Shliomis (1972, 2002). However, the physical picture or mechanism of couple stress or spin viscosity was not likely seen to be built into Brenner's 1970 model for the macroscopic stress tensor resulting from microscopic particle rotation.

In reviewing all this historical development of modeling fluid flows possessing internal angular momentum or micro/nano-particle rotations, we frequently find that the governing linear and angular momentum equations as well as constitutive relations from different and independent formulations are often very much similar in spite of the different original physical meanings defined for the kinematic variables of spin velocity, $\overline{\omega}$, and averaged particle rotation speed, $\overline{\Omega}$, in their respective modeling formulations. Perhaps this is why the distinction between the spin velocity and the averaged particle rotation speed begins to blur, and why the averaged particle rotation speed (or angular velocity) is employed in continuum mechanical conservation laws in more recent micro-polar fluid and ferrofluid literature (Lukaszewicz, 1999; Rosensweig, 2002; Feng *et al.*, 2006). Still, it remains an open question of whether the spin velocity field, $\overline{\omega}$, and the averaged particle rotation speed, $\overline{\Omega}$, are exactly and unambiguously the same (or different). The interrelationships among the spin velocity, macroscopic continuum vorticity, microscopic local vorticity, and the local micro- or nano-particle rotation speed also remain unclear and require further investigation.

The continuum mechanical theory for negative ER fluid flows with internal micro-particle electrorotation developed in the following chapters shall follow the treatment of Dahler and Scriven (1961, 1963) and Condiff and Dahler (1964) and those of the general ferrohydrodynamics literature (Rosensweig, 1997, 2002; Rinaldi, 2002; Rinaldi & Zahn, 2002; Elborai, 2006; He, 2006; Chaves *et al.*, 2007, 2008). However, we shall view the spin velocity as a continuum kinematic variable as defined in Eq. (1.2) and in the second paragraph of this section, *i.e.*, we view the macroscopic continuum spin velocity and the microscopic micro-particle rotation speed as different quantities.

1.4 Motivation, Aim, and Plan of Thesis

After reviewing the background theories and the issues involved in both the negative electrorheological effect of the second kind (nER2) and the ferrofluid spin-up flow, the present thesis is motivated by the following questions:

(i) Apart from the current treatment of nER2 by combining single particle dynamics and two-phase effective continuum theories (Brenner, 1970; Lobry & Lemaire, 1999; Cebers *et al.*, 2000; Cebers *et al.*, 2002; Lemaire *et al.*, 2006; Pannacci *et al.*, 2007*a*; Lemaire *et al.*,

2008), can we develop a fully continuum mechanical model with the developed governing equations being physically parallel and mathematically similar to those employed in analyzing ferrofluid spin-up flows for describing, analyzing, and predicting nER2 behavior from a more classical field theory based perspective?

(ii) With the developed governing equations for nER2 being physically parallel and mathematically similar to those employed in analyzing ferrofluid spin-up flows, what are the respective nER2 responses under zero spin viscosity and finite spin viscosity conditions?

(iii) To this point, very little information can be found on the polarization relaxation and equilibrium polarization for a dielectric particle-liquid suspension under the non-equilibrium influences of micro-particle rotation speed, $\overline{\Omega}$, continuum linear flow velocity, $\bar{v}$, and continuum angular spin velocity, $\overline{\omega}$. Is it possible to find a simple way of incorporating all three non-equilibrium effects to our model for describing the polarization relaxation process involved in the nER2 phenomenon?

Motivated by the above reasons, this thesis is therefore aimed at developing a classical continuum mechanical model that combines particle electrorotation as well as anti-symmetric and couple stress theories for describing the negative electrorheological behavior of a particle-liquid mixture (termed ER fluid henceforward) subjected to a DC electric field perpendicular to the direction of the flow and with a strength generally higher than the Quincke rotation threshold.

In Chapter 2, we formulate and present the general governing equations, in their full form, for studying the nER2 phenomenon from a classical phenomenological field theory based continuum mechanical perspective. Identifying the "mathematically analogous, physically parallel mechanisms" governing the respective electrorotation and ferrofluid spin-up flows as summarized in Table 1.1, the governing continuum linear and angular momentum equations originally used for ferrofluid spin-up analyses (Rosensweig, 1997, 2002; Rinaldi, 2002; Rinaldi & Zahn, 2002; Elborai, 2006; He, 2006; Chaves *et al.*, 2007, 2008) are modified by changing the external magnetic body force and torque densities (based on macroscopic ferrofluid magnetization and applied magnetic fields) into external electric body force and torque densities (based on macroscopic ER fluid polarization and applied electric fields) for analyzing and describing the nER2 responses.

The second half of Chapter 2 is devoted to the theoretical foundations of Quincke rotation of a single spherical solid micro-particle. Solutions to the electric potential, electric field, and dipole

	Electrorotation (Quincke rotation) flow	Ferrofluid spin-up flow
Particles	Insulating dielectric (plastic) micro-particle	Magnetic nano-particles
Micro scale polarity	Maxwell-Wagner (MW) polarization	Permanent magnetic dipole
Macro scale polarity	Polarization $\overline{P}$ (due to induced free surface charge)	Magnetization $\overline{M}$
Applied field	DC electric field $\overline{E}$ (combined with flow vorticity)	Rotating magnetic field $\overline{H}$
Body torque density	$\overline{P}\times\vec{E}$	$\mu_0\overline{M}\times\overline{H}$

Table 1.1 Summary of physical analogy between the electrorotation and ferrofluid spin-up flows.

momentum are to be solved for an insulating dielectric spherical solid micro-particle suspended in a slightly conducting dielectric carrier liquid subjected to a uniform DC electric field rotating at a certain angular velocity. The electric torque exerted on such a micro-particle can be derived by the dielectrophoretic approximation or the method of Maxwell stress tensor. The derived electric torque is then balanced by the carrier liquid viscous torque and steady state solutions to the particle Quincke rotation angular velocity as well as the critical electric field strength, Eq. (1.1), can be obtained, respectively.

In Chapter 3, we first review the basic ideas of Shliomis' first magnetization relaxation equation (1972, 2002), Cebers' dipole relaxation equation for single particle Quincke rotation (1980), and Xiao *et al.*'s (2008) dynamic effective medium theory based on the Lorentz cavity model. Summarizing these basic ideas, we present a first polarization relaxation equation and its corresponding equilibrium polarization that account for the three possible non-equilibrium variables, *i.e.*, the micro-particle rotation speed, $\overline{\Omega}$, continuum linear flow velocity, $\overline{v}$, and continuum angular spin velocity, $\overline{\omega}$. Note that this proposed polarization relaxation equation along with its corresponding equilibrium polarization are specifically designed for the *retarding part* of the total ER fluid polarization, that is, the part of polarization directly related to the Maxwell-Wagner (MW) polarization induced surface charges around the solid spherical micro-particles. By treating the micro-particle rotation speed, $\overline{\Omega}$, and the continuum angular spin velocity, $\overline{\omega}$, as separate quantities, we would like to promote the idea or question of whether the two quantities are exactly and unambiguously the same (or different).

With the theoretical foundations laid out and the proposed continuum mechanical model developed in Chapters 2 and 3, we apply our developed continuum mechanical model to respectively study and analyze the nER2 responses for Couette and Poiseuille flow geometries in Chapters 4 and 5. In both Chapters 4 and 5, the general governing equations presented in Chapter

2 are reduced and simplified for their respective flow geometries. For the two flow geometries, the respective simplified governing equations are then solved to obtain analytical expressions in the zero spin viscosity limit and in the finite spin viscosity small spin velocity limit. Parametric studies are then performed for the two geometries.

For Couette flow geometries discussed in Chapter 4, the spin velocity field, $\overline{\omega}$, and the effective viscosity, η_{eff}, are studied in terms of the externally applied DC electric field, $\overline{E}$, and the Couette boundary driving velocity, U_0, in the zero spin viscosity, $\eta' = 0$, limit. As for the finite spin viscosity small spin velocity limit ($\eta' \neq 0, \tau_{MW}^2 \omega_x^2 \ll 1$), the spin velocity field, $\overline{\omega}$, linear velocity field, $\overline{v}$, and the effective viscosity, η_{eff}, are analyzed as functions of the externally applied DC electric field, $\overline{E}$, the Couette boundary driving velocity, U_0, the spin viscosity, η', and the boundary condition selecting parameter, β. Similarly, for Poiseuille flow geometries discussed in Chapter 5, the spin velocity field, $\overline{\omega}$, linear velocity field, $\overline{v}$, and the two dimensional (2D) volume flow rate, Q, are studied in terms of the externally applied DC electric field, $\overline{E}$, and the Poiseuille driving pressure gradient, Γ, in the zero spin viscosity, $\eta' = 0$, limit. On the other hand, for the finite spin viscosity small spin velocity limit ($\eta' \neq 0, \tau_{MW}^2 \omega_x^2 \ll 1$), the spin velocity field, $\overline{\omega}$, linear velocity field, $\overline{v}$, and the 2D volume flow rate, Q, are analyzed as functions of the externally applied DC electric field, $\overline{E}$, the Poiseuille driving pressure gradient, Γ, the spin viscosity, η', and the boundary condition selecting parameter, β.

Chapter 6 compares the present continuum mechanical results respectively obtained for both Couette and Poiseuille flow geometries in Chapters 4 and 5 with the results obtained from experimental observation and two-phase effective medium theories as found in current literature.* Results obtained in both the zero spin viscosity limit and the finite spin viscosity small spin velocity limit are to be compared and discussed. We shall also discuss how different

*Experimental considerations as part of the present thesis work regarding material selection, ER fluid synthesis, liquid impedance measurements, viscosity measurements, construction of negative ER phenomenon testing equipment, and the electrorotation assisted Poiseuille flow rate experiment are given in **Appendix**.

choices of equilibrium polarization employed in our polarization relaxation model affect the resulting theoretical predictions of the nER2 responses at the end of Chapters 4 and 5.

Chapter 7 concludes the thesis by summarizing the principle findings and the state-of-the-art contributions of this thesis and by outlining directions for potential future work. Hopefully, the theoretical results and discussions obtained for internal micro-particle electrorotation induced negative electrorheological flow responses given in this thesis can contribute substantially to the sparse negative electrorheology research and serve as a parallel, analogous research that offers new, complementary insights to the ferrofluid spin-up problem.

The theory for internal micro-particle electrorotation induced negative electrorheological flow responses presented in this thesis should find potential applications in designing electrically actuated dampers, clutches, and smart materials (Espin *et al.*, 2005; Esmonde *et al.*, 2009) as well as in modeling or analyzing the electrorheological or magnetorheological responses of physiological and human blood flows (Happel & Brenner, 1983; Larson, 1998; Lukaszewicz, 1999; Haik *et al.*, 2001; Khashan & Haik, 2006).

Chapter 2
Theoretical Foundations and Governing Equations

In this chapter, we lay down the theoretical foundations and mathematical tools for describing and analyzing the nER2 responses. These ideas and tools are then further applied to obtain the mathematical expressions and solutions given in Chapters 3, 4, and 5.

In order to quantitatively model and describe the present negative ER flow phenomenon, several physical principles involved are considered: (i) the continuity or mass conservation, (ii) the linear momentum balance, (iii) the angular momentum balance, (iv) the electro-quasi-static (EQS) field, and (v) the polarization relaxation of the negative ER fluid flow. For the first part of this chapter, we shall formulate and present the continuum governing field equations that encompass and characterize aspects (i) through (iv), namely, the continuity equation, the linear momentum equation, the angular momentum equation, and the EQS Maxwell's equations. The second part of this chapter is then devoted to solving the electric potential, electric field, and dipole moment of a dielectric insulating spherical micro-particle suspended in a slightly conducting liquid undergoing spontaneous electrorotation, or Quincke rotation. Based on these solutions of micro-particle Quincke rotation, we develop and present the polarization relaxation equation along with its accompanying equilibrium polarization (aspect (v)) in Chapter 3. We summarize the assumptions used or employed in the theoretical development of our continuum mechanical formulation for the nER2 effect at the end of this chapter.

2.1 Electrorheology—Governing Equations for Micro-polar Fluids

As we have learned at the end of Chapter 1, a very close resemblance or similarity can be drawn between the ferrofluid spin-up flow and nER2 by identifying the "mathematically analogous, physically parallel mechanisms" governing the respective magnetic and electric counter parts as summarized in Table 1.1. The macroscopic rheological responses of the two flows are also closely related to the micro or nano scale particle dynamics as well as the entrainment of surrounding carrier liquid due to particle rotation.

With the above physical picture and by carefully examining the governing continuum mechanical field equations employed in ferrofluid spin-up flow studies (Rosensweig, 1997, 2002; Rinaldi, 2002; Rinaldi & Zahn, 2002; Elborai, 2006; He, 2006; Chaves *et al.*, 2007, 2008), we formulate and present the governing continuum mechanical equations for describing the internal micro-particle rotation induced negative ER effect, nER2, as: the mass continuity equation for incompressible flow,

$$\nabla\cdot\bar{v}=0, \tag{2.1}$$

the linear momentum equation,

$$\rho\frac{D\bar{v}}{Dt}=-\nabla p+\left(\bar{P}_t\cdot\nabla\right)\bar{E}+2\zeta\nabla\times\bar{\omega}+\nu\nabla\left(\nabla\cdot\bar{v}\right)+\eta_e\nabla^2\bar{v}, \tag{2.2}$$

and the angular momentum equation,

$$I\frac{D\bar{\omega}}{Dt}=\bar{P}_t\times\bar{E}+2\zeta\left(\nabla\times\bar{v}-2\bar{\omega}\right)+\nu'\nabla\left(\nabla\cdot\bar{\omega}\right)+\eta'\nabla^2\bar{\omega}, \tag{2.3}$$

where $\bar{v}$ is the linear flow velocity, ρ is the ER fluid density, p is the pressure in the flow field, $\bar{P}_t$ is the fluid total polarization, $\bar{E}$ is the electric field, $\bar{\omega}$ is the flow spin velocity, I is the average moment of inertia per unit volume, η' is the spin viscosity, ζ is the vortex viscosity which is related to the carrier liquid viscosity, η_0, and particle solid volume fraction, ϕ, through $\zeta\sim1.5\phi\eta_0$ for dilute suspensions with $\phi\ll1$, $\nu=\lambda+\eta-\zeta$ is the sum of the second coefficient of viscosity, λ, the zero field ER fluid viscosity, $\eta\sim\eta_0\left(1+2.5\phi\right)$, and the negative of the vortex viscosity, ζ, $\eta_e=\eta+\zeta$ is the sum of the zero field ER fluid viscosity and the vortex viscosity, $\nu'=\eta'+\lambda'$ is the sum of the spin viscosity, η', and the second coefficient of spin viscosity, λ' (Condiff & Dahler, 1964; Brenner, 1970; Rosensweig, 1997, 2002), and D/Dt is the material

derivative given by

$$\frac{D}{Dt}=\frac{\partial}{\partial t}+\left(\bar{v}\cdot\nabla\right). \tag{2.4}$$

Note that Eq. (2.2) generally follows the form of the well known Navier-Stokes equation. However, by introducing microscopic polarity and micro-particle rotation to the macroscopic fluid flow, additional terms are included in Eq. (2.2) to account for the Kelvin body force density, $\left(\bar{P}_t\cdot\nabla\right)\bar{E}$, and the anti-symmetric force density, $2\zeta\nabla\times\bar{\omega}$, as contributions in the linear momentum balances of the fluid flow. Moreover, Eq. (2.3) characterizes the ER fluid parcel spin velocity, $\bar{\omega}$, so that the torque and angular momentum balances resulting from the electrical torque input and fluid motion can be described and related to other variables pertinent to this problem. In Eq. (2.3), the left hand side (LHS) represents the angular momentum per unit volume of a continuum ER fluid parcel; the first term on the right hand side (RHS) represents the electrical torque density introduced to the flow field via the rotating micro-particles under the action of the external DC field; the second term on the RHS represents the angular momentum density transformation or conversion between the vorticity and the spin velocity fields; the third term on the RHS represents the gradient of the divergence of the spin velocity and is analogous to the "gradient of the divergence of the velocity" term in Eq. (2.2) that measures the bulk compression effects in the fluid flow; and finally, the fourth term on the RHS represents the diffusive transport of angular momentum within the flow field (Rosensweig, 1997, 2002).

Our development of Eqs. (2.1)-(2.4) closely follows those employed in the ferrofluid spin-up problem. However, we have carefully changed the fluid magnetization to ER fluid total polarization and substituted the externally applied electric field for the applied magnetic field so that the magnetic body force and torque become electric body force and torque inputs in the continuum linear and angular momentum equations.

Rigorously speaking, the expressions of the vortex viscosity, $\zeta\sim 1.5\phi\eta_0$, and the zero electric field ER fluid (suspension) viscosity, $\eta\sim\eta_0\left(1+2.5\phi\right)$, *i.e.*, the Einstein's relation, are results derived from models based on micro-/nano-particle rotation speeds (Shliomis, 1972) or a two-phase effective medium (Brenner, 1970) and are not exactly suited for use in the general continuum mechanical field equations (Dahler & Scriven, 1961; Dahler & Scriven, 1963; Condiff & Dahler, 1964; Lukaszewicz, 1999). However, since these viscosity relations are up to

now the best approximations (to the exact continuum picture) available as well as widely accepted and extensively used in the general ferrofluid literature (Rosensweig, 1997; Rinaldi, 2002; Rinaldi & Zahn, 2002; Elborai, 2006; He, 2006; Chaves *et al.*, 2007, 2008), we have employed these definitions or relations of the vortex viscosity and zero electric field viscosity in our current development of Eqs. (2.1)-(2.4) for the nER2 phenomenon.

With the governing equations for the mechanical subsystem being setup, we now turn to the development of the electrical subsystem for the present negative ER fluid flow, *i.e.*, nER2. The electric field in the ER flow field is generally described by the electro-quasi-static (EQS) Maxwell equations (Melcher, 1981; Haus & Melcher, 1989), namely,

$$\nabla \times \overline{E} \approx 0, \tag{2.5}$$

and

$$\nabla \cdot \overline{D} = \rho_f \approx 0, \tag{2.6}$$

with

$$\overline{D} = \varepsilon_0 \overline{E} + \overline{P}_t, \tag{2.7}$$

where $\overline{D}$ is the electric displacement field, ρ_f is the free space charge density, and $\varepsilon_0 = 8.854 \times 10^{-12}$ ($C^2/N \cdot m^2$, or F/m) is the electric permittivity of free space. Here, we have assumed that on the macroscopic continuum level, the free space charge density is zero. We approach this non-equilibrium problem of nER2 from the EQS Maxwell's equations instead of the full Maxwell's equations because of the following reasons: (i) the characteristic length scale of the rotating micro-particles is much less than the characteristic length scale for electromagnetic wave propagation and (ii) the characteristic frequency for Quincke rotation (~kHz, as will be seen in the following development of this thesis) is generally much less than those of most electromagnetic waves (~GHz) (Haus & Melcher, 1989).

To complete the description of the electrical subsystem, we need a continuum phenomenological polarization relaxation equation and its accompanying equilibrium polarization that account for the non-equilibrium effects of both the linear and angular motions on the ER fluid polarization. Since the torque input at the micro scale for particle electrorotation is related to the induced surface charge around the surface of the micro-particles, we shall focus on how non-equilibrium motion, *i.e.*, micro-particle rotation, $\overline{\Omega}$, continuum fluid spin velocity,

$\bar{\omega}$, and continuum fluid velocity, $\bar{v}$, affects the *retarding polarization*, $\bar{P}$ (the part of polarization directly related to the particle surface charges), instead of the total polarization of the ER fluid, $\bar{P}_t$. Nevertheless, this development of the polarization relaxation equation and its accompanying equilibrium polarization for the ER fluid will require the microscopic picture of micro-particles undergoing Quincke rotation as given in the next section, and thus will be postponed until Chapter 3.

Before closing this section, several remarks regarding the governing equations of Eqs. (2.1)-(2.7) are to be made:

(i) By using the incompressibility condition given in Eq. (2.1), we are treating the ER fluid, or particle-liquid suspension, as a homogenous single phase continuous medium with no further detailed microscopic two-phase structure. We have assumed that a representative amount or ensemble of solid micro-particles and carrier liquid molecules makes up one continuum ER fluid particle or "parcel" under the general continuum hypothesis. This assumption most likely views the ER fluid parcel as a statistical mass average instead of a volume average over the two-phase microscopic details.

(ii) With the above physical picture, the average moment of inertia per unit volume, I, given on the LHS of Eq. (2.3) is assumed to follow the physical definition given by Eq. (1.2) instead of that given by Eqs. (1.3) and (1.4). In general, the moment of inertia per unit volume (or density) is a tensor that describes the mass distributions of the carrier liquid molecules and dielectric particles in the ER parcel. To reduce the complexities involved in dealing with a tensor quantity, we consider that the ER fluid is homogeneous and isotropic and that the moment of inertia density tensor, $\bar{\bar{I}}$, is to be replaced by an averaged scalar moment of inertia per unit volume, I, in Eq. (2.3). Note however that for viscous slow flows considered in the present thesis, the inertia terms in the equations of motion, Eqs. (2.2) and (2.3), are generally negligible.

(iii) Also following the physical picture given in Remark (i), the physical quantities or variables found in Eqs. (2.1)-(2.7) such as the spin velocity field, $\bar{\omega}$, linear velocity field, $\bar{v}$, hydrodynamic pressure field, p, electric field, $\bar{E}$, displacement field, $\bar{D}$, and so on are to be defined for a homogeneous single phase continuous medium within the mathematical domain setup by the ER fluid flow.

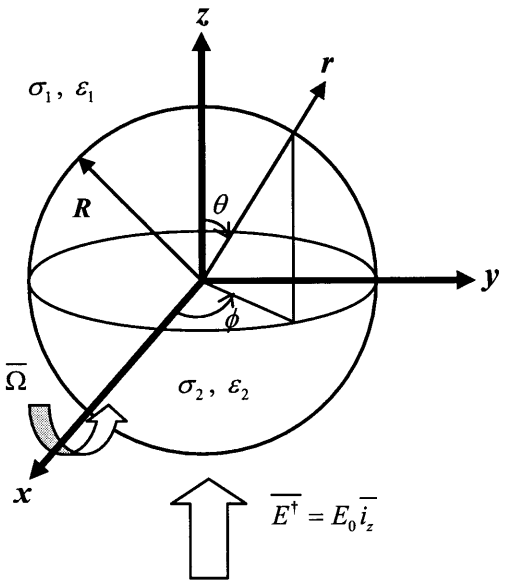

Figure 2.1. The schematic diagram for the problem of solving the EQS fields within and around a spherical particle of radius R (with conductivity of σ_2 and permittivity of ε_2) suspended in a liquid medium (with σ_1, ε_1) rotating at constant angular velocity $\overline{\Omega} = \Omega \overline{i_x}$ subjected to a uniform DC electric field, $\overline{E^\dagger} = E_0 \overline{i_z}$.

(iv) Note that by definition, the spin velocity, $\overline{\omega}$, and the linear velocity, $\overline{v}$, shown in Eqs. (2.2) and (2.3) are continuum field variables which are related to the respective averages of the internal angular momentum and linear momentum over collections of micro-particles and carrier liquid molecules in an ER fluid parcel. They should be distinguished from the micro-particle rotation velocity, $\overline{\Omega}$, which is the microscopic angular velocity of the suspended micro-particles within an ER fluid parcel. The microscopic picture or information of a suspension of micro-particles undergoing Quincke rotation as well as the Maxwell-Wagner (MW) induced surface charge and dipole moment will basically only enter (additional to the definitions of vortex and zero electric field viscosities) our present classical field theory based continuum mechanical formulation through the equilibrium polarization and the polarization relaxation equation as will be discussed in the next chapter.

2.2 Particle Electromechanics—Quincke Rotation

We start our discussions on Quincke rotation of a "single micro-particle" by considering the two region problem of the EQS fields inside ($r < R$) and outside ($r > R$) of a dielectric insulating spherical solid micro-particle with a radius of R, a permittivity of ε_2, and an electric conductivity of σ_2 rotating at a constant angular speed, $\overline{\Omega} = \Omega \overline{i_x}$, suspended in a slightly conducting liquid medium (with a permittivity of ε_1 and a conductivity of σ_1) subjected to a constant uniform DC electric field, $\overline{E^\dagger} = E_z^\dagger \overline{i_z} = E_0 \overline{i_z}$ ($\dagger$ denotes microscopic field quantities), as shown in Fig. 2.1. For this EQS problem,

$$\nabla \times \overline{E^\dagger} \approx 0, \tag{2.8}$$

and thus

$$\overline{E^\dagger} = -\nabla \Phi^\dagger, \tag{2.9}$$

where $\Phi^\dagger$ is the electric potential. Since in both regions, there is no free space charge present and the respective electric permittivities are constant, Gauss' law for the displacement field, *i.e.*,

$$\nabla \cdot \overline{D^\dagger} = 0, \tag{2.10}$$

becomes

$$\nabla \cdot \overline{E^\dagger} = 0, \tag{2.11}$$

for the two regions. By substituting Eq. (2.9) into Eq. (2.11), we write the resulting Laplace's equation in spherical coordinates as

$$\nabla^2 \Phi^\dagger = \frac{1}{r^2}\frac{\partial}{\partial r}\left(r^2 \frac{\partial \Phi^\dagger}{\partial r}\right) + \frac{1}{r^2 \sin\theta}\frac{\partial}{\partial \theta}\left(\sin\theta \frac{\partial \Phi^\dagger}{\partial \theta}\right) + \frac{1}{r^2 \sin^2\theta}\frac{\partial^2 \Phi^\dagger}{\partial \phi^2} = 0. \tag{2.12}$$

We separate the variables with the form suggested by Jackson (1999), namely,

$$\Phi^\dagger(r,\theta,\phi) = \frac{\Xi(r)}{r}\Theta(\theta)\Psi(\phi), \tag{2.13}$$

and arrive at the following set of separated equations, *i.e.*,

$$\frac{d^2\Xi}{dr^2} - l(l+1)\frac{\Xi}{r^2} = 0, \tag{2.14}$$

$$\frac{d^2\Psi}{d\phi^2} + \kappa^2 \Psi = 0, \tag{2.15}$$

and

$$\frac{1}{\sin\theta}\frac{d}{d\theta}\left(\sin\theta\frac{d\Theta}{d\theta}\right)+\left[l(l+1)-\frac{\kappa^2}{\sin^2\theta}\right]\Theta=0, \tag{2.16}$$

where l and κ are the separation constants (Jackson, 1999). Solving Eqs. (2.14), (2.15), and (2.16), we obtain the respective solutions of

$$\Xi(r)=j_1 r^{l+1}+j_2 r^{-l}, \tag{2.17}$$

$$\Psi(\phi)=j_3\cos(\kappa\phi)+j_4\sin(\kappa\phi), \tag{2.18}$$

and

$$\Theta(\theta)=Y_l^{\kappa}(\cos\theta), \tag{2.19}$$

and arrive at the general solution to $\Phi^{\dagger}(r,\theta,\phi)$, *i.e.*,

$$\Phi^{\dagger}(r,\theta,\phi)=\sum_l\sum_{\kappa}\left(j_1 r^l+j_2 r^{-(l+1)}\right)\left(j_3\cos(\kappa\phi)+j_4\sin(\kappa\phi)\right)Y_l^{\kappa}(\cos\theta), \tag{2.20}$$

where j_1, j_2, j_3, and j_4 are constants to be determined from boundary conditions and $Y_l^{\kappa}(\cos\theta)$ is the associate Legendre function (Arfken, 1970; Jackson, 1999).

The boundary conditions on the inner and outer electric potentials and fields are the electric field strength far away from the micro-particle,

$$\overline{E^{\dagger}}\to E_0\overline{i_z}=E_0\left(\cos\theta\overline{i_r}-\sin\theta\overline{i_\theta}\right)\ \text{as}\ r\to\infty, \tag{2.21}$$

the continuity of the electric potential at the solid-liquid interface,

$$\Phi^{\dagger}\left(r=R^{-},\theta,\phi\right)=\Phi^{\dagger}\left(r=R^{+},\theta,\phi\right), \tag{2.22}$$

and charge conservation at the steady rotating micro-particle surface,

$$\overline{n}\cdot\left[\!\left[\overline{J_f^{\dagger}}\right]\!\right]+\nabla_{\Sigma}\cdot\overline{K_f^{\dagger}}=0\ \text{at}\ r=R, \tag{2.23}$$

in which $\overline{n}=\overline{i_r}$ is the normal vector of the spherical surface, $\overline{J_f^{\dagger}}=\sigma\overline{E^{\dagger}}$ is the Ohmic current per unit area, $\nabla_{\Sigma}=\left(\overline{\overline{I_0}}-\overline{nn}\right)\cdot\nabla$ is the surface divergence with $\overline{\overline{I_0}}$ being the unit identity tensor (Brand, 1947; Deen, 1998), and $\overline{K_f^{\dagger}}=\sigma_f\overline{V}$ is the surface current density with σ_f being the surface charge density and $\overline{V}$ being the linear velocity on the surface of the rotating micro-particle. The description of the boundary condition, Eq. (2.23), is completed by the following relations, namely,

$$\bar{n}\cdot\left[\left[\overline{J_f^{\dagger}}\right]\right]=\sigma_1 E_r^{\dagger}\left(r=R^{+},\theta,\phi\right)-\sigma_2 E_r^{\dagger}\left(r=R^{-},\theta,\phi\right), \tag{2.24}$$

with $E_r^{\dagger}$ being the r component of the electric field,

$$\sigma_f=\varepsilon_1 E_r^{\dagger}\left(r=R^{+},\theta,\phi\right)-\varepsilon_2 E_r^{\dagger}\left(r=R^{-},\theta,\phi\right), \tag{2.25}$$

and

$$\bar{V}=\Omega\bar{i}_x\times R\bar{i}_r=\Omega R\left(\sin\theta\cos\phi\bar{i}_r+\cos\theta\cos\phi\bar{i}_\theta-\sin\phi\bar{i}_\phi\right)\times\bar{i}_r=-\Omega R\left(\sin\phi\bar{i}_\theta+\cos\theta\cos\phi\bar{i}_\phi\right). \tag{2.26}$$

By applying the boundary conditions given above, *i.e.*, Eqs. (2.21)-(2.26), to the general solution of the electric potential, Eq. (2.20), the electric potentials and fields of the present two region problem can be solved. We obtain the electric potential, $\Phi^{\dagger}$, and field components, $E_r^{\dagger}$, $E_\theta^{\dagger}$, and $E_\phi^{\dagger}$, for inside ($r<R$) the rotating micro-particle as

$$\Phi^{\dagger}\left(r,\theta,\phi\right)=r\left(\frac{a_3}{R^3}-E_0\right)\cos\theta+r\frac{a_6}{R^3}\sin\theta\sin\phi, \tag{2.27}$$

$$E_r^{\dagger}\left(\theta,\phi\right)=-\left(\frac{a_3}{R^3}-E_0\right)\cos\theta-\frac{a_6}{R^3}\sin\theta\sin\phi, \tag{2.28}$$

$$E_\theta^{\dagger}\left(\theta,\phi\right)=\left(\frac{a_3}{R^3}-E_0\right)\sin\theta-\frac{a_6}{R^3}\cos\theta\sin\phi, \tag{2.29}$$

and

$$E_\phi^{\dagger}\left(\phi\right)=-\frac{a_6}{R^3}\cos\phi, \tag{2.30}$$

and the outer ($r>R$) electric potential and field components as

$$\Phi^{\dagger}\left(r,\theta,\phi\right)=-rE_0\cos\theta+\frac{\overline{p_t^{\dagger}}\cdot\bar{i}_r}{4\pi\varepsilon_1 r^2}=-rE_0\cos\theta+\frac{4\pi\varepsilon_1}{4\pi\varepsilon_1 r^2}\left(a_3\cos\theta+a_6\sin\phi\sin\theta\right), \tag{2.31}$$

$$E_r^{\dagger}\left(r,\theta,\phi\right)=E_0\cos\theta+\frac{2}{r^3}\left(a_3\cos\theta+a_6\sin\phi\sin\theta\right), \tag{2.32}$$

$$E_\theta^{\dagger}\left(r,\theta,\phi\right)=-E_0\sin\theta-\frac{1}{r^3}\left(-a_3\sin\theta+a_6\sin\phi\cos\theta\right), \tag{2.33}$$

and

$$E_\phi^{\dagger}\left(r,\phi\right)=-\frac{1}{r^3}a_6\cos\phi, \tag{2.34}$$

where

$$a_3 = E_0 R^3 \left[\frac{\varepsilon_2 - \varepsilon_1}{2\varepsilon_1 + \varepsilon_2} + \frac{\left(\frac{\sigma_2 - \sigma_1}{2\sigma_1 + \sigma_2} - \frac{\varepsilon_2 - \varepsilon_1}{2\varepsilon_1 + \varepsilon_2} \right)}{1 + \tau_{MW}^2 \Omega^2} \right], \tag{2.35}$$

$$a_6 = -E_0 R^3 \frac{\left(\frac{\sigma_2 - \sigma_1}{2\sigma_1 + \sigma_2} - \frac{\varepsilon_2 - \varepsilon_1}{2\varepsilon_1 + \varepsilon_2} \right) \tau_{MW} \Omega}{1 + \tau_{MW}^2 \Omega^2}, \tag{2.36}$$

$$\overline{p_t^\dagger} = p_x^\dagger \overline{i_x} + p_y^\dagger \overline{i_y} + p_z^\dagger \overline{i_z}, \tag{2.37}$$

$$\overline{i_r} = \sin\theta\cos\phi \overline{i_x} + \sin\theta\sin\phi \overline{i_y} + \cos\theta \overline{i_z}, \tag{2.38}$$

and

$$\tau_{MW} \equiv \frac{2\varepsilon_1 + \varepsilon_2}{2\sigma_1 + \sigma_2}, \tag{2.39}$$

is the Maxwell-Wagner relaxation time.

We expand the outer ($r > R$) electric potential, Eq. (2.31), with Eqs. (2.37) and (2.38) and compare the coefficients to obtain the total dipole moment (as observed from outside the micro-particle) of the rotating micro-particle as

$$\overline{p_t^\dagger} = p_x^\dagger \overline{i_x} + p_y^\dagger \overline{i_y} + p_z^\dagger \overline{i_z} = 0\overline{i_x} + 4\pi\varepsilon_1 a_6 \overline{i_y} + 4\pi\varepsilon_1 a_3 \overline{i_z}, \tag{2.40}$$

and the *retarding part* of the dipole moment (Cebers, 1980; Lobry & Lemaire, 1999; Cebers *et al.*, 2000; Cebers *et al.*, 2002; Lemaire *et al.*, 2006; Pannacci *et al.*, 2007*a*; Lemaire *et al.*, 2008) as

$$\overline{p^\dagger} = 4\pi\varepsilon_1 a_6 \overline{i_y} + 4\pi\varepsilon_1 \left(a_3 - E_0 R^3 \frac{\varepsilon_2 - \varepsilon_1}{2\varepsilon_1 + \varepsilon_2} \right) \overline{i_z}. \tag{2.41}$$

Microscopically, the Maxwell-Wagner polarization induced surface charge around the spherical particle with half of the hemisphere having positive charge and the other half having negative charge is directly related to the retarding dipole moment given by Eq. (2.41) (Cebers, 1980). However, as viewed from the macroscopic level, the total charge observed far away from this induced dipole is to be zero.

The electrical torque exerted on this rotating micro-particle as shown in Fig. 2.1 can be evaluated via the *dielectrophoretic approximation* (Jones, 1995), *i.e.*,

$$\overline{T_e^\dagger} = \overline{p_t^\dagger} \times \overline{E^\dagger} = \left(4\pi\varepsilon_1 a_6 \bar{i}_y + 4\pi\varepsilon_1 a_3 \bar{i}_z\right) \times E_0 \bar{i}_z = \overline{p^\dagger} \times \overline{E^\dagger} = 4\pi\varepsilon_1 a_6 E_0 \bar{i}_x \,. \tag{2.42}$$

This torque expression given in Eq. (2.42) can be verified by calculating the electrical torque with the general Maxwell stress tensor (Sauer & Schlögl, 1985). The proof is given in the following. Generally speaking, the electrical torque exerted on the rotating spherical micro-particle is evaluated by integrating all the differential electrical force, $d\overline{F^\dagger}$, exerted on the particle's spherical surface at $r = R$ with the lever arm being $\bar{R} = R\bar{i}_r$, *i.e.*,

$$\overline{T_e^\dagger} = \int \bar{R} \times d\overline{F^\dagger} = \int R\bar{i}_r \times d\overline{F^\dagger} \,. \tag{2.43}$$

The differential electrical force, $d\overline{F^\dagger}$, is related to the Maxwell stress tensor, $\overline{\overline{\tau^\dagger}}$, and the differential area element, $d\bar{A} = \bar{n}dA = \bar{n}R^2 \sin\theta d\phi d\theta$, through

$$d\overline{F^\dagger} = d\bar{A} \cdot \left[\!\left[\overline{\overline{\tau^\dagger}}\right]\!\right] = \bar{n} \cdot \left[\!\left[\overline{\overline{\tau^\dagger}}\right]\!\right] R^2 \sin\theta d\phi d\theta \,, \tag{2.44}$$

where $\bar{n}$ is the surface normal vector, $[\![\ ]\!]$ denotes the difference of the particular physical variable across the spherical surface, and

$$\overline{\overline{\tau^\dagger}} = \tau_{ij}^\dagger = \varepsilon E_i^\dagger E_j^\dagger - \frac{1}{2}\varepsilon\delta_{ij} E_k^\dagger E_k^\dagger \,, \tag{2.45}$$

is the Maxwell stress tensor where ε is the dielectric permittivity of the particular medium or region of interest, δ_{ij} is the Kronecker delta ($\delta_{i=j} = 1$, $\delta_{i\neq j} = 0$), and $E_i^\dagger$, $E_j^\dagger$, $E_k^\dagger$ represent the electric field with i, j, or k being r, θ, or ϕ. Defining the surface normal to be pointing out of the sphere, *i.e.*, $\bar{n} = \bar{i}_r$, and expanding the Maxwell stress tensor (symmetric) as

$$\overline{\overline{\tau^\dagger}} = \tau_{ij}^\dagger = \begin{bmatrix} \tau_{rr}^\dagger & \tau_{r\theta}^\dagger & \tau_{r\phi}^\dagger \\ \tau_{\theta r}^\dagger & \tau_{\theta\theta}^\dagger & \tau_{\theta\phi}^\dagger \\ \tau_{\phi r}^\dagger & \tau_{\phi\theta}^\dagger & \tau_{\phi\phi}^\dagger \end{bmatrix}, \tag{2.46}$$

we evaluate the traction vector, $\overline{\tau_t^\dagger}$, and obtain

$$\overline{\tau_t^\dagger} = \bar{n} \cdot \overline{\overline{\tau^\dagger}} = \bar{i}_r \cdot \overline{\overline{\tau^\dagger}} = \begin{bmatrix} 1 & 0 & 0 \end{bmatrix} \begin{bmatrix} \tau_{rr}^\dagger & \tau_{r\theta}^\dagger & \tau_{r\phi}^\dagger \\ \tau_{\theta r}^\dagger & \tau_{\theta\theta}^\dagger & \tau_{\theta\phi}^\dagger \\ \tau_{\phi r}^\dagger & \tau_{\phi\theta}^\dagger & \tau_{\phi\phi}^\dagger \end{bmatrix} = \tau_{rr}^\dagger \bar{i}_r + \tau_{r\theta}^\dagger \bar{i}_\theta + \tau_{r\phi}^\dagger \bar{i}_\phi \,, \tag{2.47}$$

where

$$\tau_{rr}^{\dagger} = \varepsilon E_r^{\dagger} E_r^{\dagger} - \frac{1}{2}\varepsilon\left(E_r^{\dagger}E_r^{\dagger} + E_\theta^{\dagger}E_\theta^{\dagger} + E_\phi^{\dagger}E_\phi^{\dagger}\right), \tag{2.48}$$

$$\tau_{r\theta}^{\dagger} = \varepsilon E_r^{\dagger} E_\theta^{\dagger}, \tag{2.49}$$

$$\tau_{r\phi}^{\dagger} = \varepsilon E_r^{\dagger} E_\phi^{\dagger}, \tag{2.50}$$

with ε being dependent on the particular medium or region of interest. Using Eqs. (2.44) and (2.47), we rewrite the integral in Eq. (2.43) to obtain

$$\begin{aligned}\overline{T_e^{\dagger}} = \int R\bar{i}_r \times \Big\{&\left[\tau_{rr}^{\dagger}\left(r=R^{+}\right) - \tau_{rr}^{\dagger}\left(r=R^{-}\right)\right]\bar{i}_r \\ &+\left[\tau_{r\theta}^{\dagger}\left(r=R^{+}\right) - \tau_{r\theta}^{\dagger}\left(r=R^{-}\right)\right]\bar{i}_\theta + \left[\tau_{r\phi}^{\dagger}\left(r=R^{+}\right) - \tau_{r\phi}^{\dagger}\left(r=R^{-}\right)\right]\bar{i}_\phi\Big\} R^2 \sin\theta d\phi d\theta\end{aligned}, \tag{2.51}$$

and subsequently

$$\overline{T_e^{\dagger}} = \int_0^{2\pi}\int_0^{\pi}\left\{\left[\varepsilon_1 E_r^{\dagger}E_\theta^{\dagger}\Big|_{r=R^{+}} - \varepsilon_2 E_r^{\dagger}E_\theta^{\dagger}\Big|_{r=R^{-}}\right]\bar{i}_\phi - \left[\varepsilon_1 E_r^{\dagger}E_\phi^{\dagger}\Big|_{r=R^{+}} - \varepsilon_2 E_r^{\dagger}E_\phi^{\dagger}\Big|_{r=R^{-}}\right]\bar{i}_\theta\right\} R^3 \sin\theta d\phi d\theta . \tag{2.52}$$

Substituting

$$\bar{i}_\theta = \cos\theta\cos\phi\bar{i}_x + \cos\theta\sin\phi\bar{i}_y - \sin\theta\bar{i}_z, \tag{2.53}$$

$$\bar{i}_\phi = -\sin\phi\bar{i}_x + \cos\phi\bar{i}_y, \tag{2.54}$$

Eqs. (2.28)-(2.30), and Eqs. (2.32)-(2.34) and performing the integral in Eq. (2.52), we again arrive at Eq. (2.42) with the *y*- and *z*- components of the electrical torque being zero.

The electrical torque exerted on the rotating micro-particle is balanced by the viscous torque in low Reynolds number flows, *i.e.*,

$$\overline{T_v^{\dagger}} = -8\pi\eta_0\Omega R^3\bar{i}_x . \tag{2.55}$$

In steady state micro-particle Quincke rotation, $\overline{T_e^{\dagger}} + \overline{T_v^{\dagger}} = 0$, and thus with Eqs. (2.36), (2.42), and (2.55),

$$-4\pi\varepsilon_1 E_0^2 R^3 \frac{\left(\dfrac{\sigma_2-\sigma_1}{2\sigma_1+\sigma_2} - \dfrac{\varepsilon_2-\varepsilon_1}{2\varepsilon_1+\varepsilon_2}\right)\tau_{MW}\Omega}{1+\tau_{MW}^2\Omega^2} - 8\pi\eta_0\Omega R^3 = 0, \tag{2.56}$$

such that the steady state micro-particle Quincke rotation angular speed is found as

$$\Omega = \begin{cases} \pm\dfrac{1}{\tau_{MW}}\sqrt{\left(\dfrac{E_0}{E_c}\right)^2 - 1}, & E_0 \geq E_c \\ 0, & E_0 < E_c \end{cases}, \tag{2.57}$$

where E_c is defined in Eq. (1.1), τ_{MW} is given in Eq. (2.39), and the + and - signs denote counter clockwise and clockwise rotation with the coordinate system defined in Fig. 2.1. In Eq. (2.57), we have assumed that the particle rotation is only in the x-direction; this is because we will only be considering 2D flow geometries in the following chapters. Note however that for the most general cases, the particle rotation axis is perpendicular to the planes defined by the electric field, which has a three dimensional feature.

We further explain the result found in Eq. (2.57) with the micro-particle torque-speed curves as plotted in Fig. 2.2. Figure 2.2 shows the "magnitudes" of the respective viscous and electrical torques versus the steady state micro-particle Quincke rotation angular speeds. The linear gray

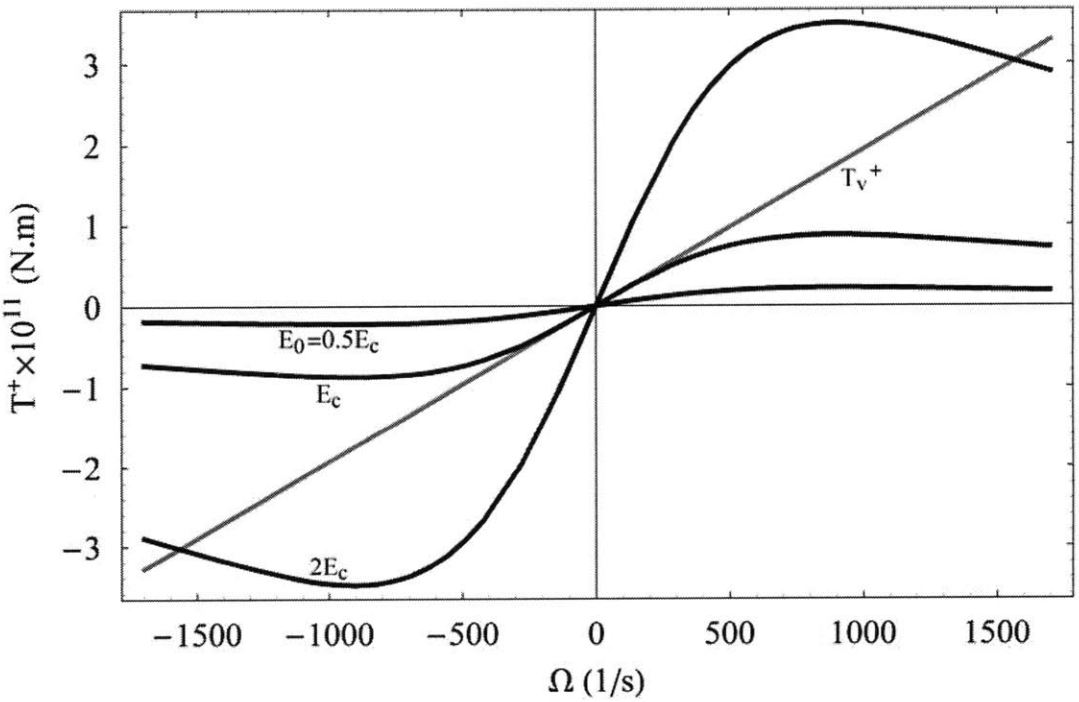

Figure 2.2. The steady state torque-speed curves of a single micro-particle undergoing Quincke rotation. The solid gray line represents the magnitude of the viscous torque, $T_v^{\dagger}$, exerted on the micro-particle whereas the solid black curves represent the magnitudes of the electric torque, $T_e^{\dagger}$, exerted on the micro-particle evaluated at $E_0 = 0.5E_c$, E_c, and $2E_c$ (V/m).

solid line denotes the magnitude of the viscous torque, $T_v^{\dagger}$, whereas the solid black curves denote the magnitudes of the electrical torque, $T_e^{\dagger}$, evaluated at electric field strengths of $E_0 = 0.5E_c$, E_c, and $2E_c$ (V/m). For the case of $E_0 = 0.5E_c$, we find that the line for the viscous torque only intersects the electrical torque curve at $\Omega = 0$, *i.e.*, no micro-particle Quincke rotation, which is the solution for $E_0 < E_c$ given in Eq. (2.57). Since the slope of the viscous torque is greater than that of the electrical torque near $\Omega = 0$ for $E_0 = 0.5E_c$ or $E_0 < E_c$, any slight perturbation in the electrical torque that causes micro-particle rotation will be quickly dampen out by the viscous torque, that is, the magnitude of the viscous torque increases much faster with respect to the rotation speed as compared to the electrical torque, and thus $\Omega = 0$ for $E_0 = 0.5E_c$ or $E_0 < E_c$ is a stable solution. As we increase the electric field strength to $E_0 = E_c$, the slope of the electrical torque becomes the same as that of the viscous torque, and the zero micro-particle rotation solution, $\Omega = 0$, becomes a neutrally stable solution. This is the point at which the micro-particle starts to have the tendency to rotate due to small noise or perturbations in the particle-liquid system (recall the physical picture of the micro-particle's dipole moment being in the opposite direction to the applied electric field for charge relaxation times of $\tau_2 > \tau_1$ or specifically for the particle being much insulating than the liquid, *i.e.*, $\sigma_1 \gg \sigma_2$, as discussed in Chapter 1). As we increase the applied electric field strength further to $E_0 = 2E_c$, the line for the viscous torque now intersects the electric torque curve at three points, namely, $\Omega = 0$ and

$$\Omega = \pm \frac{1}{\tau_{MW}} \sqrt{\left(\frac{E_0}{E_c}\right)^2 - 1} \quad (1/s), \tag{2.58}$$

where the $\pm$ signs denote either clockwise or counter clockwise rotation directions. Note however that the zero rotation solution, $\Omega = 0$, is no longer a stable solution since the slope of the viscous torque is now less than that of the electrical torque and any slight perturbations in the electrical torque cannot be dampened out by the viscous torque (for a given small value of particle rotation, $\delta\Omega$, near $\Omega = 0$, the growth of the electrical torque is greater than that of the viscous torque). The micro-particle rotation speed, Ω, thus starts to grow and finds two stable operating points, at which the slope of the viscous torque is greater than that of the electrical torque, as given by Eq. (2.58).

The physical constants and material properties employed in plotting Fig. 2.2 are given in Table 4.1 in Chapter 4. As can be seen in Fig. 2.2, the characteristic frequency obtained by this set of physical constants and material properties is on the order of kilohertz, which is generally much less than the characteristic frequencies of propagating electromagnetic waves. The solutions to the electric potential and field obtained in this section will be employed in our development of the ER fluid polarization relaxation equation along with its equilibrium polarization in Chapter 3.

Further information regarding the theory of particle Quincke rotation can be found in Jones (1984, 1995). More coordinate transformation relationships such as those given in Eqs. (2.38), (2.53), (2.54), etc. can be found in Griffiths (1999) and Zahn (2003). For detailed and elegant calculations of electrical torques exerted on cylinders and spheres using the method of Maxwell stress tensors, please refer to Sauer & Schlögl (1985).

2.3 Summary of Assumptions Built-in the Present Formulation

At the end of Chapter 2, we summarize the assumptions that have been made so far or will be made in the following chapters of Chapters 3, 4, and 5 so that this section can serve as a quick reference of all the assumptions or approximations built-in the present continuum mechanical formulation of the nER2 effect discussed in this thesis.

(i) The physical model of the ER fluid or particle-liquid suspension considered herein is a dilute collection (with solid volume fraction being $\phi \ll 1$) of insulating dielectric spherical micro-particles suspended within a slightly conducting liquid medium. The micro-particles are considered to be neutrally buoyant such that the solid phase do not sediment and separate from the liquid phase of the ER fluid. By asserting a dilute suspension, electrical and hydrodynamic interactions among the micro-particles are generally neglected at the microscopic level.

(ii) Additional to the above physical picture, we consider that both micro-particle Quincke rotation and initially imposed macroscopic flow vorticity are always required to produce the negative electrorheological effects of the second kind (nER2). So far, no nER2 effect has been observed without the presence of an initially imposed macroscopic flow vorticity.

(iii)The four remarks made at the end of Section 2.1.

(iv)In Section 2.2, we have applied the electro-quasi-static (EQS) Maxwell's equations to solve for the electric potentials and electric fields inside and outside of a rotating single micro-particle when subjected to a uniform electric field of $\overline{E^{\dagger}} = E_z^{\dagger}\overline{i_z} = E_0\overline{i_z}$. We have assumed that no bulk spatial free charge is present in either the liquid or the solid phase such that $\rho_f = 0$ and that only surface charge, σ_f, is present on the surface of the rotating micro-particle. The surface charge distribution and the subsequent dipole moment of the micro-particle obey the principle of Maxwell-Wagner interfacial polarization and the microscopic physical picture of the electrical double layer along with its finite charge distributions are neglected.

(v) On the macroscopic level, we assume the electric field applied to the ER fluid or particle-liquid suspension, $\overline{E}$, is a direct current (DC) uniform electric field. Because the ER fluid flow velocity considered in this thesis is much less than the speed of propagating electromagnetic waves, we can apply the electro-quasi-static (EQS) Maxwell's equations to the ER fluid flow problem of interest. We also assume no spatial free charge density is present in the ER flow field, *i.e.*, $\rho_f = 0$.

(vi)As will be discussed in the next chapter, the development of the polarization relaxation equation and its accompanying equilibrium polarization is focused on the retarding polarization instead of the total ER fluid polarization. The retarding polarization is the part of the total ER fluid polarization that is directly related to the surface charges on the surfaces of the rotating micro-particles induced by the Maxwell-Wagner interfacial polarization mechanism. As will be shown in the next section, a "rotating coffee cup model" is developed to characterize the retarding polarization relaxation process when the ER fluid is subjected to motion. The model consists of a retarding polarization relaxation equation along with its accompanying equilibrium retarding polarization. We define a quasi-equilibrium state for a continuum ER fluid parcel consisting of carrier liquid molecules and rotating micro-particles with all the micro-particles contained within the ER fluid parcel rotating in the same direction such that a two-component equilibrium retarding polarization is made possible.

(vii) In this thesis, two flow geometries are considered, they are the two-dimensional Couette and Poiseuille flow geometries. For each of the geometries, two limits of the classical continuum mechanical field equations as formulated in this chapter are considered. They are

the zero spin viscosity limit, $\eta' = 0$, and the finite spin viscosity small spin velocity limit, $\eta' \neq 0$ and $\tau_{MW}^2 \omega_x^2 \ll 1$. Both of the flow fields are considered to be two-dimensional, steady state, fully developed, and incompressible flows. We also consider the ER fluid flow discussed in this thesis to be slow flows so that flow instabilities and turbulence are not present.

(viii) As for the macroscopic uniform DC electric fields applied to the two flow geometries, we neglect any presence of the possible fringing electric fields for the 2D geometries. Using the physical and mathematical arguments of fully developed flow, dilute micro-particle suspension, and continuity of tangential electric fields across the interface of the ER fluid and perfectly conducting electrodes, we approximate the macroscopic electric field to be in the *z*-direction only with the *y*-component of the electric field being zero, *i.e.*, $E_y = 0$. We assume that the *z*-component of the macroscopic electric field, E_z, is related to the microscopic electric field, $E_z^\dagger$, through Eq. (4.8). Due to the dilute particle suspension, the macroscopic *z*-electric field is eventually approximated as $E_z \approx E_z^\dagger = E_0$.

(ix) Rigorously speaking, the relations of the vortex viscosity, $\zeta \sim 1.5\phi\eta_0$, and the zero electric field ER fluid viscosity, or Einstein relation, $\eta \sim \eta_0(1+2.5\phi)$, were derived from physical and mathematical models based on averaged micro-particle rotation speeds, $\overline{\Omega}$, instead of the continuum spin velocity, $\overline{\omega}$. Thus, using the relations of $\zeta \sim 1.5\phi\eta_0$ and $\eta \sim \eta_0(1+2.5\phi)$ in our developed continuum mechanical field equations is only an approximation. To this point, no explicit expressions have been derived for the vortex viscosity or zero electric field ER fluid viscosity based solely on the continuum spin velocity.

(x) Although we are neglecting the two-phase microscopic details and treating the ER fluid or the particle-liquid suspension as an homogeneous isotropic single phase continuous medium, microscopic information is still preserved and built-in to our continuum mechanical field equations through the expressions of the vortex viscosity, zero electric field ER fluid viscosity, and the equilibrium retarding polarization.

(xi) For flows fields in the zero spin viscosity limit, the continuum spin velocity is free-to-spin at the ER fluid-solid boundaries since the highest order derivative in the continuum angular momentum equation is dropped out due to a zero spin viscosity. Moreover, since both sets of

the governing equations for the respective Couette and Poiseuille geometries reduce into algebraic cubic equations in the zero spin viscosity limit, the solutions obtained from solving these algebraic equations may be imaginary or complex valued. However, only real valued solutions are physically valid and considered in this thesis.

(xii) In order to satisfy the stable micro-particle rotation condition as discussed in the literature (Lobry & Lemaire, 1999; Cebers *et al.*, 2000; Cebers *et al.*, 2002; Lemaire *et al.*, 2006; Pannacci *et al.*, 2007*a*; Lemaire *et al.*, 2008), the direction of the micro-particle rotation is assumed to always be in the direction of the macroscopically imposed flow vorticity. As will be seen in Chapter 3, the equilibrium retarding polarization generally depends on both the magnitude and direction of the micro-particle rotation speed, $\overline{\Omega}$, and thus we need to properly choose the micro-particle rotation direction in accordance with the macroscopic imposed flow vorticity before substituting this piece of microscopic information into the equilibrium polarization and solving for the subsequent continuum field equations.

(xiii) Considering a 2D parallel plate Poiseuille flow geometry as shown in Fig. 5.1 or Fig. 5.8, we find that the solid boundaries are symmetric with respect to the middle plane of the 2D flow channel and that the macroscopic imposed flow vorticity direction is actually asymmetric about the middle plane of the flow channel. Therefore, if the suspended micro-particles are rotating clockwise in the lower half of the channel, the micro-particles in the upper half of the flow channel should be rotating in the counter clockwise direction, and the micro-particle rotation speed of the micro-particles near the mid-plane of the channel is close to zero rotation velocity. This observation is also generalized for the continuum spin velocity field since due to the constraint of the two symmetric solid boundaries of Poiseuille flow, the continuum spin velocity is an odd function of the spatial coordinate perpendicular to the parallel plate boundaries with the point of asymmetry being the mid-plane of the Poiseuille flow channel.

Chapter 3
Equilibrium Polarization and Polarization Relaxation

This chapter presents the development of the equilibrium polarization and the polarization relaxation equation that describe how the ER fluid polarization is influenced by the non-equilibrium process of macroscopic flow motion and microscopic particle rotation. Previous work done by Cebers (1980) has shown a dipole relaxation equation to account for the rotation effects on the charge relaxation/conservation processes of a dielectric insulating spherical solid micro-particle undergoing Quincke rotation in a suspending slightly conducting liquid medium. In the same 1980 paper, Cebers also generalized the dipole relaxation equation to describe the macroscopic polarization relaxation process of a liquid-particle suspension with the micro scale solid particles being in a state of spontaneous electrorotation. Note however that the non-equilibrium variable in Cebers' 1980 polarization relaxation model is solely based on the microscopic averaged particle rotation speed, $\overline{\Omega}$, instead of a continuum spin velocity of the ER fluid parcel, $\overline{\omega}$.

Drawing a parallel reference from the ferrofluid spin-up flow, we find that the macroscopic magnetization relaxation equation for describing the non-equilibrium effects of flow motion on the ferrofluid magnetization is also based upon the non-equilibrium internal kinematic variable of the microscopic averaged particle rotation speed, $\overline{\Omega}$, (Shliomis, 1972, 2002). Again we are faced with the dilemma of whether the micro-particle rotation speed, $\overline{\Omega}$, and the continuum spin velocity, $\overline{\omega}$, are the same physical quantities or are they related but actually different physical

quantities as discussed in the previous two chapters. Recall that one of the main thrusts of the present thesis is to offer some possible new view points (if not arbitrarily dismissed or neglected in the past) to discuss the physical nature of the continuum spin velocity variable through the development of a set of classical continuum mechanical field equations for describing nER2 responses. Therefore, we take on the approach of treating the micro-particle rotation speed, $\overline{\Omega}$, and the continuum spin velocity, $\overline{\omega}$, differently, *i.e.*, the micro-particle particle rotation speed, $\overline{\Omega}$, being a microscopic variable and the spin velocity, $\overline{\omega}$, being a macroscopic continuum variable which is not necessarily just the average of the rotation speeds of all the micro-particles contained in an arbitrary continuum ER fluid parcel.

In the following discussions, we first review the general ideas and summarize the final results of Shliomis' first magnetization relaxation equation for ferrofluids (Shliomis, 1972, 2002; Rosensweig, 1997), Cebers' dipole relaxation equation for a single rotating micro-particle (Cebers, 1980), and Xiao *et al.*'s dynamic effective medium theory for finding the macroscopic effective electric permittivity resulting from a collection of rotating micro-particles (Xiao *et al.*, 2008). We then combine the concepts of the above three models to formulate our proposed "rotating coffee cup model" and the subsequent polarization relaxation equation with its accompanying equilibrium polarization (specifically designed for the *retarding part* of the total polarization) for modeling the non-equilibrium effects of the continuum spin velocity, $\overline{\omega}$, continuum linear velocity, $\overline{v}$, and micro-particle rotation speed, $\overline{\Omega}$, on the ER fluid polarization in an nER2 flow field. This developed polarization relaxation equation is to be coupled with the continuum linear momentum equation, Eq. (2.2), and the continuum angular momentum equation, Eq. (2.3), respectively through the continuum linear velocity, $\overline{v}$, and the continuum spin velocity, $\overline{\omega}$, such that together with the continuity equation, Eq. (2.1), and the EQS Maxwell's equations, Eqs. (2.5)-(2.7), a complete set of governing continuum mechanical field equations encompassing both the mechanical and electrical aspects of the present nER2 problem is formulated. Nevertheless, we do not completely omit the microscopic picture of micro-paricles rotating spontaneously in the micro scale. The microscopic information of a particle-liquid suspension with the suspended particles undergoing Quincke rotation is to be controlled or inserted into our present continuum model through our proposed form of equilibrium polarization.

The last section of this chapter is devoted to a comparison of several different equilibrium polarization schemes that we have investigated along the course of developing our proposed "rotating coffee cup model." We would like to offer some possible physical explanations or physical pictures that best describe the respective different schemes. The limitations of our proposed "rotating coffee cup model" will also be summarized hopefully to offer some pointers or directions for future development of more advanced or sophisticated polarization relaxation models.

3.1 Review of Shliomis' First Magnetization Relaxation Equation (Shliomis, 1972, 2002; Rosensweig, 1997)

In his first model, Shliomis considered an observer in a frame of reference rotating along with the average micro-/nano-particle rotation speed so that in this particular frame, denoted by a superscript of "$^{\Omega}$", the observed averaged particle rotation speed is

$$\overline{\Omega^{\Omega}} = 0, \tag{3.1}$$

and that the magnetization of the ferrofluid follows a "Debye" form (Shliomis, 2002) of

$$\frac{D^{\Omega}\overline{M}}{Dt} = -\frac{\left(\overline{M} - \overline{M_{eq}}\right)}{\tau_M}, \tag{3.2}$$

where $\overline{M}$ is the magnetization of the ferrofluid, τ_M is the characteristic magnetic relaxation time determined by the Néel and Brownian relaxation mechanisms, D/Dt is the material derivative defined by Eq. (2.4) , and $\overline{M_{eq}}$ is the equilibrium magnetization which is generally given by the Langevin relation for nano scaled Brownian particles (Rosensweig, 1997; Shliomis, 2002). Since the average particle rotation produces a shift in the ferrofluid magnetization vector as observed in the stationary or laboratory frame, Eq. (3.2) becomes

$$\frac{D\overline{M}}{Dt} = \overline{\Omega} \times \overline{M} - \frac{1}{\tau_M}\left(\overline{M} - \overline{M_{eq}}\right), \tag{3.3}$$

in the stationary or laboratory frame with $\overline{\Omega}$ being the averaged particle rotation speed (Shliomis, 1972, 2002; Rosensweig, 1997).

3.2 Review of Cebers' Dipole Relaxation Equation for a Single Rotating Micro-particle (Cebers, 1980)

Cebers' dipole relaxation equation for a single particle undergoing Quincke rotation can be obtained using the electric potential and field solutions that we have derived in Section 2.2 with reference to the coordinate system shown in Fig. 2.1. Here, we outline some of the intermediate steps required for obtaining Cebers' final expression and for showing the fundamental physics involved in the model.

The surface charge density, σ_f, given in Eq. (2.25) is explicitly evaluated by substituting Eqs. (2.28) and (2.32) with $r = R$ such that

$$\sigma_f = \frac{(2\varepsilon_1 + \varepsilon_2)}{R^3}\left[a_6 \sin\phi \sin\theta + \left(a_3 - \frac{\varepsilon_2 - \varepsilon_1}{2\varepsilon_1 + \varepsilon_2} R^3 E_0 \right) \cos\theta \right]. \tag{3.4}$$

Recognizing the terms within the bracket of Eq. (3.4) being the vector dot product of the surface normal vector, $\bar{n} = \bar{i}_r$ with $\bar{i}_r$ defined in Eq. (2.38), and the retarding dipole moment, $\overline{p^\dagger}/4\pi\varepsilon_1$ with $\overline{p^\dagger}$ defined in Eq. (2.41), Eq. (3.4) can be rewritten as

$$\sigma_f = \frac{2\varepsilon_1 + \varepsilon_2}{R^3} \frac{\overline{p^\dagger} \cdot \bar{n}}{4\pi\varepsilon_1}, \tag{3.5}$$

(Cebers, 1980; Pannacci *et al.*, 2007*b*). Note that there is an additional $1/4\pi$ factor in Cebers' original expression of Eq. (3.5) due to the differences in the definition of charge in the respective Gaussian and SI unit systems. In this thesis, we only use SI units.

The other piece of information required to derive the dipole relaxation equation is the general (unsteady) form of the charge conservation equation at the surface of the rotating micro-particle, *i.e.*,

$$\bar{n} \cdot \left[\!\left[\overline{J_f^\dagger} + \rho_f^\dagger \overline{v^\dagger} \right]\!\right] + \nabla_\Sigma \cdot \overline{K_f^\dagger} = -\frac{\partial \sigma_f}{\partial t} \text{ at } r = R, \tag{3.6}$$

or

$$\bar{n} \cdot \left[\!\left[\overline{J_f^\dagger} \right]\!\right] + \nabla_\Sigma \cdot \overline{K_f^\dagger} = -\frac{\partial \sigma_f}{\partial t} \text{ at } r = R, \tag{3.7}$$

since it is assumed that only surface charges are present at the solid-liquid interface with no spatial charges in the respective two bulk phases. As compared to Eq. (2.23), we have kept the

unsteady derivative term in Eq. (3.7) to account for the transient effects. Using $\overline{K_f^\dagger} = \sigma_f \overline{V}$ and Eq. (2.26), the surface divergence term in Eq. (3.7), $\nabla_\Sigma \cdot \overline{K_f^\dagger}$, is expanded as

$$\nabla_\Sigma \cdot \overline{K_f^\dagger} = -\Omega \sin\phi \frac{\partial \sigma_f}{\partial \theta} - \Omega \cot\theta \cos\phi \frac{\partial \sigma_f}{\partial \phi}. \tag{3.8}$$

Substituting Eq. (3.4) into Eq. (3.8) and recognizing the expansion of $\left(\overline{\Omega} \times \overline{p^\dagger}\right) \cdot \bar{n} / 4\pi\varepsilon_1$ with $\bar{n} = \bar{i}_r$ and $\overline{\Omega} = \Omega \bar{i}_x$, Eq. (3.8) can be condensed into

$$\nabla_\Sigma \cdot \overline{K_f^\dagger} = -\frac{2\varepsilon_1 + \varepsilon_2}{R^3} \frac{\left(\overline{\Omega} \times \overline{p^\dagger}\right) \cdot \bar{n}}{4\pi\varepsilon_1}. \tag{3.9}$$

We evaluate the jump in the current density by inserting Eqs. (2.28) and (2.32) into Eq. (2.24) and arrive at

$$\begin{aligned} \bar{n} \cdot \left[\!\left[\overline{J_f^\dagger}\right]\!\right] = {} & \frac{2\sigma_1 + \sigma_2}{R^3} \times \\ & \left[a_6 \sin\phi \sin\theta + \left(a_3 - \frac{\varepsilon_2 - \varepsilon_1}{2\varepsilon_1 + \varepsilon_2} R^3 E_0 \right) \cos\theta - \left(\frac{\sigma_2 - \sigma_1}{2\sigma_1 + \sigma_2} - \frac{\varepsilon_2 - \varepsilon_1}{2\varepsilon_1 + \varepsilon_2} \right) R^3 E_0 \cos\theta \right], \end{aligned} \tag{3.10}$$

with "×" in Eq. (3.10) being simply the multiplication notation instead of the cross product. Again, using $\bar{n} = \bar{i}_r$ and $\overline{p^\dagger} / 4\pi\varepsilon_1$ as well as defining the equilibrium retarding dipole moment as the retarding dipole moment at zero particle rotation (see Fig. 2.1 for the definition of the spatial coordinates), *i.e.*,

$$\overline{p_{eq}^\dagger} = 4\pi\varepsilon_1 \left(\frac{\sigma_2 - \sigma_1}{2\sigma_1 + \sigma_2} - \frac{\varepsilon_2 - \varepsilon_1}{2\varepsilon_1 + \varepsilon_2} \right) R^3 E_0 \bar{i}_z, \tag{3.11}$$

Eq. (3.10) is reduced into the following form of

$$\bar{n} \cdot \left[\!\left[\overline{J_f^\dagger}\right]\!\right] = \frac{2\sigma_1 + \sigma_2}{R^3} \frac{\left(\overline{p^\dagger} - \overline{p_{eq}^\dagger}\right) \cdot \bar{n}}{4\pi\varepsilon_1}. \tag{3.12}$$

Finally, we substitute Eqs. (3.5), (3.9), and (3.12) into Eq. (3.7) and obtain Cebers' dipole relaxation equation as

$$\frac{d\overline{p^\dagger}}{dt} = \overline{\Omega} \times \overline{p^\dagger} - \frac{1}{\tau_{MW}} \left(\overline{p^\dagger} - \overline{p_{eq}^\dagger} \right), \tag{3.13}$$

in which the partial time derivative has been changed to a total derivative following Cebers'

original definition (Cebers, 1980). A macroscopic version of Eq. (3.13) can also be obtained by assuming all the micro-particles are rotating in the same direction and multiplying Eq. (3.13) with the number density of micro-particles per unit volume, n, namely,

$$\frac{d\overline{P}}{dt} = \overline{\Omega} \times \overline{P} - \frac{1}{\tau_{MW}}\left(\overline{P} - \overline{P_{eq}^{0}}\right), \tag{3.14}$$

where τ_{MW} is the Maxwell-Wagner relaxation time defined in Eq. (2.39), $\overline{P}$ is the retarding polarization and $\overline{P_{eq}^{0}}$ is the equilibrium retarding polarization defined by Eq. (3.11) at zero particle rotation.

Reviewing the above derivation, it can be learned that the dipole relaxation equation is simply a direct result from charge conservation at the surface of the rotating micro-particles. This is why Cebers and co-workers (Cebers, 1980; Lobry & Lemaire, 1999; Cebers *et al.*, 2000; Cebers *et al.*, 2002; Lemaire *et al.*, 2006; Pannacci *et al.*, 2007*a*, *b*; Lemaire *et al.*, 2008) have specifically coined the term of "retarding dipole moment," which is the part of the total dipole moment directly related to the surface charge density, Eq. (3.5), of the rotating micro-particles. The dipole relaxation is generally related to the charge relaxation at the solid-liquid interfaces of the micro-particles and does not depend on the infinite frequency (or instantaneous) response of the dipole moment, *i.e.*,

$$\overline{p_{\infty}^{\dagger}} = 4\pi\varepsilon_1 \frac{\varepsilon_2 - \varepsilon_1}{2\varepsilon_1 + \varepsilon_2} R^3 E_0 \overline{i_z} \,. \tag{3.15}$$

The infinite frequency response of the dipole moment given in Eq. (3.15) will always be in the same direction as the applied electric field direction and thus will not contribute to the electrical torque exerted on the micro-particles and does not enter the charge or dipole relaxation process.

Comparing Eqs. (3.3) and (3.14), it can be found that the two relaxation equations share very much the same form despite the different physical arguments involved in deriving the respective equations. Moreover, Eqs. (3.13) and (3.14) are derived only with reference to the stationary or laboratory frame as compared to the stationary and particle rotation frames employed in deriving Eq. (3.3). Note however that both of the equations are based on the averaged micro-particle rotation speed (or angular velocity), $\overline{\Omega}$, instead of a continuum spin velocity, $\overline{\omega}$. Before we take on the task of differentiating these two kinematic variables, we first turn our attention to a dynamic effective medium theory proposed by Xiao *et al.* (2008) that is employed in deriving the

macroscopic effective electric permittivity due to a collection of micro-particles (or suspension of particles) rotating at a given speed of $\overline{\Omega}$ at the microscopic level.

3.3 Review of the Dynamic Effective Medium Theory (Xiao *et al.*, 2008)

In their work, Xiao *et al.* (2008) considered the macroscopic effective electric permittivity, $\overline{\overline{\varepsilon_{eff}}}$ (which most generally is a tensor), of a dilute collection of micro-particles (with a permittivity of ε_2) rotating at a given constant speed, $\overline{\Omega}$, suspended in a medium having a permittivity of ε_0 at the microscopic level. In other words, they treated the dilute particle-free space suspension as an effective homogeneous medium with a permittivity of $\overline{\overline{\varepsilon_{eff}}}$.

Recall from Chapter 1 that for a dilute collection of solid micro-particles undergoing Quincke rotation in a quiescent liquid medium, there is no *a priori* preferred direction for particle electrorotation except the limitation of the particle axis of rotation being perpendicular to the direction of the applied electric field. Considering the schematics and coordinate system defined in Fig. 2.1 with the electric field being applied in the z-direction, *i.e.*, $\overline{E^{\dagger}} = E_0 \overline{i_z}$, it can be learned that the macroscopic effective (retarding) polarization resulting from a collection of micro-particles undergoing Quincke rotation in a quiescent liquid medium is generally directed in the z-direction with the x- and y-components of the effective polarization being averaged to zero due to the randomness of the micro-particle dipole orientations in the quiescent carrier liquid. Nonetheless, Xiao *et al.* (2008) considered the case of all the micro-particles rotating in the same direction at a given constant angular speed in their particle-free space suspension, which is a condition equivalent to the physical picture of micro-particle Quincke rotation in the presence of some initial background flow vorticity as discussed in Chapter 1. Hence, the macroscopic polarization vector obtained in their model generally has three components (in 3D, two components in 2D), and the macroscopic effective electric permittivity, $\overline{\overline{\varepsilon_{eff}}}$, as well as the molecular (or microscopic) polarizability, $\overline{\overline{\alpha}}$, become tensors.

From general electromagnetism texts (Reitz *et al.*, 1992; Griffiths, 1999; Zahn, 2003), we know that the microscopic molecular electric field, $\overline{E_m}$, can be related to the macroscopic

averaged electric field, $\overline{E}$, and total polarization, $\overline{P_t}$, in a dielectric medium through the Lorentz cavity model relation (Reitz *et al.*, 1992), *i.e.*,

$$\overline{E_m} = \overline{E} + \frac{1}{3\varepsilon_0}\overline{P_t}. \tag{3.16}$$

We rewrite the macroscopic electric displacement field, $\overline{D}$, on the LHS of Eq. (2.7) in terms of the macroscopic averaged field, $\overline{E}$, and a macroscopic effective electric permittivity tensor, $\overline{\overline{\varepsilon_{eff}}}$, *i.e.*,

$$\overline{D} = \overline{\overline{\varepsilon_{eff}}} \cdot \overline{E}, \tag{3.17}$$

such that the total polarization can be expressed as

$$\overline{P_t} = \left(\overline{\overline{\varepsilon_{eff}}} - \varepsilon_0 \overline{\overline{I_0}}\right) \cdot \overline{E}, \tag{3.18}$$

where ε_0 is the permittivity of free space and $\overline{\overline{I_0}}$ is the unit identity tensor. With all the micro-particles rotating in the same direction and with the suspending medium being free space, the total polarization resulting from all the total dipole moments of the rotating micro-particles in the particle-free space suspension is written as

$$\overline{p_t^{\dagger}} = \overline{p_t^m} = \overline{\overline{\alpha}} \cdot \overline{E_m} = \overline{P_t}/n, \tag{3.19}$$

where $\overline{p_t^{\dagger}}$ is the total dipole moment of the rotating micro-particle, $\overline{p_t^m}$ is the molecular dipole moment, $\overline{\overline{\alpha}}$ is the molecular polarizability tensor, and n is the number density of the micro-particles. Note that in Xiao *et al.*'s (2008) formulation, they have treated the total dipole moment of the rotating micro-particles, $\overline{p_t^{\dagger}}$, as the molecular dipole moment, $\overline{p_t^m}$, and the number density of micro-particles as the number density of molecular dipoles. In other words, they have generalized the original Lorentz cavity model, Eq. (3.16), by treating the rotating micro-particles as "molecules." This view point is very similar and close to our physical picture of an ER fluid parcel consisting of a representative amount or ensemble of rotating micro-particles and background carrier liquid molecules as presented in Chapter 1. However, the total dipole moment of the rotating micro-particles, $\overline{p_t^{\dagger}}$, considered by Xiao *et al.* (2008) is the "*lossless dielectric dipole moment*" instead of a Maxwell-Wagner polarization induced dipole for leaky

dielectric systems (Melcher & Taylor, 1969). Combining Eqs. (3.16), (3.18), and (3.19), Xiao *et al.* (2008) arrived at the following expression for the effective electric permittivity, namely,

$$\overline{\overline{\varepsilon_{eff}}} - \varepsilon_0 \overline{\overline{I_0}} = \frac{n}{3\varepsilon_0} \overline{\overline{\alpha}} \cdot \left(\overline{\overline{\varepsilon_{eff}}} + 2\varepsilon_0 \overline{\overline{I_0}} \right). \tag{3.20}$$

We expand Eq. (3.20) for a 2D geometry defined by the *z-y* plane based on the spatial *x-y-z* coordinate shown in Fig. 2.1 and obtain

$$\begin{bmatrix} \varepsilon_{yy} - \varepsilon_0 & \varepsilon_{yz} \\ \varepsilon_{zy} & \varepsilon_{zz} - \varepsilon_0 \end{bmatrix} = \frac{n}{3\varepsilon_0} \begin{bmatrix} \alpha_{yy} & \alpha_{yz} \\ \alpha_{zy} & \alpha_{zz} \end{bmatrix} \begin{bmatrix} \varepsilon_{yy} + 2\varepsilon_0 & \varepsilon_{yz} \\ \varepsilon_{zy} & \varepsilon_{zz} + 2\varepsilon_0 \end{bmatrix}, \tag{3.21}$$

where α_{ij} and ε_{ij} are the tensor elements of the polarizability and permittivity tensors, respectively. Equation (3.21) will be further applied in the development of our proposed equilibrium retarding polarization shown in the next section.

3.4 The Proposed "Rotating Coffee Cup Model" for the Polarization Relaxation Equation with its Equilibrium Polarization

Consider an ER fluid parcel (consisting of a representative amount or ensemble of rotating micro-particles and carrier liquid molecules) rotating at a macroscopic continuum spin velocity of $\overline{\omega}$. The internal micro-particles of this ER fluid parcel are rotating at an average particle rotation speed of $\overline{\Omega}$ at the microscopic level. For an observer rotating along with the spin velocity of the ER fluid parcel, we assume the retarding polarization of the ER fluid parcel, $\overline{P}$, follows the Debye form, namely,

$$\frac{D^{\omega}\overline{P}}{Dt} = -\frac{\left(\overline{P} - \overline{P_{eq}^{\omega}}\right)}{\tau_{MW}}, \tag{3.22}$$

where τ_{MW} is the Maxwell-Wagner relaxation time as defined in Eq. (2.39), the superscript "ω" denotes the reference frame moving or rotating along with the spin velocity, and $\overline{P_{eq}^{\omega}}$ is the equilibrium retarding polarization as observed in the frame rotating along with the spin velocity. Following Shliomis' idea (Shliomis, 1972, 2002; Rosensweig, 1997), we convert Eq. (3.22) into the stationary or laboratory frame as

$$\frac{D\overline{P}}{Dt} = \overline{\omega} \times \overline{P} - \frac{1}{\tau_{MW}}\left(\overline{P} - \overline{P_{eq}^{\omega}}\right), \tag{3.23}$$

where D/Dt is the material derivative as defined in Eq. (2.4), *i.e.*,

$$\frac{D\overline{P}}{Dt} = \frac{\partial \overline{P}}{\partial t} + \left(\overline{v} \cdot \nabla\right)\overline{P} = \overline{\omega} \times \overline{P} - \frac{1}{\tau_{MW}}\left(\overline{P} - \overline{P_{eq}^{\omega}}\right). \tag{3.24}$$

Equation (3.24) describes the non-equilibrium influences of the macroscopic continuum linear velocity, $\overline{v}$, and spin velocity, $\overline{\omega}$, on the retarding polarization, $\overline{P}$. It follows a similar form to those given in Eqs. (3.3) and (3.14), but we have changed the averaged micro-particle rotation speed into a continuum spin velocity to account for the shift in the retarding polarization. The treatment of employing the term $\overline{\omega} \times \overline{P}$ in Eq. (3.24) is similar to the original polarization relaxation equation derived by Dahler and Scriven (1963) for "polarized molecules" via statistical methods. Here, we have limited the use of Eq. (3.24) to the retarding polarization, $\overline{P}$, instead of the total polarization, $\overline{P_t}$. The reason for employing this limit is given in the following development and formulation of the equilibrium retarding polarization, $\overline{P_{eq}^{\omega}}$, for the polarization relaxation equation, Eq. (3.24).

We start our formulation by considering the two-phase nature or details, *i.e.*, looking inside the ER fluid parcel, of a leaky dielectric system of a dilute particle-liquid suspension (with the liquid having a conductivity of σ_1 and a permittivity of ε_1, the micro-particles having a conductivity of σ_2 and a permittivity of ε_2, and the micro-particle solid volume fraction being $\phi \ll 1$) subjected to a uniform DC electric field, $\overline{E}$, with a field strength much greater than the critical electric field, E_c, such that the suspended micro-particles are in a state of spontaneous Quincke rotation. Again, we utilize the electric potential and field solutions solved in Section 2.2 and refer to the schematic diagram and spatial coordinate system defined in Fig. 2.1 in our discussions. We assume a 2D geometry based on the *z*-*y* plane defined by the spatial coordinate system shown in Fig. 2.1.

For simplicity, we first consider the suspended micro-particles rotating in a quiescent carrier liquid such that there is no *a priori* preferred direction for Quincke rotation and that the polarization due to the sum of the induced dipole moment of the rotating micro-particles when subjected to $\overline{E} = E_z \overline{i_z}$ is in the *z*-direction only (*y*-components being averaged to zero).

Neglecting the tensorial details, we consider a "scalar" macroscopic effective electric permittivity, ε_{eff}, for the total macroscopic polarization, $\overline{P_t}$, of the particle-liquid suspension and modify Eq. (3.18) into

$$\overline{P_t} = \left(\varepsilon_{eff} - \varepsilon_0\right)\overline{E}\,. \tag{3.25}$$

Using the solution to the total dipole moment of a micro-particle undergoing Quincke rotation, *i.e.*, the z-component in Eq. (2.40), we apply the Maxwell mixture theory (Jones, 1995; Morgan & Green, 2003) and obtain the scalar effective electric permittivity ε_{eff} as

$$\varepsilon_{eff} = \varepsilon_1\left\{1+3\phi\left[\frac{\varepsilon_2-\varepsilon_1}{2\varepsilon_1+\varepsilon_2}+\frac{\dfrac{\sigma_2-\sigma_1}{2\sigma_1+\sigma_2}-\dfrac{\varepsilon_2-\varepsilon_1}{2\varepsilon_1+\varepsilon_2}}{1+\tau_{MW}^2\Omega^2}\right]\right\}, \tag{3.26}$$

where the micro-particle rotation speed is given by Eq. (2.57). Substituting Eq. (3.26) into Eq. (3.25), we find the total polarization of the particle-liquid suspension consists of three parts, namely,

$$\overline{P_t} = \overline{P_l} + \overline{P_\infty} + \overline{P}, \tag{3.27}$$

where

$$\overline{P_l} = \left(\varepsilon_1 - \varepsilon_0\right)E_z\overline{i_z}, \tag{3.28}$$

is the polarization contribution from the carrier liquid phase (we have absorbed the free space permittivity into $\overline{P_l}$),

$$\overline{P_\infty} = 3\phi\varepsilon_1\frac{\varepsilon_2-\varepsilon_1}{2\varepsilon_1+\varepsilon_2}E_z\overline{i_z} = 4\pi\varepsilon_1 nR^3\frac{\varepsilon_2-\varepsilon_1}{2\varepsilon_1+\varepsilon_2}E_z\overline{i_z}, \tag{3.29}$$

is the polarization contribution due to the infinite frequency response (*e.g.*, Eq. (3.15)) of the suspended rotating micro-particles, and

$$\overline{P} = 3\phi\varepsilon_1\frac{\dfrac{\sigma_2-\sigma_1}{2\sigma_1+\sigma_2}-\dfrac{\varepsilon_2-\varepsilon_1}{2\varepsilon_1+\varepsilon_2}}{1+\tau_{MW}^2\Omega^2}E_z\overline{i_z} = 4\pi\varepsilon_1 nR^3\frac{\dfrac{\sigma_2-\sigma_1}{2\sigma_1+\sigma_2}-\dfrac{\varepsilon_2-\varepsilon_1}{2\varepsilon_1+\varepsilon_2}}{1+\tau_{MW}^2\Omega^2}E_z\overline{i_z}, \tag{3.30}$$

is the polarization contribution from the retarding polarization (*e.g.*, see z-component of Eq. (2.41)) of the suspended rotating micro-particles. In Eqs. (3.29) and (3.30), the micro-particle solid volume fraction, ϕ, is converted into the micro-particle number density, n, via

$$\phi = n\left(\frac{\pi d^3}{6}\right) \sim O\left(nR^3\right), \tag{3.31}$$

with $d = 2R$ being the micro-particle diameter. During the derivation of Eqs. (3.25)-(3.30), we have also assumed that the macroscopic averaged electric field, $\overline{E} = E_z \overline{i}_z$, is roughly the same as the microscopic electric field, $\overline{E^\dagger} = E_0 \overline{i}_z$ (see definition in Section 2.2). This assumption is only true when the suspension is dilute, *i.e.*, $\phi \ll 1$, since the macroscopic averaged field, $\overline{E} = E_z \overline{i}_z$, only differs from the microscopic field, $\overline{E^\dagger} = E_0 \overline{i}_z$, with a correction term on the order of magnitude of ϕ in Cebers' (1980) analysis of the averaged electric field produced by a particle-liquid suspension with the micro-particles undergoing Quincke rotation when subjected to a microscopic electric field of $\overline{E^\dagger} = E_0 \overline{i}_z$.

Examining the polarization contributions from Eqs. (3.28) and (3.29), we find that the mathematical forms of the two equations indicate both the liquid polarization and the infinite frequency response of the micro-particle dipole moment do not depend on the micro-particle rotation speed, $\overline{\Omega}$, and respond instantly to changes in the applied electric field, $\overline{E} = E_z \overline{i}_z$. Moreover, the liquid polarization as given in Eq. (3.28) is always in the same direction as that of the applied macroscopic electric field, $\overline{E} = E_z \overline{i}_z$. Hence, the polarization contributions from the carrier liquid, Eq. (3.28), and the infinite frequency response of the particle dipole moment, Eq. (3.29), generally do not contribute to the body electrical torque input through the ER fluid parcel and are less likely required to be relaxed via a polarization relaxation equation when the particle-liquid suspension is in full motion with all the continuum linear and spin velocities as well as the microscopic particle rotation speed coming into the non-equilibrium physical picture. This is the reason why we have limited the polarization relaxation process to the retarding polarization in Eq. (3.24) since the body electrical torque input exerted on the ER fluid parcel is mostly concentrated on the microscopic particle-liquid interface where the interfacial charges accumulate (recall the physical arguments given in Section 3.2 for deriving Cebers' (1980) model for micro-particle dipole relaxation).

Having the knowledge of only the retarding polarization is required to be relaxed, we need to find a suitable microscopic equilibrium state to define our equilibrium retarding polarization,

$\overline{P_{eq}^{\omega}}$, such that combined with the retarding polarization relaxation equation, Eq. (3.24), all the non-equilibrium characteristics of the continuum linear velocity, $\bar{v}$, the continuum spin velocity, $\bar{\omega}$, and the micro-particle rotation speed, $\bar{\Omega}$, can possibly be incorporated in our model for the ER fluid flow.

A simplest and most intuitive microscopic state of (dynamic) equilibrium can be defined for our ER fluid parcel as: a leaky dielectric system of a particle-liquid suspension subjected to both an applied macroscopic electric field, $\bar{E} = E_z \bar{i}_z \approx \overline{E^{\dagger}} = E_0 \bar{i}_z$, and an "infinitesimal" initial macroscopic background flow vorticity so that the direction of micro-particle Quincke rotation is all aligned in the same direction as that of the flow vorticity (to satisfy the stable micro-particle rotation condition (Lobry & Lemaire, 1999; Cebers *et al.*, 2000; Cebers *et al.*, 2002; Lemaire *et al.*, 2006; Pannacci *et al.*, 2007*a*; Lemaire *et al.*, 2008)), and that the angular speed of micro-particle Quincke rotation is given by Eq. (2.57). We define this state as a *quasi-static-equilibrium* state for the ER fluid parcel. Assuming the mutual electrical and hydrodynamic interactions between the suspended micro-particles can be neglected (*i.e.*, dilute suspension with $\phi \ll 1$), the macroscopic *equilibrium retarding polarization* of the ER fluid parcel, $\overline{P_{eq}}$, resulting from the above described microscopic dynamic equilibrium state can be obtained by multiplying the retarding dipole moment of the rotating micro-particle, Eq. (2.41), with the particle number density, n, *i.e.*,

$$\overline{P_{eq}} = n\overline{p^{\dagger}} = P_{eq}^{y}\bar{i}_y + P_{eq}^{z}\bar{i}_z, \tag{3.32}$$

with

$$\begin{bmatrix} P_{eq}^{y} \\ P_{eq}^{z} \end{bmatrix} = 4\pi\varepsilon_1 nR^3 \begin{bmatrix} -\dfrac{\tau_{MW}\Omega\left(\dfrac{\sigma_2-\sigma_1}{2\sigma_1+\sigma_2}-\dfrac{\varepsilon_2-\varepsilon_1}{2\varepsilon_1+\varepsilon_2}\right)}{1+\tau_{MW}^2\Omega^2} \\ \dfrac{\left(\dfrac{\sigma_2-\sigma_1}{2\sigma_1+\sigma_2}-\dfrac{\varepsilon_2-\varepsilon_1}{2\varepsilon_1+\varepsilon_2}\right)}{1+\tau_{MW}^2\Omega^2} \end{bmatrix} E_0, \tag{3.33}$$

where the magnitude of the micro-particle rotation speed, Ω, is given by Eq. (2.57) and the direction of micro-particle rotation, either plus or minus sign in Eq. (2.57) for a 2D geometry defined by the *z-y* plane shown in Fig. 2.1, is to follow that of the macroscopic flow vorticity.

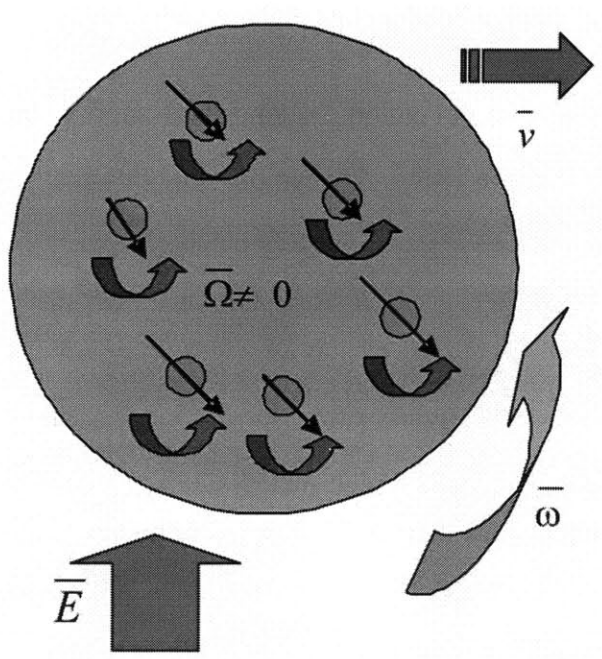

Figure 3.1. The schematic or cartoon illustrating the physical concept of the "rotating coffee cup model" describing the retarding polarization relaxation process for an ER fluid parcel.

Equations (3.32) and (3.33) represents the macroscopic retarding polarization of a static, motionless ER fluid, namely, $\bar{\omega} = 0$ and $\bar{v} = 0$. However, this does not mean that at macroscopic equilibrium, the micro-particles cannot rotate at the microscopic level, *i.e.*. $\bar{\Omega} \neq 0$, when the applied electric field is larger than the critical electric field given in Eq. (1.1), that is, $E_0 \geq E_c$. As for the cases of $E_0 < E_c$, Ω is set to zero in Eqs. (3.32) and (3.33) since an applied field less than the critical field will give imaginary values of Ω and the real root can only be zero as in Eq. (2.57).

Rigorously speaking, one more piece of information is required to complete the whole description of the equilibrium retarding polarization—the equilibrium retarding polarization, $\overline{P_{eq}^{\omega}}$, employed in Eq. (3.24) generally needs to be a vector quantity observed in the reference frame rotating along with the continuum spin velocity, $\bar{\omega}$. In other words, the micro-particle rotation speed employed in Eqs. (3.32) and (3.33) should be the vector particle rotation speed observed in the reference frame rotating along with the spin velocity instead of those given in Eq. (2.57). However, detailed rotation dynamics of a rotating micro-particle subjected to both shear flow and an applied electric field needs to be solved in order to correct for the differences in the vector values of the equilibrium retarding polarization (or the retarding dipole moments

due to micro-particle rotation, $\overline{\Omega}$) as observed in the respective spin velocity and stationary frames. Moreover, we will also require the interrelationships among the spin velocity, macroscopic continuum vorticity, microscopic local vorticity, and the local micro-particle rotation speed to better describe the micro-particle rotation dynamics in a consistent manner under our continuum framework. Nonetheless, both of these required physics are still very much open to further investigation and will add substantial complexities to our model rendering the mathematical analysis of the nER2 problem unfeasible or impractical in terms of engineering analysis. As a first approach, we approximate and assign Eqs. (3.32) and (3.33) to be $\overline{P_{eq}^{\omega}}$, *i.e.*,

$$\overline{P_{eq}} \to \overline{P_{eq}^{\omega}}, \tag{3.34}$$

with magnitude of the micro-particle rotation speed being given by Eq. (2.57) and the direction of the micro-particle rotation being determined by the macroscopic flow vorticity direction. Inserting Eq. (3.34) into Eq. (3.24), we have

$$\frac{D\overline{P}}{Dt} = \frac{\partial \overline{P}}{\partial t} + \left(\overline{v}\cdot\nabla\right)\overline{P} = \overline{\omega}\times\overline{P} - \frac{1}{\tau_{MW}}\left(\overline{P} - \overline{P_{eq}}\right), \tag{3.35}$$

such that together with Eqs. (2.57), (3.32), and (3.33), the non-equilibrium effects of the micro-particle rotation velocity, $\overline{\Omega}$, ER fluid continuum spin velocity, $\overline{\omega}$, and ER fluid continuum linear velocity, $\overline{v}$, on the retarding polarization of the ER fluid parcel can be described and characterized. Due to the approximation made in Eq. (3.34), the application of Eqs. (2.57), (3.32), (3.33), and (3.35) is limited to ER flow conditions of slow flow velocity and low to moderate applied external electric field strengths. In the development of Eqs. (2.57), (3.32), (3.33), and (3.35), we have assumed that the induced dipole moment on the micro-particles obeys the Maxwell-Wagner polarization—the induced charges are distributed on the surface of the particles in the micro scale. We have also assumed that only the retarding part of the macroscopic ER fluid polarization, *i.e.*, the polarization directly related to the interfacial charges, needs to be relaxed according to the non-equilibrium motions. Unlike the ferrofluid equilibrium magnetization, the equilibrium retarding polarization, Eqs. (3.32) and (3.33), does not follow a Langevin function (Rosensweig, 1997). This is because we are considering the rotation of micro-sized dielectric insulating particles on which Brownian motion has little influence (Jones, 1995).

Figure 3.1 shows a cartoon that illustrates the physical concept or "big-picture" for the relaxation process of the ER fluid retarding polarization characterized by the combined equations

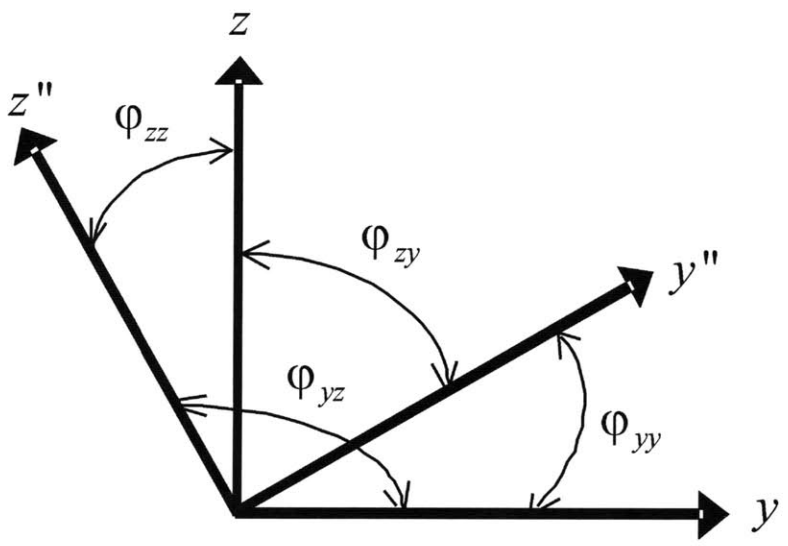

Figure 3.2. Schematic for the coordinate transformation between the $z-y$ coordinate and the $z"-y"$ coordinate as described by Eq. (3.38).

of Eqs. (2.57), (3.32), (3.33), and (3.35). In the cartoon, it can be seen that an ER fluid parcel is rotating with a spin velocity of $\overline{\omega}$ and slowly translating with a linear velocity of $\overline{v}$ through a uniform DC electric field, $\overline{E}$. If we move along with the ER fluid parcel, the micro-particle rotation velocity is observed to assume some finite value instead of zero. Thus, while the ER fluid parcel is rotating on the macro scale, the micro-particles contained within the parcel are also rotating in the micro scale. This is an analogous situation to the rotating coffee cup machines commonly seen in amusement parks or carnivals—the platform supporting the coffee cups is rotating at a certain angular velocity while the coffee cups (carrying kids or people) above the platform is also rotating at some other angular velocity. Drawing this analogy, we term our polarization relaxation model for the retarding polarization as the "rotating coffee cup model."

Some final remarks can be made on Eqs. (3.32) and (3.33). By setting the micro-particle rotation speed Ω to zero, the equilibrium retarding polarization shown in Eqs. (3.32) and (3.33) reduces back to the one given by Cebers (1980), *i.e.*, $\overline{P_{eq}}$ given in Eqs. (3.32) and (3.33) becomes $\overline{P_{eq}^0}$ in Eq. (3.14), or Eq. (3.11) times the particle number density, n. The different physical implications respectively given by $\overline{P_{eq}}$ and $\overline{P_{eq}^0}$ will be compared in Section 3.5. Lastly,

Eqs. (3.32) and (3.33) can also be derived via the dynamic effective medium model proposed by Xiao *et al.* (2008) as discussed in Section 3.4. The proof is given in the following.

With the micro-particles in the dilute particle-liquid suspension rotating in the same direction, say $\overline{\Omega} = \Omega \overline{i_x}$, in the *z*-*y* plane as shown in Fig. 2.1, we treat the rotating micro-particles as "molecules" and the applied microscopic electric field, $\overline{E^{\dagger}} = E_0 \overline{i_z}$, as the molecular electric field, $\overline{E_m}$, denoted in Eq. (3.19). Note however that we substitute the total dipole moment of the rotating micro-particles used in Eq. (3.19) with the retarding dipole moment of the particles, *i.e.*,

$$\overline{p^{\dagger}} = \overline{p^m} = \overline{\overline{\alpha}} \cdot \overline{E_m} = \overline{P}/n, \tag{3.36}$$

such that the retarding dipole moment of the micro-particles, $\overline{p^{\dagger}}$ from Eq. (2.41), become the "molecular dipole moments," $\overline{p^m}$. In other words,

$$\overline{p^m} = \overline{p^{\dagger}} = p_{my}\overline{i_y} + p_{mz}\overline{i_z} = -4\pi\varepsilon_1 R^3 \frac{\tau_{MW}\Omega\left(\dfrac{\sigma_2-\sigma_1}{2\sigma_1+\sigma_2} - \dfrac{\varepsilon_2-\varepsilon_1}{2\varepsilon_1+\varepsilon_2}\right)}{1+\tau_{MW}^2\Omega^2} E_0\overline{i_y} + 4\pi\varepsilon_1 R^3 \frac{\left(\dfrac{\sigma_2-\sigma_1}{2\sigma_1+\sigma_2} - \dfrac{\varepsilon_2-\varepsilon_1}{2\varepsilon_1+\varepsilon_2}\right)}{1+\tau_{MW}^2\Omega^2} E_0\overline{i_z}, \tag{3.37}$$

for each of the rotating micro-particles (or molecules) within the ER fluid suspension with the magnitude of Ω given by Eq. (2.57) and the direction of Ω given by the flow vorticity (either positive or negative in a 2D flow field defined by the *z*-*y* coordinate). Again, the physical picture of treating the rotating micro-particles as "molecules" is consistent with our definition of a continuum ER fluid parcel consisting of a representative amount or ensemble of micro-particles and carrier liquid molecules.

Referring to the coordinate transformation shown in Fig. 3.2, which relates the *z*-*y* coordinate as shown in Fig. 2.1 to some arbitrary $z"-y"$ coordinate through

$$\begin{bmatrix} y \\ z \end{bmatrix} = \begin{bmatrix} \cos\varphi_{yy} & \cos\varphi_{zy} \\ \cos\varphi_{yz} & \cos\varphi_{zz} \end{bmatrix} \begin{bmatrix} y" \\ z" \end{bmatrix}, \tag{3.38}$$

(Kundu & Cohen, 2004), we project the applied microscopic electric field, $\overline{E^{\dagger}} = E_0\overline{i_z}$, and the molecular dipole moment given in Eq. (3.37) to the new $z"-y"$ coordinate respectively as

$$\overline{E_m} = \overline{E^{\dagger}} = E_0\overline{i_z} = E_0\cos\varphi_{yz}\overline{i_y"} + E_0\cos\varphi_{zz}\overline{i_z"}, \tag{3.39}$$

and

$$\overline{p^m} = p_{my}\overline{i_y} + p_{mz}\overline{i_z} = \left(p_{my}\cos\varphi_{yy} + p_{mz}\cos\varphi_{yz}\right)\overline{i_y''} + \left(p_{my}\cos\varphi_{zy} + p_{mz}\cos\varphi_{zz}\right)\overline{i_z''}, \tag{3.40}$$

with p_{my} and p_{mz} defined in Eq. (3.37). Notice that the direction cosines shown in Fig. 3.2 have the relationships of: $\cos\varphi_{yy} = \cos\varphi_{zz}$ and $\cos\varphi_{yz} = -\cos\varphi_{zy}$. Expanding Eq. (3.40) with Eq. (3.37) and recognizing Eq. (3.39) in the expansion of Eq. (3.40), we arrive at the form of $\overline{p^m} = \overline{\overline{\alpha}} \cdot \overline{E_m}$ in Eq. (3.36) with $\overline{p^m}$ given by the expanded Eq. (3.40), $\overline{E_m}$ given by Eq. (3.39), and the molecular polarizability $\overline{\overline{\alpha}}$ given by

$$\overline{\overline{\alpha}} = \begin{bmatrix} \alpha_{yy} & \alpha_{yz} \\ \alpha_{zy} & \alpha_{zz} \end{bmatrix}, \tag{3.41}$$

where

$$\alpha_{yy} = \alpha_{zz} = 4\pi\varepsilon_1 R^3 \frac{\left(\dfrac{\sigma_2 - \sigma_1}{2\sigma_1 + \sigma_2} - \dfrac{\varepsilon_2 - \varepsilon_1}{2\varepsilon_1 + \varepsilon_2}\right)}{1 + \tau_{MW}^2 \Omega^2}, \tag{3.42}$$

and

$$\alpha_{yz} = -\alpha_{zy} = -4\pi\varepsilon_1 R^3 \frac{\tau_{MW}\Omega\left(\dfrac{\sigma_2 - \sigma_1}{2\sigma_1 + \sigma_2} - \dfrac{\varepsilon_2 - \varepsilon_1}{2\varepsilon_1 + \varepsilon_2}\right)}{1 + \tau_{MW}^2 \Omega^2}. \tag{3.43}$$

The expressions given in Eqs. (3.41)-(3.43) are consistent with those derived by Xiao *et al.* (2008) for a 2D geometry. Since the macroscopic effective permittivity tensor, $\overline{\overline{\varepsilon_{eff}}}$, depends on the molecular polarizability tensor, $\overline{\overline{\alpha}}$, as in Eq. (3.21), the elements of $\overline{\overline{\varepsilon_{eff}}}$ should also have the following relations, that is, $\varepsilon_{yy} = \varepsilon_{zz}$ and $\varepsilon_{yz} = -\varepsilon_{zy}$.

Expanding Eq. (3.21), we have the following to coupled relations, namely,

$$\varepsilon_{yz} = \frac{n}{3\varepsilon_0}\left[\alpha_{yy}\varepsilon_{yz} + \alpha_{yz}\left(\varepsilon_{zz} + 2\varepsilon_0\right)\right], \tag{3.44}$$

and

$$\varepsilon_{zz} + 2\varepsilon_0 = \frac{3\varepsilon_0 + \dfrac{n}{3\varepsilon_0}\alpha_{zy}\varepsilon_{yz}}{1 - \dfrac{n}{3\varepsilon_0}\alpha_{zz}}. \tag{3.45}$$

For dilute suspensions, *i.e.*, $\phi \ll 1$, we recognize the following relations, namely,

$$\frac{n}{3\varepsilon_0}\alpha_{yy} = \frac{n}{3\varepsilon_0}\alpha_{zz} = \phi\frac{\varepsilon_1}{\varepsilon_0}\frac{\left(\dfrac{\sigma_2-\sigma_1}{2\sigma_1+\sigma_2} - \dfrac{\varepsilon_2-\varepsilon_1}{2\varepsilon_1+\varepsilon_2}\right)}{1+\tau_{MW}^2\Omega^2}, \tag{3.46}$$

and

$$\frac{n}{3\varepsilon_0}\alpha_{yz} = -\frac{n}{3\varepsilon_0}\alpha_{zy} = -\phi\frac{\varepsilon_1}{\varepsilon_0}\frac{\tau_{MW}\Omega\left(\dfrac{\sigma_2-\sigma_1}{2\sigma_1+\sigma_2} - \dfrac{\varepsilon_2-\varepsilon_1}{2\varepsilon_1+\varepsilon_2}\right)}{1+\tau_{MW}^2\Omega^2}, \tag{3.47}$$

with the use of Eq. (3.31). Introducing Eqs. (3.46) and (3.47) into Eqs. (3.44) and (3.45) and retaining to the first order of the solid volume fraction, *i.e.*, $\sim O(\phi)$, we solve the coupled relations of Eqs. (3.44) and (3.45) to obtain

$$\varepsilon_{yz} \sim n\alpha_{yz} = -4\pi\varepsilon_1 nR^3\frac{\tau_{MW}\Omega\left(\dfrac{\sigma_2-\sigma_1}{2\sigma_1+\sigma_2} - \dfrac{\varepsilon_2-\varepsilon_1}{2\varepsilon_1+\varepsilon_2}\right)}{1+\tau_{MW}^2\Omega^2}, \tag{3.48}$$

and

$$\varepsilon_{zz}-\varepsilon_0 \sim n\alpha_{zz} = 4\pi\varepsilon_1 nR^3\frac{\left(\dfrac{\sigma_2-\sigma_1}{2\sigma_1+\sigma_2} - \dfrac{\varepsilon_2-\varepsilon_1}{2\varepsilon_1+\varepsilon_2}\right)}{1+\tau_{MW}^2\Omega^2}. \tag{3.49}$$

For an applied macroscopic electric field in the z-direction, $\overline{E} = E_z\overline{i}_z \approx E_0\overline{i}_z$ (which will be the case in the following analyses of Chapters 4 and 5), we again arrive at Eq. (3.33) by substituting $\overline{E} = E_z\overline{i}_z \approx E_0\overline{i}_z$ as well as Eqs. (3.48) and (3.49) into a modified version of Eq. (3.18) for the equilibrium retarding polarization, *i.e.*,

$$\overline{P_{eq}} = \left(\overline{\overline{\varepsilon_{eff}}} - \varepsilon_0\overline{\overline{I}}_0\right)\cdot\overline{E} = \begin{bmatrix}\varepsilon_{yy}-\varepsilon_0 & \varepsilon_{yz}\\ \varepsilon_{zy} & \varepsilon_{zz}-\varepsilon_0\end{bmatrix}\begin{bmatrix}0\\ E_0\end{bmatrix}. \tag{3.50}$$

3.5 Comparison among Different Equilibrium Polarization Schemes

In order to completely describe the retarding polarization relaxation of an ER fluid parcel, the retarding polarization relaxation equation, Eq. (3.35), is accompanied by the equilibrium retarding polarization, Eqs. (3.32) and (3.33), with the magnitude and direction of the micro-particle rotation speed given respectively by Eq. (2.57) and the direction of the macroscopic flow

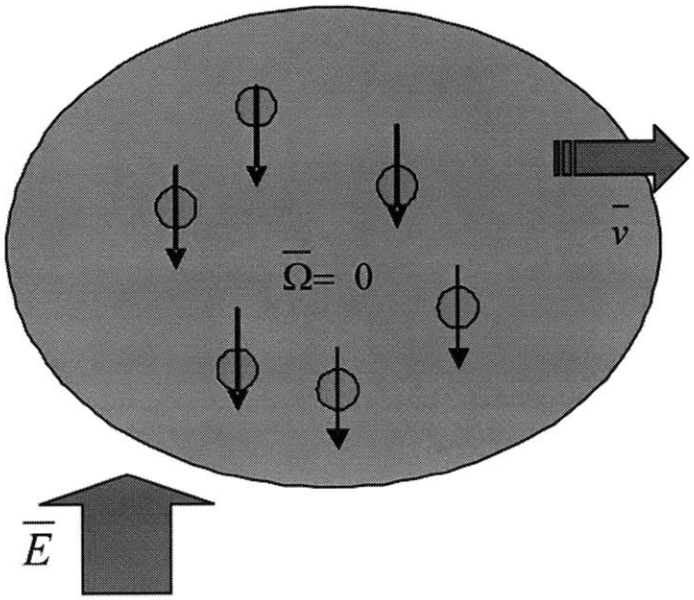

Figure 3.3. Cartoon illustrating the physical picture of the equilibrium retarding polarization based on the equilibrium retarding dipole moment, Eq. (3.11), employed in Cebers' (1980) polarization relaxation equation, Eq. (3.14).

vorticity under the framework of the "rotating coffee cup model" presented in the previous section. However, there are also other choices available for the polarization relaxation model or for the equilibrium polarization. In this section, we first describe the possible physical implications of several different polarization relaxation or equilibrium polarization models. The reason or need for our proposed "rotating coffee cup model" from a continuum mechanical perspective then becomes evident by comparing the strengths and weaknesses among the different models available. Finally, the limitations of the "rotating coffee cup model" is to be summarized so as to offer further insights and future directions for more advanced polarization relaxation modeling.

We first consider Cebers' (1980) polarization relaxation equation, Eq. (3.14), which has its origin from the microscopic dipole relaxation equation, Eq. (3.13), with the equilibrium retarding polarization $\overline{P_{eq}^{0}} = n\overline{p_{eq}^{\dagger}}$ being defined by the equilibrium retarding dipole moment, $\overline{p_{eq}^{\dagger}}$ in Eq. (3.11), times the particle number density, n. The cartoon characterizing this model is given in Fig. 3.3 with $\bar{E}$ being the applied electric field, $\bar{\Omega}$ being the micro-particle rotation speed, $\bar{v}$ being the linear flow velocity, and the arrows denoting the retarding dipole moment of the micro-particles. Though Eqs. (3.13) and (3.14) are developed in a stationary frame of reference, the

arguments of Shliomis' (1972, 2002) first magnetization relaxation equation can still be applied to alternatively derive Eqs. (3.13) and (3.14) since the equilibrium retarding polarization, $\overline{P_{eq}^{0}} = n\overline{p_{eq}^{\dagger}}$, and the equilibrium dipole moment, $\overline{p_{eq}^{\dagger}}$, are both defined by a zero micro-particle rotation velocity, $\overline{\Omega} = 0$ (see Fig. 3.3). Therefore, for an observer rotating along with the averaged micro-particle rotation speed, $\overline{\Omega^{\Omega}} = 0$, the retarding polarization can also be written as a Debye form with the equilibrium retarding polarization, $\overline{P_{eq}^{0}} = n\overline{p_{eq}^{\dagger}}$, being given at zero micro-particle rotation velocity (as seen in the "$^{\Omega}$" frame). Equation (3.14) can then be obtained by converting the Debye form back to the stationary frame and the total derivative in Eq. (3.14) can be generally replaced by the material derivative, Eq. (2.4). Therefore, Cebers' (1980) model most generally can encompass the influences of the non-equilibrium motions of the linear flow velocity and the averaged micro-particle rotation speed on the polarization relaxation. However, as can be seen in Fig. 3.3, this model is more focused on the two-phase particle-liquid suspension nature as mainly defined by the micro-particle rotation speed, $\overline{\Omega}$, and does not incorporate the non-equilibrium effects of a continuum spin velocity, $\overline{\omega}$, *i.e.*, a representative amount or ensemble of the suspended micro-particles and the carrier liquid molecules contained within an ER fluid parcel rotating at $\overline{\omega}$ with respect to the center of mass of the ensemble of the suspended micro-particles and the carrier liquid molecules (or ER fluid parcel). The physical picture shown in Fig. 3.3 is more likely interpreted as an local element of particle-liquid suspension with the suspended micro-particles rotating at $\overline{\Omega}$ while being convected along the flow with a speed of $\overline{v}$. Note however that in previous studies on the nER2 effect (Lobry & Lemaire, 1999; Cebers *et al.*, 2000; Cebers *et al.*, 2002; Lemaire *et al.*, 2006; Pannacci *et al.*, 2007*a*; Lemaire *et al.*, 2008), Cebers' dipole relaxation equation, Eq. (3.13), is combined with the angular momentum balance equation of a "single micro-particle" to solve for the micro-particle rotation speed, $\overline{\Omega}$. After the micro-particle rotation speed of the single particle is obtained, the stable solution to $\overline{\Omega}$ is substituted into an effective viscosity expression based on averaged particle rotation speeds as derived by Brenner (1970).

Based on Cebers' (1980) formulation, we can take a second step further and combine our proposed spin velocity based continuum retarding polarization relaxation equation, Eq. (3.35), with Cebers' equilibrium retarding polarization at zero micro-particle rotation speeds,

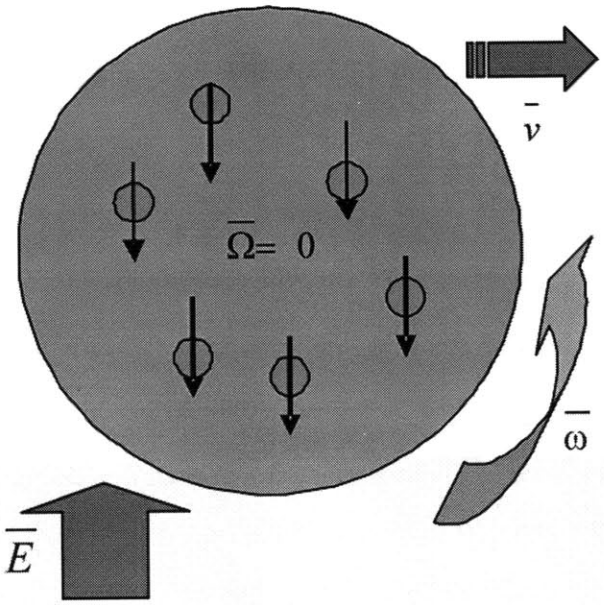

Figure 3.4. Cartoon illustrating the physical implications of employing Cebers' (1980) equilibrium retarding polarization in the present continuum spin velocity based retarding polarization relaxation equation, Eq. (3.35).

$\overline{P_{eq}} = \overline{P_{eq}^{0}} = n\overline{p_{eq}^{\dagger}}$ with $\overline{p_{eq}^{\dagger}}$ given in Eq. (3.11), to incorporate the non-equilibrium effects of the spin velocity as well as the physical picture of a representative amount or ensemble of the suspended micro-particles and the carrier liquid molecules contained within an ER fluid parcel rotating at $\bar{\omega}$ with respect to the center of mass of the ER fluid parcel. The schematic diagram or cartoon illustrating this idea is given in Fig. 3.4 with $\bar{E}$ being the applied electric field, $\bar{\Omega}$ being the micro-particle rotation speed, $\bar{v}$ being the continuum linear flow velocity, $\bar{\omega}$ being the continuum spin velocity, and the arrows denoting the retarding dipole moment of the micro-particles. With the equilibrium retarding polarization defined at zero micro-particle rotation speeds, *i.e.*, $\overline{P_{eq}} = \overline{P_{eq}^{0}} = n\overline{p_{eq}^{\dagger}}$, an observer rotating and moving along with the reference frame of the spin velocity "ω" observes zero micro-particle rotation, $\bar{\Omega} = 0$, meaning all the micro-particles are rigidly frozen or embedded within the ER fluid parcel when the ER fluid parcel is rotating at a spin velocity of $\bar{\omega}$ and being convected at a linear velocity of $\bar{v}$. In other words, the micro-particle rotation speed is always synchronized with the continuum spin velocity (as observed in the stationary frame) such that when observed in the spin velocity reference frame, we see a zero particle rotation, $\bar{\Omega} = 0$. Yet, a more realistic physical picture should also capture two more physical aspects: (i) a micro-particle with a dipole moment (or a component of the

dipole moment) in the opposite direction of the applied external electric field is generally in a state of unstable equilibrium and (ii) with the electrical torque input concentrated on the suspended micro-particles, the micro-particles should be rotating at a greater angular speed, $\overline{\Omega}$, as compared to the spin velocity, $\overline{\omega}$, (when both observed in the stationary frame) such that the rotating micro-particles entrain an enough or representative amount of nearby micro-particles and carrier liquid molecules that constitutes or defines a continuum ER fluid parcel. Due to the above two reasons, we may expect that this second approach to the polarization relaxation process as illustrated in Fig. 3.4 is likely a good approximation to low applied electric field and very viscous ER fluid flows since under low field viscous dominant conditions, both the spin velocity and the micro-particle rotation speed approach the macroscopic flow vorticity. Moreover, since the micro-particles are rigidly frozen or embedded in the ER fluid parcel when viewed from the spin velocity reference frame, the body torque input on the ER fluid parcel is likely to be greater and may overestimate the reduction in the effective viscosity of an nER2 fluid flow. This overestimation of the reduction in the effective viscosity can be generally verified by comparing the Couette effective viscosity results obtained by employing $\overline{P_{eq}} = \overline{P_{eq}^0} = n\overline{p_{eq}^\dagger}$ in Eq. (3.35) as to those obtained by substituting Eqs. (3.32) and (3.33) in Eq. (3.35) (*i.e.*, the rotating coffee cup model) at moderate to high electric field strengths after the full analytic expressions of the Couette solutions are solved in the zero spin viscosity limit, $\eta' = 0$, in Chapter 4. It can also be found that the Couette effective viscosity solutions obtained by substituting $\overline{P_{eq}} = \overline{P_{eq}^0} = n\overline{p_{eq}^\dagger}$ in Eq. (3.35) in the zero spin viscosity limit of our present continuum mechanical field equations fall relatively close to the effective viscosity results predicted by the combined single particle dynamics and two-phase effective medium theory as found in current literature (Pannacci *et al.*, 2007*a*; Lemaire *et al.*, 2008).

A third possible choice for the equilibrium retarding polarization shown in Eq. (3.35), $\overline{P_{eq}}$, is to define a dynamic equilibrium state in which the micro-particles contained within one ER fluid parcel are rotating in complete random directions such that the equilibrium retarding polarization is collinear but opposite to the direction of the applied electric field with polarization components in directions other than the electric field direction being averaged to zero due to the randomness in particle rotation. The cartoon showing this state of microscopic dynamic

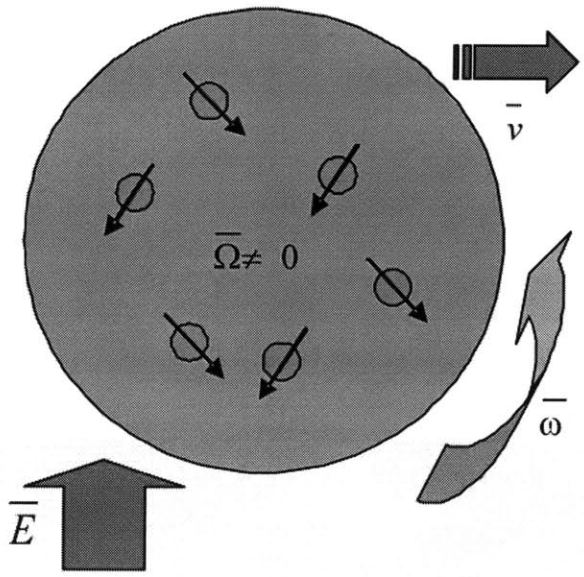

Figure 3.5. Cartoon illustrating a state of dynamic equilibrium for the equilibrium retarding polarization of an ER fluid parcel with the suspended micro-particles rotating in complete random directions within the ER fluid parcel. This dynamic equilibrium state best represents the condition of micro-particles rotating in random directions in a quiescent carrier liquid.

equilibrium is given in Fig. 3.5 where $\bar{E}$ is the applied electric field, $\bar{\Omega}$ is the micro-particle rotation speed, $\bar{v}$ is the continuum linear flow velocity, $\bar{\omega}$ is the continuum spin velocity, and the arrows are the retarding dipole moments of the micro-particles. In mathematical terms, the equilibrium retarding polarization described by Fig. 3.5 is simply substituting Eq. (3.30) (with the magnitude of the micro-particle rotation speed given by Eq. (2.57)) for $\overline{P_{eq}}$ in the continuum retarding polarization relaxation equation shown in Eq. (3.35). Nevertheless, we need to point out that this model (as defined above and by Fig 3.5) for the equilibrium retarding polarization is only good for infinitesimal macroscopic ER fluid motions, *i.e.*, a nearly quiescent ER fluid with the suspended micro-particles rotating at random directions in the micro scale, and generally cannot produce significant electrical body torque or the subsequent nER2 effect, which is likely consistent to the experimental observation and physical picture that both initial imposed flow vorticity and micro-particle Quincke rotation are required to induce the nER2 phenomenon.

After reviewing the other possible models for the equilibrium polarization, it is now evident why we need to propose a "rotating coffee cup model" to formulate our continuum polarization relaxation equation, Eq. (3.35), and its accompanying equilibrium retarding polarization, Eqs. (3.32) and (3.33) for describing the polarization relaxation process of the nER2 fluid flow from a

classical field theory based continuum mechanical point of view. Using the "rotating coffee cup model," we can incorporate the non-equilibrium effects due to a continuum spin velocity, $\overline{\omega}$, while also be consistent with the microscopic picture of (i) a micro-particle with a dipole moment (or a component of the dipole moment) in the opposite direction of the applied external electric field is generally in a state of unstable equilibrium and (ii) with the electrical torque input concentrated on the suspended micro-particles, the micro-particles should be rotating at a greater angular speed, $\overline{\Omega}$, as compared to the spin velocity, $\overline{\omega}$, (when both observed in the stationary frame) such that the rotating micro-particles entrain an enough or representative amount of nearby micro-particles and carrier liquid molecules that constitutes or defines a continuum ER fluid parcel.

As already mentioned in Section 3.4, the equilibrium retarding polarization, $\overline{P_{eq}}$, employed in Eq. (3.35) should rigorously be the polarization observed in the reference frame moving or rotating along with the continuum spin velocity, *i.e.*, $\overline{P_{eq}^{\omega}}$ (please compare the Jaumann derivative, or corotational derivative, in its vector form (Fredrickson, 1964; Brenner, 1984; Rinaldi, 2002) with Eqs. (3.3), (3.14), (3.23), and (3.35)). However, since correcting for this frame difference will add a significant amount of complexity both in physical and mathematical modeling, we have made the approximation of Eq. (3.34) and employed Eqs. (3.32) and (3.33) in the polarization relaxation equation of Eq. (3.35). The magnitude and direction of the micro-particle rotation speed employed in Eq. (3.33) are respectively determined by Eq. (2.57) and the macroscopic flow vorticity. Therefore, from Eq. (2.57), the equilibrium retarding polarization of Eqs. (3.32) and (3.33) reduces to the one used in Cebers' (1980) original equilibrium retarding polarization, with $\overline{P_{eq}} = \overline{P_{eq}^{0}} = n\overline{p_{eq}^{\dagger}}$ and $\overline{p_{eq}^{\dagger}}$ given by Eq. (3.11), when the externally applied electric field strength is lower than that of the Quincke rotation critical electric field, E_c. In other words, our "rotating coffee cup model" as shown in Fig. 3.1 consistently reduces to the physical picture given in Fig. 3.4 by using $\overline{P_{eq}} = \overline{P_{eq}^{0}} = n\overline{p_{eq}^{\dagger}}$ in Eq. (3.35) for low electric field strengths, *i.e.*, $E_0 < E_c$. The proposed rotating coffee cup model therefore should fairly capture the polarization relaxation process within our present continuum mechanical framework for low to moderate applied electrical field strengths.

Lastly, unlike Cebers' (1980) dipole relaxation equation, Eq. (3.13), the present rotating coffee cup model for the polarization relaxation of the ER fluid is developed or formulated on a phenomenological basis rather than on a charge relaxation/conservation basis. The present "rotating coffee cup model" cannot capture the whole micro- and macroscopic picture of the charge relaxation/conservation within the ER fluid parcel consisting of both rotating micro-particles and carrier liquid molecules when in non-equilibrium motion. To rigorously account for the charge conservation within an ER fluid parcel, the microscopic electrical double layers (EDL) around the rotating micro-particles come into the physical picture and a charged species mass transport analysis based on the Nerst-Plank equation is required (Probstein, 1994). These research topics are however still open for further investigation and is beyond the scope of the present thesis.

Chapter 4

Couette Flows with Internal Micro-particle Electrorotation

After laying down the foundations in the previous two chapters, we now further apply the developed governing classical continuum mechanical field equations, namely, the continuity equation, Eq. (2.1), the linear momentum equation, Eq. (2.2), the angular momentum equation, Eq. (2.3), the EQS Maxwell's equations, Eqs. (2.5)-(2.7), and the retarding polarization relaxation equation with its accompanying equilibrium retarding polarization, Eqs. (2.57), (3.32), (3.33), and (3.35), to study and analyze the negative electrorheological responses of ER fluid flows with internal micro-particle electrorotation, *i.e.*, the nER2 effect, in two-dimensional (2D) Couette flow geometries.

Using the assumptions outlined in Section 2.3, we first present the simplified set of governing equations in the zero spin viscosity limit, $\eta' = 0$, for Couette flows in Section 4.1. With this simplified set of equations, Section 4.2 presents the analytic expressions of the continuum spin velocity, ω_x (or ω^*), and effective viscosity, η_{eff} (or η^*), as functions of the shear rate, γ^* (or the Couette boundary driving velocity, U_0), and externally applied DC electric field, E_0 (or E^*). Parametric studies are then performed on these solutions obtained, and the results are discussed for the nER2 response in the zero spin viscosity limit.

Similarly, Section 4.3 presents the simplified set of governing equations for Couette flows with internal micro-particle electrorotation in the finite spin viscosity small spin (velocity) limit, *i.e.*, $\eta' \neq 0$ and $\tau_{MW}^2 \omega_x^2 \ll 1$. By employing suitable boundary conditions, the coupled set of

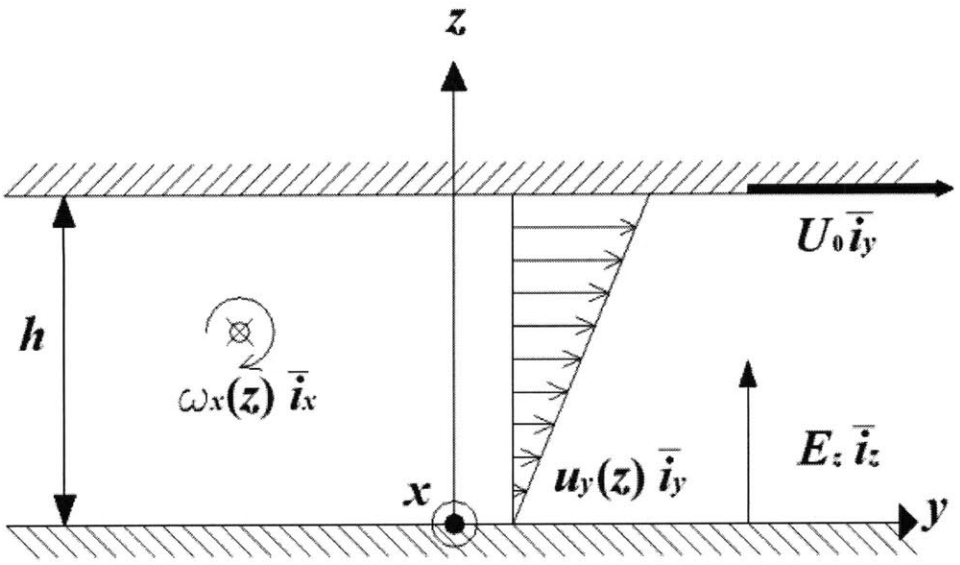

Figure 4.1. The schematic diagram illustrating the geometry, dimensions, and physical parameters for Couette flow with internal micro-particle electrorotation.

differential equations are then solved to obtain analytical solutions to the spin velocity field, ω_x (or ω^*), linear velocity field, u_y (or u^*), and effective viscosity, η_{eff} (or η^*), as functions of the shear rate, γ^* (or U_0), the applied DC electric field, E_0 (or E^*), the boundary condition selection parameter, β, and the spin viscosity, η'. Results of the parametric studies performed on these finite spin viscosity, small spin solutions are finally discussed. These solutions, results, and discussions are given in Section 4.4.

4.1 The Simplified Governing Equations in the Zero Spin Viscosity Limit for Couette Flow Geometries

Consider the Couette flow geometry shown in the schematic diagram of Fig. 4.1. The lower plate of the parallel plate system is fixed at zero velocity while the upper plate is applied with a constant velocity, U_0, in the positive y-direction. We assume that the flow is steady ($\partial/\partial t = 0$), incompressible, fully developed ($\partial/\partial y = 0$), and two-dimensional ($\partial/\partial x = 0$) in Cartesian coordinates. Under these assumptions, the continuity equation, Eq. (2.1), with $\bar{v} = u_y\bar{i}_y + u_z\bar{i}_z$ is readily reduced to $du_z/dz = 0$ and subsequently to $u_z = 0$ since the z-velocity component, u_z, has to satisfy the no-slip and non-penetrating (impermeable walls) boundary conditions at $z = 0$

and h with h being the height of the 2D channel. Moreover, by using the EQS Faraday's equation, Eq. (2.5), with $\overline{E} = E_y \overline{i_y} + E_z \overline{i_z}$ and the condition of fully developed flow, we find $dE_y/dz = 0$ such that E_y is just a constant throughout the 2D channel. Noting that the boundaries at $z = 0$ and h are perfectly conducting electrodes, and that the tangential component of the electric field is continuous across the boundaries, the constant E_y is simply zero. Therefore, the applied DC electric field is to be in the z-direction only. The fringing effects at the ends of the channel are to be neglected.

The governing equations are further simplified by considering a zero spin viscosity, *i.e.*, $\eta' = 0$, in the angular momentum equation, Eq. (2.3). Given the above assumptions combined with the continuity and zero spin viscosity conditions, Eqs. (2.2), (2.3), and (3.35), are then simplified into the following:

$$-\tau_{MW}\omega_x P_z - \left(P_y - P_{eq}^y\right) = 0, \tag{4.1}$$

$$\tau_{MW}\omega_x P_y - \left(P_z - P_{eq}^z\right) = 0, \tag{4.2}$$

$$2\zeta \frac{d\omega_x}{dz} + \eta_e \frac{d^2 u_y}{dz^2} = 0, \tag{4.3}$$

and

$$P_y E_z + 2\zeta\left(-\frac{du_y}{dz} - 2\omega_x\right) = 0, \tag{4.4}$$

where u_y is the y-velocity component, ω_x is the x-spin velocity component (note: $\overline{\omega} = \omega_x \overline{i_x}$ in 2D), E_z is the z-component of the applied DC electric field, and P_y and P_z are respectively the retarding polarization components in the y- and z- directions, *i.e.*, $\overline{P} = P_y \overline{i_y} + P_z \overline{i_z}$. Note that we have substituted the total polarization, P_{ty}, with the retarding polarization, P_y, in Eq. (4.4). This is because the DC electric field is applied in the z-direction only with $E_y = 0$. Thus the total polarization in the y-direction comes from the dipole moment tilt of the rotating micro-particles in the micro scale, which, on the macroscopic level, is generally the y-component of the retarding polarization. Finally, the z-linear momentum equation reduces to an equation which relates only the pressure gradient to the Kelvin body force density, and thus can be treated separately from the other equations.

Substituting Eq. (3.33) into Eqs. (4.1) and (4.2), we can solve for the y- and z- components of the retarding polarization as

$$P_y = n\frac{\alpha_y - \tau_{MW}\omega_x\alpha_z}{1+\tau_{MW}^2\omega_x^2}E_0, \tag{4.5}$$

$$P_z = n\frac{\alpha_z + \tau_{MW}\omega_x\alpha_y}{1+\tau_{MW}^2\omega_x^2}E_0, \tag{4.6}$$

where

$$\begin{bmatrix}\alpha_y\\ \alpha_z\end{bmatrix} = \begin{bmatrix}\alpha_{yz}\\ \alpha_{zz}\end{bmatrix} = 4\pi\varepsilon_1 R^3 \begin{bmatrix} -\dfrac{\tau_{MW}\Omega\left(\dfrac{\sigma_2-\sigma_1}{2\sigma_1+\sigma_2}-\dfrac{\varepsilon_2-\varepsilon_1}{2\varepsilon_1+\varepsilon_2}\right)}{1+\tau_{MW}^2\Omega^2} \\ \dfrac{\left(\dfrac{\sigma_2-\sigma_1}{2\sigma_1+\sigma_2}-\dfrac{\varepsilon_2-\varepsilon_1}{2\varepsilon_1+\varepsilon_2}\right)}{1+\tau_{MW}^2\Omega^2} \end{bmatrix}, \tag{4.7}$$

with α_{zz} and α_{yz} respectively defined in Eqs. (3.42) and (3.43), and the magnitude and direction of the micro-particle rotation speed, Ω, being respectively given by Eq. (2.57) and that of the macroscopic flow vorticity. Generally speaking, the z-component of the electric field, E_z, in Eq. (4.4) depends on the flow linear and spin velocities, and the EQS equations, Eqs. (2.5) and (2.6), need to be solved together with the retarding polarization, Eqs. (4.5), (4.6), and (4.7), linear momentum, Eq. (4.3), and angular momentum, Eq. (4.4), equations with the suitable electrical and mechanical boundary conditions applied at $z=0$ and h. However, the coupled set of governing equations becomes much more non-linear and less practical in engineering analyses. Assuming that, due to flow motion, corrections to the z-electric field, E_z, can be related to the microscopic applied electric field and the micro-particle solid volume fraction through

$$E_z \sim E_z^{\dagger} + \phi e_1 + \phi^2 e_2 + \cdots \sim E_0 + \phi e_1 + \phi^2 e_2 + \cdots, \tag{4.8}$$

where e_i's are the correction terms, we substitute Eq. (4.5) into Eq. (4.4) and approximate to the first order of magnitude of the volume fraction, ϕ, $E_z \approx E_0 + \phi e_1 + \cdots$ for dilute suspensions, *i.e.*, $\phi \ll 1$, so that the electrical field equations, Eqs. (2.5) and (2.6), can be decoupled from the mechanical field equations, Eqs. (2.1)-(2.3), or Eqs. (4.3) and (4.4). Hence the governing equations specific to the Couette flow geometry with internal particle electrorotation is obtained as Eq. (4.3) and

$$\frac{\alpha^* - \tau_{MW}\omega_x}{1+\tau_{MW}^2\omega_x^2} n\alpha_z E_0^2 + 2\zeta\left(-\frac{du_y}{dz} - 2\omega_x\right) = 0, \tag{4.9}$$

where $\alpha^* = \alpha_y/\alpha_z = -\tau_{MW}\Omega$. In Eq. (4.9), the first order correction, e_1, to the z-electric field has been neglected because e_1 has become a second order term after being substituted into Eq. (4.4), *i.e.*, $n\alpha_z E_0 E_z \approx n\alpha_z E_0\left(E_0 + \phi e_1 + \cdots\right)$ with $\phi \ll 1$ and $n\alpha_z \sim nR^3 \sim nd^3 \sim O(\phi)$ as in Eq. (3.31).

The boundary conditions for the velocity field, $\bar{v} = u_y \bar{i}_y$, is the general no-slip boundary condition, *i.e.*, $\bar{v} = 0$ at $z = 0$ and $\bar{v} = U_0 \bar{i}_y$ at $z = h$. On the other hand, the angular momentum equation, Eq. (4.9), eventually reduces to an algebraic equation for zero spin viscosity conditions as will be discussed shortly in Section 4.2; hence, there are no additional constraints to be applied at the boundaries for the Couette spin velocity field. This "free-to-spin" condition on ω_x for $\eta' = 0$ is likely an analogous case to the Euler equation for inviscid fluid flow—the linear flow velocity is allowed to slip at the solid-fluid boundaries when the fluid viscosity goes to zero.

4.2 Continuum Analysis in the Zero Spin Viscosity Limit

4.2.1 Solutions to the Spin Velocity, Linear Velocity, and Effective Viscosity

Integrating Eq. (4.3) with respect to z, we have

$$2\zeta\omega_x + \eta_e \frac{du_y}{dz} = C_c, \tag{4.10}$$

where C_c is a constant. Substituting Eq. (4.10) into Eq. (4.9), we find that the spin velocity, ω_x, does not depend on the spatial coordinate, z, and therefore Eq. (4.3) reduces to the original governing equation for simple Couette flow, *i.e.*,

$$\frac{d^2 u_y}{dz^2} = 0, \tag{4.11}$$

and the solution to Eq. (4.11) is

$$u_y(z) = \frac{U_0}{h} z. \tag{4.12}$$

Inserting Eq. (4.12) into Eq. (4.9) and using the following non-dimensionalization scheme, namely,

$$\omega^* = \tau_{MW}\omega_x,\ \gamma^* = \tau_{MW}\frac{U_0}{h},\ \text{and}\ M^* = \frac{2\zeta}{n\alpha_z E_0^2 \tau_{MW}}, \tag{4.13}$$

the non-dimensional angular momentum equation is obtained as

$$\omega^{*3} + \frac{\gamma^*}{2}\omega^{*2} + \left(1 + \frac{1}{2M^*}\right)\omega^* + \left(\frac{\gamma^*}{2} - \frac{\alpha^*}{2M^*}\right) = 0. \tag{4.14}$$

Equation (4.14) can be solved to obtain analytical expressions by symbolic calculation packages (Mathematica, Wolfram Research, Inc.) and the three roots of Eq. (4.14) are expressed as functions of γ^* and M^*. The three roots to Eq. (4.14) are:

$$\omega_{C1}^* = -\frac{\gamma^*}{6} + \varphi_{C1}\left[3\sqrt[3]{4}M^*\left(\varphi_{C2} + \sqrt{4\varphi_{C1}^3 + \varphi_{C2}^2}\right)^{1/3}\right]^{-1} - \frac{1}{6\sqrt[3]{2}M^*}\left(\varphi_{C2} + \sqrt{4\varphi_{C1}^3 + \varphi_{C2}^2}\right)^{1/3}, \tag{4.15}$$

$$\omega_{C2}^* = -\frac{\gamma^*}{6} - \varphi_{C1}\left(1 + i\sqrt{3}\right)\left[6\sqrt[3]{4}M^*\left(\varphi_{C2} + \sqrt{4\varphi_{C1}^3 + \varphi_{C2}^2}\right)^{1/3}\right]^{-1} + \frac{1}{12\sqrt[3]{2}M^*}\left[\left(1 - i\sqrt{3}\right)\left(\varphi_{C2} + \sqrt{4\varphi_{C1}^3 + \varphi_{C2}^2}\right)^{1/3}\right], \tag{4.16}$$

and

$$\omega_{C3}^* = -\frac{\gamma^*}{6} - \varphi_{C1}\left(1 - i\sqrt{3}\right)\left[6\sqrt[3]{4}M^*\left(\varphi_{C2} + \sqrt{4\varphi_{C1}^3 + \varphi_{C2}^2}\right)^{1/3}\right]^{-1} + \frac{1}{12\sqrt[3]{2}M^*}\left[\left(1 + i\sqrt{3}\right)\left(\varphi_{C2} + \sqrt{4\varphi_{C1}^3 + \varphi_{C2}^2}\right)^{1/3}\right], \tag{4.17}$$

where

$$\varphi_{C1} = 6M^* + 12M^{*2} - M^{*2}\gamma^{*2}, \tag{4.18}$$

and

$$\varphi_{C2} = -18M^{*2}\gamma^* + 72M^{*3}\gamma^* + 2M^{*3}\gamma^{*3} - 108M^{*2}\alpha^*. \tag{4.19}$$

Nevertheless, it should be pointed out that not all the three roots to ω^* are likely to be physically meaningful and interpretable for the flow phenomena of interest presented herein. Moreover, each of the three roots may vary from real to complex valued (or vice versa) in different parametric regimes. In order to find the most physically meaningful and interpretable solution or combination of solutions from the three possible roots to the current problem, the following considerations and conditions are applied to the flow field: (i) only real valued

solutions are considered, (ii) the ER fluid is "free-to-spin" at the solid-ER fluid boundaries since the governing physics reduce from a boundary value problem to an algebraic problem in zero spin viscosity conditions, and (iii) due to micro scale viscous interactions, the micro-particle angular velocity, $\overline{\Omega}$, should rotate in the same direction as that of the macroscopic ER flow vorticity so that the micro-particle rotation is always stable (Lobry & Lemaire, 1999; Cebers *et al.*, 2000; Cebers *et al.*, 2002; Lemaire *et al.*, 2006; Pannacci *et al.*, 2007*a*; Lemaire *et al.*, 2008).

We have shown that the spin velocity is a constant throughout the channel when $\eta' = 0$ in the Couette geometry. Hence, ω^* assumes some finite value at the solid-ER fluid boundaries, which is readily self-consistent with the "free-to-spin" condition. To satisfy condition (iii) for $E_0 \geq E_c$, we need to substitute into Eqs. (4.5)-(4.7) the micro-particle angular velocity with the minus sign in Eq. (2.57) which has the same negative sign (or clockwise rotation) as the macroscale Couette flow vorticity, namely, $\nabla \times \bar{v} = -\left(du_y/dz\right)\overline{i_x} = -\left(U_0/h\right)\overline{i_x}$, with the coordinate systems defined in Figs. 2.1 and 4.1. For $E_0 < E_c$, we employ $\Omega = 0$ (see Eq. (2.57)) in Eqs. (4.5)-(4.7) and select or pick out the root to the spin velocity, ω^* or ω_x, that has the same negative sign as the Couette flow vorticity. For the parametric regimes of our interests, we identify the stable and real valued solution to the spin velocity as: for $E_0 \geq E_c$ (use negative Ω value in Eqs. (2.57), (4.5), (4.6), and (4.7)),

$$\omega_{C2}^* = -\frac{\gamma^*}{6} - \varphi_{C1}\left(1+i\sqrt{3}\right)\left[6\sqrt[3]{4}M^*\left(\varphi_{C2}+\sqrt{4\varphi_{C1}^3+\varphi_{C2}^2}\right)^{1/3}\right]^{-1} + \frac{1}{12\sqrt[3]{2}M^*}\left[\left(1-i\sqrt{3}\right)\left(\varphi_{C2}+\sqrt{4\varphi_{C1}^3+\varphi_{C2}^2}\right)^{1/3}\right], \tag{4.16}$$

for $E_0 \leq 0.8E_c$ (use $\Omega = 0$ in Eqs. (2.57), (4.5), (4.6), and (4.7)),

$$\omega_{C1}^* = -\frac{\gamma^*}{6} + \varphi_{C1}\left[3\sqrt[3]{4}M^*\left(\varphi_{C2}+\sqrt{4\varphi_{C1}^3+\varphi_{C2}^2}\right)^{1/3}\right]^{-1} - \frac{1}{6\sqrt[3]{2}M^*}\left(\varphi_{C2}+\sqrt{4\varphi_{C1}^3+\varphi_{C2}^2}\right)^{1/3}, \tag{4.15}$$

and for $0.8E_c < E_0 < E_c$ with $\Omega = 0$ in Eqs. (2.57), (4.5), (4.6), and (4.7), ω^* is given by both ω_{C1}^* and ω_{C2}^*, *i.e.*, Eqs. (4.15) and (4.16), where

$$\varphi_{C1} = 6M^* + 12M^{*2} - M^{*2}\gamma^{*2}, \tag{4.18}$$

and

$$\varphi_{C2} = -18M^{*2}\gamma^{*} + 72M^{*3}\gamma^{*} + 2M^{*3}\gamma^{*3} - 108M^{*2}\alpha^{*}. \tag{4.19}$$

Note that the results shown in Eqs. (4.15), (4.16), (4.18), and (4.19) are obtained under the "Solve" command of Mathematica. In $0.8E_c < E_0 < E_c$, part of the real valued solution to ω^{*} is given by Eq. (4.15) and the other part is given by Eq. (4.16), thus, both solutions have to be used in the evaluation of the spin velocity solutions.

The effective viscosity of Couette flows with particle electrorotation, η_{eff}, is derived by recognizing the relationship between the wall shear stress, τ_s, and the average shear rate (or the velocity of the upper plate, U_0, divided by the channel height, h) when the shear stress is held constant for a given flow or experimental condition, *i.e.*,

$$\tau_s = \eta_{eff}\frac{U_0}{h} = \eta_{eff}\frac{\gamma^{*}}{\tau_{MW}} = \bar{i}_z \cdot [\![\bar{\bar{T}}]\!] \cdot \bar{i}_y, \tag{4.20}$$

in which $[\![\ ]\!]$ denotes the shear stress differences across the solid-ER fluid interface, $\bar{i}_z$ is the row vector $[0 \quad 0 \quad 1]$, $\bar{i}_y$ is the column vector $[0 \quad 1 \quad 0]^t$, and $\bar{\bar{T}} = \bar{\bar{T}}_s + \bar{\bar{T}}_a$ is the total stress tensor with the symmetric part being

$$\bar{\bar{T}}_s = -p\bar{\bar{I}}_0 + \eta\left[\nabla\bar{v} + (\nabla\bar{v})^t\right] = \begin{bmatrix} -p & 0 & 0 \\ 0 & -p & \eta\dfrac{du_y}{dz} \\ 0 & \eta\dfrac{du_y}{dz} & -p \end{bmatrix}, \tag{4.21}$$

and the anti-symmetric part being

$$\bar{\bar{T}}_a = \zeta\bar{\bar{\varepsilon}}\cdot(\nabla\times\bar{v} - 2\bar{\omega}) = \begin{bmatrix} 0 & 0 & 0 \\ 0 & 0 & \zeta\left(-\dfrac{du_y}{dz} - 2\omega_x\right) \\ 0 & -\zeta\left(-\dfrac{du_y}{dz} - 2\omega_x\right) & 0 \end{bmatrix}, \tag{4.22}$$

where $\bar{\bar{I}}_0$ is the unit identity tensor, $\bar{\bar{\varepsilon}}$ is the permutation tensor, and the superscript t denotes the transpose of a matrix (Rosensweig, 1997). By expanding the total stress tensor into matrix form as in Eqs. (4.21) and (4.22) and substituting the velocity field, Eq. (4.12), and the spin

velocity field, Eq. (4.16) and/or (4.15), into Eqs. (4.20)-(4.22), the effective viscosity can be obtained as

$$\eta_{eff} = \eta_e + 2\zeta \frac{\omega^*}{\gamma^*}, \tag{4.23}$$

or in dimensionless terms,

$$\eta^* \equiv \frac{\eta_{eff}}{\eta} = \frac{\eta_e}{\eta} + \frac{2\zeta}{\eta}\frac{\omega_{Ci}^*}{\gamma^*}, \tag{4.24}$$

where $\omega_{Ci}^* = \omega_{C1}^*$ and/or ω_{C2}^* depending on the regimes of the electric field strength, and $\eta \approx \eta_0(1+2.5\phi)$ is the zero field ER fluid (particle-liquid mixture) viscosity as defined in Section 2.1. The shear stress differences in Eq. (4.20) are all evaluated at $z = 0$ in this thesis.

4.2.2 Modeling Results and Discussions

After obtaining the velocity and spin velocity fields as well as the effective viscosity, we now

Item	Description	Value	Units
d	Micro-particle diameter	8.00×10^{-5}	m
E_c	Critical electric field strength	1.30×10^{6}	$V\cdot m^{-1}$
h	Channel height	1.00×10^{-3}	m
n	Particle number density	3.73×10^{11}	m^{-3}
ε_1	Permittivity of carrier liquid	3.27×10^{-11}	$C^2N^{-1}m^{-2}$
ε_2	Permittivity of particles	2.30×10^{-11}	$C^2N^{-1}m^{-2}$
ϕ	Solid volume fraction of the particles	1.00×10^{-1}	--
η_0	Carrier liquid viscosity (no particles)	1.20×10^{-2}	$Pa\cdot s$
η'	Spin viscosity	0	$N\cdot s$
η	Zero field fluid viscosity (w/ particles)	1.53×10^{-2}	$Pa\cdot s$
η_e	$\eta_e = \eta + \zeta$	1.76×10^{-2}	$Pa\cdot s$
σ_1	Conductivity of the carrier liquid	4.00×10^{-8}	$S\cdot m^{-1}$
σ_2	Conductivity of the particles	1.00×10^{-14}	$S\cdot m^{-1}$
τ_{MW}	Maxwell-Wagner relaxation time	1.11×10^{-3}	s
ζ	Vortex viscosity	1.80×10^{-3}	$Pa\cdot s$

Table 4.1. System parameters, physical constants, and material properties used in the numerical evaluations (Lobry & Lemaire, 1999; Cebers *et al.*, 2000; Cebers *et al.*, 2002; Lemaire *et al.*, 2006; Pannacci *et al.*, 2007*a*; Lemaire *et al.*, 2008).

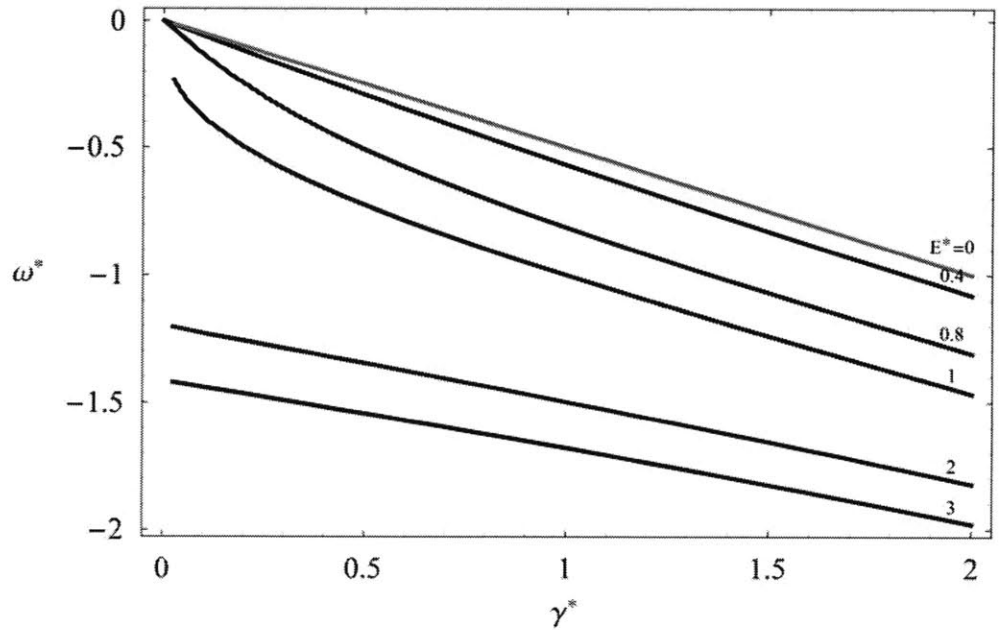

Figure 4.2. The dimensionless Couette spin velocity, ω^*, plotted with respect to the average shear rate, γ^*, evaluated at $E^* = 0$, 0.4, 0.8, 1.0, 2.0, and 3.0. For $E^* \geq 1.0$, the spin velocity is given by Eq. (4.16), *i.e.*, $\omega^* = \omega^*_{C2}$ (negative valued Ω from Eq. (2.57) used in Eqs. (4.5)-(4.7)), whereas for the cases of $E^* \leq 0.8$, ω^* is given by Eq. (4.15), $\omega^* = \omega^*_{C1}$, with the micro-particle rotation speed, Ω, set to zero in Eqs. (4.5)-(4.7). The gray line denotes the zero electric field spin velocity, namely, half of the fluid vorticity, $\omega^*_0 = -\gamma^*/2$.

further present the numerical evaluations of the analytical expressions given in Eqs. (4.15), (4.16), (4.23), and (4.24). The system parameters, physical constants, and material properties used in our evaluations follow those given in Lobry and Lemaire (1999), Cebers *et al.* (2000), Cebers *et al.* (2002), Lemaire *et al.* (2006), Pannacci *et al.* (2007*a*), and Lemaire *et al.* (2008) so as to facilitate a more effective comparison between the current continuum model and the two-phase effective continuum formulation found in the literature. These data are summarized in Table 4.1.

Shown in Fig. 4.2 is the Couette spin velocity, $\omega^* = \tau_{MW}\omega_x$, given by Eq. (4.16), *i.e.*, $\omega^* = \omega^*_{C2}$, for $E_0 \geq E_c$ and by Eq. (4.15), *i.e.*, $\omega^* = \omega^*_{C1}$, for $E_0 \leq 0.8E_c$ plotted with respect to the average shear rate, $\gamma^* = \tau_{MW}U_0/h$, evaluated at $E^* = E_0/E_c = 0$, 0.4, 0.8, 1.0, 2.0, and 3.0 where $E_c = 1.3\times10^6$ (V/m) is the critical electric field for the onset of particle Quincke rotation evaluated by Eq. (1.1). It is learned from Fig. 4.2 that the magnitude of the spin velocity within

the flow field increases as the applied electric field strength is increased with γ^* kept constant. On the other hand, the ER fluid spin magnitude also increases as the average shear rate, γ^*, or the applied velocity of the upper boundary, U_0, increases while the electric field strength is kept constant. As the applied electric field, E_0 or E^*, is gradually reduced, the ER fluid spin velocity gradually reduces back to the zero electric field angular velocity of a continuum fluid parcel, *i.e.*, $\omega_0^* = -\gamma^*/2$, or half of the Couette flow vorticity, which can be readily deduced from Eq. (4.14) by letting $M^* \to \infty$ or $E_0 \to 0$. This solution is noted by the gray line with $E^* = 0$ in Fig. 4.2.

Notice that for a given field strength and shear rate, the spin velocity, ω^* or ω_x, is a constant throughout the channel and, thus, does not depend on the spatial z-coordinate as already discussed in Sections 4.1 and 4.2.1 for the Couette geometry. With the spin velocity being a constant in Eq. (4.3), the velocity field of Couette flow with internal micro-particle electrorotation is found to be the same as that of Couette flow *without* particles—a result consistent with those given in Shliomis (1972) and Rosensweig (1997). Thus, the velocity field of Couette flow with micro-particle electrorotation is not further presented herein since plots of the linear profile given by Eq. (4.12) can be easily found in standard fluid mechanics text books, *e.g.*, Fox and McDonald (1998).

Figure 4.3 shows the effective viscosity, $\eta^* = \eta_{eff}/\eta$, of Couette flow with internal micro-particle electrorotation as given in Eqs. (4.23) and (4.24). The effective viscosity is plotted with respect to the average shear rate, γ^*, with the electric field strength being evaluated at $E^* = 0$, 0.4, 0.8, 1.0, 2.0, and 3.0. Again, the spin velocity solution given by Eq. (4.16) is employed in Eqs. (4.23) and (4.24) for conditions of $E^* = E_0/E_c \geq 1$, whereas Eq. (4.15) is employed in Eqs. (4.23) and (4.24) for $E^* \leq 0.8$. It is readily seen that the effective viscosity decreases as the applied DC electric field strength increases. However, as the magnitude of the shear rate increases, the amount of reduction in the effective viscosity decreases regardless of the applied electric field strength. Since the effective viscosity is normalized and non-dimensionalized by the zero electric field ER fluid viscosity, η, we further point out that the value of η^* should approach to one as the applied electric field goes to zero, which is a result easily found by substituting $\omega_0^* = -\gamma^*/2$ into Eq. (4.24). The zero electric field result is indicated by the gray

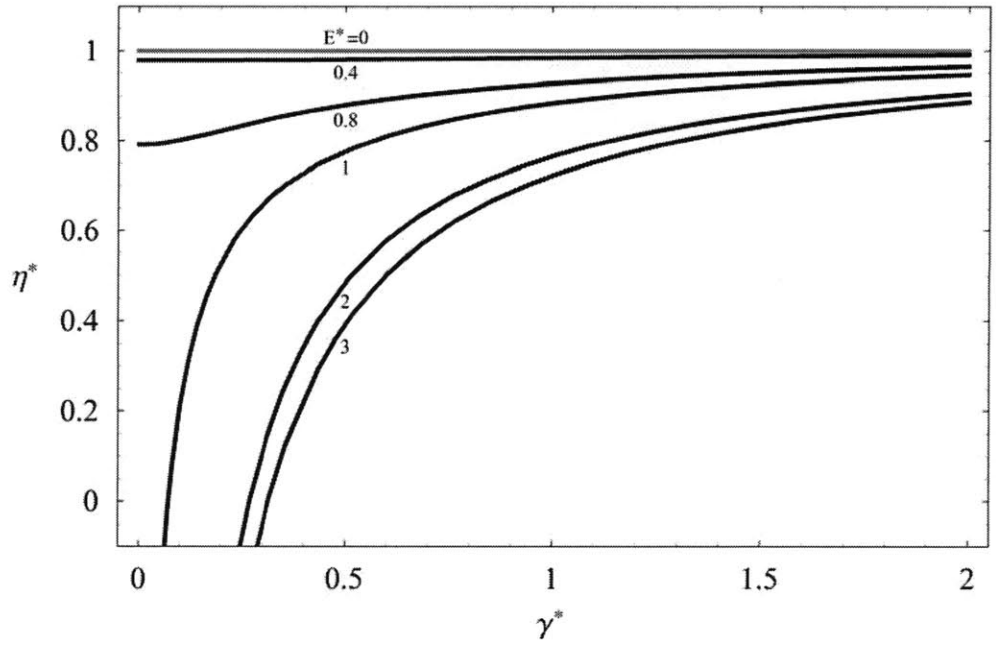

Figure 4.3. The effective viscosity, η^*, found for Couette flow plotted with respect to the average shear rate, γ^*, evaluated at $E^* = 0$, 0.4, 0.8, 1.0, 2.0, and 3.0. For $E^* \geq 1.0$, the spin velocity given by Eq. (4.16), *i.e.*, $\omega^* = \omega^*_{C2}$, is used in the evaluation of Eqs. (4.23) and (4.24), whereas for $E^* \leq 0.8$, $\omega^* = \omega^*_{C1}$ given by Eq. (4.15) is employed in Eqs. (4.23) and (4.24). The gray line denotes the zero electric field value of the effective viscosity, *i.e.*, $\eta^* = \eta_{eff}/\eta = 1$, with the value of η given in Table 4.1.

line in Fig. 4.3. It can be seen from the figure that the predicted effective viscosities η^* approach to one when the shear rate, γ^*, goes large or when the applied electric field strength is reduced towards zero.

From Fig. 4.3, we find that zero or negative viscosities are attainable when the applied DC electric field strength is strong enough. By using the terms "zero or negative viscosities," we do not mean that the true fluid viscosity is zero or negative, but that the effective or apparent viscosity comes out to be zero or a negative value through performing the force balance described by Eqs. (4.20)-(4.24) when the boundary shear stress, τ_s, is maintained a constant. In experimental terms, as the applied electric field strength becomes large, the "pumping" or "conveyer belt" effect of the micro-particles undergoing electrorotation on the ER fluid continuum becomes so significant that the ER fluid spin or rotation itself, instead of some externally applied force or torque, provides the shear stress required to move the upper plate of

the Couette geometry. Therefore, we may observe a finite shear rate, γ^*, or plate velocity, U_0, while the readings on the rheometer or viscometer indicate a zero torque applied to the fluid. As for negative effective viscosity conditions, the electrorotation conveyer belt is even more effective that the rheometer or viscometer eventually has to "hold back" the Couette driving plate to maintain some value of applied torque or shear rate. Further discussions can be found in Lobry and Lemaire (1999) for the rheometric experimental considerations and in Rinaldi *et al.* (2005) for experimental torque measurements on ferrofluids subjected to rotating magnetic fields.

4.3 The Simplified Governing Equations with Finite Spin Viscosities in the Small Spin Velocity Limit for Couette Flow Geometries

After examining and analyzing the continuum nER2 responses of Couette flows with internal micro-particle electrorotation in the zero spin viscosity limit, *i.e.*, $\eta' = 0$, we now turn out attention to the continuum nER2 responses with finite spin viscosities in the angular momentum equation but linearized for small spin velocity conditions, *i.e.*, $\eta' \neq 0$ and $\tau_{MW}^2 \omega_x^2 \ll 1$.

Following the same assumptions given in Section 4.1 with the 2D Couette geometry defined in Fig. 4.1, we obtain $u_z = 0$ and $E_y = 0$ due respectively to the non-penetrating (impermeable walls) boundary condition and the continuity of tangential electric field for perfectly conducting electrodes at $z = 0$ and h. By employing these results, the linear momentum equation, Eq. (2.2), angular momentum equation, Eq. (2.3), and the retarding polarization relaxation equation, Eq. (3.35), are simplified for finite spin viscosity conditions, namely,

$$-\tau_{MW}\omega_x P_z - \left(P_y - P_{eq}^y\right) = 0, \tag{4.1}$$

$$\tau_{MW}\omega_x P_y - \left(P_z - P_{eq}^z\right) = 0, \tag{4.2}$$

$$2\zeta \frac{d\omega_x}{dz} + \eta_e \frac{d^2 u_y}{dz^2} = 0, \tag{4.3}$$

and

$$P_y E_z + 2\zeta\left(-\frac{du_y}{dz} - 2\omega_x\right) + \eta' \frac{d^2\omega_x}{dz^2} = 0, \tag{4.25}$$

where the definitions of the variables shown in Eqs. (4.1), (4.2), (4.3), and (4.25) are the same as

those given in Section 4.1. Again, as in Eq. (4.4), we have replaced the total ER fluid polarization, P_{ty}, with the retarding polarization, P_y, in Eq. (4.25) since the DC electric field is applied in the z-direction with $E_y = 0$ and thus the polarization in the y-direction is basically due to the (retarding) dipole moment tilt resulting from micro-particle electrorotation. The reduced version of the z-linear momentum equation relates merely the z-pressure gradient to the z-component of the Kelvin body force density, $\left(\overline{P}_t \cdot \nabla\right)\overline{E}$, and is treated apart (or neglected) from Eq. (4.1), (4.2), (4.3), and (4.25).

Using the equilibrium retarding polarization given in Eq. (3.33), we solve Eqs. (4.1) and (4.2) to obtain

$$P_y = n\frac{\alpha_y - \tau_{MW}\omega_x\alpha_z}{1+\tau_{MW}^2\omega_x^2}E_0, \tag{4.5}$$

$$P_z = n\frac{\alpha_z + \tau_{MW}\omega_x\alpha_y}{1+\tau_{MW}^2\omega_x^2}E_0, \tag{4.6}$$

where

$$\begin{bmatrix}\alpha_y \\ \alpha_z\end{bmatrix} = \begin{bmatrix}\alpha_{yz} \\ \alpha_{zz}\end{bmatrix} = 4\pi\varepsilon_1 R^3 \begin{bmatrix} -\dfrac{\tau_{MW}\Omega\left(\dfrac{\sigma_2-\sigma_1}{2\sigma_1+\sigma_2} - \dfrac{\varepsilon_2-\varepsilon_1}{2\varepsilon_1+\varepsilon_2}\right)}{1+\tau_{MW}^2\Omega^2} \\ \dfrac{\left(\dfrac{\sigma_2-\sigma_1}{2\sigma_1+\sigma_2} - \dfrac{\varepsilon_2-\varepsilon_1}{2\varepsilon_1+\varepsilon_2}\right)}{1+\tau_{MW}^2\Omega^2} \end{bmatrix}, \tag{4.7}$$

with α_{zz} and α_{yz} respectively defined in Eqs. (3.42) and (3.43), and the magnitude and direction of the micro-particle rotation speed, Ω, being respectively given in Eq. (2.57) and that of the macroscopic flow vorticity. We apply the same approximation to the z-component of the electric field, *i.e.*, Eq. (4.8), and substitute Eqs. (4.5) and (4.8) into Eq. (4.25) to obtain

$$\frac{\alpha^* - \tau_{MW}\omega_x}{1+\tau_{MW}^2\omega_x^2} n\alpha_z E_0^2 + 2\zeta\left(-\frac{du_y}{dz} - 2\omega_x\right) + \eta'\frac{d^2\omega_x}{dz^2} = 0, \tag{4.26}$$

where $\alpha^* = \alpha_y/\alpha_z = -\tau_{MW}\Omega$ and the electrical body torque term, $P_y E_z$, has been retained to the first order of the particle solid volume fraction, ϕ, for dilute suspensions, *i.e.*, $\phi \ll 1$, since $n\alpha_z E_0 E_z \approx n\alpha_z E_0\left(E_0 + \phi e_1 + \cdots\right)$ and $n\alpha_z \sim nR^3 \sim nd^3 \sim O(\phi)$ as in Eq. (3.31).

We now further linearize Eq. (4.26) with the condition of small spin velocities, *i.e.*, $\tau_{MW}^2\omega_x^2 \ll 1$, such that Eq. (4.26) becomes

$$\left(\alpha^* - \tau_{MW}\omega_x\right)n\alpha_z E_0^2 + 2\zeta\left(-\frac{du_y}{dz} - 2\omega_x\right) + \eta'\frac{d^2\omega_x}{dz^2} = 0. \tag{4.27}$$

Equations (4.3), (4.7), and (4.27) together form the simplified governing equations for analyzing and describing the continuum nER2 responses of the Couette flow with internal micro-particle electrorotation in the finite spin viscosity small spin velocity limit, *i.e.*, $\eta' \neq 0$ and $\tau_{MW}^2\omega_x^2 \ll 1$. As a caveat, the criterion of $\tau_{MW}^2\omega_x^2 \ll 1$ for linearization gives an estimate of the maximum range of spin velocity valid for our analyses. Since the Maxwell-Wagner relaxation time has the order of magnitude of $O\left(10^{-3}\right)$ for the selected materials given in the present work (see Table 4.1), the dimensional spin velocity can at most be at the order of $O\left(10^{0}\right)$ to $O\left(10^{1}\right)$ so that $\tau_{MW}^2\omega_x^2 \sim O\left(10^{-2}\right)$ to $O\left(10^{-4}\right)$, which is roughly a general estimate for a physical value that is much less than one.

The boundary condition on the velocity field, $\bar{v} = u_y\,\bar{i}_y$, is once again the no-slip boundary condition, *i.e.*, $\bar{v} = 0$ at $z = 0$ and $\bar{v} = U_0\,\bar{i}_y$ at $z = h$. However, unlike the case of zero spin viscosity conditions, Eq. (4.27) does not reduce to an algebraic equation and the condition of "free-to-spin" no longer applies to Eq. (4.27). For finite spin viscosity conditions, the boundary condition on the continuum spin velocity field, $\bar{\omega} = \omega_x\,\bar{i}_x$, is given by

$$\bar{\omega} = \frac{\beta}{2}\left(\nabla \times \bar{v}\right), \tag{4.28}$$

at $z = 0$ and h, where β is a boundary condition selection parameter ranging from zero to one, *i.e.*,

$$0 \le \beta \le 1, \tag{4.29}$$

as described in Kaloni (1992), Lukaszewicz (1999), Rinaldi (2002), and Rinaldi and Zahn (2002). Notice that previous work (Kaloni, 1992) has reported that the boundary condition of $\bar{\omega} = \omega_x\bar{i}_x = 0$ may give theoretical predictions inconsistent with experimental observations for some micro-polar fluid flow conditions. As will be discussed in the following section, inconsistency is also found between the results predicted by our present continuum mechanical

model when $\overline{\omega} = \omega_x \overline{i_x} = 0$ at the boundaries and those experimentally observed in previous literature (Lobry & Lemaire, 1999; Cebers *et al.*, 2000; Cebers *et al.*, 2002; Lemaire *et al.*, 2006; Pannacci *et al.*, 2007*a*; Lemaire *et al.*, 2008).

4.4 Continuum Analysis with Finite Spin Viscosities in the Small Spin Velocity Limit

4.4.1 Solutions to the Spin Velocity, Linear Velocity, and Effective Viscosity

Integrating Eq. (4.3), we have

$$2\zeta\omega_x + \eta_e \frac{du_y}{dz} = \mu_1, \tag{4.30}$$

where μ_1 is a constant. By employing the following non-dimensionalization scheme, namely,

$$\omega^* = \tau_{MW}\omega_x,\ z^* = \frac{z}{h},\ u^* = \frac{u_y}{U_0}, \text{ and } \gamma^* = \tau_{MW}\frac{U_0}{h}, \tag{4.31}$$

and substituting Eq. (4.30) into Eq. (4.27), the linear momentum equation, Eq. (4.30), and the angular momentum equation, Eq. (4.27) (combined with Eq. (4.30)), are respectively non-dimensionalized as

$$\frac{du^*}{dz^*} = \frac{\tau_{MW}}{\eta_e \gamma^*}\mu_1 - \frac{2\zeta}{\eta_e \gamma^*}\omega^*, \tag{4.32}$$

and

$$\frac{d^2\omega^*}{dz^{*2}} - A^2\omega^* = B, \tag{4.33}$$

where

$$A = \sqrt{\frac{\tau_{MW}h^2}{\eta'}\left(n\alpha_z E_0^2 + \frac{4\zeta}{\tau_{MW}} - \frac{4\zeta^2}{\eta_e \tau_{MW}}\right)}, \tag{4.34}$$

and

$$B = \frac{\tau_{MW}h^2}{\eta'}\left(\frac{2\zeta}{\eta_e}\mu_1 - n\alpha_y E_0^2\right), \tag{4.35}$$

with the stars "*" denoting dimensionless variables (A and B also being dimensionless but μ_1 has dimensions). Equation (4.33), a linear, second order constant coefficient ordinary differential equations, can further be solved as

$$\omega^*\left(z^*\right)=\mu_3\cosh\left(Az^*\right)+\mu_4\sinh\left(Az^*\right)-\frac{B}{A^2}, \tag{4.36}$$

where μ_3 and μ_4 are constants. After substituting Eq. (4.36) into Eq. (4.32), we integrate the linear momentum equation, Eq. (4.32), and arrive at

$$u^*\left(z^*\right)=\frac{\tau_{MW}}{\eta_e\gamma^*}\mu_1 z^*-\frac{2\zeta}{\eta_e\gamma^*}\frac{\mu_3}{A}\sinh\left(Az^*\right)-\frac{2\zeta}{\eta_e\gamma^*}\frac{\mu_4}{A}\cosh\left(Az^*\right)+\frac{2\zeta}{\eta_e\gamma^*}\frac{B}{A^2}z^*+\mu_2, \tag{4.37}$$

with μ_2 being a constant and B being related to μ_1 through Eq. (4.35). The boundary conditions on the linear and spin velocity fields can also be non-dimensionalized via Eq. (4.31); the non-dimensional no-slip boundary condition and Eq. (4.28) then becomes

$$u^*=0 \text{ at } z^*=0 \text{ and } u^*=1 \text{ at } z^*=1, \tag{4.38}$$

and

$$\omega^*=-\frac{1}{2}\beta\gamma^*\frac{du^*}{dz^*} \text{ at } z^*=0,1, \tag{4.39}$$

respectively. We apply Eqs. (4.38) and (4.39) to Eqs. (4.36) and (4.37) and solve for the coefficients, μ_1, μ_2, μ_3, and μ_4, as

$$\mu_1=\frac{(\beta\zeta-\eta_e)\eta_e\left[A\left(A^2\gamma^*\eta_e\eta'+2h^2n\zeta\tau_{MW}\alpha_y E_0^2\right)\cosh\left(\frac{A}{2}\right)-4E_0^2h^2n\zeta\tau_{MW}\alpha_y\sinh\left(\frac{A}{2}\right)\right]}{A\left(\beta\zeta-\eta_e\right)\left(4h^2\zeta^2+A^2\eta_e\eta'\right)\tau_{MW}\cosh\left(\frac{A}{2}\right)-2\zeta\left(4h^2\zeta\left(\beta\zeta-\eta_e\right)+A^2\beta\eta_e\eta'\right)\tau_{MW}\sinh\left(\frac{A}{2}\right)}, \tag{4.40}$$

$$\mu_2=\frac{2\zeta}{\eta_e\gamma^*}\frac{\mu_4}{A}, \tag{4.41}$$

$$\mu_3=\frac{-A\eta_e\left\{A^2\beta\gamma^*\eta_e\eta'+2h^2\left[2\gamma^*\zeta\left(\beta\zeta-\eta_e\right)+E_0^2n\eta_e\tau_{MW}\alpha_y\right]\right\}\cosh\left(\frac{A}{2}\right)}{-2A\left(\beta\zeta-\eta_e\right)\left(4h^2\zeta^2+A^2\eta_e\eta'\right)\cosh\left(\frac{A}{2}\right)+4\zeta\left(4h^2\zeta\left(\beta\zeta-\eta_e\right)+A^2\beta\eta_e\eta'\right)\sinh\left(\frac{A}{2}\right)}, \tag{4.42}$$

and

$$\mu_4=\frac{A\eta_e\left\{A^2\beta\gamma^*\eta_e\eta'+2h^2\left[2\gamma^*\zeta\left(\beta\zeta-\eta_e\right)+E_0^2n\eta_e\tau_{MW}\alpha_y\right]\right\}\tanh\left(\frac{A}{2}\right)}{-2A\left(\beta\zeta-\eta_e\right)\left(4h^2\zeta^2+A^2\eta_e\eta'\right)+4\zeta\left(4h^2\zeta\left(\beta\zeta-\eta_e\right)+A^2\beta\eta_e\eta'\right)\tanh\left(\frac{A}{2}\right)}. \tag{4.43}$$

Note that the polarizabilities of α_y and α_z found in Eqs. (4.34), (4.35), and (4.40)-(4.43) are expressed in terms of the micro-particle rotation speed, Ω as defined in Eq. (2.57), through Eq. (4.7). For the present 2D Couette geometry shown in Fig. 4.1 and the spatial coordinates defined in both Figs. 2.1 and 4.1, the macroscopically "imposed" flow vorticity, *i.e.*, $\nabla \times \bar{v} \approx -U_0/h\, \bar{i}_x$, is in the negative x-direction or clockwise direction pointing into the plane. Therefore, in order to satisfy the stable micro-particle rotation requirement as discussed in Section 4.2, we employ a negatively valued micro-particle rotation speed, *i.e.*, choose $\Omega < 0$ solution from Eq. (2.57), in the variables of α_y and α_z (given by Eq. (4.7)) found in Eqs. (4.34), (4.35), and (4.40)-(4.43) for DC electric field strengths greater than the Quincke rotation critical electric field, *i.e.*, $E_0 \geq E_c$, with E_c defined in Eq. (1.1). On the other hand, for the cases of DC electric field strengths less than the critical electric field, *i.e.*, $E_0 < E_c$, we employ the $\Omega = 0$ solution from Eq. (2.57) in the α_y and α_z found in Eqs. (4.34), (4.35), and (4.40)-(4.43) and require a physically reasonable solution of the spin velocity field, ω^* as in Eq. (4.36), to be negatively valued or to be rotating in the same direction as the macroscopically imposed vorticity. As will be seen in Section 4.4.2, the spin velocity solution automatically satisfies (without any manual selection of roots) the above requirement of rotating in the same direction as that of the imposed vorticity when $\Omega = 0$ in Eqs. (2.57), (4.7), (4.34), (4.35), and (4.40)-(4.43) for $E_0 < E_c$ conditions in the $\eta' \neq 0$, $\tau_{MW}^2 \omega_x^2 \ll 1$ limit of the continuum governing equations.

The effective viscosity of Couette flows with internal micro-particle electrorotation, η_{eff}, for finite spin viscosities in the small spin velocity limit can again be derived by substituting the solved spin and linear velocity fields (Eqs. (4.36) and (4.37), respectively) into Eqs. (4.20)-(4.22), *i.e.*,

$$\tau_s = \eta_{eff} \frac{U_0}{h} = \eta_{eff} \frac{\gamma^*}{\tau_{MW}} = \bar{i}_z \cdot [\![\bar{\bar{T}}]\!] \cdot \bar{i}_y , \tag{4.20}$$

in which $[\![\ ]\!]$ denotes the shear stress differences across the solid-ER fluid interface, $\bar{i}_z$ is the row vector $[0 \quad 0 \quad 1]$, $\bar{i}_y$ is the column vector $[0 \quad 1 \quad 0]'$, and $\bar{\bar{T}} = \bar{\bar{T}}_s + \bar{\bar{T}}_a$ is the total stress tensor with the symmetric part being

$$\overline{\overline{T_s}} = -p\overline{\overline{I_0}} + \eta\left[\nabla\bar{v} + \left(\nabla\bar{v}\right)^t\right] = \begin{bmatrix} -p & 0 & 0 \\ 0 & -p & \eta\dfrac{du_y}{dz} \\ 0 & \eta\dfrac{du_y}{dz} & -p \end{bmatrix}, \tag{4.21}$$

and the anti-symmetric part being

$$\overline{\overline{T_a}} = \zeta\overline{\overline{\varepsilon}}\cdot\left(\nabla\times\bar{v} - 2\bar{\omega}\right) = \begin{bmatrix} 0 & 0 & 0 \\ 0 & 0 & \zeta\left(-\dfrac{du_y}{dz} - 2\omega_x\right) \\ 0 & -\zeta\left(-\dfrac{du_y}{dz} - 2\omega_x\right) & 0 \end{bmatrix}, \tag{4.22}$$

where $\overline{\overline{I_0}}$ is the unit identity tensor, $\overline{\overline{\varepsilon}}$ is the permutation tensor, and the superscript t denotes the transpose of a matrix (Rosensweig, 1997). For the current finite spin viscosity small spin velocity conditions, the effective viscosity resulting from the nER2 effects in the Couette flow geometry can then be obtained as

$$\eta_{eff} = \eta_e \left.\frac{du^*}{dz^*}\right|_{z^*=0} + 2\zeta\frac{\left.\omega^*\right|_{z^*=0}}{\gamma^*}, \tag{4.44}$$

or in dimensionless terms,

$$\eta^* = \frac{\eta_e}{\eta}\left.\frac{du^*}{dz^*}\right|_{z^*=0} + \frac{2\zeta}{\eta}\frac{\left.\omega^*\right|_{z^*=0}}{\gamma^*}, \tag{4.45}$$

where the spin velocity is given by Eq. (4.36), the derivative of the linear velocity is given by the derivative of Eq. (4.37) with respect to z^*, and $\eta \approx \eta_0\left(1+2.5\phi\right)$ is the zero field ER fluid (particle-liquid mixture) viscosity as defined in Section 2.1. Again, the shear stress differences in Eq. (4.20) are all evaluated at $z = 0$.

4.4.2 Modeling Results and Discussions

After obtaining the solutions to the spin velocity, ω_x or ω^*, linear velocity, u_y or u^*, and effective viscosity, η_{eff} or η^*, in the previous subsection, we further investigate the negative

electrorheological behavior and fluid flow phenomenon due to internal micro-particle electrorotation in 2D Couette flow geometries by performing a series of parametric studies. The dimensionless spin velocity profiles, ω^*, linear velocity profiles, u^*, and effective viscosities, η^*, are plotted as functions of the spatial coordinate, z^* (for ω^* and u^*), applied DC electric field strength, E_0, boundary driving velocity, U_0, boundary condition selection parameter, β, and spin viscosity, η', so that the variations in the flow patterns and rheological properties with respect to the pertinent governing or driving parameters can be illustrated and examined systematically for $\eta' \neq 0$, $\tau_{MW}^2 \omega_x^2 \ll 1$ conditions.

Since the polarizabilities of α_y and α_z found in Eqs. (4.34), (4.35), and (4.40)-(4.43) and subsequently the spin and linear velocities (Eqs. (4.36) and (4.37), respectively) depend upon the magnitude and direction of the micro-particle rotation speed, Ω, as given in Eq. (2.57) for different regimes of the applied electric field strengths, E_0, we employ the negatively valued micro-particle rotation speed, $\Omega < 0$ solution from Eq. (2.57), in the α_y and α_z polarizabilities of Eqs. (4.34)-(4.37) and (4.40)-(4.43) for electric field strengths greater than the critical electric field for Quincke rotation, E_c defined in Eq. (1.1), and used the zero micro-particle rotation solution, $\Omega = 0$ solution in Eq. (2.57), in α_y and α_z of Eqs. (4.34)-(4.37) and (4.40)-(4.43) for electric field strengths less than E_c so as to satisfy the stable micro-particle rotation requirement as discussed in the previous sections.

To facilitate the presentation of our results and discussion, several of the physical variables employed in the following are non-dimensionalized by the following scheme:

$$z^* = \frac{z}{h},\ u^* = \frac{u_y}{U_0},\ \omega^* = \tau_{MW}\omega_x,\ E^* = \frac{E_0}{E_c},\ \gamma^* = \tau_{MW}\frac{U_0}{h},\ \eta^* = \frac{\eta_{eff}}{\eta},\ \text{and}\ \eta_p^* = \frac{\eta'}{\eta'_0}, \tag{4.46}$$

where h is the 2D channel height, U_0 is the Couette boundary driving velocity, τ_{MW} is the Maxwell-Wagner relaxation time defined in Eq. (2.39), E_c is the Quincke rotation critical electric field for a single solid micro-particle as defined in Eq. (1.1), $\eta \approx \eta_0(1+2.5\phi)$ is the zero electric field ER fluid (pure particle-liquid mixture) viscosity as defined in Section 2.1, and η'_0 is a reference spin viscosity given as $\eta'_0 = 1.53\times10^{-8}$ $(N\cdot s)$. The numerical value for η'_0 is chosen by the expression of

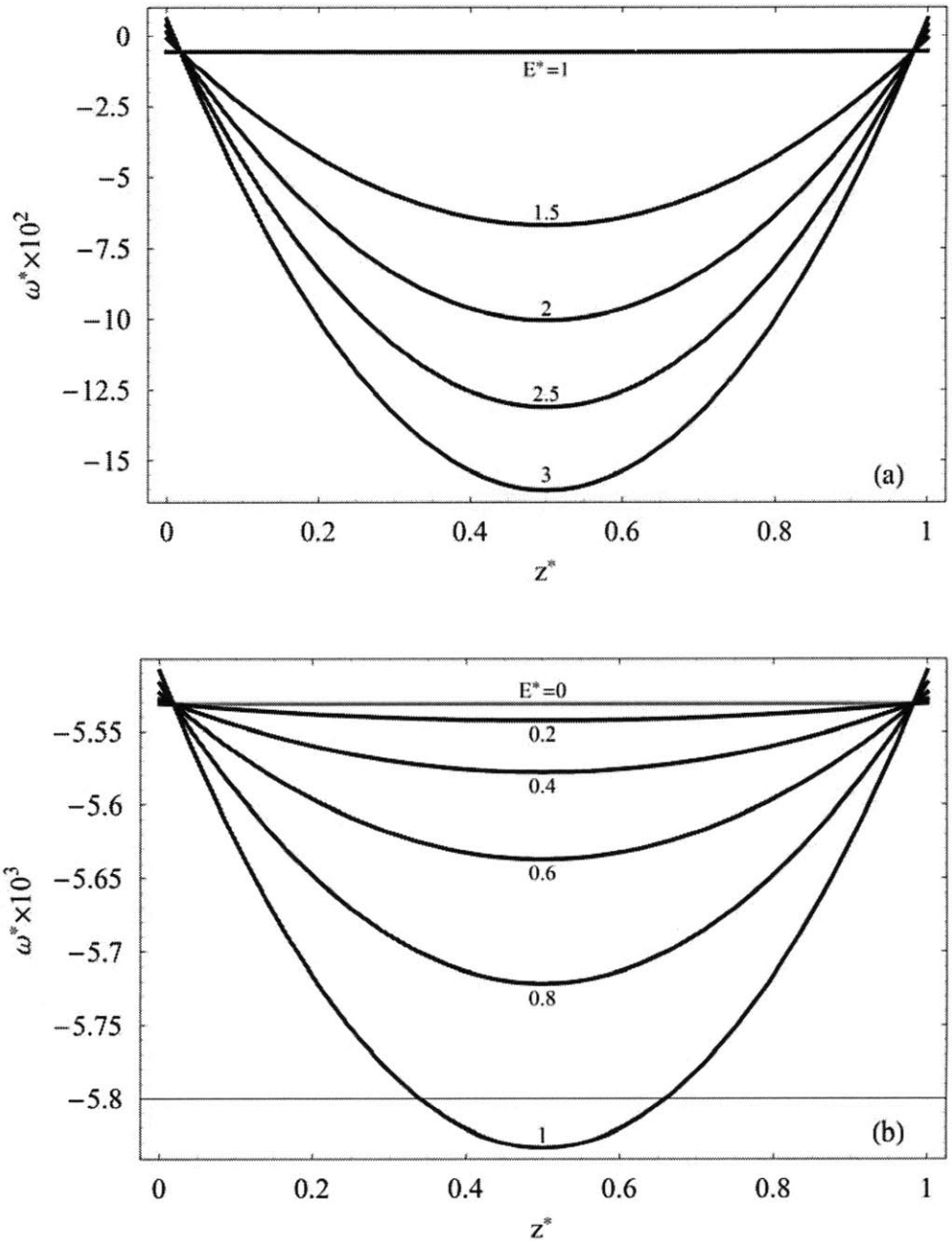

Figure 4.4. The spatial variations of the total spin velocity profiles, ω^*, given by Eq. (4.36) evaluated for (a) $E^* \geq 1$ and (b) $E^* \leq 1$ with $\beta = 1$, $\eta_p^* = 1$, and $U_0 = 0.01$ (m/s) (or $\gamma^* \approx 0.01$) kept constant. The gray line in Fig. 4.4(b) denotes the zero electric field solution of $\omega_0^* = -\gamma^*/2$ when the applied DC electric field is reduced to zero.

$$\eta' \sim l_D^2 \eta\,, \tag{4.47}$$

derived from the theory of Zaitsev and Shliomis (1969) with l_D being the characteristic diffusion

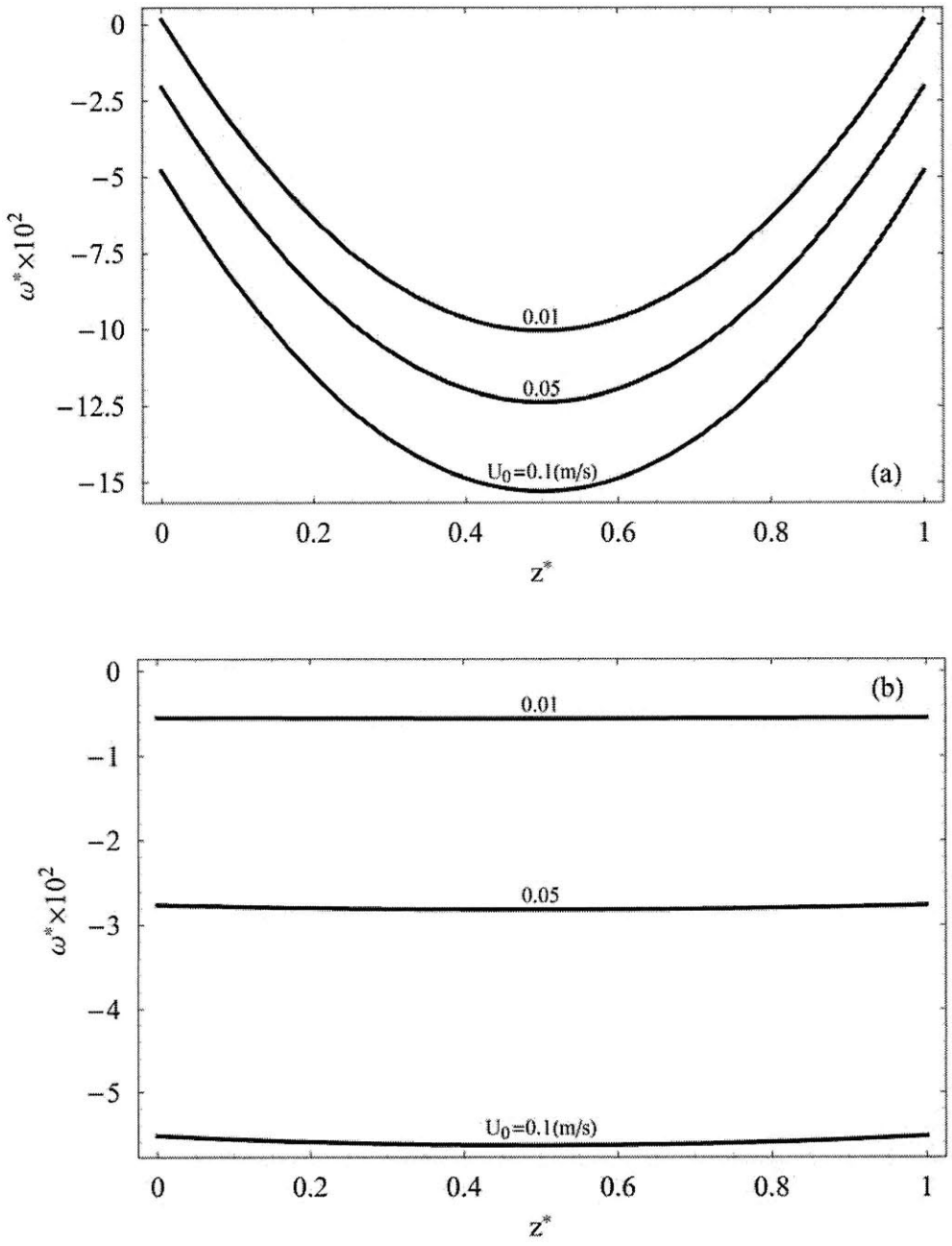

Figure 4.5. The spatial variations of the total spin velocity profiles, ω^* (in (a) and (b)), and the normalized spin velocity profiles, $\widetilde{\omega^*}$ (in (c) and (d)), evaluated at distinct values of the Couette boundary driving velocity, *i.e.*, $U_0 = 0.01$, 0.05, and 0.1 (m/s) (or equivalently, $\gamma^* \approx 0.01$, 0.05, and 0.1), for $E^* = 2 \geq 1$ (in (a) and (c)) and $E^* = 0.6 < 1$ (in (b) and (d)) while the other parameters of $\beta = 1$ and $\eta_p^* = 1$ are kept constant. (Cont. next page)

length for angular momentum. Although Zaitsev and Shliomis' (1969) original definition of l_D was "the averaged distance between the suspended rotating micro-particles," we generalize this

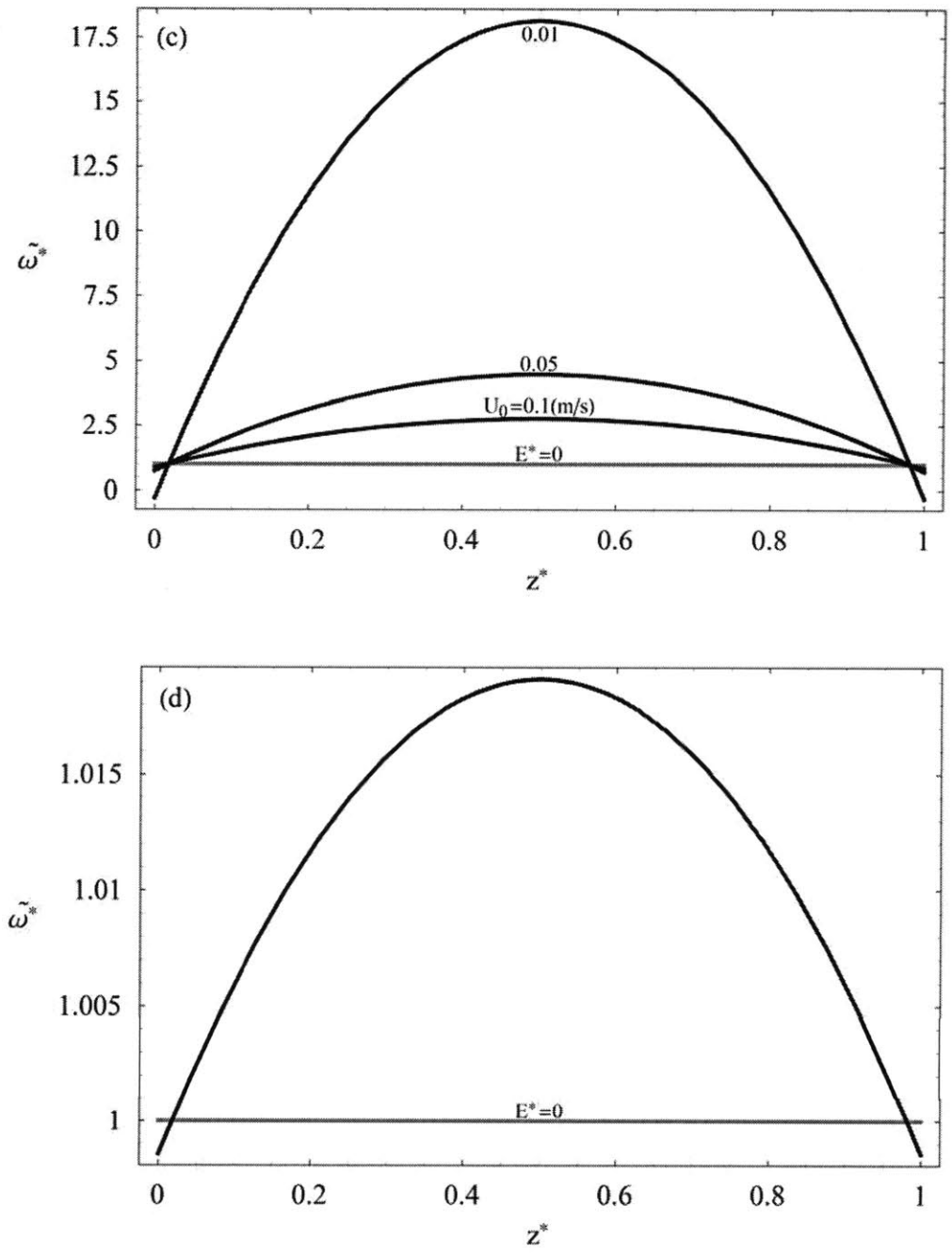

(Cont. Fig. 4.5) The solid gray lines in (c) and (d) denote the zero electric field solution of $\omega_0^* = -\gamma^*/2$.

characteristic length to be the averaged size of an ER fluid parcel (consisting of a representative amount of rotating micro-particles and carrier liquid molecules) as viewed from a continuum scale. Since for steady state fully developed internal flows, continuum diffusion processes, *e.g.*, boundary layer growth, are generally limited by the length scale of the channel, the characteristic diffusion length for angular momentum, l_D, by our generalized definition then scales as the

height of the parallel plate channel, *i.e.*, $l_D \sim h$, and thus we arrive at Eq. (4.47). Numerical values for the material properties, physical constants, and system dimensions used in our numerical evaluations of the analytical solutions are summarized in Table 4.1.

Shown in Figs. 4.4(a) and 4.4(b) are the total spin velocity profiles, ω^* given by Eq. (4.36), plotted with respect to the spatial coordinate, z^*, for Couette flow with internal micro-particle electrorotation for electric field strengths larger than the critical electric field, *i.e.*, $E^* = 1$, 1.5, 2, 2.5, and 3, and for field strengths less than the critical field, *i.e.*, $E^* = 0$, 0.2, 0.4, 0.6, 0.8, and 1, respectively. For both Figs. 4.4(a) and 4.4(b), we have employed $\beta = 1$, $\eta_p^* = 1$, and $U_0 = 0.01$ (m/s) (corresponding to a dimensionless shear rate of $\gamma^* = 0.0110625$) in the evaluation of the spin velocity profile solutions; we choose this combination of parametric regimes such that we follow the assumption of small spin velocity solutions, *i.e.*, $\tau_{MW}^2 \omega_x^2 \ll 1$, under our theoretical framework. It can be seen from the two figures that, irrespective of the different regimes of the applied electric field strength, the magnitude of the spin velocity, ω^*, increases as the applied electric field strength is increased, whereas the magnitude of the spin velocity is reduced as the applied electric field strength is decreased. We can also confirm that the rotation direction of the spin velocity field is indeed consistent with that of the macroscopically imposed vorticity, both in the negative *x*-direction with the coordinates defined in Fig. 4.1, so that the solutions satisfy the stable micro-particle rotation requirement. Note however that the spin velocity solutions respectively shown in Figs. 4.4(a) and 4.4(b) are still of different orders of magnitude due to the different regimes of electric field strengths and the different polarizabilities employed in Eqs. (4.34)-(4.37) and (4.40)-(4.43). As we gradually reduce the applied electric field strength, E^*, from $E^* \geq 1$ to $E^* < 1$, we find that the magnitude of the spin velocity also decreases and eventually reduces to the zero electric field solution of $\omega_0^* = \tau_{MW} \nabla \times \bar{v}/2 = -0.5\tau_{MW}\, du_y/dz = -\gamma^*/2 = -5.53125 \times 10^{-3}$, as denoted by the gray curve shown in Fig. 4.4 (b), which is simply half the vorticity of the ER fluid flow when no electric field is applied to the ER fluid. Figure 4.4 also suggests that the values of the spin velocities are greatest, *i.e.*, the ER fluid rotation is strongest, in the middle of the two dimensional channel. This implies that the fluid flow in the upper half of the channel, $z^* = 0.5 \sim 1.0$, is likely to be accelerated and the fluid flow in the

lower half of the channel, $z^* = 0.0 \sim 0.5$, is to be reduced. We shall come back to this result when we examine the linear velocity field.

We next examine the effects of the applied shear rate, γ^*, on the total spin velocity field, ω^*, by varying γ^* in the two regimes of the applied electric field strength, *i.e.*, $E^* \geq 1$ and $E^* < 1$, as shown in Figs. 4.5(a) and 4.5(b), respectively. In Fig. 4.5(a), we have evaluated the spin velocity field, ω^*, with respect to z^* at $U_0 = 0.01$, 0.05, and 0.1 (m/s) (corresponding to a dimensionless shear rate of $\gamma^* \approx 0.01$, 0.05, and 0.1, respectively) with $E^* = 2$, $\beta = 1$, and $\eta_p^* = 1$ whereas in Fig. 4.5(b), we have employed $U_0 = 0.01$, 0.05, and 0.1 (m/s) with $E^* = 0.6$, $\beta = 1$, and $\eta_p^* = 1$ in our evaluations of the spin velocity field. The combination of parameters is again chosen so that $\tau_{MW}^2 \omega_x^2 \ll 1$ is generally satisfied. From both Figs. 4.5(a) and 4.5(b), it can be found that the magnitude of the spin velocity field, ω^*, increases as the applied shear rate, γ^*, or Couette boundary driving velocity is increased, and that the magnitude of ω^* is decreased as γ^* is reduced regardless of which regime of electric field strength is of interest. This result is simply a manifestation of the fact that the greater the mechanical driving force the greater the response in ER fluid flow at the respective constant electric field strengths. Due to the different regimes of electric field strengths employed, the variations of the spin velocity profiles with respect to the spatial coordinate, z^*, as shown in Fig. 4.5(a) are much more significant as compared to flat profiles found in Fig. 4.5(b). Yet, the order of magnitudes of the spin velocity solutions in both Figs. 4.5(a) and 4.5(b) are now the same. We can further normalize the dimensionless spin velocity profiles, ω^*, with $\omega_0^* = -\gamma^*/2$ so that the normalized spin velocity profile is given as

$$\widetilde{\omega^*} = \frac{\omega^*}{\omega_0^*}, \tag{4.48}$$

and the normalized spin velocity profile at zero electric field strengths, *i.e.*, half the vorticity of the ER fluid flow when $E^* = 0$, becomes one and is independent of the applied shear rate or Couette boundary driving velocity, *i.e.*,

$$\widetilde{\omega_0^*} = \frac{\omega_0^*}{\omega_0^*} = 1. \tag{4.49}$$

These solutions are shown in Figs. 4.5(c) and 4.5(d) for the respective electric field strengths of

$E^* = 2$ and $E^* = 0.6$ with the rest of the parameters used in the evaluation of the solutions being the same as those given in Figs. 4.5(a) and 4.5(b). As can be learned from Fig. 4.5(c) for electric field strengths greater than the critical electric field, the normalized spin velocity profile, $\widetilde{\omega}^*$, gradually meets the zero electric field solution, $\widetilde{\omega}_0^* = 1$ noted by the gray line in the figure, as the applied Couette boundary driving velocity or shear rate is increased. This result implies that as the applied shear rate becomes large, the mechanical viscous driving force dominates over the electrical torque input such that the normalized spin velocity solution becomes closer to the value found at zero electric field strengths, *i.e.*, the solution found only when viscous force is present. The consistency between the solutions presented in Fig. 4.5(c) and the physical picture described above also implies that the spin velocity field solutions we have obtained are generally correct. Note however that for the $E^* = 0.6 < 1$ solutions given in Fig. 4.5(d), the spin velocity field is independent of the applied shear rate (with the numerical values of the differences among the spin velocity profiles evaluated at the respective shear rates being within $O\left(10^{-16}\right)$) and does not converge to $\widetilde{\omega}_0^* = 1$ as noted by the gray line in the figure as the applied shear rate grows large. This result found in Fig. 4.5(d) is basically due to the different form of the polarizability (α_y and α_z with the micro-particle rotation speed being set to zero) used in Eqs. (4.34)-(4.37) and (4.40)-(4.43) for $E^* = 0.6 < 1$ as compared to the result obtained from Fig. 4.5(c) and does not necessarily suggest that the solutions given in Fig. 4.5(d) is incorrect. By comparing Figs. 4.5(c) and 4.5(d), it can be learned that there is a difference in the flow field responses when we employ different forms of polarizabilities (α_y and α_z) in regard of the different regimes of the applied electric field strengths. In other words, the model of the polarizabilities (α_y and α_z) and subsequently the equilibrium retarding polarization, Eqs. (3.32) and (3.33), employed in the polarization relaxation equation, Eq. (3.35), may generally have influence on the final negative electrorheological response of the nER2 fluid flows.

Before examining how the total spin velocity profile varies with respect to changes in the boundary condition selection parameter, β, we define two difference variables based on the spin velocity as

$$\begin{aligned}&\Delta\omega^*\left(z^*, E^*=2, \eta_p^*=1, \beta, U_0=0.01\right)\\&\quad\equiv \omega^*\left(z^*, E^*=2, \eta_p^*=1, \beta, U_0=0.01\right)-\omega^*\left(z^*, E^*=2, \eta_p^*=1, \beta=1, U_0=0.01\right)\end{aligned}, \tag{4.50}$$

for $E^*=2\geq 1$ and

$$\begin{aligned}&\Delta\omega^*\left(z^*, E^*=0.6, \eta_p^*=1, \beta, U_0=0.01\right)\\&\quad\equiv \omega^*\left(z^*, E^*=0.6, \eta_p^*=1, \beta, U_0=0.01\right)-\omega^*\left(z^*, E^*=0.6, \eta_p^*=1, \beta=1, U_0=0.01\right)\end{aligned}, \tag{4.51}$$

for $E^*=0.6<1$. Note that since the spin velocity, ω^*, evaluated are rotating in the same direction as that of the macroscopically imposed flow vorticity, the spin velocities, ω^*, shown in Eqs. (4.50) and (4.51) are negative values (*i.e.*, ω^* rotating in the negative x-direction).

Figures 4.6(a) and 4.6(b) illustrate the spatial variations of the differences in the spin velocity as respectively defined in Eqs. (4.50) and (4.51) for distinct values of the boundary condition selection parameter, *i.e.*, $\beta=0$, 0.25, 0.5, and 0.75. Since the spin velocities, ω^*, are of negative values in Eq. (4.50), we find in Fig. 4.6(a) that as β is reduced from 0.75, 0.5, 0.25, to 0, the total spin velocity, ω^*, becomes slightly more negative as compared to the total spin velocity evaluated at $\beta=1$, *i.e.*, $\omega^*(\beta=1)$, for the electric field strength of $E^*=2\geq 1$. Similarly, for the negatively valued total spin velocity in Eq. (4.51), we find in Fig. 4.6(b) that as β is decreased from 0.75, 0.5, 0.25, to 0, the total spin velocity, ω^*, becomes considerably less negative as compared to the total spin velocity evaluated at $\beta=1$, *i.e.*, $\omega^*(\beta=1)$, for the electric field strength of $E^*=0.6<1$. From these two figures shown in Fig. 4.6, it can be found that varying the boundary condition selection parameter, β, results in different responses in the total spin velocity field, ω^*, for the different polarizabilities (α_y and α_z as in Eq. (4.7)) utilized within the different regimes of electric field strengths of interest. Consequently, the negative electro-rheological responses of nER2 are also dependent on the boundary condition selection parameter, β, and the different polarizabilities utilized for the different regimes of electric field strengths applied since both the linear velocity field, u^*, and the effective viscosity, η^*, both depend on the total spin velocity field, ω^*.

Figure 4.7 shows the spatial variations of the total spin velocities evaluated at distinct values of the spin viscosity, η' or η_p^*, for the Couette flow geometry with $E^*=2\geq 1$ in Fig. 4.7(a) and

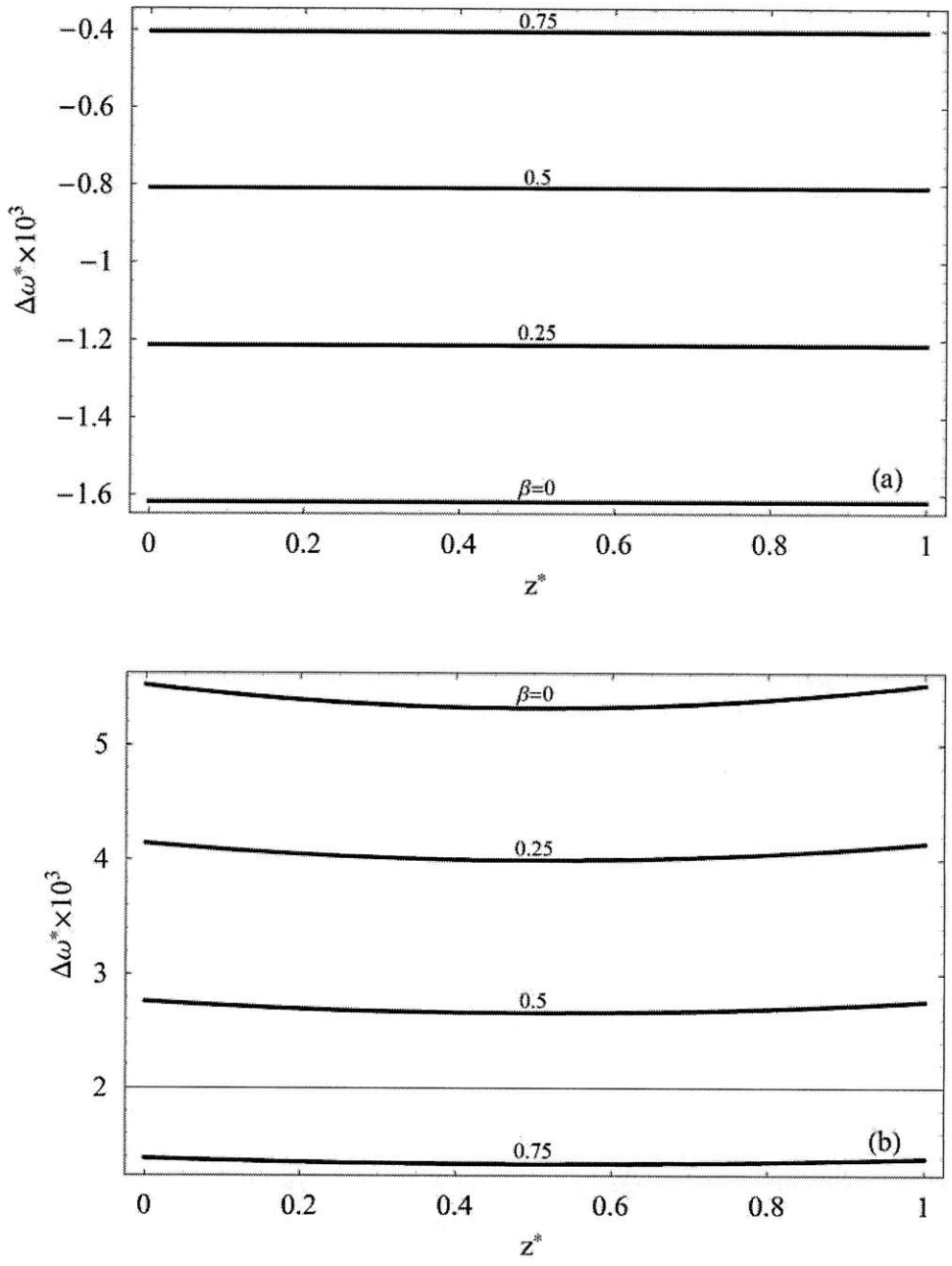

Figure 4.6. Spatial variations of the differences in the total spin velocity profile, $\Delta\omega^*$, as defined in Eqs. (4.50) and (4.51) evaluated at $\eta_p^* = 1$, $U_0 = 0.01$ (m/s), and $\beta = 0$, 0.25, 0.5, and 0.75 for (a) $E^* = 2 \geq 1$ and (b) $E^* = 0.6 < 1$.

with $E^* = 0.6 < 1$ in Fig. 4.7(b). In both plots, we have employed $\beta = 1$ and $U_0 = 0.01$ (m/s) (corresponding to a shear rate of $\gamma^* \approx 0.01$), and the value of spin viscosity is varied from

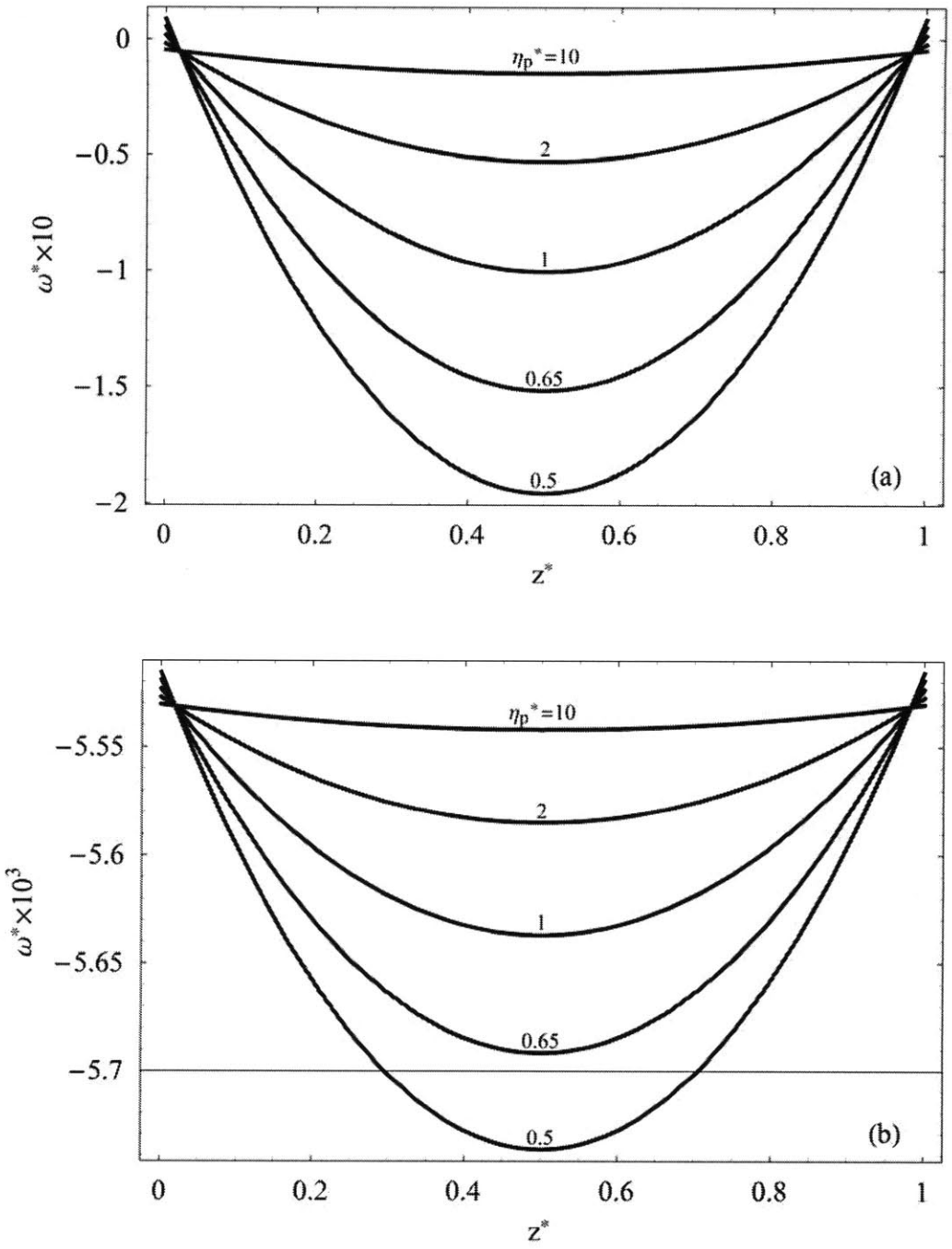

Figure 4.7. Spatial variations of the total spin velocity profile, ω^*, plotted with $\beta = 1$ and $U_0 = 0.01$ (m/s) at spin viscosity values of $\eta_p^* = 0.5, 0.65, 1, 2,$ and 10 for (a) $E^* = 2 \geq 1$ and (b) $E^* = 0.6 < 1$.

$\eta' = 1.53\times10^{-7}$, 3.06×10^{-8}, 1.53×10^{-8}, 9.945×10^{-9}, and finally to 7.65×10^{-9} $(N\cdot s)$, which corresponds to $\eta_p^* = 10, 2, 1, 0.65,$ and 0.5 as shown in the figures.

Despite the different orders of magnitudes of the total spin velocities, ω^*, shown in the two figures of Fig. 4.7, it can be learned that the magnitude of the total spin velocity of the ER fluid parcel is enhanced as the spin viscosity, η_p^*, is reduced for both Figs. 4.7(a) and 4.7(b). This result is consistent with the mathematical nature of the diffusive term, $\partial^2/\partial z^2$ or d^2/dz^2, presented in the governing equation, Eq. (4.27), of the spin velocity field, that is, the diffusive term in the equation tends to smooth out the concentrated values, or singularities, in our calculation domain. Therefore, the larger the spin viscosity, the stronger the diffusive transport of the ER fluid angular momentum (from the electrical torque) is obtained. In other words, as η' or η_p^* increases, the total spin velocity profile, ω^*, becomes smoother or flatter with a smaller magnitude regardless of the electric field strengths of interest. On the contrary, when the spin viscosity is reduced, the diffusive transport of the angular momentum introduced by the external electric field through the electrical body torque of the ER fluid is also reduced, and the total spin velocity is then more concentrated or enlarged. Nevertheless, there is a limitation to the reduction of the spin viscosity in the present continuum model since as η' is reduced to a certain value, the spin velocity grows so large that it violates the $\tau_{MW}^2\omega^2 \ll 1$ criteria, as can be suggested by the dramatic increase in the magnitude of the total spin velocity in Fig. 4.7(a) while η_p^* is reduced from 10 to 0.5. Also notice that with the other variables, *i.e.*, E^*, β, and γ^* (or U_0), kept constant, the total spin velocity profiles, ω^*, shown in both Figs. 4.7(a) and 4.7(b) gradually meet the zero electric field solution of $\omega_0^* = -\gamma^*/2 = -5.53125\times10^{-3}$ when the spin viscosity, η_p^*, is gradually increased (note: zero electric field solution not shown here since ω^* falls pretty close to ω_0^* when $\eta_p^* = 10$ in both figures). Again, for this Couette flow geometry, Fig. 4.7 indicates that the linear flow velocity is increased in the upper half of the channel and the velocity is decreased in the lower half of the channel due to the fact that the spin velocities found in the two plots are the greatest in the middle of the flow channel.

In the following discussions on the linear velocity field, we define a micro-particle Quincke rotation induced velocity as

$$u_q^* \equiv u^* - u_0^* = u^* - z^*, \tag{4.52}$$

which is simply the total linear velocity, u^*, subtracted by the zero electric field linear velocity,

$u_0^* = z^*$, *i.e.*, the (dimensionless) ordinary Couette flow linear velocity when no external electric field is applied as given in Eq. (4.12). The reason for defining u_q^* in Eq. (4.52) is because the total linear velocity fields, u^*, obtained for the nER2 effect by our continuum analysis in the finite spin viscosity small spin velocity limit generally fall close to the zero electric field solution given by Eq. (4.12), or in dimensionless terms, $u_0^* = z^*$, and are thus difficult to be distinguished from the zero electric field solution. We therefore present the Quincke rotation induced linear velocity, u_q^*, instead of the total linear velocity, u^*, so as to magnify or better illustrate the variations in the velocity fields with respect to the different physical parameters involved in the nER2 problem.

The Quincke rotation (or electrorotation) induced velocity profiles, namely, u_q^* given by Eqs. (4.37) and (4.52), are plotted for the electric field regimes of $E^* \geq 1$ and $E^* < 1$ in Figs. 4.8(a) and 4.8(b), respectively. By keeping the parameters of $\beta = 1$, $\eta_p^* = 1$, and $U_0 = 0.01$ (m/s) (corresponding to a shear rate of $\gamma^* \approx 0.01$) constant, we plot the spatial variations of u_q^* at $E^* = 1.01$, 1.5, 2, 2.5, and 3 in Fig. 4.8(a) and plot the spatial variations of u_q^* at $E^* = 0$, 0.2, 0.4, 0.6, 0.8, and 1 in Fig. 4.8(b) (note: when $E^* = 1$ the micro-particle rotation speed is zero, $\Omega = 0$, as calculated from Eq. (2.57), thus the polarizabilities of α_y and α_z also have the same $\Omega = 0$ condition as what we would employ for the cases of $E^* < 1$). For both plots in Fig. 4.8, the induced velocity, u_q^*, is positive in the upper half of the channel while the lower half of the channel has a negative induced velocity. Hence, when we add u_q^* and $u_0^* = z^*$ together to obtain the total linear velocity field, u^*, the total flow velocity in the upper channel is accelerated while the total velocity in the lower channel is reduced. This result is generally consistent with the physical picture we have discussed for the spin velocity profiles in Fig. 4.4. Moreover, it can also be seen in both Figs. 4.8(a) and 4.8(b) that the strength or magnitude of the induced velocity is enhanced as the applied electric field, E^*, is increased whereas the magnitude of the induced velocity is decreased as the applied electric field strength is reduced. Yet, the order of magnitude of the induced velocities shown in Fig. 4.8(a) for $E^* \geq 1$ is much greater than those found in Fig. 4.8(b) for the electric field strengths of $E^* < 1$. As we gradually reduce the applied electric field

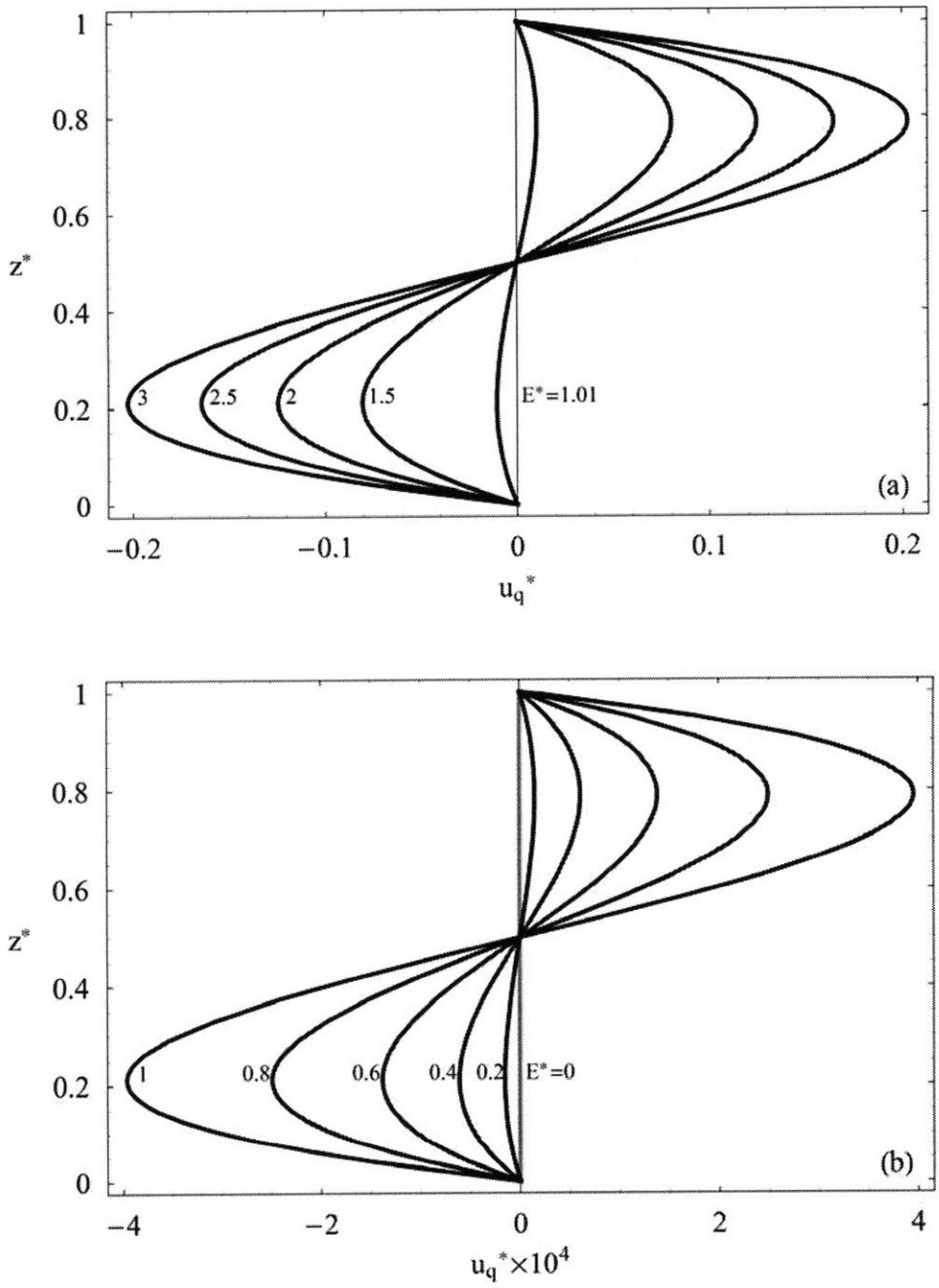

Figure 4.8. Spatial variations of the Quincke rotation induced linear velocity profiles, u_q^*, given by Eqs. (4.37) and (4.52) evaluated at $\beta = 1$, $\eta_p^* = 1$, and $U_0 = 0.01$ (m/s) (or $\gamma^* \approx 0.01$) for (a) $E^* \geq 1$ and (b) $E^* \leq 1$. The solid gray line shown in (b) represents the zero electric field solution of zero induced linear velocity.

strength from $E^* \geq 1$ in Fig. 4.8(a), to $E^* < 1$ in Fig. 4.8(b), and finally to $E^* = 0$ (noted by the gray line in Fig. 4.8(b)), we find that the Quincke rotation induced linear velocity, u_q^*, also

gradually decreases and eventually goes to zero, *i.e.*, $u_q^* = 0$, which gives exactly the zero electric field total linear velocity of $u^* = u_q^* + u_0^* = 0 + u_0^* = z^*$. The symmetries about the point of $\left(u_q^*, z^*\right) = \left(0, 0.5\right)$ in the induced velocity profiles of the two plots shown in Fig. 4.8 indicate that the Quincke rotation induced 2D flow rate for Couette flow is likely to be negligible or close to zero because the positive induced linear velocity in the upper half of the flow channel is generally canceled by the negative induced linear velocity in the lower half of the channel. Therefore, the effective viscosity, η^* or η_{eff}, rather than the Quincke rotation induced 2D volume flow rate is generally a better candidate for experimentally measuring the macroscopic negative electrorheological effects when an external DC electric field is applied to the Couette flow geometry.

We next consider the effects of the applied Couette boundary driving velocity, U_0, or equivalently the applied shear rate, γ^*, on the Quincke rotation induced linear velocity field, u_q^*. Since the linear velocities, u_y and u_q, are made dimensionless based upon the Couette boundary driving velocity, U_0, the dimensionless linear velocities, u^* and u_q^*, are also normalized such that no further normalization of the dimensionless variables is required as we have done for the spin velocities, ω^*. Shown in Fig. 4.9(a) are the spatial variations of the Quincke rotation induced linear velocity, u_q^*, evaluated at $U_0 = 0.01$, 0.05, and 0.1 (m/s) (or equivalently, $\gamma^* \approx 0.01$, 0.05, and 0.1) with $E^* = 2 \geq 1$, $\beta = 1$, and $\eta_p^* = 1$. As for Fig. 4.9(b), the spatial variations of u_q^* are evaluated at $U_0 = 0.01$, 0.05, and 0.1 (m/s) (or equivalently, $\gamma^* \approx 0.01$, 0.05, and 0.1) with $E^* = 0.6 < 1$, $\beta = 1$, and $\eta_p^* = 1$. As can be seen in Fig. 4.9(a), the induced linear velocity, u_q^* (dimensionless and normalized), is reduced as the applied shear rate, γ^*, or Couette boundary driving velocity, U_0, is increased. In other words, as the applied shear rate becomes large, the induced linear velocity, u_q^*, gradually becomes zero, which is simply the zero electric field solution of zero induced linear velocity. This result is consistent with that of the normalized spin velocity profiles, $\widetilde{\omega^*}$, as shown in Fig. 4.5(c) and again verifies the physical picture of with the applied electric field kept constant, mechanical viscous forces gradually dominates the ER

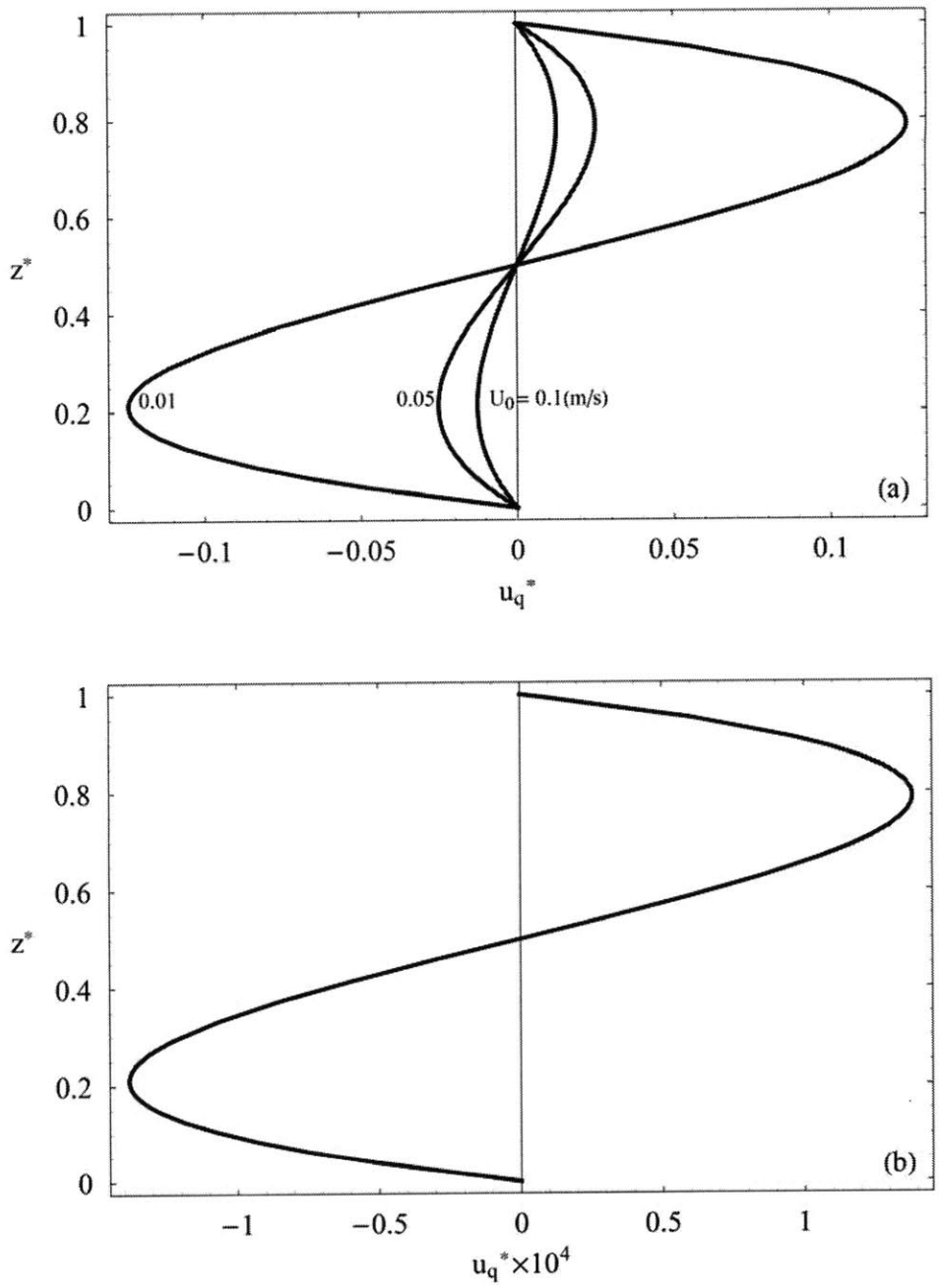

Figure 4.9. Spatial variations of the induced linear velocity profile, u_q^*, evaluated at $\beta = 1$, $\eta_p^* = 1$, and $U_0 = 0.01$, 0.05, and 0.1 (m/s) (or $\gamma^* \approx 0.01$, 0.05, and 0.1) for (a) $E^* = 2 \geq 1$ and (b) $E^* = 0.6 < 1$. Note that the three linear velocity profiles respectively evaluated at $U_0 = 0.01$, 0.05, and 0.1 (m/s) have collapsed into one curve in (b) for the DC electric field strength of $E^* = 0.6 < 1$.

fluid flow responses as the applied Couette boundary driving velocity or the shear rate is increased. On the other hand, we find that the induced linear velocity profiles, u_q^*, evaluated

respectively at $U_0 = 0.01$, 0.05, and 0.1 (m/s) (or equivalently, $\gamma^* \approx 0.01$, 0.05, and 0.1) for $E^* = 0.6 < 1$, $\beta = 1$, and $\eta_p^* = 1$ have collapsed into one profile (the differences among the u_q^*'s respectively evaluated at different shear rates are very small) in Fig. 4.9(b). Note however that the order of magnitude of this collapsed induced linear velocity profile is much smaller as compared to that found in Fig. 4.9(a) for the electric field regime of $E^* = 2 \geq 1$. The result shown in Fig. 4.9(b) is also consistent with the normalized spin velocity profile, $\widetilde{\omega^*}$, as given in Fig. 4.5(d), and is generally due to a zero micro-particle rotation speed, $\Omega = 0$, that we have employed in the polarizabilities α_y and α_z as well as the subsequent equilibrium retarding polarization, Eq. (3.33), and the resulting spin and linear velocity solutions (Eqs. (4.36) and (4.37), respectively) for the electric field regime of $E^* = 0.6 < 1$.

The influences of different values of the boundary condition selection parameter, β, on the spatial variations of the Quincke rotation induced linear velocity profile, u_q^*, are shown in Figs. 4.10(a) and 4.10(b) for electric field regimes of $E^* = 2 \geq 1$ and $E^* = 0.6 < 1$, respectively. Despite the different electric field regimes considered, we have employed the constant values of $\eta_p^* = 1$ and $U_0 = 0.01$ (m/s) (or $\gamma^* \approx 0.01$) and varied the boundary condition selection parameter from $\beta = 0$, 0.25, 0.5, 0.75, and to 1 in both Figs. 4.10(a) and 4.10(b). It can be found from Fig. 4.10(a) that the induced linear velocity profiles respectively evaluated at distinct values of β have collapsed into one profile with the induced linear velocity being positive in the upper half of the flow channel and negative in the lower half of the channel for $E^* = 2 \geq 1$. The differences between or among the induced linear velocity profiles evaluated respectively at $\beta = 0$, 0.25, 0.5, 0.75, and 1 generally fall within the order of magnitude of $O\left(10^{-13}\right)$ in Fig. 4.10(a). Unlike the velocity profiles shown in Fig. 4.10(a), the induced velocity, u_q^*, varies considerably as the boundary condition selection parameter, β, is changed in Fig. 4.10(b) for $E^* = 0.6 < 1$. It can be learned from Fig. 4.10(b) that as β is increased from 0 to 1, the magnitude of the induced velocity u_q^* is reduced, which is a result different from what we have learned from the variations of the spin velocity profile shown in Fig. 4.6(b). In Fig. 4.6(b), we find that the differences of the spin velocity, $\Delta\omega^*$ as defined in Eq. (4.51), are positive values

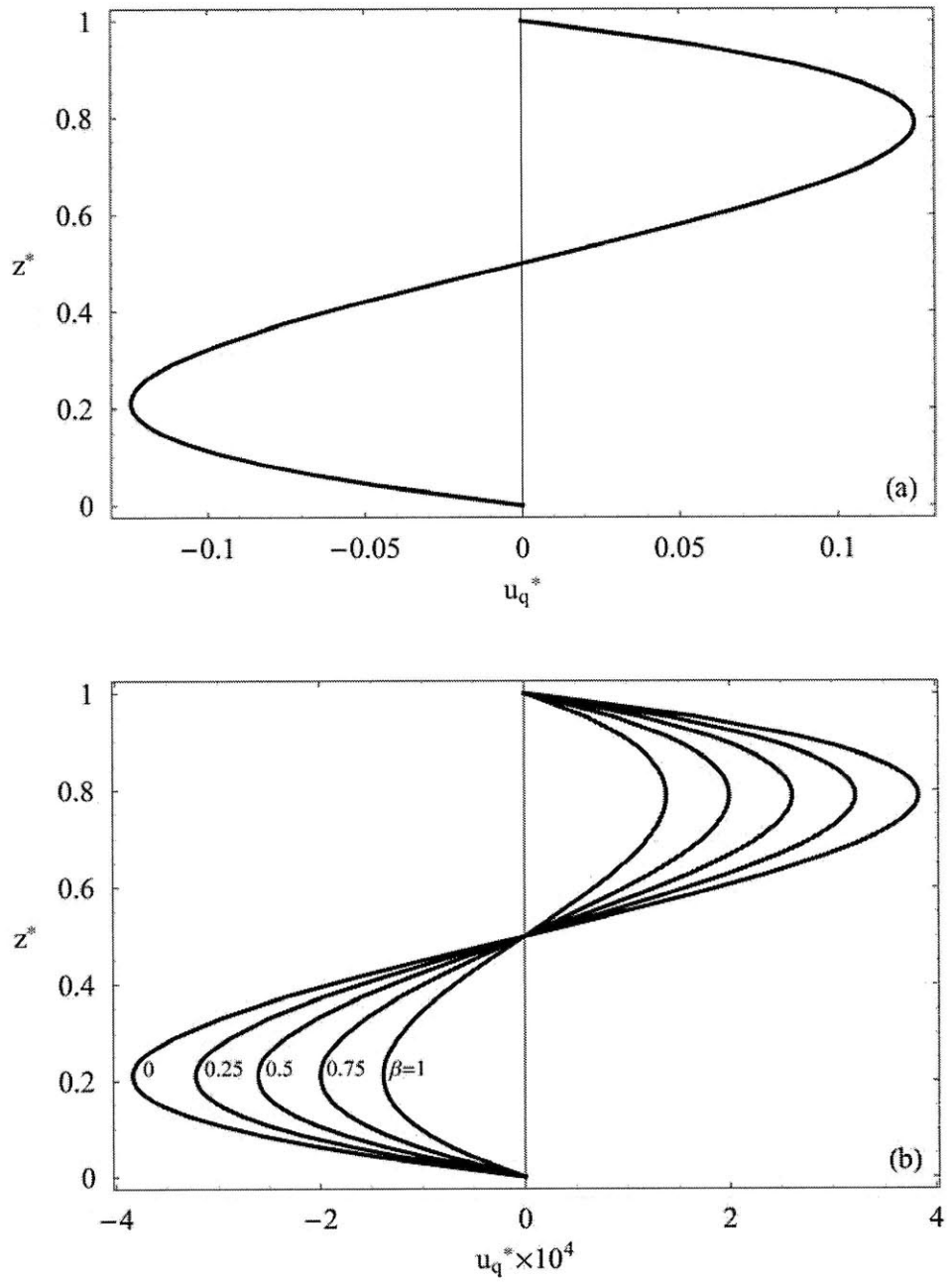

Figure 4.10. Spatial variations of the induced linear velocity profile, u_q^*, evaluated at $\eta_p^* = 1$, $U_0 = 0.01$ (m/s), and $\beta = 0$, 0.25, 0.5, 0.75, and 1 for (a) $E^* = 2 \geq 1$ and (b) $E^* = 0.6 < 1$. In (a), the five profiles evaluated for their respective values of β have collapsed into one profile.

and increase as β is reduced. This means that as compared to the total spin velocity evaluated at $\beta = 1$ (with other parameters kept constant), the total spin velocity becomes less negative (the magnitude of ω^* being decreased) as the boundary condition selection parameter, β, is

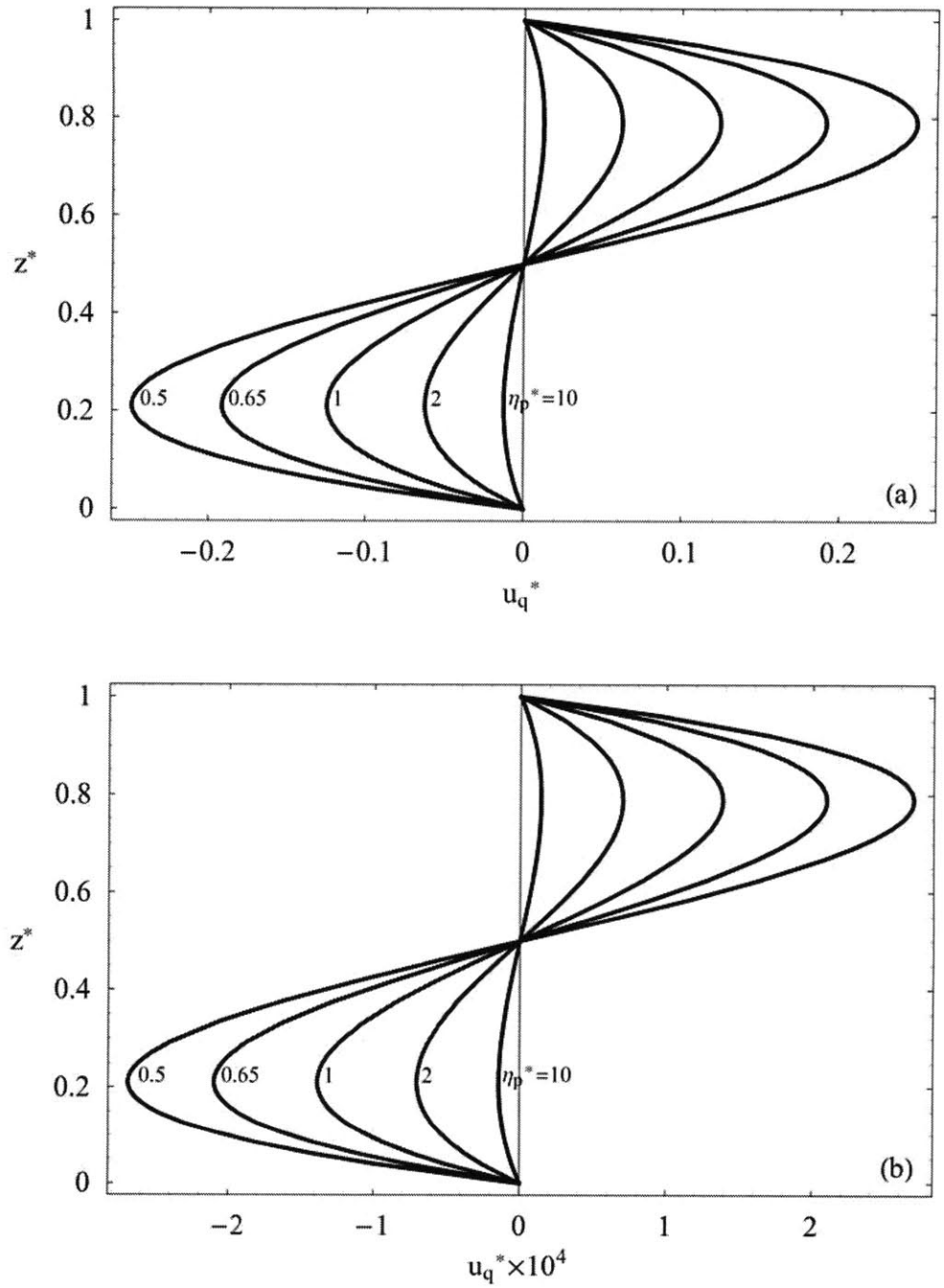

Figure 4.11. The spatial variations of the induced linear velocity, u_q^*, evaluated at $\beta = 1$, $U_0 = 0.01$ (m/s), and $\eta_p^* = 0.5, 0.65, 1, 2,$ and 10 for (a) $E^* = 2 \geq 1$ and (b) $E^* = 0.6 < 1$.

decreased (recall the total spin velocity ω^* is negatively valued, *i.e.*, rotating in the same negative x-direction as the imposed flow vorticity). However, as seen in Fig. 4.10(b), the magnitude of the induced linear velocity increases as β is decreased. This result implies that the

spin velocity and the induced linear velocity generally do not share the same trends of variation with respect to the boundary condition parameter, β, and that either ω^* or u_q^* (or u^*) cannot solely determine exactly the final macroscopic negative electrorheological responses of the Couette ER fluid flow. From the functional forms of Eqs. (4.44) and (4.45), we learn that both the total spin velocity field and the derivative of the total linear velocity field are required in order to evaluate the final effective viscosity solution that characterizes the macroscopic negative ER phenomenon.

Figures 4.11(a) and 4.11(b) present the spatial variations of the Quincke rotation induced linear velocity profile, u_q^*, with respect to distinct values of the spin viscosity, η' or η_p^*, for the respective applied electric field regimes of $E^* = 2 \geq 1$ and $E^* = 0.6 < 1$. For both figures in Fig. 4.11, we employ the constant values of $\beta = 1$ and $U_0 = 0.01$ (m/s), *i.e.*, $\gamma^* \approx 0.01$, and vary the spin viscosity from $\eta_p^* = 0.5$, 0.65, 1, 2, to 10. Although the order of magnitudes of the induced velocities found in both Figs. 4.11(a) and 4.11(b) are much different, the magnitudes of the induced velocity profiles in both figures are increased as the value of the spin viscosity is decreased. If contrarily, we increase the value of the spin viscosity, η_p^*, while keeping the other parameters constant, it can be found that the magnitudes of the induced linear velocity profiles, u_q^*, are reduced and eventually become zero, *i.e.*, zero induced linear velocity, which is exactly the zero electric field solution as discussed previously. This result from examining the induced linear velocity profile is consistent with that obtained from examining the total spin velocity profile as shown in Figs. 4.7(a) and 4.7(b). Again, because of the additional diffusion mechanism introduced into the ER fluid flow by the spin viscosity, η' or η_p^*, the induced linear velocity profiles, u_q^*, are smoother or flatter for large values of η_p^* whereas the shapes of u_q^* shown in Fig. 4.11 become more concentrated or singular for small values of η_p^*.

After examining the ER responses of the total spin velocity, ω^*, and the induced linear velocity, u_q^*, profiles in the 2D Couette geometry, we now turn our attention to the effective viscosity, η_{eff} or η^*, as given by Eq. (4.44) or (4.45), which characterizes the final macroscopic negative electrorheological responses of Couette flow with internal micro-particle electro-rotation.

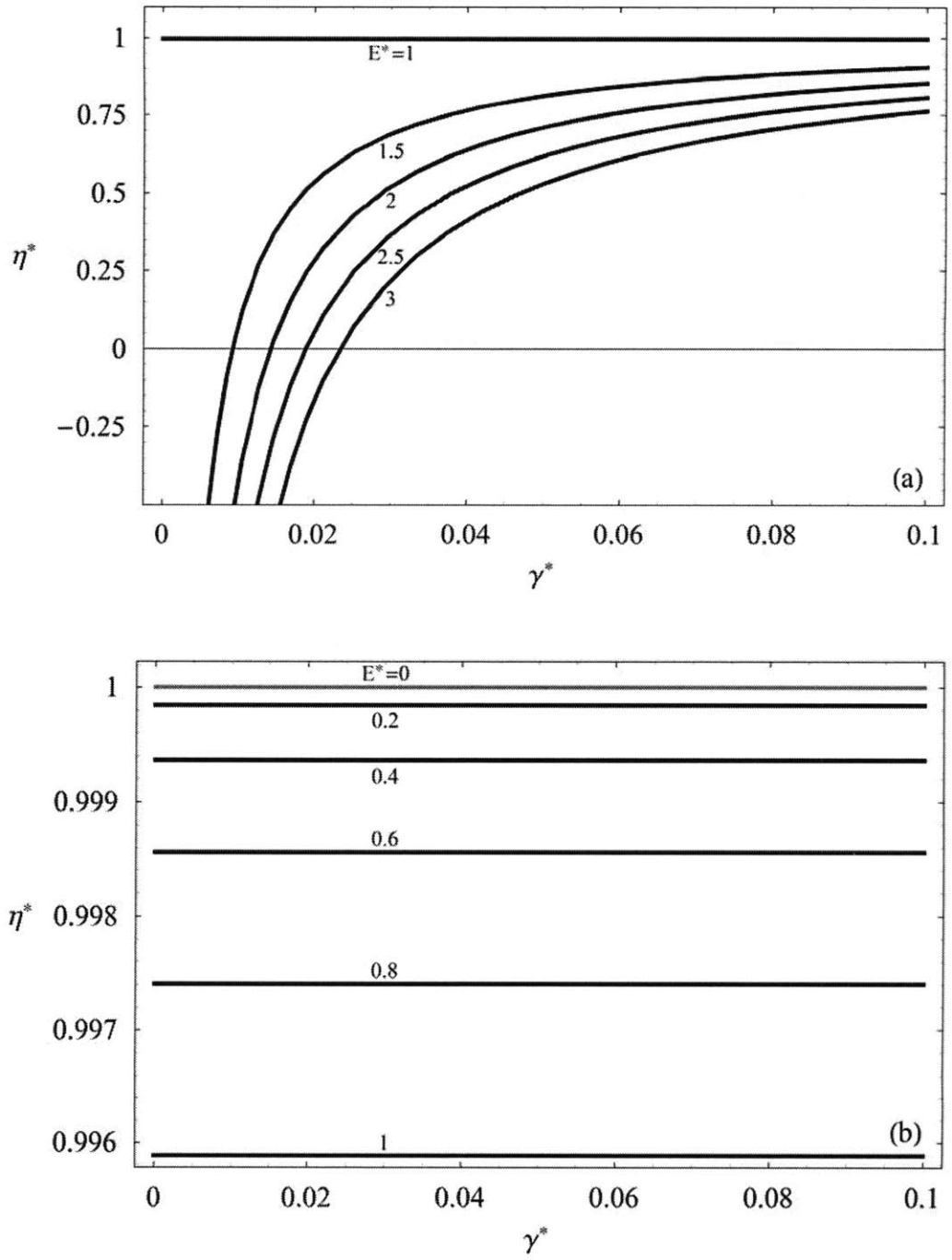

Figure 4.12. Variations of the effective viscosity, η^*, with respect to the applied shear rate, γ^*, evaluated at $\beta = 1$ and $\eta_p^* = 1$ for (a) $E^* \geq 1$ and (b) $E^* \leq 1$. Note that we have plotted $E^* = 1$ in both (a) and (b) because the micro-particle rotation speed equals to zero, $\Omega = 0$, when $E^* = 1$ as calculated via Eq. (2.57) for (a), which is equivalent to setting $\Omega = 0$ in (b).

In Figs. 4.12(a) and 4.12(b), the dimensionless effective viscosity, η^* given by Eq. (4.45), is

plotted with respect to the applied shear rate, γ^* (*i.e.*, the Couette boundary driving velocity, U_0), for the respective electric field strength regimes of $E^* = 1$, 1.5, 2, 2.5, and 3 ($E^* \geq 1$ in Fig. 4.12(a)) and of $E^* = 0$, 0.2, 0.4, 0.6, 0.8, and 1 ($E^* \leq 1$ in Fig. 4.12(b)) with the other variables of $\beta = 1$ and $\eta_p^* = 1$ kept constant. Note that the $E^* = 1$ solution is also plotted in Fig. 4.12(b) since the micro-particle rotation speed is zero, *i.e.*, $\Omega = 0$, when $E^* = 1$ as calculated by Eq. (2.57) and hence is the same as setting $\Omega = 0$ for the electric field regime of $E^* < 1$. From the effective viscosity solutions shown in Fig. 4.12(a), it can be learned that as the applied DC electric field strength is increased, the effective viscosity of the ER fluid flow is decreased. It can also be learned from the solutions for $E^* = 1.5$, 2, 2.5, and 3 as shown in Fig. 4.12(a) that as the magnitude of the applied shear rate becomes large, the reduction in the effective viscosity is reduced irrespective of the applied DC electric field strength, that is, the effective viscosity is dependent on the applied shear rate. Nevertheless, the shear rate dependence is not observed for the effective viscosity solution evaluated at $E^* = 1$ as well as for the $E^* < 1$ solutions shown in Fig. 4.12(b). In Fig. 4.12(b), the effective viscosity solutions are generally independent of the applied shear rate, γ^*, regardless of the applied DC electric field. As the DC electric field strength is increased in Fig. 4.12(b), we find that the effective viscosity decreases, *i.e.*, the negative ER effect. If however, we reduce the applied DC electric field strength, the reduction in the effective viscosity is also reduced and eventually approaches the zero electric field solution of $\eta^* = 1$ (as denoted by the gray line in Fig. 4.12(b)), which is simply the zero electric field viscosity, $\eta_{eff} = \eta \approx \eta_0 (1 + 2.5\phi)$, as mentioned in the previous sections. Referring back to the $E^* \geq 1$ results shown in Fig. 4.12(a), it can also be seen that as the applied shear rate, γ^*, increases, the effective viscosity solutions gradually approach the zero electric field solution of $\eta^* = 1$, which again verifies the physical picture of the mechanical viscous forces become dominant when the applied shear rate is increased with the applied DC electric field kept constant as already discussed for the total spin velocity field and the induced linear velocity field. We also find that zero or negative effective viscosities are attainable for the $E^* > 1$ solutions shown in Fig. 4.12(a). The finite spin viscosity small spin velocity results presented in Fig. 4.12(a) are very much similar to those obtained in the zero spin viscosity limit as shown in Fig. 4.3, but the effective viscosity results for $E^* = 1$ and $E^* < 1$ (see Fig. 4.12(b)) do not share the

non-linear dependency on the shear rate found in Figs. 4.3 and 4.12(a). This behavior is perhaps due to the different forms of equilibrium retarding polarization, Eq. (3.33), or polarizabilities of α_y and α_z, Eq. (4.7), resulting from the respective finite micro-particle rotation speeds, $\Omega \neq 0$, for $E^* > 1$ and zero micro-particle rotation speed, $\Omega = 0$, for $E^* \leq 1$ employed for the final solutions of Eqs. (4.36), (4.37), (4.44), and (4.45). Thus, in the finite spin viscosity small spin velocity limit, non-linearity is likely to be introduced to the linear solutions obtained by treating the spin velocity, ω^* or ω_x, and the micro-particle rotation speed, Ω, as different physical variables with a non-zero micro-particle rotation speed.

We next examine the influences of different boundary condition selection parameter, β, on the effective viscosity solutions in Fig. 4.13. In Fig. 4.13(a), we keep $E^* = 2 \geq 1$ and $\eta_p^* = 1$ constant and plot the effective viscosity, η^*, with respect to the applied shear rate, γ^*, at distinct values of the boundary condition selection parameter, *i.e.*, $\beta = 0$, 0.25, 0.5, 0.75, and 1. On the other hand, we keep $E^* = 0.6 < 1$ and $\eta_p^* = 1$ constant and plot the effective viscosity, η^*, with respect to the applied shear rate, γ^*, at $\beta = 0$, 0.25, 0.5, 0.75, and 1 in Fig. 4.13(b). As can be seen in Fig. 4.13(a), effective viscosities less than the zero electric field solution, $\eta^* = 1$, are generally achieved regardless of the boundary condition selection parameter employed. As the applied shear rate is increased, the reduction in the effective viscosity shown in Fig. 4.13(a) is also decreased, which is a result we have already learned from examining Fig. 4.12(a). However, the reduction in the effective viscosity decreases much faster and the effective viscosity approaches $\eta^* = 1$ much sooner for small values of β (as compared to η^* evaluated at large β) when the applied shear rate becomes large. Hence, the negative ER effect in the Couette geometry is likely to be more significant for β closer to 1 when the DC electric field strength, the applied shear rate, and the spin viscosity are kept constant. For the effective viscosity solutions shown in Fig. 4.13(b), we find that the effective viscosity solutions are again independent of the applied shear rate. However, the effective viscosity increases from a value slightly less than $\eta^* = 1$ to a value greater than $\eta^* = 1.1$, *i.e.*, a positive ER effect, when the boundary condition selection parameter β is decreased from 1 to 0 for the DC electric field strength regime of $E^* = 0.6 < 1$ in Fig. 4.13(b). This positive ER effect, increase in effective

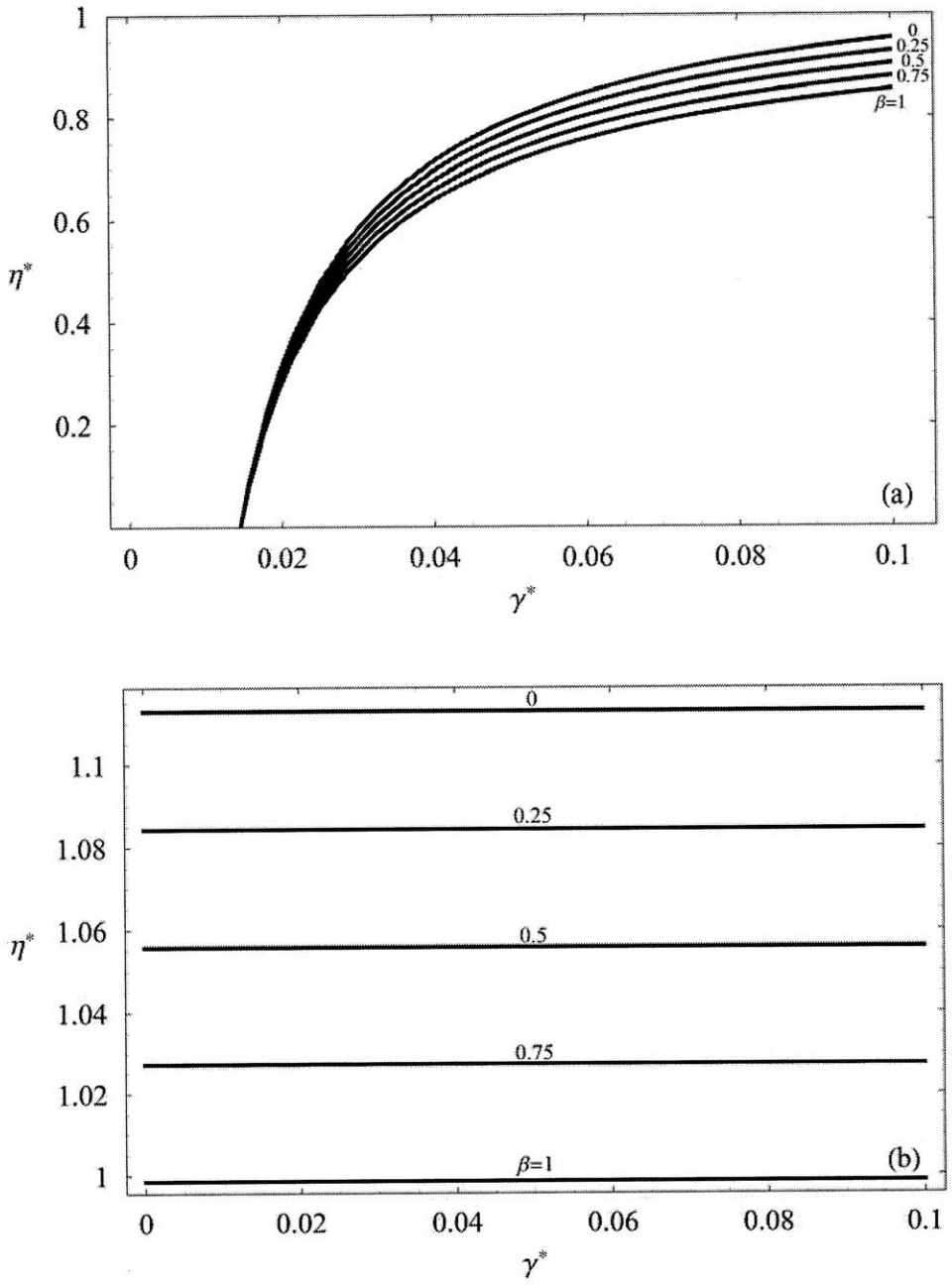

Figure 4.13. Variations of the effective viscosity, η^*, plotted with respect to the applied shear rate, γ^*, evaluated at $\eta_p^* = 1$ and $\beta = 0, 0.25, 0.5, 0.75$, and 1 for (a) $E^* = 2 \geq 1$ and (b) $E^* = 0.6 < 1$.

viscosity, is generally inconsistent with the experimental observations on Couette flow with internal micro-particle electrorotation as reported in Lobry & Lemaire (1999), Pannacci *et al.* (2007*a*), and Lemaire *et al.* (2008). Although it has been reported by Kaloni (1992) that

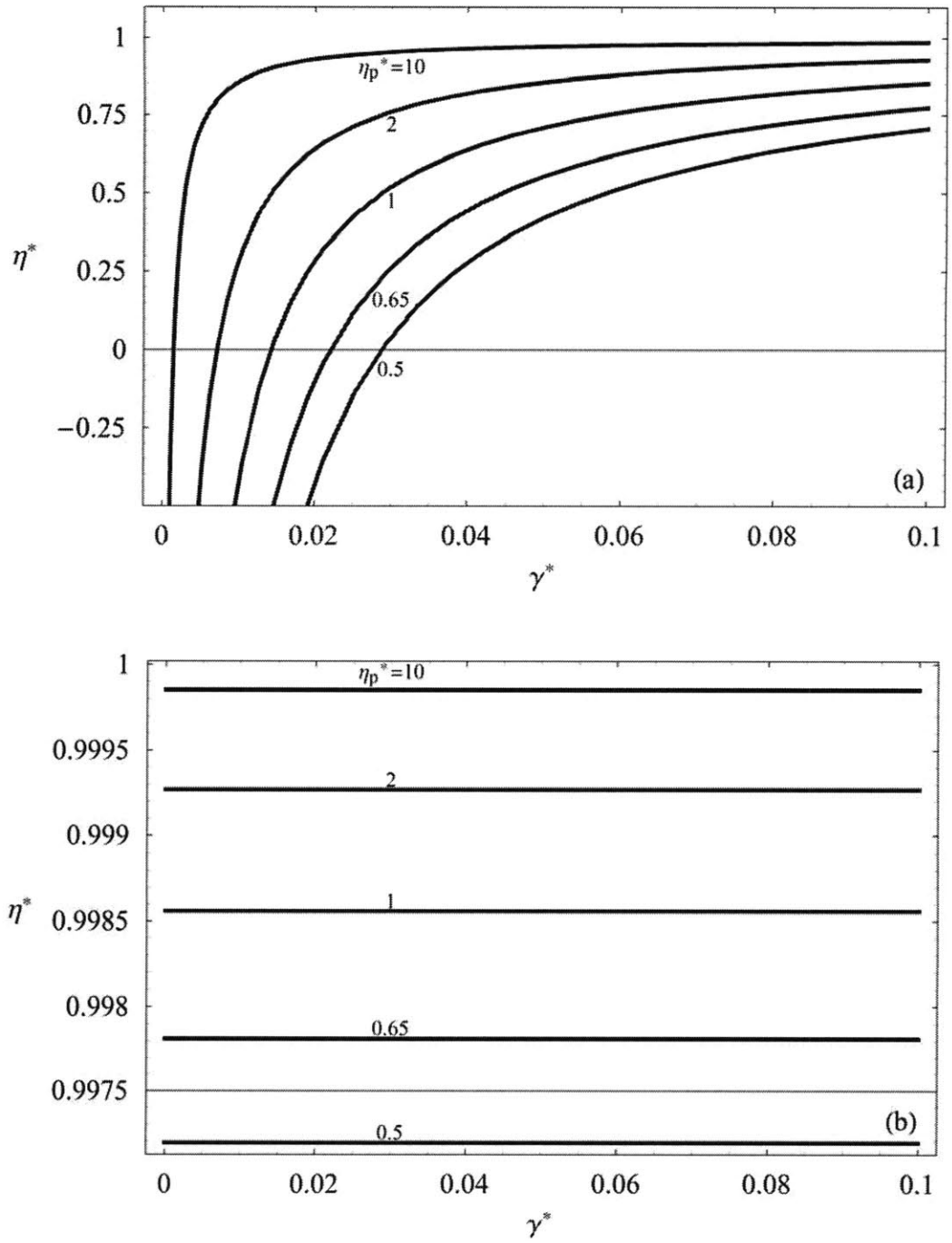

Figure 4.14. Variations of the effective viscosity, η^*, plotted with respect to the shear rate, γ^*, evaluated at $\beta = 1$ and $\eta_p^* = 0.5, 0.65, 1, 2$, and 10 for (a) $E^* = 2 \geq 1$ and (b) $E^* = 0.6 < 1$.

theoretical predictions and experimental observations may disagree for some flow conditions when $\beta = 0$ or $\overline{\omega} = 0$ at the boundaries, at this point, we cannot hastily draw the conclusion of

the inconsistency between our continuum mechanical model predictions and the experimental observations by Lobry & Lemaire (1999), Pannacci *et al.* (2007*a*), and Lemaire *et al.* (2008) is solely due to a zero boundary condition selection parameter or zero spin boundary conditions. We will return to this issue when we examine the induced 2D Poiseuille volume flow rate in Chapter 5.

Finally, we discuss how the effective viscosity solutions vary with respect to different values of the spin viscosity, η_p^*, for DC electric field strengths of $E^* = 2 \geq 1$ and $E^* = 0.6 < 1$ in Figs. 4.14(a) and 4.14(b), respectively. In both figures, the effective viscosities are plotted with respect to the applied shear rate and evaluated at $\eta_p^* = 0.5$, 0.65, 1, 2, and 10 while $\beta = 1$ and the respective DC electric field strengths are kept constant. Again, in Fig. 4.14(a), it can be seen that the effective viscosity results are similar to those obtained in Figs. 4.12(a) and 4.13(a) as well as those obtained in the zero spin viscosity limit, *i.e.*, Fig. 4.3. For the spin viscosity values of interest, a negative ER effect or an effective viscosity less than $\eta^* = 1$ is generally achieved. Moreover, zero or negative effective viscosity conditions are also attainable at low shear rates. However, as we increase the value of the spin viscosity, η_p^*, the reduction in the effective viscosity (strength or magnitude of the negative ER effect) is decreased and approaches the zero electric field solution of $\eta^* = 1$ at a much faster rate when the applied shear rate is increased. Thus, the negative ER effect, or reduction in the effective viscosity, η^*, (as compared to the zero electric field solution of $\eta^* = 1$) is generally more significant for small spin viscosities (η_p^*) as compared to large spin viscosities, η_p^*. Lastly, the effective viscosity solutions given in Fig. 4.14(b) also show negative ER behavior, *i.e.*, effective viscosities less than the zero electric field solution of $\eta^* = 1$, regardless of the spin viscosities, η_p^*, employed in the evaluation of the solutions. Also irrespective of the spin viscosities employed, we again find that the effective viscosity solutions do not depend on the applied shear rate, γ^*, for the DC electric field strength regime of $E^* = 0.6 < 1$. Nonetheless, despite the fact that η^* is independent of γ^*, the reduction in the effective viscosity is decreased as the spin viscosity is increased. The effective viscosity also approaches the zero electric field solution of $\eta^* = 1$ as the value of the spin viscosity

becomes large. These results are similar to those we have obtained in Fig. 4.14(a)—the negative ER effect is more significant for small spin viscosity conditions.

Before closing this chapter, a general remark can be made on the results found from the effective viscosity solutions presented in Figs. 4.12, 4.13, and 4.14. By examining the effective viscosity versus applied shear rate plots shown in Figs. 4.12(a), 4.13(a), and 4.14(a) for the DC electric field strength regime of $E^* > 1$, we find that the effective viscosity solutions obtained from our present continuum mechanical model in the finite spin viscosity small spin velocity limit are very much similar to those obtained from our continuum analysis in the zero spin viscosity limit as shown in Fig. 4.3. In the general parametric regime of $E^* > 1$, the effective viscosity solutions obtained in the two limits both decrease as the applied DC electric field strength is increased, depend on the magnitude of the applied shear rate, and approach the zero electric field solution of $\eta^* = 1$ as the applied shear rate becomes large. Note however that despite the dependency on the applied shear rate of the effective viscosities obtained for $E^* = 0.6$ and 0.8 in the zero spin viscosity limit, $\eta' = 0$, as shown in Fig. 4.3, we find that the effective viscosity solutions obtained for the DC electric field regime of $E^* < 1$ in the $\eta' \neq 0$, $\tau_{MW}^2 \omega_x^2 \ll 1$ limit as shown in Figs. 4.12(b), 4.13(b), and 4.14(b) generally do not depend on the magnitude of the applied shear rate, γ^*. The reason for the different behavior discussed above is likely due to the different polarizabilities of α_y and α_z (given in Eq. (4.7)) or the subsequent equilibrium retarding polarizations (given in Eq. (3.33)) employed for the respective regimes of DC electric field strengths, *i.e.*, $E^* > 1$ and $E^* \leq 1$.

For electric field strengths of $E^* \leq 1$, the micro-particle rotation speed is set to zero, $\Omega = 0$, in the equilibrium retarding polarization (or α_y and α_z). Thus, the equilibrium retarding polarization, $\overline{P_{eq}}$, does not depend on the micro-particle rotation speed or the applied electric field strength, and the retarding polarization relaxation process basically depend only upon the kinematic variable of the continuum spin velocity, $\overline{\omega}$, for both the zero spin viscosity and the finite spin viscosity small spin velocity limits. It is likely that the non-linear polarization relaxation features for field strengths of $E^* \leq 1$ cannot be fully captured by the linearized governing angular momentum equation, Eq. (4.27), for finite spin viscosities as compared to the fully non-linear cubic algebraic angular momentum equation, Eq. (4.14), for zero spin

viscosities. And thus, there is an apparent difference between the results shown in Figs. 4.12(b), 4.13(b), and 4.14(b) and those found in Fig. 4.3 for DC electric field strengths of $E^* \leq 1$.

As for the electric field strengths of $E^* > 1$, we employ a non-zero micro-particle rotation speed in the equilibrium retarding polarization (or α_y and α_z) with the magnitude and direction of the micro-particle rotation speed being respectively given by Eq. (2.57) and the imposed macroscopic vorticity direction. In this case, the equilibrium retarding polarization, $\overline{P_{eq}}$, does depend on the micro-particle rotation speed (or the applied electric field strength), and the retarding polarization relaxation process will depend on both the micro-particle rotation speed, $\overline{\Omega}$, and the continuum spin velocity, $\overline{\omega}$, for both the zero spin viscosity and the finite spin viscosity small spin velocity limits. Therefore, even if the angular momentum equation given by Eq. (4.27) is linearized for finite spin viscosity small spin velocities, some non-linear features of the polarization relaxation of the ER fluid flow may still likely be captured by the finite micro-particle rotation speed built-in the equilibrium retarding polarization, $\overline{P_{eq}}$. In other words, by treating the micro-particle rotation speed, $\overline{\Omega}$, and the continuum spin velocity, $\overline{\omega}$, as separate kinematic variables at the respective microscopic and macroscopic levels, some non-linear features as well as information of the polarization relaxation of the ER fluid flow are likely to be preserved through the finite microscopic particle rotation speed for $E^* > 1$ in the finite spin viscosity small spin velocity limit. And thus, for the field strengths of $E^* > 1$, we find similar resemblance in the effective viscosity solutions presented in Figs. 4.12(a), 4.13(a), and 4.14(a) and those presented in Fig. 4.3 for the two respective limits.

Chapter 5

Poiseuille Flow with Internal Micro-particle Electrorotation

In this chapter, we apply the governing classical continuum mechanical field equations, namely, the continuity equation, Eq. (2.1), the linear momentum equation, Eq. (2.2), the angular momentum equation, Eq. (2.3), the EQS Maxwell's equations, Eqs. (2.5)-(2.7), and the retarding polarization relaxation equation with its accompanying equilibrium retarding polarization, Eqs. (2.57), (3.32), (3.33), and (3.35), to study and analyze the negative electrorheological responses of ER fluid flows with internal micro-particle electrorotation, *i.e.*, the nER2 effect, in two-dimensional (2D) Poiseuille flow geometries. The flow of presentation given in this chapter follows that of Chapter 4.

With the general assumptions summarized in Section 2.3, we first present the simplified set of governing equations in the zero spin viscosity limit, $\eta' = 0$, for Poiseuille flows in Section 5.1. Solving this simplified set of equations, Section 5.2 presents the analytic expressions of the continuum spin velocity, ω_x (or ω^*), continuum linear velocity, u_y (or u^*), and 2D volume flow rate, Q, as functions of the Poiseuille driving pressure gradient, $\Gamma = -dp/dy$ (or Γ^*), and the externally applied DC electric field, E_0 (or E^*). Parametric studies are then performed on these solutions, and the results are discussed for understanding the Poiseuille nER2 responses in the zero spin viscosity limit.

Section 5.3 then further presents the simplified set of governing equations for Poiseuille flows with internal micro-particle electrorotation in the finite spin viscosity small spin (velocity)

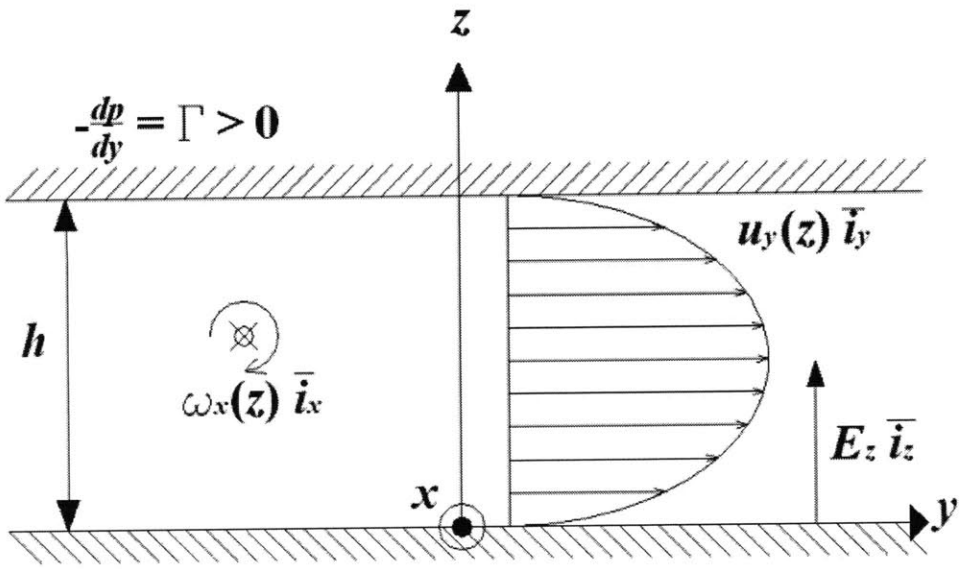

Figure 5.1. The schematic diagram illustrating the geometry, dimensions, and physical parameters for Poiseuille flow with internal micro-particle electrorotation.

limit, *i.e.*, $\eta' \neq 0$ and $\tau_{MW}^2 \omega_x^2 \ll 1$. By employing suitable boundary conditions, the coupled set of differential equations are then solved to obtain analytical solutions to the spin velocity field, ω_x (or ω^*), linear velocity field, u_y (or u^*), and 2D volume flow rate, Q, as functions of the Poiseuille driving pressure gradient, Γ (or Γ^*), the externally applied DC electric field, E_0 (or E^*), the boundary condition selection parameter, β, and the spin viscosity, η'. Results of the parametric studies performed on these "finite spin viscosity small spin" solutions are again finally discussed. These solutions, results, and discussions are presented in Section 5.4.

5.1 The Simplified Governing Equations in the Zero Spin Viscosity Limit for Poiseuille Flow Geometries

Figure 5.1 shows the schematic diagram of a 2D parallel plate Poiseuille flow geometry. Instead of an upper plate moving at a constant velocity U_0, the upper and lower plates are now both fixed at zero velocity, and a pressure gradient, $\Gamma \equiv -\partial p/\partial y$, is applied in the positive y-direction, *i.e.*, $\Gamma > 0$, through the channel to drive the fluid flow. Based on the similar geometries given for both Couette and Poiseuille cases, we again assume that the flow is steady, incompressible, two-dimensional, and fully developed so that the z-velocity component, *i.e.*, u_z

in $\bar{v} = u_y \bar{i}_y + u_z \bar{i}_z$, is identically zero and that the applied pressure gradient, Γ, is at most a constant for a fully developed flow. The applied DC electric field is further approximated to be only in the z-direction, namely, $\bar{E} = E_z \bar{i}_z$, with $E_z \approx E_0$ and E_0 being a constant across the channel height, h, as we have already discussed in Section 4.1.

For zero spin viscosity conditions, Eqs. (2.2), (2.3), and (3.35) then reduce to

$$-\tau_{MW}\omega_x P_z - \left(P_y - P_{eq}^y\right) = 0, \tag{4.1}$$

$$\tau_{MW}\omega_x P_y - \left(P_z - P_{eq}^z\right) = 0, \tag{4.2}$$

$$P_y E_z + 2\zeta\left(-\frac{du_y}{dz} - 2\omega_x\right) = 0, \tag{4.4}$$

and

$$\Gamma + 2\zeta\frac{d\omega_x}{dz} + \eta_e\frac{d^2u_y}{dz^2} = 0, \tag{5.1}$$

where u_y is the y-velocity component, ω_x is the x-spin velocity component (note: $\bar{\omega} = \omega_x \bar{i}_x$ in 2D), E_z is the z-component of the applied DC electric field, and P_y and P_z are respectively the retarding polarization components in the y- and z- directions, *i.e.*, $\bar{P} = P_y \bar{i}_y + P_z \bar{i}_z$. Note that we have substituted the total polarization, P_{ty}, with the retarding polarization, P_y, in Eq. (4.4). This is because the DC electric field is applied in the z-direction only with $E_y = 0$ as already mentioned in Section 4.1. The z-linear momentum equation reduces to an equation which relates only the pressure gradient to the Kelvin body force density, and thus can be treated separately from the other equations.

After substituting Eq. (3.33) into Eqs. (4.1) and (4.2) and subsequently solving the resulting two equations, we again arrive at

$$P_y = n\frac{\alpha_y - \tau_{MW}\omega_x\alpha_z}{1+\tau_{MW}^2\omega_x^2}E_0, \tag{4.5}$$

$$P_z = n\frac{\alpha_z + \tau_{MW}\omega_x\alpha_y}{1+\tau_{MW}^2\omega_x^2}E_0, \tag{4.6}$$

where

$$\begin{bmatrix} \alpha_y \\ \alpha_z \end{bmatrix} = \begin{bmatrix} \alpha_{yz} \\ \alpha_{zz} \end{bmatrix} = 4\pi\varepsilon_1 R^3 \begin{bmatrix} -\dfrac{\tau_{MW}\Omega\left(\dfrac{\sigma_2-\sigma_1}{2\sigma_1+\sigma_2}-\dfrac{\varepsilon_2-\varepsilon_1}{2\varepsilon_1+\varepsilon_2}\right)}{1+\tau_{MW}^2\Omega^2} \\ \dfrac{\left(\dfrac{\sigma_2-\sigma_1}{2\sigma_1+\sigma_2}-\dfrac{\varepsilon_2-\varepsilon_1}{2\varepsilon_1+\varepsilon_2}\right)}{1+\tau_{MW}^2\Omega^2} \end{bmatrix}, \tag{4.7}$$

with α_{zz} and α_{yz} respectively defined in Eqs. (3.42) and (3.43), and the magnitude and direction of the micro-particle rotation speed, Ω, being respectively given by Eq. (2.57) and that of the macroscopic flow vorticity. Using Eqs. (4.5) and (4.7) in Eq. (4.4), we obtain the set of simplified governing equations for Poiseuille flow with internal micro-particle electrorotation in the zero spin viscosity limit, that is,

$$\Gamma + 2\zeta\frac{d\omega_x}{dz} + \eta_e\frac{d^2u_y}{dz^2} = 0, \tag{5.1}$$

and

$$\frac{\alpha^* - \tau_{MW}\omega_x}{1+\tau_{MW}^2\omega_x^2} n\alpha_z E_0^2 + 2\zeta\left(-\frac{du_y}{dz} - 2\omega_x\right) = 0, \tag{4.9}$$

where $\alpha^* = \alpha_y/\alpha_z = -\tau_{MW}\Omega$.

Since we are considering zero spin viscosities in the angular momentum equation, the spin velocity field, $\overline{\omega} = \omega_x \overline{i_x}$, again follows the "free-to-spin" condition at the boundaries while we apply the no-slip BC, $\overline{v} = 0$, at $z = 0$ and h on the velocity field, $\overline{v} = u_y(z)\,\overline{i_y}$. Yet, for a Poiseuille geometry, the spin velocity is no longer a constant throughout the flow field, *i.e.*, $\overline{\omega} = \omega_x(z)\,\overline{i_x}$, and thus a geometric condition for the spin velocity field, namely, $\overline{\omega} \to 0$, is needed as $z \to h/2$ so as to satisfy the asymmetry between the upper and lower halves of the flow channel as imposed by the symmetric parallel plate Poiseuille flow boundaries (He, 2006). Moreover, we apply an additional condition on the micro-particle rotation speed, namely, $\overline{\Omega} \to 0$ as $z \to h/2$, since the suspended micro-particles are required to rotate in the macroscopically imposed flow vorticity direction, which is now also constrained by the symmetric Poiseuille parallel plate boundaries.

5.2 Continuum Analysis in the Zero Spin Viscosity Limit

5.2.1 Solutions to the Spin Velocity, Linear Velocity, and 2D Volume Flow Rate

Following a similar procedure to that of the Couette geometry case, we integrate Eq. (5.1) to have

$$\Gamma z + 2\zeta\omega_x + \eta_e \frac{du_y}{dz} = C_p, \tag{5.2}$$

where C_p is a constant. Equation (5.2) is then substituted into Eq. (4.9) so that the angular momentum equation becomes

$$\frac{\alpha^* - \tau_{MW}\omega_x}{1+\tau_{MW}^2\omega_x^2} n\alpha_z E_0^2 + 2\zeta\left(\frac{\Gamma}{\eta_e}z + \frac{2\zeta}{\eta_e}\omega_x - \frac{C_p}{\eta_e} - 2\omega_x\right) = 0. \tag{5.3}$$

By applying the symmetry conditions, $\overline{\omega} \to 0$ (or $\omega_x \to 0$) and $\overline{\Omega} \to 0$ (or $\Omega \to 0$) as $z \to h/2$, to Eq. (5.3), the constant C_p is determined to be $\Gamma h/2$, and Eq. (5.3) is rewritten as

$$\frac{\alpha^* - \tau_{MW}\omega_x}{1+\tau_{MW}^2\omega_x^2}\frac{n\alpha_z E_0^2}{2\zeta} + \frac{\Gamma h}{\eta_e}\left(\frac{z}{h} - \frac{1}{2}\right) - \frac{2\eta}{\eta_e}\omega_x = 0, \tag{5.4}$$

which is an algebraic, cubic equation with the z-coordinate being a spatially varying coefficient and $\alpha^* = \alpha_y/\alpha_z = -\tau_{MW}\Omega$. Using the following non-dimensionalization scheme, namely,

$$\omega^* = \tau_{MW}\omega_x,\ z^* = \frac{z}{h},\ m^* = \frac{2\zeta\eta}{n\alpha_z E_0^2 \tau_{MW}\eta_e},\ \text{and}\ V^* = \frac{\Gamma h \tau_{MW}}{\eta}m^*, \tag{5.5}$$

Eq. (5.4) is non-dimensionalized and the dimensionless angular momentum equation for the Poiseuille case becomes

$$\omega^{*3} - \frac{V^*}{2m^*}\left(z^* - \frac{1}{2}\right)\omega^{*2} + \left(1 + \frac{1}{2m^*}\right)\omega^* - \frac{V^*}{2m^*}\left(z^* - \frac{1}{2}\right) - \frac{\alpha^*}{2m^*} = 0. \tag{5.6}$$

We solve Eq. (5.6) by standard symbolic calculation packages (Mathematica, Wolfram Research, Inc.) to express ω^* in terms of V^*, z^*, and m^*, or equivalently, to express ω_x in terms of z, Γ, and E_0. The three roots to Eq. (5.6) are:

$$\omega_{P1}^* = \frac{2V^*z^* - V^*}{12m^*} + \varphi_{P1}\left[6\sqrt[3]{4}m^*\left(\varphi_{P2} + \sqrt{\varphi_{P2}^2 + 4\varphi_{P1}^3}\right)^{1/3}\right]^{-1} - \frac{1}{12\sqrt[3]{2}m^*}\left(\varphi_{P2} + \sqrt{\varphi_{P2}^2 + 4\varphi_{P1}^3}\right)^{1/3}, \tag{5.7}$$

$$\omega_{P2}^{*}=\frac{2V^{*}z^{*}-V^{*}}{12m^{*}}-\varphi_{P1}\left(1+i\sqrt{3}\right)\left[12\sqrt[3]{4}m^{*}\left(\varphi_{P2}+\sqrt{\varphi_{P2}^{2}+4\varphi_{P1}^{3}}\right)^{1/3}\right]^{-1}+\frac{1}{24\sqrt[3]{2}m^{*}}\left[\left(1-i\sqrt{3}\right)\left(\varphi_{P2}+\sqrt{\varphi_{P2}^{2}+4\varphi_{P1}^{3}}\right)^{1/3}\right], \tag{5.8}$$

and

$$\omega_{P3}^{*}=\frac{2V^{*}z^{*}-V^{*}}{12m^{*}}-\varphi_{P1}\left(1-i\sqrt{3}\right)\left[12\sqrt[3]{4}m^{*}\left(\varphi_{P2}+\sqrt{\varphi_{P2}^{2}+4\varphi_{P1}^{3}}\right)^{1/3}\right]^{-1}+\frac{1}{24\sqrt[3]{2}m^{*}}\left[\left(1+i\sqrt{3}\right)\left(\varphi_{P2}+\sqrt{\varphi_{P2}^{2}+4\varphi_{P1}^{3}}\right)^{1/3}\right], \tag{5.9}$$

where

$$\varphi_{P1}=24m^{*}\left(1+2m^{*}\right)-\left(2V^{*}z^{*}-V^{*}\right)^{2}, \tag{5.10}$$

and

$$\varphi_{P2}=-72m^{*}V^{*}+288m^{*2}V^{*}+2V^{*3}+144m^{*}V^{*}z^{*}-576m^{*2}V^{*}z^{*}-12V^{*3}z^{*}+24V^{*3}z^{*2}-16V^{*3}z^{*3}-864m^{*2}\alpha^{*}. \tag{5.11}$$

The stability, real valued, and free-to-spin conditions are then applied to select or pick out the most physically meaningful solution or combination of solutions to the spin velocity, ω^{*}, from the three possible roots, *e.g.*, ω_{P1}^{*}, ω_{P2}^{*}, and ω_{P3}^{*} (or respectively, Eqs. (5.7), (5.8), and (5.9)), found in solving the angular momentum equation, Eq. (5.6). Recall from Chapter 4 that for $E_0 \geq E_c$, we require the suspended micro-particles to rotate in the direction of the macroscopic flow vorticity, which in this case, is the imposed Poiseuille flow vorticity direction. Based on this requirement and referring to the coordinate systems shown in Figs. 2.1 and 5.1, we apply the negative valued micro-particle rotation speed Ω, *i.e.*, clockwise or pointing into the plane, in Eq. (2.57) to Eqs. (4.5)-(4.7) for the lower half of the channel, *i.e.*, $0 \leq z^{*} < 1/2$, and the positive valued Ω, *i.e.*, counter clockwise or pointing out of the plane, in Eq. (2.57) to Eqs. (4.5)-(4.7) for the upper half of the channel, *i.e.*, $1/2 < z^{*} \leq 1$. On the other hand, for $E_0 < E_c$, we set $\Omega = 0$ in Eqs. (4.5)-(4.7) and require the real valued spin velocity ω^{*} to be negative in $0 \leq z^{*} < 1/2$ and to be positive in $1/2 < z^{*} \leq 1$. Summarizing the above convention so that the stable micro-particle rotation as well as the symmetry conditions can be satisfied by the micro-particle rotation speed, $\overline{\Omega}$, we have

$$\overline{\Omega} = \Omega \overline{i_x} = \left\{ \begin{array}{ll} \dfrac{1}{\tau_{MW}} \sqrt{\left(\dfrac{E_0}{E_c}\right)^2 - 1}\, \overline{i_x}, & \dfrac{1}{2} < z^* \le 1 \\ 0, & z^* = \dfrac{1}{2} \\ \dfrac{-1}{\tau_{MW}} \sqrt{\left(\dfrac{E_0}{E_c}\right)^2 - 1}\, \overline{i_x}, & 0 \le z^* < \dfrac{1}{2} \end{array} \right\}, \text{ for } E_0 \ge E_c, \tag{5.12}$$

and

$$\overline{\Omega} = \Omega \overline{i_x} = 0, \text{ for } 0 \le z^* \le 1 \text{ and } E_0 < E_c, \tag{5.13}$$

which are to be substituted into the polarizabilities α_y and α_z in Eq. (4.7) when solving for the angular momentum equation, Eq. (5.6), or evaluating the three roots to the spin velocity as given by Eqs. (5.7)-(5.9).

Figure 5.2 shows the real valued results of the spin velocity, ω^*, plotted with respect to the spatial coordinate, z^*, with $\Gamma = 2 \times 10^4$ (Pa/m) at $E^* = 1.0$, 1.01, and 1.05 for both Figs. 5.2(a) and 5.2(b) and at $E^* = 0.7$, 0.8, 0.9, 0.95, and 0.99 for Fig. 5.2(c) where $E^* = E_0 / E_c$ with $E_c = 1.3 \times 10^6$ (V/m); the dash-dash curves represent the first root, ω_{P1}^* in Eq. (5.7), the dash-dot-dash curves represent the second root, ω_{P2}^* in Eq. (5.8), and the solid gray curves represent the last root, ω_{P3}^* in Eq. (5.9). Although the spin velocity profiles extend across the whole channel domain, $0 \le z^* \le 1$, the solutions for $E^* > 1$ shown in Fig. 5.2(a) are only valid for $1/2 < z^* \le 1$ since we have employed in Eqs. (4.5)-(4.7) the positive valued Ω of Eq. (5.12) that corresponds to the positive vorticity in $1/2 < z^* \le 1$ to satisfy the stable micro-particle rotation requirement during the numerical evaluation of the figure. Similarly, the spin velocity profiles for $E^* > 1$ shown in Fig. 5.2(b) are only valid for $0 \le z^* < 1/2$ since the negative valued particle rotation speed Ω of Eq. (5.12) corresponding to the negative vorticity in $0 \le z^* < 1/2$ has been employed in Eqs. (4.5)-(4.7) when evaluating the solutions throughout the whole spatial domain. For spin velocity profiles shown in Fig. 5.2(c) as well as for the $E^* = 1$ solutions shown in both Figs. 5.2(a) and 5.2(b), we find that with $\Omega = 0$ in Eqs. (4.5)-(4.7) (note: Eq. (2.57) or (5.12) goes to zero when $E^* = 1$), the spin velocity profiles become s-shaped centered at $z^* = 0.5$, and become multi-valued with respect to the spatial coordinate, z^*, near the middle of the flow

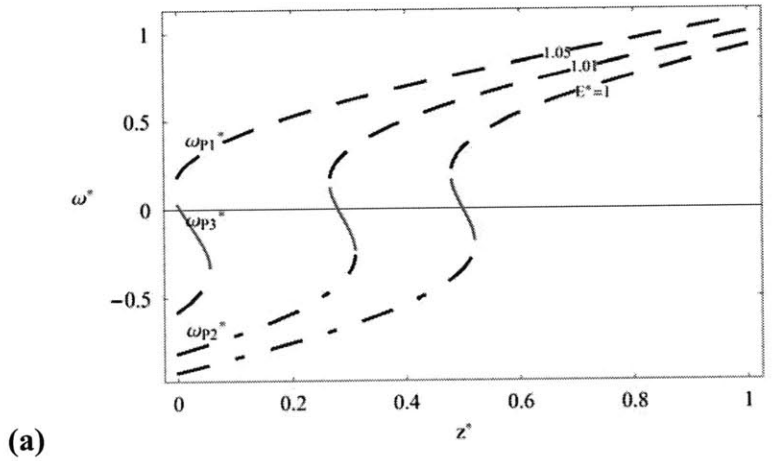

(a)

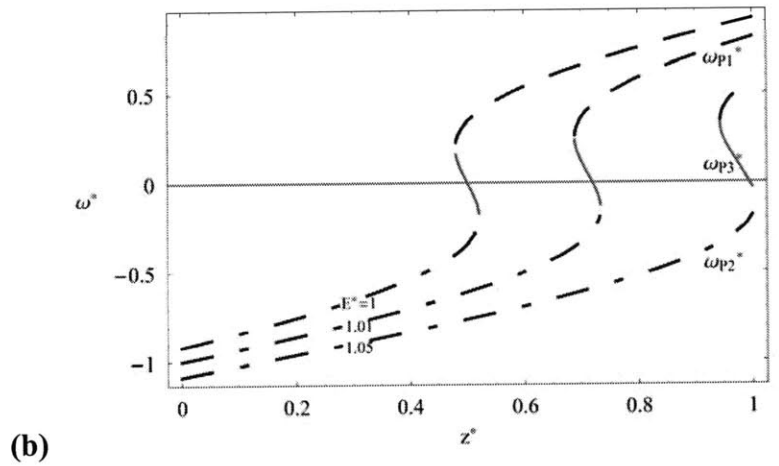

(b)

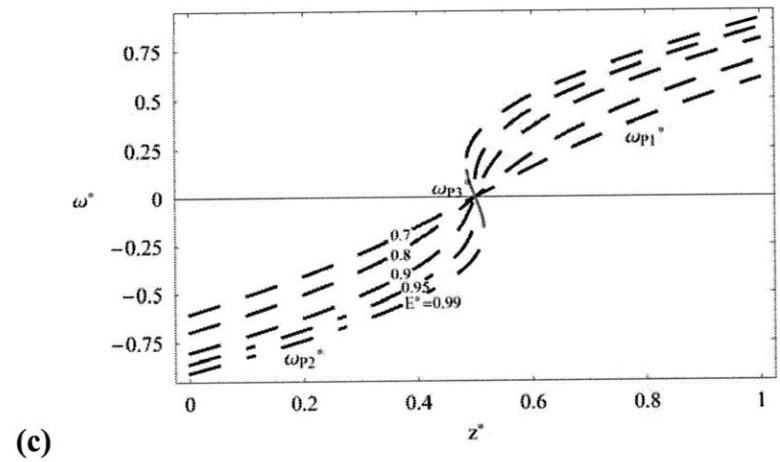

(c)

Figure 5.2. See facing page top for captions.

channel when $\Gamma = 2\times10^4$ (Pa/m) and $E^* = 0.95\sim1.0$. This is a similar non-linear behavior found in AC or traveling wave ferrofluid spin velocity profiles under zero spin viscosity, $\eta' = 0$,

Figure 5.2. The three roots, ω_{P1}^*, ω_{P2}^*, and ω_{P3}^* (given respectively in Eqs. (5.7), (5.8), and (5.9)), of the dimensionless Poiseuille spin velocity, ω^*, to the angular momentum equation, Eq. (5.6). The spin velocity profiles are plotted with respect to the spatial coordinate, z^*, at $\Gamma = 2\times10^4$ (Pa/m) and $E^* = E_0/E_c$ =1.0, 1.01, and 1.05 for both Figs. 5.2(a) and 5.2(b), and $E^* = 0.7$, 0.8, 0.9, 0.95, and 0.99 for Fig. 5.2(c) with $E_c = 1.3\times10^6$ (V/m). The dash-dash curves denote ω_{P1}^* (Eq. (5.7)), the dash-dot-dash curves denote ω_{P2}^* (Eq.(5.8)), and the solid gray curves denote ω_{P3}^* (Eq. (5.9)). In Fig. 5.2(a), we have substituted the positive valued particle rotation speed, Ω, of Eq. (2.57) or (5.12) into Eqs. (4.5)-(4.7) in evaluating the spin velocity profiles. Therefore, the profiles shown in Fig. 5.2(a) are only valid within the spatial region of $0.5 < z^* \le 1$. Similarly, a negative valued Ω from Eq. (2.57) or (5.12) has been used in Eqs. (4.5)-(4.7), and thus, the spin velocity profiles shown in Fig. 5.2(b) are only valid within $0 \le z^* < 0.5$. As for Fig. 5.2(c), the particle rotation speed is set to zero, $\Omega = 0$, in Eqs. (4.5)-(4.7). It can be seen that the spin velocity profiles evaluated at electric fields strengths of $E^* = 0.95$~1 become multi-valued in space near the middle of the flow channel (note that Ω goes to zero for $E^* = 1$ in Eq. (2.57) or (5.12)).

conditions as discussed in Zahn and Pioch (1998, 1999). However, since multi-valued spin velocity profiles will eventually lead to linear velocity profiles that are multi-valued in space, the situation is less likely to be physical for steady, viscous, and fully developed fluid flows (Zahn & Pioch, 1998, 1999). Therefore, resolution is made by requiring $\omega^* \to \omega_{P3}^* = 0$ at $z^* = 1/2$ and discarding the ω_{P1}^* and ω_{P3}^* solutions in $0 \le z^* < 1/2$ and the ω_{P2}^* and ω_{P3}^* solutions in $1/2 < z^* \le 1$, that is, use the negative valued ω^*, *i.e.*, ω_{P2}^*, in $0 \le z^* < 1/2$ and the positive ω^*, *i.e.*, ω_{P1}^*, in $1/2 < z^* \le 1$, so that the final solution is real valued, stable, symmetric, free-to-spin, and more likely physical for $\Gamma = 2\times10^4$ (Pa/m) and $E^* = 0.95$~1.0 conditions. Finally, for the spin velocity profiles evaluated at $\Gamma = 2\times10^4$ (Pa/m) and $E^* \le 0.9$ as shown in Fig. 5.2(c), only one root, ω_{P1}^*, is found to be valid, that is, real valued and rotation direction in the vorticity direction, throughout the spatial domain, $0 \le z^* \le 1$.

By carefully examining Fig. 5.2 and applying all the above reasoning and conditions, the explicit expressions of the final solution to the spin velocity of Poiseuille flow with internal micro-particle electrorotation is obtained for $E_0 \ge E_c$ as: (i) in $0.5 < z^* \le 1$ (substitute positive valued Ω of Eq. (5.12) in Eqs. (4.5)-(4.7)),

$$\omega_{P1}^{*}=\frac{2V^{*}z^{*}-V^{*}}{12m^{*}}+\varphi_{P1}\left[6\sqrt[3]{4}m^{*}\left(\varphi_{P2}+\sqrt{\varphi_{P2}^{2}+4\varphi_{P1}^{3}}\right)^{1/3}\right]^{-1}-\frac{1}{12\sqrt[3]{2}m^{*}}\left(\varphi_{P2}+\sqrt{\varphi_{P2}^{2}+4\varphi_{P1}^{3}}\right)^{1/3}, \quad (5.7)$$

(ii) at $z^{*}=0.5$,

$$\omega_{P3}^{*}=0, \quad (5.14)$$

and (iii) in $0\le z^{*}<0.5$ (using negative valued Ω of Eq. (5.12) in Eqs. (4.5)-(4.7)),

$$\omega_{P2}^{*}=\frac{2V^{*}z^{*}-V^{*}}{12m^{*}}-\varphi_{P1}\left(1+i\sqrt{3}\right)\left[12\sqrt[3]{4}m^{*}\left(\varphi_{P2}+\sqrt{\varphi_{P2}^{2}+4\varphi_{P1}^{3}}\right)^{1/3}\right]^{-1}+\frac{1}{24\sqrt[3]{2}m^{*}}\left[\left(1-i\sqrt{3}\right)\left(\varphi_{P2}+\sqrt{\varphi_{P2}^{2}+4\varphi_{P1}^{3}}\right)^{1/3}\right], \quad (5.8)$$

where

$$\varphi_{P1}=24m^{*}\left(1+2m^{*}\right)-\left(2V^{*}z^{*}-V^{*}\right)^{2}, \quad (5.10)$$

and

$$\varphi_{P2}=-72m^{*}V^{*}+288m^{*2}V^{*}+2V^{*3}+144m^{*}V^{*}z^{*}-576m^{*2}V^{*}z^{*}-12V^{*3}z^{*}+24V^{*3}z^{*2}-16V^{*3}z^{*3}-864m^{*2}\alpha^{*}. \quad (5.11)$$

As for electric field strengths below the critical electric field, *i.e.*, $E_0<E_c$, the micro-particle rotation speed, Ω, is set to zero in Eqs. (4.5)-(4.7), and Eq. (5.7) is generally valid throughout $0\le z^{*}\le 1$ for the pressure gradients of interest with $E_0\le 0.9E_c$. For electric field strengths of $0.95E_c\le E_0<E_c$, Eqs. (5.7), (5.8), and (5.14) are used with $\Omega=0$ in Eqs. (4.5)-(4.7) during the evaluation of the spin velocity profile. The analytic expressions given above are obtained under the "Solve" command using Mathematica.

Again notice that the solution or combination of solutions given to Eq. (5.6) need to satisfy all the above conditions and reasoning within the parametric regimes of interest since it is less likely to be physical for solutions being complex or multi-valued. The combination of solutions, Eqs. (5.7), (5.8), and (5.14), presented herein is generally for the parametric range of $E^{*}=E_0/E_c=1\sim 3$ with $E_c=1.3\times 10^{6}\ (V/m)$ and $\Gamma^{*}=\Gamma/\Gamma_r=0\sim 2$ with $\Gamma_r=2\times 10^{4}\ (Pa/m)$ in $0\le z^{*}\le 1$, whereas Eq. (5.7) is generally valid for $E^{*}\le 0.9$ and $0\le\Gamma^{*}\le 2$ throughout $0\le z^{*}\le 1$. For other parametric regimes of particular interests, the combination of solutions and the parametric range where the solutions becomes multi-valued *may be* different from the ones discussed herein. In this case, we need to start from Eq. (5.6) and solve for the three roots, then

simultaneously apply the stability, symmetry, real valued, and "free-to-spin" conditions to the roots to finally choose, select, or pick out the suitable and most physical combination for the desired spin velocity field just like the procedure we have shown in this section. Also notice that the jump or discontinuity made in the final spin velocity profile at $z^* = 0.5$ is permitted self-consistently by the "free-to-spin" condition for the zero spin viscosity cases studied herein. This is an analogous situation to the "inviscid" parallel shear flow with the *velocity field* being $\bar{v} = U\bar{i}_y$ for $z > 0$ and $\bar{v} = -U\bar{i}_y$ for $z < 0$ as one of the possible base solutions to Kelvin-Helmholtz instability studies (Kundu & Cohen, 2004).

We can always rewrite Eq. (5.6) and express the spatial coordinate, z^*, as a function of the spin velocity, ω^*, (*i.e.*, plot z^* by varying ω^* instead of plot ω^* by varying z^*) so as to avoid encountering complex valued solutions or transition of the real valued solution from one root to another as shown in Rosensweig (1997) for ferrofluid Couette flows subjected to uniform magnetic fields. However, even by this method, we will still encounter the problem of multi-valued solutions and of finding the most physically likely solution that satisfies the stable micro-particle rotation requirement for the present electrorotation flows. Moreover, as will be shortly shown in the following, since the linear velocity profile, u^*, and the 2D volume flow rate, Q, solutions depend on integrations of the spin velocity profile, ω^*, it is much more straight forward, in terms of performing the integrations with respect to z^* without obscuring the fundamental physical meanings, to express the spin velocity as a function of the spatial coordinate, *i.e.*, $\omega^* = \omega^*\left(z^*\right)$, as compared to expressing the spatial coordinate as a function of the spin velocity, $z^* = z^*\left(\omega^*\right)$. This is why we have chosen a seemly more difficult way of tackling Eq. (5.6) and explained in detail about the reasoning and conditions applied during the solution process.

After substituting the spin velocity solutions, ω^* or ω_x, and $C_p = \Gamma h/2$ into Eq. (5.2) and also noticing that for $E^* \geq 1$, ω^* is expressed by Eqs. (5.7) and (5.8) in the respective regions of $0.5 < z^* \leq 1$ and $0 \leq z^* < 0.5$, we integrate Eq. (5.2) with respect to the spatial coordinate, z^*, to obtain the velocity field as: (i) for $0.5 < z^* \leq 1$,

$$u_{UP}^{*}\left(z^{*}\right)=\frac{\eta}{\eta_e}\left[z^{*}\left(1-z^{*}\right)+\frac{4\zeta}{\Gamma h\tau_{MW}}\int_{z^{*}}^{1}\omega_{P1}^{*}\left(\widehat{z^{*}}\right)d\widehat{z^{*}}\right], \tag{5.15}$$

and (ii) for $0\le z^{*}<0.5$,

$$u_{DN}^{*}\left(z^{*}\right)=\frac{\eta}{\eta_e}\left[z^{*}\left(1-z^{*}\right)-\frac{4\zeta}{\Gamma h\tau_{MW}}\int_{0}^{z^{*}}\omega_{P2}^{*}\left(\widehat{z^{*}}\right)d\widehat{z^{*}}\right], \tag{5.16}$$

where the velocity field, Eqs. (5.15) and (5.16), is made dimensionless by dividing with $\Gamma h^2/2\eta$ (*note*: use η not η_e), *i.e.*, $u^{*}\left(z^{*}\right)=2\eta u_y\left(z^{*}\right)/\Gamma h^2$, ω_{P1}^{*} and ω_{P2}^{*} are respectively defined in Eqs. (5.7) and (5.8), and $\widehat{z^{*}}$ is a dummy index in both equations. For $E^{*}\le 0.9$, use ω_{P1}^{*}, *i.e.*, Eq. (5.7), in place of ω_{P2}^{*}, *i.e.*, Eq. (5.8), in Eq. (5.16), that is, use Eq. (5.7) for the spin velocities throughout $0\le z^{*}\le 1$ in the integration of Eqs. (5.15) and (5.16). From general mathematical point of views, the velocity field of the flow, u_y, needs to be continuous and smooth (continuous in du_y/dz) throughout the channel because of finite ER fluid viscosities, η. However, since we have manually (with physical reasoning) made the spin velocity, ω_x, discontinuous at the middle of the channel, the smoothness of the velocity distribution near $z^{*}=0.5$ may not exactly be preserved under the framework of zero spin viscosity limits—a cusp may arise at $z^{*}=0.5$ in the velocity profile given by Eqs. (5.15) and (5.16) for certain parametric regimes of interest. This issue will be further discussed in Section 5.2.

We next calculate the two dimensional volumetric flow rate, Q, by integrating the velocity fields, *i.e.*,

$$Q=\int_0^h u_y(z)dz=\frac{\Gamma h^3}{2\eta}\left[\int_0^{0.5}u_{DN}^{*}\left(z^{*}\right)dz^{*}+\int_{0.5}^{1}u_{UP}^{*}\left(z^{*}\right)dz^{*}\right], \tag{5.17}$$

with Eq. (5.15) used for $0.5<z^{*}\le 1$ and Eq. (5.16) used for $0\le z^{*}<0.5$. In terms of the spin velocities, Eq. (5.17) is rewritten as, for $E^{*}\ge 1$,

$$Q=\left(\frac{\Gamma h^3}{12\eta}\right)\left(\frac{\eta}{\eta_e}\right)\left\{1+\frac{24\zeta}{\Gamma h\tau_{MW}}\left[\int_{0.5}^{1}\int_{z^{*}}^{1}\omega_{P1}^{*}\left(\widehat{z^{*}}\right)d\widehat{z^{*}}dz^{*}-\int_{0}^{0.5}\int_{0}^{z^{*}}\omega_{P2}^{*}\left(\widehat{z^{*}}\right)d\widehat{z^{*}}dz^{*}\right]\right\}, \tag{5.18}$$

where $\widehat{z^{*}}$ is the dummy index and Eqs. (5.7) and (5.8) are used in the integration ranges of $0.5<z^{*}\le 1$ and $0\le z^{*}<0.5$, respectively. Again, for $E^{*}\le 0.9$, use ω_{P1}^{*}, *i.e.*, Eq. (5.7),

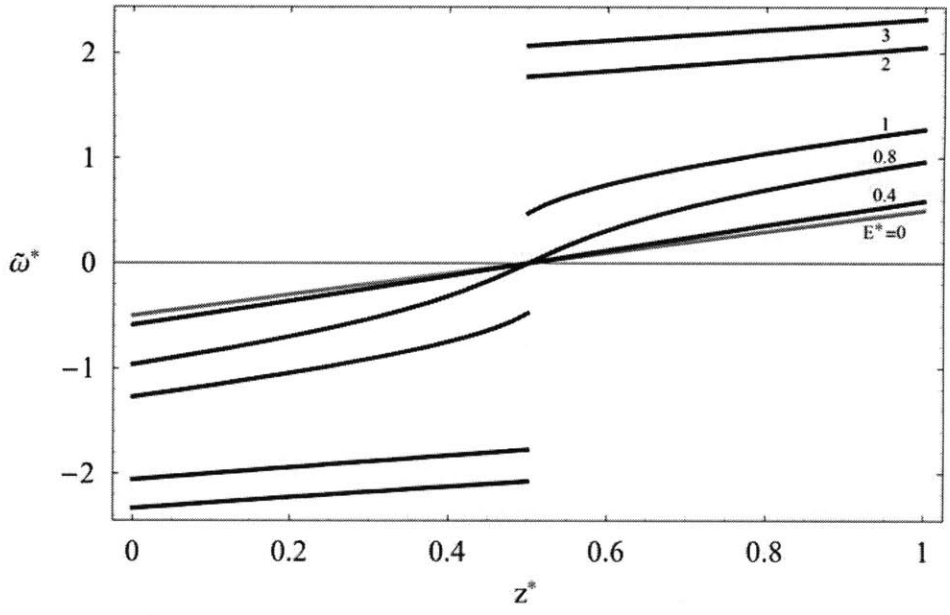

Figure 5.3. The normalized Poiseuille spin velocity profile, $\widetilde{\omega^*}$, plotted with respect to the spatial coordinate, z^*, evaluated at $E^* = 0$, 0.4, 0.8, 1.0, 2.0, and 3.0, with $\Gamma^* = 1$. The gray curve denotes the zero electric field value for the spin velocity, *i.e.*, the vorticity of ordinary Poiseuille flow. Note that Eqs. (5.7) and (5.8), with the proper selection of the micro-particle rotation speeds in Eq. (2.57) or (5.12), are used in the evaluation of the spin velocity for $E^* \geq 1$, whereas for $E^* \leq 0.9$, Eq. (5.7) (with $\Omega = 0$ in Eqs. (4.5)-(4.7)) is used throughout the spatial domain of interest.

throughout $0 \leq z^* \leq 1$ in the integration of Eq. (5.17) or (5.18). It is now obvious why we use η, zero electric field ER fluid viscosity, instead of $\eta_e = \eta + \zeta$ in non-dimensionalizing the velocity field of Eqs. (5.15) and (5.16). The intention is to utilize the ordinary Poiseuille flow solution (no electric field applied to the ER fluid) as a reference datum so that the variation and deviation in the electrorotation modified Poiseuille velocities and flow rates from those of the zero electric field solutions, *i.e.*, $u_0^*(z^*) = (2\eta/\Gamma h^2)u_y(z^*) = z^*(1-z^*)$ and $Q_0 = \Gamma h^3/12\eta$, can be respectively compared.

Results of the spin velocity profile, (linear) velocity profile, and the volume flow rate will be respectively presented in the following subsection. The system parameters, physical constants, and material properties used in the numeric evaluations can be found in Table 4.1 unless otherwise specified.

5.2.2 Modeling Results and Discussions

Before presenting the spin velocity profiles, we first normalize the Poiseuille spin velocity, Eqs. (5.7), (5.8), and (5.14) by $\Gamma h\tau_{MW}/2\eta$, namely, $\widetilde{\omega^*} = \widetilde{\omega^*_{P1}} = 2\eta\omega^*_{P1}/\Gamma h\tau_{MW}$ for $0.5 < z^* \le 1$, $\widetilde{\omega^*} = \widetilde{\omega^*_{P2}} = 2\eta\omega^*_{P2}/\Gamma h\tau_{MW}$ for $0 \le z^* < 0.5$, and $\widetilde{\omega^*} = \widetilde{\omega^*_{P3}} = 2\eta\omega^*_{P3}/\Gamma h\tau_{MW} = 0$ for $z^* = 0.5$. Employing this normalization, we find that the zero electric field solution, $\omega^*_0 = \Gamma h\tau_{MW}\left(z^* - 0.5\right)/2\eta$, becomes independent of the applied pressure gradient and only depends on the spatial position in the channel, *i.e.*, $\widetilde{\omega^*_0} = \left(z^* - 0.5\right)$. The zero electric field solution then becomes a reference datum invariant of both the applied electric field strength and the driving pressure gradient and facilitates a more physically meaningful comparison among the solutions.

Illustrated in Fig. 5.3 are the spatial variations of the electrorotation assisted Poiseuille spin velocity profiles given by Eqs. (5.7), (5.8), (5.14) normalized by $\Gamma h\tau_{MW}/2\eta$ plotted with respect to distinct strengths of the applied electric field, $E^* = E_0/E_c$. With the pressure gradient kept constant, *i.e.*, $\Gamma^* = \Gamma/\Gamma_r = 1$ where $\Gamma_r = 2\times10^4$ (Pa/m), the normalized spin velocity $\widetilde{\omega^*}$ is evaluated at $E^* = 0$, 0.4, 0.8, 1.0, 2.0, and 3.0 with $E_c = 1.3\times10^6$ (V/m) (the critical electric field strength is evaluated by substituting the numerical values of the physical parameters given in Table 4.1 into Eq. (1.1)). The solid gray curve shown in Fig. 5.3 represents the zero electric field solution, $\widetilde{\omega^*_0} = \left(z^* - 0.5\right)$, or half of the Poiseuille vorticity when there is no electric field and internal micro-particle electrorotation effects. From the figure, the positive and negative valued spin velocities found in the respective regions of $0.5 < z^* \le 1$ and $0 \le z^* < 0.5$ (with $\widetilde{\omega^*} = \widetilde{\omega^*_{P3}} = 0$ at $z^* = 0.5$) show that we have chosen, based on the macroscopic Poiseuille vorticity directions, the combination of solutions that satisfies the symmetry, real valued, and stable micro-particle rotation conditions. The apparent jump or discontinuity in the spin velocity profile at $z^* = 0.5$ is self-consistently permitted by the "free-to-spin" condition under the framework of the zero spin viscosity limit as already mentioned in the previous sections.

As can be seen in Fig. 5.3, the magnitude of the normalized spin velocity of Poiseuille flow with internal particle electrorotation increases as the applied DC electric field strength is increased. If, on the contrary, we reduce the applied electric field strength from $E^* = 1.0$, 0.8 to

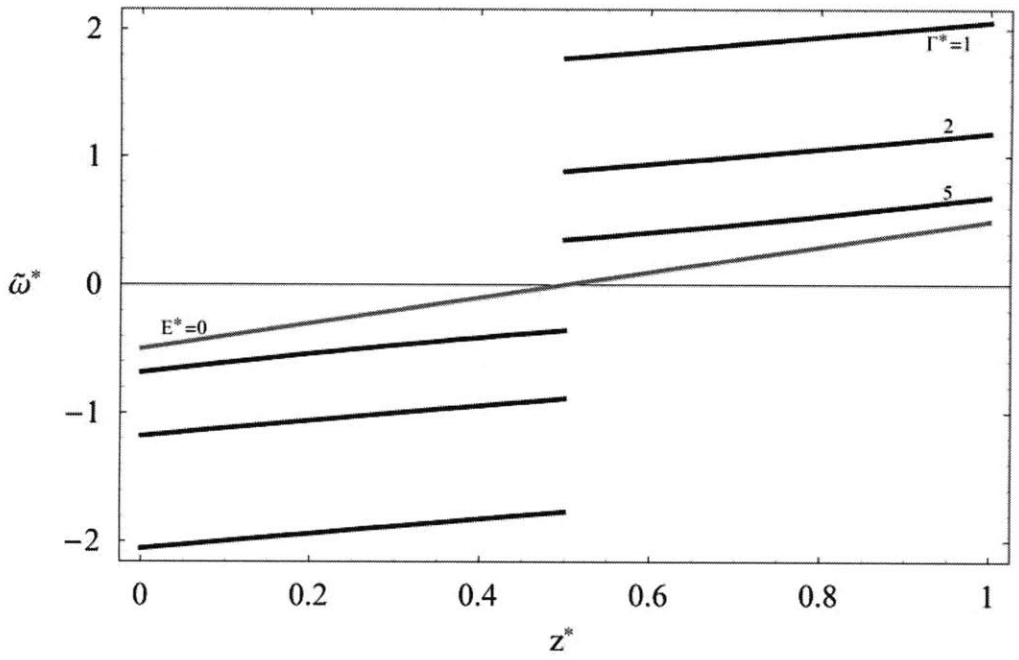

Figure 5.4. The normalized Poiseuille spin velocity profile, $\widetilde{\omega^*}$, plotted with respect to the spatial coordinate, z^*, evaluated at $\Gamma^* = 1$, 2, and 5, with $E^* = 2$. The gray curve denotes the zero electric field value for the spin velocity, *i.e.*, the vorticity of ordinary viscous Poiseuille flow. Note that Eqs. (5.7) and (5.8), with the proper selection of the micro-particle rotation speeds in Eq. (2.57) or (5.12), are employed in the evaluation of the spin velocity shown in this figure.

0.4, we find that the spin velocity gradually approaches the zero electric field solution noted by the gray curve in Fig. 5.3. Moreover, the strength of the jump or discontinuity at $z^* = 0.5$ in the normalized spin velocity field reduces and eventually smoothes out (see the smooth and continuous curves for $E^* = 0.4$ and 0.8) as the applied electric field is decreased. Note that in this figure, the solutions to $E^* = 0.4$ and 0.8 are fully represented by $\widetilde{\omega^*} = \widetilde{\omega^*_{P1}}$, *i.e.*, Eq. (5.7), throughout the spatial domain, $0 \le z^* \le 1$, at $\Gamma^* = 1$. However, the spin velocity solutions to $E^* = 1.0$, 2.0, and 3.0 are represented by $\widetilde{\omega^*} = \widetilde{\omega^*_{P1}}$ (Eq. (5.7)) for $0.5 < z^* \le 1$, $\widetilde{\omega^*} = \widetilde{\omega^*_{P2}}$ (Eq. (5.8)) for $0 \le z^* < 0.5$, and zero (Eq. (5.14)) for $z^* = 0.5$ at $\Gamma^* = 1$. The transition among the different roots verifies the cubic nature of the governing equation, Eq. (5.6).

Turning our attention to Fig. 5.4, we can also examine the responses of the normalized spin velocity, $\widetilde{\omega^*}$, with respect to the zero electric field solution, $\widetilde{\omega^*_0} = \left(z^* - 0.5\right)$ (noted by the solid

gray line in Fig. 5.4), by varying the applied pressure gradient from $\Gamma^* = 1$, 2, to 5 while keeping the applied DC electric field strength constant at $E^* = 2$. From this figure, it can be learned that as the pressure gradient is increased while the applied DC field is kept constant, the normalized spin velocity, $\widetilde{\omega^*}$, approaches back to the zero electric field solution, $\widetilde{\omega_0^*} = \left(z^* - 0.5\right)$. In addition, it can also be seen that the severity or magnitude of the jump in the spin velocity profile also reduces as the pressure gradient becomes large while the strength of the DC electric field is fixed. This is not surprising since the pressure driving force becomes relatively more and more important as Γ^* becomes a very large value while the electric field is maintained constant, or equivalently, the constant electric field strength and the associated electrorotation effects relatively diminish as compared to the increasing driving pressure gradient. Therefore, the mechanical (viscous and pressure) driving forces eventually dominate the flow responses, and the ER fluid flow eventually behaves as if there were no electrical forces or torques applied to the flow system, *i.e.*, pure viscous flow as characterized by $\widetilde{\omega_0^*} = \left(z^* - 0.5\right)$. Remember that the solutions shown in Fig. 5.4 are normalized values instead of actual "to scale" ones. The actual spin velocity or ER fluid rotation still increases as the driving pressure gradient is increased. Again, the normalized spin velocity field solutions for the Poiseuille ER fluid flow presented in Fig. 5.4 are evaluated by using $\widetilde{\omega^*} = \widetilde{\omega_{P1}^*}$ (Eq. (5.7)) for $0.5 < z^* \le 1$, $\widetilde{\omega^*} = \widetilde{\omega_{P2}^*}$ (Eq. (5.8)) for $0 \le z^* < 0.5$, and zero (Eq. (5.14)) for $z^* = 0.5$.

After the spin velocity field is found, the linear velocity field, u^*, is easily obtained by integrating Eqs. (5.15) and (5.16). The results of the velocity field, u^* (or u_y), are plotted with respect to the spatial coordinate z^* in Fig. 5.5 for $\Gamma^* = 1$ with $E^* = 0$, 0.4, 0.8, 1.0, 2.0, and 3.0. The gray solid curve represents the zero electric field solution, $u_0^* = z^*\left(1 - z^*\right)$, *i.e.*, the velocity field of ordinary Poiseuille flow without internal micro-particle electrorotation. Recall that the velocity field was already normalized by $\Gamma h^2/2\eta$ in the non-dimensional definition of Eqs. (5.15) and (5.16); hence, there is no more need to define a normalized velocity field as in the previous case of the spin velocity.

Based upon the above convention, we find in Fig. 5.5 that with $\Gamma^* = 1$ kept constant, the flow velocity is considerably enhanced and the cusp in the velocity profile at $z^* = 0.5$ is sharpened as

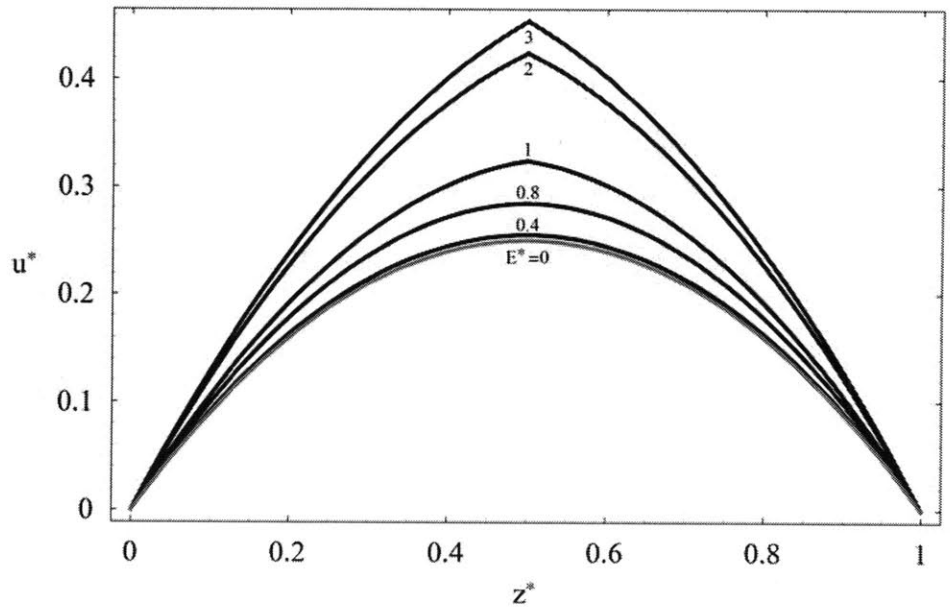

Figure 5.5. The normalized linear velocity profile, u^*, of Poiseuille flow with internal micro-particle electrorotation plotted with respect to the spatial coordinate, z^*, evaluated at $E^* = 0$, 0.4, 0.8, 1.0, 2.0, and 3.0, with $\Gamma^* = 1$. The gray curve denotes the zero electric field velocity profile, which is the original Poiseuille parabolic profile. Equations (5.7) (*use positive* Ω *from Eq. (2.57) or (5.12) in Eqs. (4.5)-(4.7)*) and (5.8) (*use negative* Ω *from Eq. (2.57) or (5.12) in Eqs. (4.5)-(4.7)*) are respectively employed in the integrals of Eqs. (5.15) and (5.16) for $E^* \geq 1$. The evaluation of u^* for $E^* \leq 0.9$ is done by employing Eq. (5.7) in both Eqs. (5.15) and (5.16) with $\Omega = 0$ in Eqs. (4.5)-(4.7).

the strength of the applied DC electric field is increased. If we reduce the strength of the electric field while the pressure gradient is maintained constant, the cusp at $z^* = 0.5$ becomes blunt and the electrorotation enhanced velocity profile gradually reduces and converges back to the $E^* = 0$ solution, *i.e.*, the parabolic Poiseuille flow velocity field without internal particle electrorotation as noted by the solid gray curve in the figure. The $E^* = 0.4$ and 0.8 velocity fields shown are evaluated by substituting Eq. (5.7), *i.e.*, ω_{P1}^*, into the integrals of both Eqs. (5.15) and (5.16) with $\Omega = 0$ in Eqs. (4.5)-(4.7) since in this parametric regime, ω_{P1}^* assumes a real value and is valid throughout the spatial domain of $0 \leq z^* \leq 1$. As for $E^* = 1.0$, 2.0, and 3.0, Eq. (5.7) is employed in the integral of Eq. (5.15) whereas Eq. (5.8) is used in Eq. (5.16). The cusped velocity profile shown in Fig. 5.5 is interestingly similar to the velocity profiles of a power law fluid in circular pipe Poiseuille flow geometries for large power indices (Chhabra & Richardson, 1999) though,

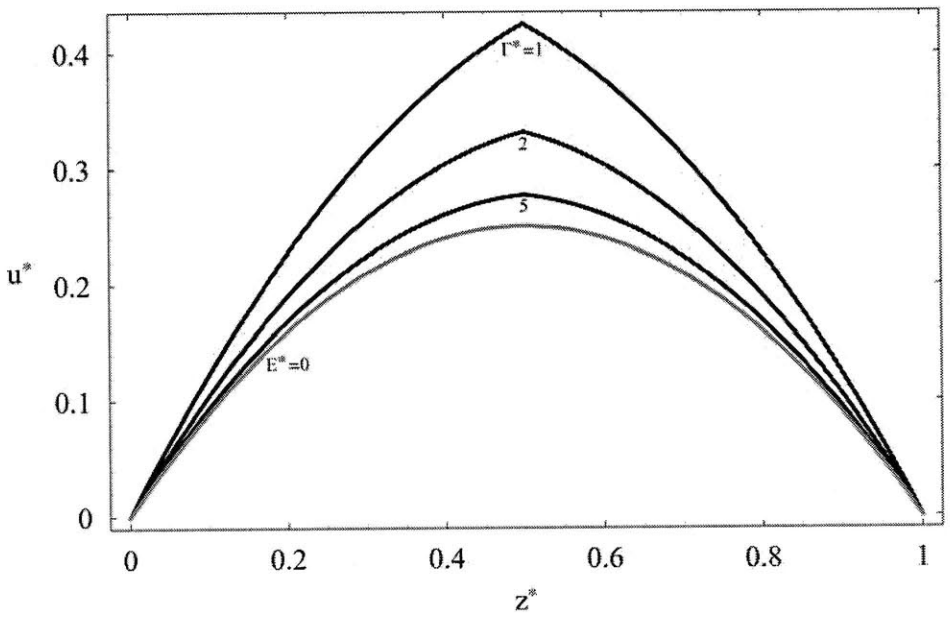

Figure 5.6. The normalized linear velocity profile, u^*, of Poiseuille flow with internal micro-particle electrorotation plotted with respect to the spatial coordinate, z^*, evaluated at $\Gamma^* = 1$, 2, and 5, with $E^* = 2$. The gray curve denotes the zero electric field velocity profile, which is the original Poiseuille parabolic profile. Equations (5.7) (*use positive* Ω *from Eq. (2.57) or (5.12) in Eqs. (4.5)-(4.7)*) and (5.8) (*use negative* Ω *from Eq. (2.57) or (5.12) in Eqs. (4.5)-(4.7)*) are respectively employed in the integrals of Eqs. (5.15) and (5.16) for the linear velocity profiles shown herein.

of course, the electrorotation and power law fluid flows work respectively on different principles.

Similarly, Fig. 5.6 illustrates the spatial variations of the dimensionless linear velocity profile, u^*, evaluated at driving pressure gradients of $\Gamma^* = \Gamma/\Gamma_r = 1$, 2, and 5 with $E^* = E_0/E_c = 2$ where $\Gamma_r = 2\times10^4$ (Pa/m) and $E_c = 1.3\times10^6$ (V/m), which is the critical electric field evaluated by substituting the numerical values of the physical parameters given in Table 4.1 into Eq. (1.1). The solid gray curve shown in Fig. 5.6 represents zero electric field solution, *i.e.*, pure viscous Poiseuille flow, to the linear velocity profile, $u_0^* = z^*\left(1-z^*\right)$. It can be learned from Fig. 5.6 that the effect of electrorotation enhancement on the velocity field as well as the cusp structure at $z^* = 0.5$ diminish and approach the "$E^* = 0$" Poiseuille velocity field as the driving pressure gradient increases when the flow is subjected to a constant electric field, $E^* = 2$. In other words, the relatively increasing pressure gradient gradually overcomes or dominates over

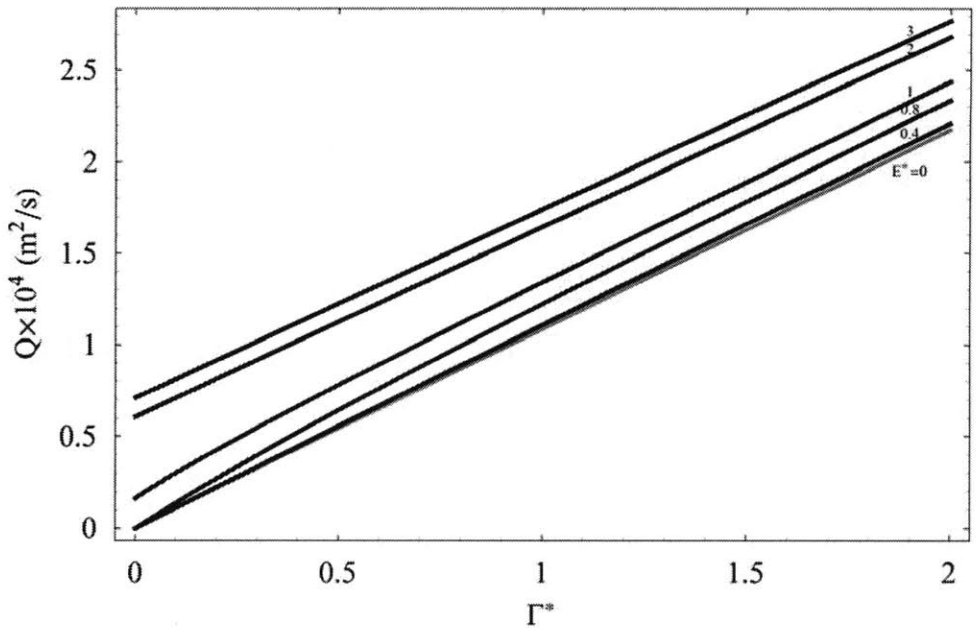

Figure 5.7. The two dimensional Poiseuille volume flow rate, Q (m^2/s), plotted with respect to the applied pressure gradient, Γ^*, evaluated at $E^* = 0$, 0.4, 0.8, 1.0, 2.0, and 3.0. The gray curve represents the zero electric field volume flow rate given by $Q_0 = \Gamma h^3/12\eta$.

the pumping of fluid due to the electrical torque input through the electrorotation of the suspended micro-particles when the applied electric field is held constant. The opposite effect is readily observed if we reduce the strength of the pressure gradient while maintaining the same electric field strength, that is, internal particle electrorotation becomes more and more dominant on the pumping of the fluid flow when the driving pressure gradient is relatively decreasing. In this opposite case, the parabolic velocity profile sharpens and the cusp structure is formed at $z^* = 0.5$ as the strength of the pressure gradient is reduced. Again, notice that all the velocity profiles presented in Fig. 5.6 are non-dimensionalized as well as normalized by $\Gamma h^2/2\eta$; the actual magnitude of the velocity field at $\Gamma^* = 5$ is still larger than that of the $\Gamma^* = 1$ solution.

Finally, using the physical parameters and material properties given in Table 4.1, the two dimensional volume flow rate of Poiseuille flow with internal micro-particle electrorotation, Q (m^2/s), is plotted with respect to the driving pressure gradient, $\Gamma^* = \Gamma/\Gamma_r$ with $\Gamma_r = 2\times10^4$ (Pa/m), at distinct values of the applied DC electric field strength, $E^* = E_0/E_c$ with $E_c = 1.3\times10^6$ (V/m). The results are shown in Fig. 5.7 for $E^* = 0$, 0.4, 0.8, 1.0, 2.0, and 3.0 with

the solid gray curve noted by $E^* = 0$ corresponding to the two dimensional volume flow rate of Poiseuille flow without internal micro-particle electrorotation, *i.e.*, $Q_0 = \Gamma h^3/12\eta$.

From Fig. 5.7, we find that the volume flow rate increases as the applied DC electric field strength is increased while the driving pressure gradient is kept constant. On the other hand, the electrorotation enhanced volume flow rate gradually reduces back to the zero electric field solution, $Q_0 = \Gamma h^3/12\eta$, as the applied electric field is reduced. These results are consistent with our previous examination of the velocity fields shown in Fig. 5.5 and agree with the experimental observations reported in Lemaire *et al.* (2006). Note that the flow rate solutions evaluated at $E^* =$ 1.0, 2.0, and 3.0 suggest non-zero volume flow rates at zero driving pressure gradients when the flow is subjected to an applied electric field strength greater than or equal to the critical electric field for the onset of Quincke rotation. This result is particularly due to the fact that we have used the combination of solutions to the spin velocity, Eqs. (5.7), (5.8), and (5.14), that satisfies the symmetry, real valued, stable micro-particle rotation, and free-to-spin conditions in the modeling and evaluation of the volume flow rate, Q, under zero spin viscosity conditions, *i.e.*, $\eta' = 0$. Nonetheless, we need to point out that unless there is some initial flow ($\Gamma^* \neq 0$) applied to give the suspended micro-particles a favorable direction for electrorotation, the direction for Quincke rotation is merely a matter of chance with the particle rotation axis either pointing into or out of the planes defined by the electric field under zero flow or equivalently zero driving pressure gradient conditions. Up to this point, no experimental evidence has observed a negative ER effect with zero initial flow when an electric field strength, $E_0 \geq E_c$, is applied (Lobry & Lemaire, 1999)—both initial vorticity and micro-particle Quincke rotation are needed for the present negative ER effect. The finite jump of volume flow rate at zero driving pressure gradients diminishes and eventually becomes zero, *i.e.*, zero flow rate at zero pressure gradient, as we reduce the applied electric field strength from $E^* = 1.0$, 0.8, to 0.4 as can be found in Fig. 5.7. Again, for the $E^* \leq 0.9$ solutions, *i.e.*, $E^* = 0.4$ and 0.8, shown in Fig. 5.7, we have used ω_{P1}^*, Eq. (5.7), throughout the spatial domain, $0 \leq z^* \leq 1$.

Summing up the findings from examining Figs. 5.3, 5.5, and 5.7, it is found that, in general, the magnitude of the normalized spin velocity, the normalized flow velocity, and the 2D volume flow rate is increased as the applied electric field, E^*, is increased with the driving pressure

gradient, Γ^*, kept constant. Moreover, increasing the applied electric field gives rise to a more severe jump or discontinuity at $z^* = 0.5$ in the normalized spin velocity profile, sharpens the cusp structure at $z^* = 0.5$ in the (normalized) velocity profile, and results in a finite value of volume flow rate at zero pressure gradients. Contrarily, reducing the strength of the electric field smoothes out the cusp in the velocity profile and reduces the severity of the discontinuity at $z^* = 0.5$ in the spin velocity field while the pressure gradient is kept constant. The (normalized) velocity and spin velocity profiles as well as the 2D volume flow rate gradually reduce back to the zero electric field solutions as the applied electric field strength is reduced. Lastly, with the applied electric field being fixed as in Figs. 5.4 and 5.6, a relatively increasing driving pressure gradient gradually overcomes the pumping effects due to internal particle electrorotation, and hence both the normalized velocity and spin velocity profiles converge back to the zero electric field solutions, *i.e.*, pure viscous flow solutions, which is a result consistent with the physical picture we have already obtained from the discussions on Couette flow in Chapter 4.

As a general conclusion of the results presented in this section, we find that, in the zero spin viscosity limit, the full continuum governing equations (from anti-symmetric stress theories) employed in this section reduce to a "particulate limit" and predict similar trends of variation of the effective viscosities for Couette flow and of the two dimensional volume flow rates for Poiseuille flow as compared to the theoretical predictions from the two-phase volume averaged effective continuum model (single particle dynamics based) found in the literature for describing the internal micro-particle electrorotation modified flow phenomena (Brenner, 1970; Lobry & Lemaire, 1999; Cebers *et al.*, 2000; Cebers *et al.*, 2002; Lemaire *et al.*, 2006; Pannacci *et al.*, 2007*a*; Lemaire *et al.*, 2008).

5.3 The Simplified Governing Equations with Finite Spin Viscosities in the Small Spin Velocity Limit for Poiseuille Flow Geometries

Before presenting the simplified governing equations, we redefine the 2D Poiseuille flow geometry as shown in Fig. 5.8 in which we have shifted the positions of the upper and lower parallel plates to the respective coordinates of $z = h/2$ and $z = -h/2$ instead of those shown in Fig. 5.1 of $z = 0$ and $z = h$. We redefine the coordinates of the parallel plates so as to simplify

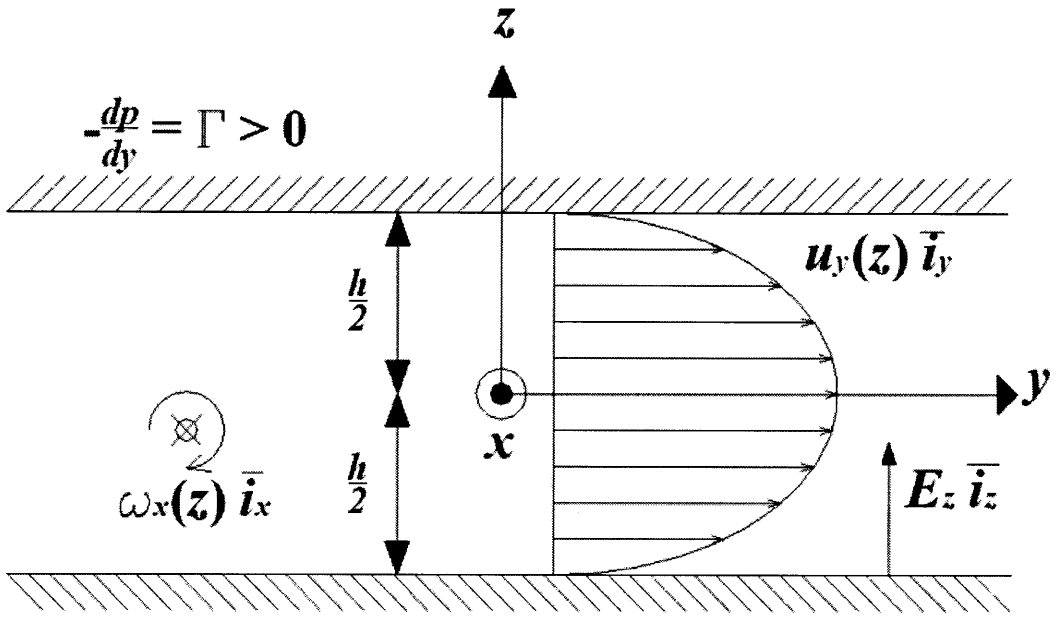

Figure 5.8. The schematic diagram illustrating the new coordinate system employed for analyzing Poiseuille flow with internal micro-particle electrorotation in the finite spin viscosity small spin velocity limit.

our following analysis and the final expressions of the analytical solutions to the spin velocity, linear velocity, and 2D volume flow rate.

Using the new yet similar geometry defined in Fig. 5.8, we again assume that the flow is steady, incompressible, two-dimensional, and fully developed so that the applied pressure gradient, $\Gamma = -dp/dy > 0$, is at most a constant for a fully developed flow, and that $u_z = 0$ and $E_y = 0$ due respectively to the non-penetrating (impermeable walls) boundary condition and the continuity of tangential electric field for perfectly conducting electrodes at $z = h/2$ and $-h/2$. The applied DC electric field is further approximated to be only in the z-direction, namely, $\bar{E} = E_z \bar{i}_z$, with $E_z \approx E_0$ and E_0 being a constant across the channel height, h, as we have already discussed in Sections 4.1 and 5.1 (*i.e.*, Eq.(4.8)). By employing these assumptions and approximations, the linear momentum equation, Eq. (2.2), angular momentum equation, Eq. (2.3), and the retarding polarization relaxation equation, Eq. (3.35), are simplified for finite spin viscosity conditions, namely,

$$-\tau_{MW}\omega_x P_z - \left(P_y - P_{eq}^y\right) = 0, \tag{4.1}$$

$$\tau_{MW}\omega_x P_y - \left(P_z - P_{eq}^z\right) = 0, \tag{4.2}$$

$$\Gamma + 2\zeta \frac{d\omega_x}{dz} + \eta_e \frac{d^2 u_y}{dz^2} = 0, \tag{5.1}$$

and

$$P_y E_z + 2\zeta \left(-\frac{du_y}{dz} - 2\omega_x \right) + \eta' \frac{d^2 \omega_x}{dz^2} = 0, \tag{4.25}$$

where the definitions of the variables shown in Eqs. (4.1), (4.2), (5.1), and (4.25) are the same as those given in Section 5.1. Again, we have replaced the total ER fluid polarization, P_{ty}, with the retarding polarization, P_y, in Eq. (4.25) since the DC electric field is applied in the z-direction with $E_y = 0$ and thus the polarization in the y-direction is basically due to the (retarding) dipole moment tilt resulting from micro-particle electrorotation. The simplified version of the z-linear momentum equation relates merely the z-pressure gradient to the z-component of the Kelvin body force density, $\left(\overline{P}_t \cdot \nabla\right)\overline{E}$, and is treated apart (or neglected) from Eq. (4.1), (4.2), (5.1), and (4.25).

Employing the equilibrium retarding polarization given in Eq. (3.33), we solve Eqs. (4.1) and (4.2) to obtain

$$P_y = n \frac{\alpha_y - \tau_{MW} \omega_x \alpha_z}{1 + \tau_{MW}^2 \omega_x^2} E_0, \tag{4.5}$$

$$P_z = n \frac{\alpha_z + \tau_{MW} \omega_x \alpha_y}{1 + \tau_{MW}^2 \omega_x^2} E_0, \tag{4.6}$$

where

$$\begin{bmatrix} \alpha_y \\ \alpha_z \end{bmatrix} = \begin{bmatrix} \alpha_{yz} \\ \alpha_{zz} \end{bmatrix} = 4\pi\varepsilon_1 R^3 \begin{bmatrix} -\dfrac{\tau_{MW}\Omega \left(\dfrac{\sigma_2 - \sigma_1}{2\sigma_1 + \sigma_2} - \dfrac{\varepsilon_2 - \varepsilon_1}{2\varepsilon_1 + \varepsilon_2} \right)}{1 + \tau_{MW}^2 \Omega^2} \\ \dfrac{\left(\dfrac{\sigma_2 - \sigma_1}{2\sigma_1 + \sigma_2} - \dfrac{\varepsilon_2 - \varepsilon_1}{2\varepsilon_1 + \varepsilon_2} \right)}{1 + \tau_{MW}^2 \Omega^2} \end{bmatrix}, \tag{4.7}$$

with α_{zz} and α_{yz} respectively defined in Eqs. (3.42) and (3.43), and the magnitude and direction of the micro-particle rotation speed, Ω, being respectively given in Eq. (2.57) and that of the macroscopic flow vorticity. Based on the operating regimes of the applied electric field strengths

as well as the stable micro-particle rotation requirement imposed by the macroscopic Poiseuille flow vorticity, Eq. (2.57) (or Eq. (5.12)) can be re-written as

$$\overline{\Omega} = \Omega \overline{i_x} = \left\{ \begin{array}{ll} \dfrac{1}{\tau_{MW}} \sqrt{\left(\dfrac{E_0}{E_c}\right)^2 - 1}\, \overline{i_x}, & 0 < z^* = \dfrac{z}{h} \le \dfrac{1}{2} \\ 0, & z^* = \dfrac{z}{h} = 0 \\ \dfrac{-1}{\tau_{MW}} \sqrt{\left(\dfrac{E_0}{E_c}\right)^2 - 1}\, \overline{i_x}, & -\dfrac{1}{2} \le z^* = \dfrac{z}{h} < 0 \end{array} \right\}, \text{ for } E_0 \ge E_c, \tag{5.19}$$

and

$$\overline{\Omega} = \Omega \overline{i_x} = 0, \text{ for } -1/2 \le z^* = z/h \le 1/2 \text{ when } E_0 < E_c, \tag{5.13}$$

which are the micro-particle rotation speeds to be substituted into the polarizabilities α_y and α_z in Eq. (4.7) in the following analysis.

After substituting $\overline{E} = E_z \overline{i_z} \approx E_0 \overline{i_z}$ (see Eq. (4.8)) and Eq. (4.5) into Eq. (4.25), we obtain

$$\frac{\alpha^* - \tau_{MW}\omega_x}{1 + \tau_{MW}^2 \omega_x^2} n\alpha_z E_0^2 + 2\zeta\left(-\frac{du_y}{dz} - 2\omega_x\right) + \eta' \frac{d^2\omega_x}{dz^2} = 0, \tag{4.26}$$

where $\alpha^* = \alpha_y / \alpha_z = -\tau_{MW}\Omega$ and the electrical body torque term, $P_y E_z$, has been retained to the first order of the particle solid volume fraction, ϕ, for dilute suspensions, *i.e.*, $\phi \ll 1$, since $n\alpha_z E_0 E_z \approx n\alpha_z E_0 \left(E_0 + \phi e_1 + \cdots\right)$ and $n\alpha_z \sim nR^3 \sim nd^3 \sim O(\phi)$ as in Eq. (3.31). Equation (4.26) is further linearized by the condition of small spin velocities, *i.e.*, $\tau_{MW}^2 \omega_x^2 \ll 1$, such that

$$\left(\alpha^* - \tau_{MW}\omega_x\right) n\alpha_z E_0^2 + 2\zeta\left(-\frac{du_y}{dz} - 2\omega_x\right) + \eta' \frac{d^2\omega_x}{dz^2} = 0. \tag{4.27}$$

Together, Eqs. (5.1), (4.7), and (4.27) form the simplified governing equations for analyzing and describing the continuum nER2 responses of the Poiseuille flow with internal micro-particle electrorotation in the finite spin viscosity small spin velocity limit, *i.e.*, $\eta' \ne 0$ and $\tau_{MW}^2 \omega_x^2 \ll 1$. The criterion of $\tau_{MW}^2 \omega_x^2 \ll 1$ for linearization gives an estimate of the maximum range of spin velocity valid for our analyses. Since the Maxwell-Wagner relaxation time has the order of magnitude of $O\left(10^{-3}\right)$ for the selected materials given in the present work (see Table 4.1), the

dimensional spin velocity can at most be at the order of $O(10^0)$ to $O(10^1)$ so that $\tau_{MW}^2\omega_x^2 \sim O(10^{-2})$ to $O(10^{-4})$, which is roughly a general estimate for a physical value that is much less than one.

The boundary condition on the linear velocity field, $\bar{v} = u_y \bar{i}_y$, is once again the no-slip boundary condition, *i.e.*, $\bar{v} = 0$ at $z = h/2$ and at $z = -h/2$. However, unlike the case of zero spin viscosity conditions, Eq. (4.27) does not reduce to a cubic algebraic equation and the condition of "free-to-spin" no longer applies to Eq. (4.27). For finite spin viscosity conditions, the boundary condition on the continuum spin velocity field, $\bar{\omega} = \omega_x \bar{i}_x$, is given by

$$\bar{\omega} = \frac{\beta}{2}\left(\nabla \times \bar{v}\right), \tag{4.28}$$

at $z = h/2$ and at $z = -h/2$, where β is a boundary condition selection parameter ranging from zero to one, *i.e.*,

$$0 \le \beta \le 1, \tag{4.29}$$

as described in Kaloni (1992), Lukaszewicz (1999), Rinaldi (2002), and Rinaldi and Zahn (2002). Kaloni (1992) has reported that the boundary condition of $\bar{\omega} = \omega_x \bar{i}_x = 0$ may give theoretical predictions inconsistent with experimental observations for some micro-polar fluid flow conditions. As will be discussed in the next section, inconsistency is also found between the results predicted by our present continuum mechanical model when $\bar{\omega} = \omega_x \bar{i}_x = 0$ at the boundaries and those experimentally observed in previous literature (Lobry & Lemaire, 1999; Cebers *et al.*, 2000; Cebers *et al.*, 2002; Lemaire *et al.*, 2006; Pannacci *et al.*, 2007*a*; Lemaire *et al.*, 2008).

Generally speaking, the no-slip boundary condition and Eq. (4.28) give four conditions on the Poiseuille flow boundaries and should be sufficient to completely solve the fourth order coupled systems equations, *i.e.*, Eqs. (5.1) and (4.27), that respectively describe the linear and angular momentum balances in the Poiseuille ER fluid flow. However, due to the asymmetry of the imposed Poiseuille flow vorticity between the upper and lower halves of the flow channel, we find that the micro-particles belonging to the respective upper and lower halves of the channel are actually rotating in opposite directions, *i.e.*, a sign function nature as can be seen in Eq. (5.19), which introduces further complexities to the mathematical analysis of the differential

equations if we were to treat the whole flow channel as one computation domain by merely applying the no-slip condition and Eq. (4.28) at $z = h/2$ and at $z = -h/2$. To resolve this problem, we divide or split the whole Poiseuille flow channel into two computation domains, namely, the upper half of the channel defined by $0 \le z \le h/2$ and the lower half of the channel defined by $-h/2 \le z \le 0$, and solve for the spin and linear velocities separately in the two respective computation domains. Hence, we solve Eqs. (4.7), (4.27), (5.1), and (5.19) for the upper half of the channel, $0 \le z \le h/2$, with the boundary conditions of

$$\begin{cases} \bar{v} = u_y \bar{i}_y = 0 \\ \bar{\omega} = \omega_x \bar{i}_x = \dfrac{\beta}{2}\left(\nabla \times \bar{v}\right) = -\dfrac{\beta}{2}\dfrac{du_y}{dz} \end{cases} \text{ at } z = \frac{h}{2} \text{ and } \begin{cases} \bar{\omega} = \omega_x \bar{i}_x = 0 \\ \dfrac{du_y}{dz} = 0 \end{cases} \text{ at } z = 0, \tag{5.20}$$

whereas we solve Eqs. (4.7), (4.27), (5.1), and (5.19) for the lower half of the channel, $-h/2 \le z \le 0$, with the boundary conditions of

$$\begin{cases} \bar{v} = u_y \bar{i}_y = 0 \\ \bar{\omega} = \omega_x \bar{i}_x = \dfrac{\beta}{2}\left(\nabla \times \bar{v}\right) = -\dfrac{\beta}{2}\dfrac{du_y}{dz} \end{cases} \text{ at } z = -\frac{h}{2} \text{ and } \begin{cases} \bar{\omega} = \omega_x \bar{i}_x = 0 \\ \dfrac{du_y}{dz} = 0 \end{cases} \text{ at } z = 0, \tag{5.21}$$

with β given by Eq. (4.29). The $\bar{\omega} = 0$ and $du_y/dz = 0$ conditions shown in the above two equations are stated by (i) recognizing the geometric symmetry conditions of $\bar{\omega} \to 0$ and $\bar{\Omega} \to 0$ (see Eqs. (5.13) and (5.19)) as $z \to 0$ (coordinates defined in Fig. 5.8) as discussed in Section 5.1 and (ii) by substituting the symmetry conditions to Eq. (4.26) or (4.27), respectively.

5.4 Continuum Analysis with Finite Spin Viscosities in the Small Spin Velocity Limit

5.4.1 Solutions to the Spin Velocity, Linear Velocity, and Two Dimensional Volume Flow Rate

We first integrate Eq. (5.1) with respect to the spatial coordinate, z, and arrive at the following relation,

$$\Gamma z + 2\zeta\omega_x + \eta_e \frac{du_y}{dz} = \Pi_1, \tag{5.22}$$

where Π_1 is a constant of integration. By using the following non-dimensionalization scheme, namely,

$$\omega^* = \tau_{MW}\omega_x,\ z^* = \frac{z}{h},\ u^* = \frac{u_y}{V_0},\ \text{and}\ \delta^* = \tau_{MW}\frac{V_0}{h}, \tag{5.23}$$

and substituting Eq. (5.22) into Eq. (4.27), the linear momentum equation, Eq. (5.22), and the angular momentum equation, Eq. (4.27) (combined with Eq. (5.22)), are respectively non-dimensionalized as

$$\frac{du^*}{dz^*} = \frac{\tau_{MW}\Pi_1}{\eta_e\delta^*} - \frac{\Gamma h\tau_{MW}}{\eta_e\delta^*}z^* - \frac{2\zeta}{\eta_e\delta^*}\omega^*, \tag{5.24}$$

and

$$\frac{d^2\omega^*}{dz^{*2}} - A^2\omega^* = B - \Lambda z^*, \tag{5.25}$$

where

$$A = \sqrt{\frac{\tau_{MW}h^2}{\eta'}\left(n\alpha_z E_0^2 + \frac{4\zeta}{\tau_{MW}} - \frac{4\zeta^2}{\eta_e\tau_{MW}}\right)}, \tag{5.26}$$

$$B = \frac{\tau_{MW}h^2}{\eta'}\left(\frac{2\zeta}{\eta_e}\Pi_1 - n\alpha_y E_0^2\right), \tag{5.27}$$

$$\Lambda = \frac{2\zeta\Gamma\tau_{MW}h^3}{\eta'\eta_e}, \tag{5.28}$$

and

$$V_0 = \frac{Q_0}{h} = \frac{\Gamma h^2}{12\eta}, \tag{5.29}$$

where the stars "*" denote dimensionless variables (A, B, and Λ also being dimensionless, while Π_1 has dimensions) and $Q_0 = \Gamma h^3/12\eta$ is simply the zero electric field 2D Poiseuille volume flow rate based on the zero electric field viscosity, $\eta \approx \eta_0(1+2.5\phi)$ as defined in Section 2.1. The general solution to Eq. (5.25) is

$$\omega^*(z^*) = \Pi_3\cosh(Az^*) + \Pi_4\sinh(Az^*) - \frac{B}{A^2} + \frac{\Lambda}{A^2}z^*, \tag{5.30}$$

in which Π_3 and Π_4 are constants. Equation (5.30) can then be substituted into Eq. (5.24), and the linear momentum equation, Eq. (5.24), is integrated as

$$u^*\left(z^*\right)=\left(\frac{\tau_{MW}\Pi_1}{\eta_e\delta^*}+\frac{2\zeta}{\eta_e\delta^*}\frac{B}{A^2}\right)z^*-\frac{1}{2}z^{*2}\left(\frac{\Gamma h\tau_{MW}}{\eta_e\delta^*}+\frac{2\zeta}{\eta_e\delta^*}\frac{\Lambda}{A^2}\right) \\ -\frac{2\zeta}{\eta_e\delta^*}\frac{\Pi_3}{A}\sinh\left(Az^*\right)-\frac{2\zeta}{\eta_e\delta^*}\frac{\Pi_4}{A}\cosh\left(Az^*\right)+\Pi_2 \quad , \tag{5.31}$$

with Π_2 being a constant and B being related to Π_1 through Eq. (5.27). Since we are solving for the continuum spin and linear velocity profiles for the two respective spatial regions of $0\le z^*\le 1/2$ and $-1/2\le z^*\le 0$, we re-write Eqs. (5.30) and (5.31) in terms of the A and B respectively defined in Eqs. (5.26) and (5.27) for the upper half of the flow channel, *i.e.*, $0\le z^*\le 1/2$, as

$$\omega_{UP}^*\left(z^*\right)=\Pi_3^{UP}\cosh\left(A_{UP}z^*\right)+\Pi_4^{UP}\sinh\left(A_{UP}z^*\right)-\frac{B_{UP}}{A_{UP}^2}+\frac{\Lambda}{A_{UP}^2}z^*, \tag{5.32}$$

and

$$u_{UP}^*\left(z^*\right)=\left(\frac{\tau_{MW}\Pi_1^{UP}}{\eta_e\delta^*}+\frac{2\zeta}{\eta_e\delta^*}\frac{B_{UP}}{A_{UP}^2}\right)z^*-\frac{1}{2}z^{*2}\left(\frac{\Gamma h\tau_{MW}}{\eta_e\delta^*}+\frac{2\zeta}{\eta_e\delta^*}\frac{\Lambda}{A_{UP}^2}\right) \\ -\frac{2\zeta}{\eta_e\delta^*}\frac{\Pi_3^{UP}}{A_{UP}}\sinh\left(A_{UP}z^*\right)-\frac{2\zeta}{\eta_e\delta^*}\frac{\Pi_4^{UP}}{A_{UP}}\cosh\left(A_{UP}z^*\right)+\Pi_2^{UP} \quad , \tag{5.33}$$

and for the lower half of the flow channel, *i.e.*, $-1/2\le z^*\le 0$, as

$$\omega_{DW}^*\left(z^*\right)=\Pi_3^{DW}\cosh\left(A_{DW}z^*\right)+\Pi_4^{DW}\sinh\left(A_{DW}z^*\right)-\frac{B_{DW}}{A_{DW}^2}+\frac{\Lambda}{A_{DW}^2}z^*, \tag{5.34}$$

and

$$u_{DW}^*\left(z^*\right)=\left(\frac{\tau_{MW}\Pi_1^{DW}}{\eta_e\delta^*}+\frac{2\zeta}{\eta_e\delta^*}\frac{B_{DW}}{A_{DW}^2}\right)z^*-\frac{1}{2}z^{*2}\left(\frac{\Gamma h\tau_{MW}}{\eta_e\delta^*}+\frac{2\zeta}{\eta_e\delta^*}\frac{\Lambda}{A_{DW}^2}\right) \\ -\frac{2\zeta}{\eta_e\delta^*}\frac{\Pi_3^{DW}}{A_{DW}}\sinh\left(A_{DW}z^*\right)-\frac{2\zeta}{\eta_e\delta^*}\frac{\Pi_4^{DW}}{A_{DW}}\cosh\left(A_{DW}z^*\right)+\Pi_2^{DW} \quad , \tag{5.35}$$

where the superscripts/subscripts of "*UP*" and "*DW*" denote the respective solutions to the upper, $0\le z^*\le 1/2$, and lower, $-1/2\le z^*\le 0$, halves of the Poiseuille flow channel. The boundary conditions given in Eqs. (5.20) and (5.21) can also be made dimensionless by the non-dimensionalization scheme shown in Eq. (5.23). For the upper half of the flow channel, $0\le z^*\le 1/2$, Eq. (5.20) becomes

$$\begin{cases} u^* = 0 \\ \omega^* = -\dfrac{1}{2}\beta\delta^* \dfrac{du^*}{dz^*} \end{cases} \text{ at } z^* = \frac{1}{2} \text{ and } \begin{cases} \omega^* = 0 \\ \dfrac{du^*}{dz^*} = 0 \end{cases} \text{ at } z^* = 0, \tag{5.36}$$

whereas for the lower half of the flow channel, $-1/2 \le z^* \le 0$, Eq. (5.21) becomes

$$\begin{cases} u^* = 0 \\ \omega^* = -\dfrac{1}{2}\beta\delta^* \dfrac{du^*}{dz^*} \end{cases} \text{ at } z^* = -\frac{1}{2} \text{ and } \begin{cases} \omega^* = 0 \\ \dfrac{du^*}{dz^*} = 0 \end{cases} \text{ at } z^* = 0. \tag{5.37}$$

The four coefficients shown in Eqs. (5.32) and (5.33) for $0 \le z^* \le 1/2$ can be solved by applying Eq. (5.36) to Eqs. (5.32) and (5.33); they are

$$\Pi_1^{UP} = 0, \tag{5.38}$$

$$\Pi_3^{UP} = \frac{B_{UP}}{A_{UP}^2}, \tag{5.39}$$

$$\Pi_2^{UP} = \frac{1}{8A_{UP}^3\delta^*\eta_e^2(\eta_e - \beta\zeta)\eta'} \times$$
$$\left\{ h\tau_{MW}\left[4\zeta\left(4h(\beta\zeta - \eta_e)\left(h\Gamma\zeta + E_0^2 n\alpha_y\eta_e\right) + A_{UP}^2\beta\Gamma\eta_e\eta'\right)\coth\left(\frac{A_{UP}}{2}\right) + \right.\right. \tag{5.40}$$
$$\left.\left. (\eta_e - \beta\zeta)\left(4A_{UP}h\zeta\left(h\Gamma\zeta + 2E_0^2 n\alpha_y\eta_e\right) + A_{UP}^3\Gamma\eta_e\eta' + 16E_0^2 hn\alpha_y\zeta\eta_e \operatorname{csch}\left(\frac{A_{UP}}{2}\right)\right)\right]\right\}$$

and

$$\Pi_4^{UP} = \frac{1}{4A_{UP}^2\eta_e(\eta_e - \beta\zeta)\eta'}\left\{ h\tau_{MW}\left[4h(\beta\zeta - \eta_e)\left(h\Gamma\zeta + E_0^2 n\alpha_y\eta_e\right) + A_{UP}^2\beta\Gamma\eta_e\eta' \right.\right.$$
$$\left.\left. + 4E_0^2 hn\alpha_y\eta_e(\eta_e - \beta\zeta)\cosh\left(\frac{A_{UP}}{2}\right)\right]\operatorname{csch}\left(\frac{A_{UP}}{2}\right)\right\}, \tag{5.41}$$

where "×" simply denotes multiplication instead of the vector cross product. Similarly, the four coefficients shown in Eqs. (5.34) and (5.35) for $-1/2 \le z^* \le 0$ are solved by applying the boundary conditions of Eq. (5.37) to Eqs. (5.34) and (5.35), *i.e.*,

$$\Pi_1^{DW} = 0, \tag{5.42}$$

$$\Pi_3^{DW} = \frac{B_{DW}}{A_{DW}^2}, \tag{5.43}$$

$$\Pi_2^{DW}=\frac{1}{8A_{DW}^3\delta^*\eta_e^2(\eta_e-\beta\zeta)\eta'}\times$$
$$\left\{h\tau_{MW}\left[4\zeta\left(4h(\beta\zeta-\eta_e)\left(h\Gamma\zeta-E_0^2n\alpha_y\eta_e\right)+A_{DW}^2\beta\Gamma\eta_e\eta'\right)\coth\left(\frac{A_{DW}}{2}\right)-\right.\right. \quad , \quad (5.44)$$
$$\left.\left.(\eta_e-\beta\zeta)\left(4A_{DW}h\zeta\left(2E_0^2n\alpha_y\eta_e-h\Gamma\zeta\right)-A_{DW}^3\Gamma\eta_e\eta'+16E_0^2hn\alpha_y\zeta\eta_e\operatorname{csch}\left(\frac{A_{DW}}{2}\right)\right)\right]\right\}$$

and

$$\Pi_4^{DW}=\frac{1}{4A_{DW}^2\eta_e(\eta_e-\beta\zeta)\eta'}\left\{h\tau_{MW}\left[4h(\beta\zeta-\eta_e)\left(h\Gamma\zeta-E_0^2n\alpha_y\eta_e\right)+A_{DW}^2\beta\Gamma\eta_e\eta'\right.\right.$$
$$\left.\left.-4E_0^2hn\alpha_y\eta_e(\eta_e-\beta\zeta)\cosh\left(\frac{A_{DW}}{2}\right)\right]\operatorname{csch}\left(\frac{A_{DW}}{2}\right)\right\}, \quad (5.45)$$

where again "×" simply denotes multiplication instead of the vector cross product.

The 2D Poiseuille volume flow rate, Q, is next calculated by evaluating the following integration, namely,

$$Q=\int_{-h/2}^{h/2}u_y(z)dz=V_0h\int_{-1/2}^{1/2}u^*(z^*)dz^*=V_0h\left(\int_0^{1/2}u_{UP}^*(z^*)dz^*+\int_{-1/2}^{0}u_{DW}^*(z^*)dz^*\right). \quad (5.46)$$

Substituting u_{UP}^*, Eq. (5.33), and u_{DW}^*, Eq. (5.35), along with their corresponding coefficients, Eq. (5.46) is explicitly written as

$$\frac{Q}{V_0h}=\frac{1}{8}\left(\frac{\Pi_1^{UP}\tau_{MW}}{\eta_e\delta^*}+\frac{2\zeta}{\eta_e\delta^*}\frac{B_{UP}}{A_{UP}^2}\right)-\frac{1}{48}\left(\frac{\Gamma h\tau_{MW}}{\eta_e\delta^*}+\frac{2\zeta}{\eta_e\delta^*}\frac{\Lambda}{A_{UP}^2}\right)$$
$$-\frac{2\zeta}{\eta_e\delta^*}\frac{\Pi_3^{UP}}{A_{UP}^2}\left[\cosh\left(\frac{A_{UP}}{2}\right)-1\right]-\frac{2\zeta}{\eta_e\delta^*}\frac{\Pi_4^{UP}}{A_{UP}^2}\sinh\left(\frac{A_{UP}}{2}\right)+\frac{\Pi_2^{UP}}{2}$$
$$-\frac{1}{8}\left(\frac{\Pi_1^{DW}\tau_{MW}}{\eta_e\delta^*}+\frac{2\zeta}{\eta_e\delta^*}\frac{B_{DW}}{A_{DW}^2}\right)-\frac{1}{48}\left(\frac{\Gamma h\tau_{MW}}{\eta_e\delta^*}+\frac{2\zeta}{\eta_e\delta^*}\frac{\Lambda}{A_{DW}^2}\right) \quad . \quad (5.47)$$
$$-\frac{2\zeta}{\eta_e\delta^*}\frac{\Pi_3^{DW}}{A_{DW}^2}\left[1-\cosh\left(-\frac{A_{DW}}{2}\right)\right]+\frac{2\zeta}{\eta_e\delta^*}\frac{\Pi_4^{DW}}{A_{DW}^2}\sinh\left(-\frac{A_{DW}}{2}\right)+\frac{\Pi_2^{DW}}{2}$$

Note that for the present 2D Poiseuille geometry shown in Fig. 5.8 and the spatial coordinates defined in both Figs. 2.1 and 5.8, the macroscopically "imposed" flow vorticity is in the positive x-direction or counter clockwise direction pointing out of the plane for the upper half of the channel, $0\le z^*\le 1/2$, and the imposed vorticity is in the negative x-direction or clockwise direction pointing into the plane for the lower half of the channel, $-1/2\le z^*\le 0$. Therefore, in

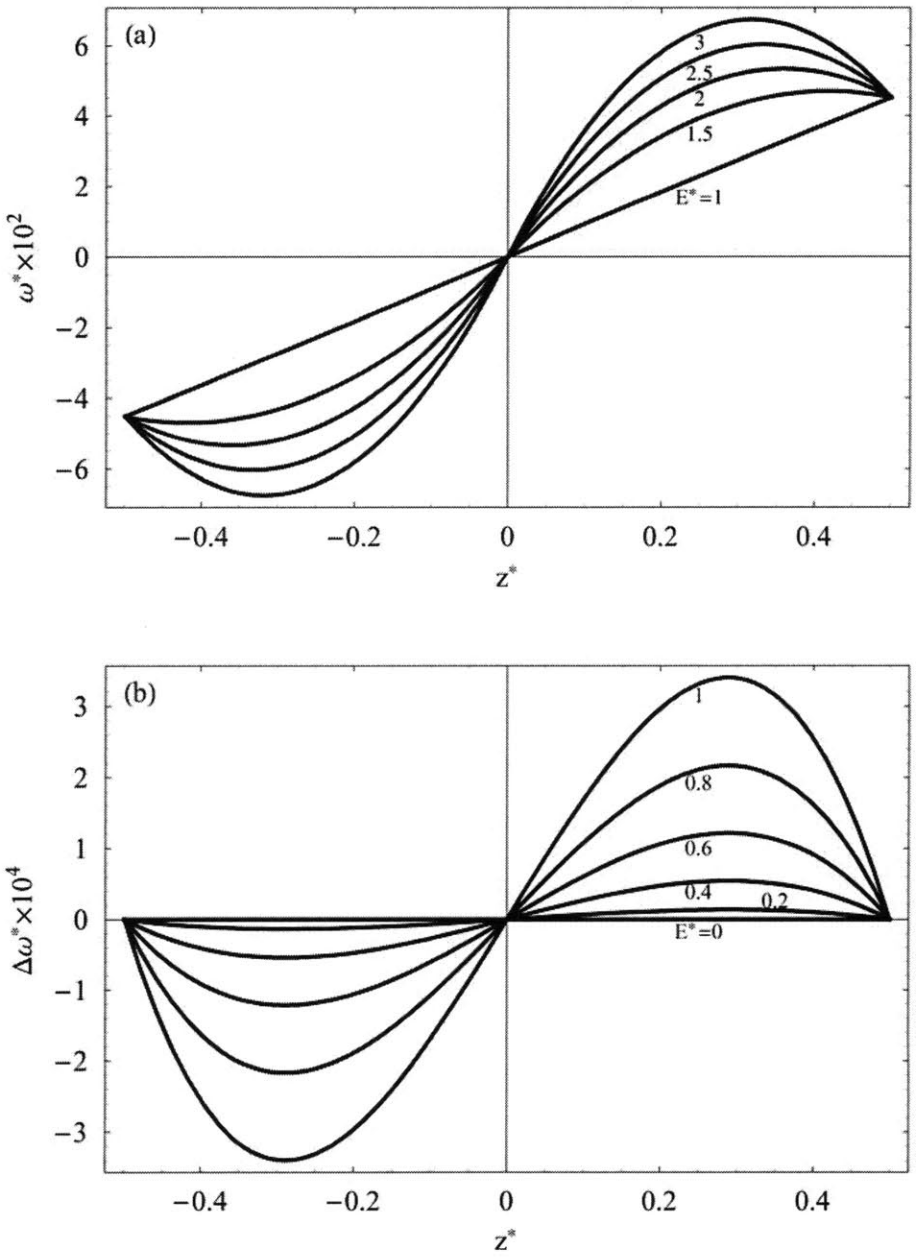

Figure. 5.9. (a) Spatial variations of the total spin velocity profile evaluated at $E^* = 1$, 1.5, 2, 2.5, and 3 with $\beta = 1$, $\eta_p^* = 1$, and $\Gamma^* = 0.125$ (or $\Gamma = 2500$ (Pa/m)) kept constant. (b) Spatial variations of the differences in total spin velocity, $\Delta\omega^*$ as defined in Eq. (5.49), evaluated at $E^* = 0$, 0.2, 0.4, 0.6, 0.8, and 1 with $\beta = 1$, $\eta_p^* = 1$, and $\Gamma^* = 0.125$ (or $\Gamma = 2500$ (Pa/m)) kept constant.

order to satisfy the stable micro-particle rotation requirement as discussed previously, we employ a positively valued micro-particle rotation speed, *i.e.*, choose $\Omega > 0$ solution from Eq. (2.57) or

(5.19), in the polarizabilities of α_y and α_z (given by Eq. (4.7)) found in A_{UP}, B_{UP}, Π_2^{UP}, Π_3^{UP}, Π_4^{UP}, ω_{UP}^*, u_{UP}^*, and Q (*i.e.*, Eqs. (5.26), (5.27), (5.40), (5.39), (5.41), (5.32), (5.33), and (5.47), respectively), and employ a negatively valued micro-particle rotation speed, *i.e.*, choose $\Omega < 0$ solution from Eq. (2.57) or (5.19), in the polarizabilities of α_y and α_z (given by Eq. (4.7)) found in A_{DW}, B_{DW}, Π_2^{DW}, Π_3^{DW}, Π_4^{DW}, ω_{DW}^*, u_{DW}^*, and Q (*i.e.*, Eqs. (5.26), (5.27), (5.44), (5.43), (5.45), (5.34), (5.35), and (5.47), respectively) for DC electric field strengths greater than the Quincke rotation critical electric field, *i.e.*, $E_0 \geq E_c$, with E_c defined in Eq. (1.1). On the other hand, for the cases of DC electric field strengths less than the critical electric field, *i.e.*, $E_0 < E_c$, we employ the $\Omega = 0$ solution from Eq. (2.57) or (5.13) in the polarizabilities of α_y and α_z found in Eqs. (5.26)-(5.27), (5.32)-(5.35), (5.39)-(5.41), (5.43)-(5.45), and (5.47) and require the physically reasonable solutions to the spin velocity fields of ω_{UP}^* (as in Eq. (5.32)) and ω_{DW}^* (as in Eq. (5.34)) to rotate in the directions consistent with those of the macroscopically imposed vorticity in the respective upper and lower halves of the flow channel. As will be seen in Section 5.4.2, the spin velocity solution automatically satisfies the above requirement of rotating in the same direction as that of the imposed vorticity when $\Omega = 0$ in Eqs. (4.7), (5.26)-(5.27), (5.32)-(5.35), (5.39)-(5.41), (5.43)-(5.45), and (5.47) for $E_0 < E_c$ conditions in the $\eta' \neq 0$, $\tau_{MW}^2 \omega_x^2 \ll 1$ limit of the continuum governing equations.

5.4.2 Modeling Results and Discussions

This section presents the parametric study on the analytical solutions to the continuum spin velocity profile, ω^* (or ω_x), the continuum linear velocity profile, u^* (or u_y), and the 2D volume flow rate, Q, as obtained in the previous section. We investigate the negative electrorheological behavior and fluid flow phenomenon due to internal micro-particle electrorotation in the 2D Poiseuille geometry defined in Fig. 5.8 by successively varying (while the other variables are kept constant) the applied DC electric field strength, E_0, the Poiseuille driving pressure gradient, Γ, the boundary condition selection parameter, β, and the spin viscosity, η', so that changes and variations in the flow patterns or responses (with respect to the

pertinent parameters) can be illustrated and compared systematically for the limit of $\eta' \neq 0$ and $\tau_{MW}^2 \omega_x^2 \ll 1$.

To facilitate the presentation of our results and discussion, some of the above mentioned physical parameters or variables are non-dimensionalized by the following scheme:

$$z^* = \frac{z}{h},\ u^* = \frac{u_y}{V_0},\ \omega^* = \tau_{MW}\omega_x,\ E^* = \frac{E_0}{E_c},\ \Gamma^* = \frac{\Gamma}{\Gamma_r},\ \eta^* = \frac{\eta_{eff}}{\eta},\ \text{and}\ \eta_p^* = \frac{\eta'}{\eta'_0}, \tag{5.48}$$

where V_0 is defined in Eq. (5.29), E_c is defined in Eq. (1.1), $\Gamma_r = 2\times10^4$ (Pa/m), η is the zero electric field ER fluid viscosity given by $\eta \approx \eta_0(1+2.5\phi)$, and $\eta'_0 = 1.53\times10^{-8}$ $(N\cdot s)$. Again, the choice of the numerical value for η'_0 follows the physical argument presented in Section 4.4.2, or Eq. (4.47), by using the channel height of the 2D Poiseuille flow channel, h, as the characteristic diffusion length for steady state fully developed internal flows under the continuum mechanical framework. Numerical values for the material properties, physical constants, and system dimensions used in our numerical evaluations of the analytical solutions are generally summarized in Table 4.1 unless otherwise specified. The parametric regimes employed in our results and discussions are chosen so that the criteria of $\tau_{MW}^2 \omega_x^2 \ll 1$ is generally satisfied.

Figure 5.9(a) presents the spatial variations of the total spin velocity profiles, ω^*, evaluated at distinct electric field strengths of $E^* = 1$, 1.5, 2, 2.5, and 3 with $\beta = 1$, $\eta_p^* = 1$, and $\Gamma = 2500$ (Pa/m) (or $\Gamma^* = 0.125$). From the figure, it can be learned that as the applied electric field strength is increased, the magnitude or strength of the spin velocity is increased, and that as the DC field is decreased, the magnitude of the spin velocity is reduced. Moreover, it can also be found that the total spin velocity in the upper half of the flow channel, $0 \le z^* \le 1/2$, is positively valued (or rotating in the counter clockwise direction) and that the spin velocity in the lower half of the channel, $-1/2 \le z^* \le 0$, is negatively valued (or rotating in the clockwise direction), which is a result consistent with the direction of rotation of the macroscopically imposed Poiseuille flow vorticity. On the other hand, the spatial variations of the differences in the total spin velocity profiles, *i.e.*,

$\Delta\omega^*\left(z^*, E^*, \Gamma^* = 0.125, \beta = 1, \eta_p^* = 1\right) \equiv$

$$\omega^*\left(z^*, E^*, \Gamma^* = 0.125, \beta = 1, \eta_p^* = 1\right) - \omega^*\left(z^*, E^* = 0, \Gamma^* = 0.125, \beta = 1, \eta_p^* = 1\right), \qquad (5.49)$$

are evaluated at $E^* = 0$, 0.2, 0.4, 0.6, 0.8, and 1, with $\beta = 1$, $\eta_p^* = 1$, and $\Gamma = 2500$ (Pa/m) (or $\Gamma^* = 0.125$) as shown in Fig. 5.9(b). Note that the micro-particle rotation speed, Ω, found in the expressions of the polarizabilities of α_y and α_z (as in Eq. (4.7)) and subsequently in those of the A, B, and Π_i parameters equals to zero when $E^* = 1$ and thus is equivalent to letting $\Omega = 0$ for $E^* < 1$ conditions as described in Eq. (5.13). Similar to Fig. 5.9(a), the magnitude of the differences in the total spin velocity profiles found in Fig. 5.9(b), $\Delta\omega^*$, increases as the applied electric field is increased and decreases as the DC electric field strength is gradually reduced to zero. In other words, as compared to the zero electric field spin velocity profile (which is generally the zero electric field pure viscous Poiseuille flow vorticity), the magnitude or strength of the total spin velocity increases as the applied electric field strength is increased, and the magnitude of ω^* is decreased as the applied DC electric field strength is reduced in the parametric regime of $E^* < 1$. In addition, since $\Delta\omega^*$ is positively valued in the upper half of the channel and negatively valued in the lower half as compared to the zero electric field spin velocity, we can also verify that in the parametric regime of $E^* < 1$, the total spin velocity, ω^*, is automatically rotating in the direction of the macroscopically imposed Poiseuille flow vorticity without in advance assigning the proper micro-particle rotation directions as given in Eq. (5.19) for the respective spatial regions of the upper and lower halves of the flow channel. Due to the fact that half of the ER fluid rotates in one direction and the rest of the ER fluid rotates in the other in our parallel plate channel, counter rotation of the ER fluids occurs in the midway of the geometry, which consequently implies that the linear flow velocity in the middle of the channel is likely to be accelerated. We shall come back and re-examine this physical picture later when we evaluate the linear velocity profiles of this negative ER fluid flow.

Illustrated in Figs. 5.10(a) and 5.10(b) are the spatial variations of the total spin velocity profiles, ω^*, plotted for the respective electric field regimes of $E^* = 2 > 1$ and $E^* = 0.6 < 1$. For both figures, the total spin velocity profiles are evaluated at $\Gamma = 1500$, 2000, 2500, 3000, and 3500 (Pa/m) (corresponding to $\Gamma^* = 0.075$, 0.1, 0.125, 0.15, and 0.175, respectively) while $\beta = 1$, $\eta_p^* = 1$, and the respective DC electric field strengths are maintained constant. It can be found from the two figures that the magnitude of the total spin velocity profiles increases (or

decreases) as the driving Poiseuille pressure gradient increases (or decreases), and that the direction of rotation for the spin velocities are again consistent with that of the macroscopically imposed Poiseuille vorticity. The order of magnitudes of the spin velocity profiles shown in Figs. 5.10(a) and 5.10(b) are roughly the same in spite of the respective different electric field strength regimes of interest. However, the total spin velocity profiles for $E^* = 2 > 1$ are more wiggled or curved as compared to those for the regime of $E^* = 0.6 < 1$. The results shown in these two figures simply imply the fact that the larger the mechanical driving pressure force the greater the resulting flow response observed. We can further normalize the total spin velocity, $\omega^* = \tau_{MW}\omega_x$, with the parameter of $\Gamma h\tau_{MW}/2\eta$ such that

$$\widetilde{\omega}^* = \frac{2\eta\omega^*}{\Gamma h\tau_{MW}}, \tag{5.50}$$

and that the normalized spin velocity profile at zero electric field strengths, *i.e.*, half the vorticity of the ER fluid flow when $E^* = 0$, becomes independent of the Poiseuille driving pressure gradient, namely,

$$\widetilde{\omega}_0^* = \frac{\tau_{MW}\left(\Gamma h/2\eta\right)z^*}{\Gamma h\tau_{MW}/2\eta} = z^*, \tag{5.51}$$

which is based on the zero electric field Poiseuille flow vorticity solution derived from the coordinate system defined in Fig. 5.8. The spatial variations of the normalized spin velocity solutions, $\widetilde{\omega}^*$, evaluated at $\Gamma = 1500$, 2000, 2500, 3000, and 3500 (Pa/m) (corresponding to $\Gamma^* = 0.075$, 0.1, 0.125, 0.15, and 0.175, respectively) with $E^* = 2 > 1$, $\beta = 1$, and $\eta_p^* = 1$ kept constant are given in Fig. 5.10(c). It can be learned from Fig. 5.10(c) that for electric field strengths greater than the critical electric field, the normalized spin velocity profile, $\widetilde{\omega}^*$, gradually approaches the zero electric field solution, $\widetilde{\omega}_0^* = z^*$ (or Eq. (5.51)), noted by the gray line in the figure, as the applied Poiseuille driving pressure gradient is increased. This result again implies that as the applied pressure gradient becomes large, the mechanical (viscous and pressure) driving force dominates over the electrical body torque input such that the normalized spin velocity solution becomes closer to the value found at zero electric field strengths, *i.e.*, the solution found only when viscous force is present, as we have already discussed in Chapter 4 and in Section 5.2. This agreement between the solutions presented in Fig. 5.10(c) and the physical

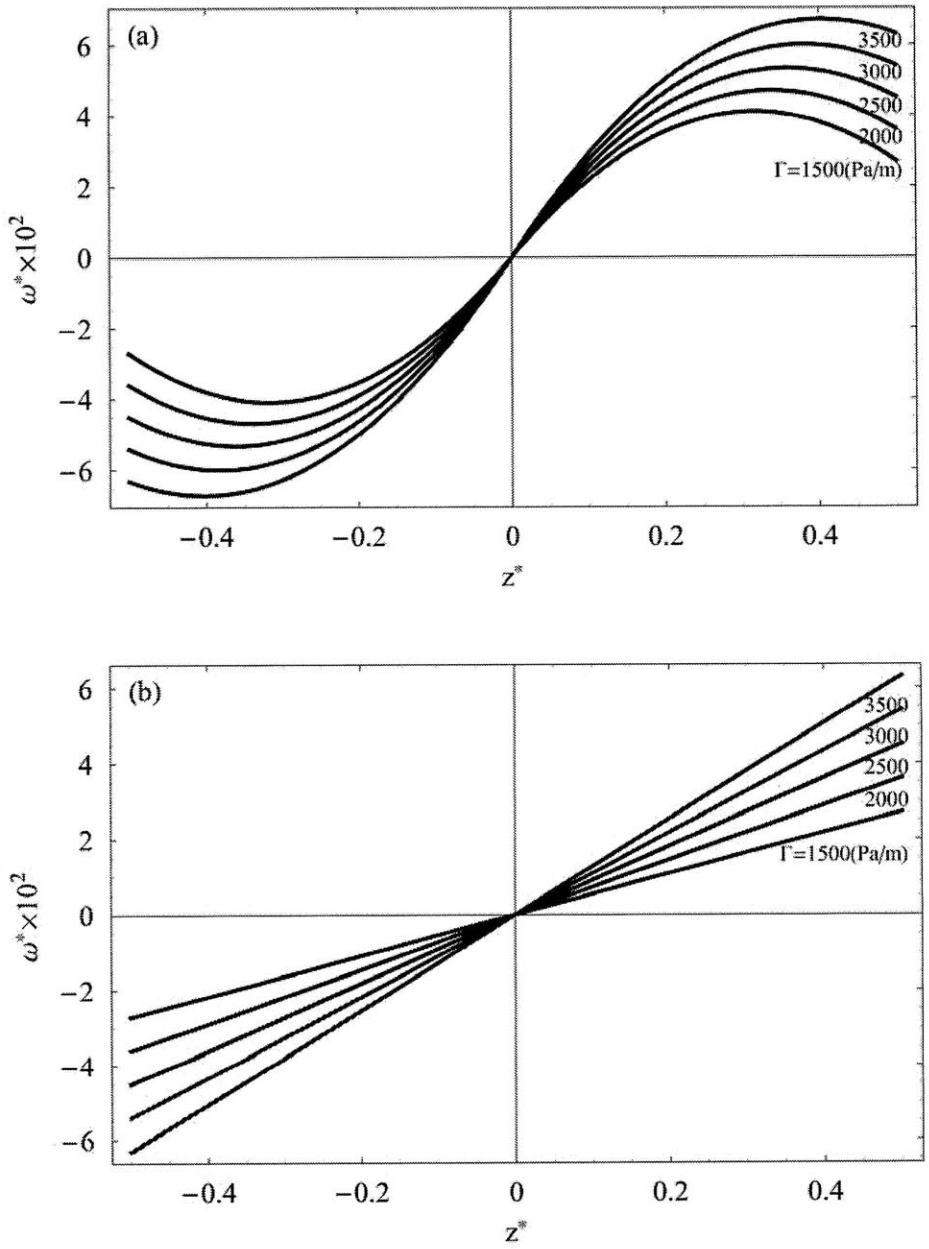

Figure 5.10. (a) and (b) show the spatial variations of the total spin velocity, ω^*, evaluated at $\Gamma = 1500$, 2000, 2500, 3000, and 3500 (Pa/m) (or $\Gamma^* = 0.075$, 0.1, 0.125, 0.15, and 0.175, respectively) while $\beta = 1$, $\eta_p^* = 1$ and the respective electric field strengths of $E^* = 2$ (Fig. 5.10(a)) and $E^* = 0.6$ (Fig. 5.10(b)) are maintained constant. (c) Spatial variations of the normalized spin velocity, $\widetilde{\omega^*}$ as defined in Eq. (5.50), evaluated at $\Gamma = 1500$, 2000, 2500, 3000, and 3500 (Pa/m) while $\beta = 1$, $\eta_p^* = 1$ and $E^* = 2$ are kept constant. (Cont.)

picture described previously also suggests that the spin velocity field solutions we have obtained for the Poiseuille geometry are generally correct. Meanwhile, we show in Fig. 5.10(d) the spatial

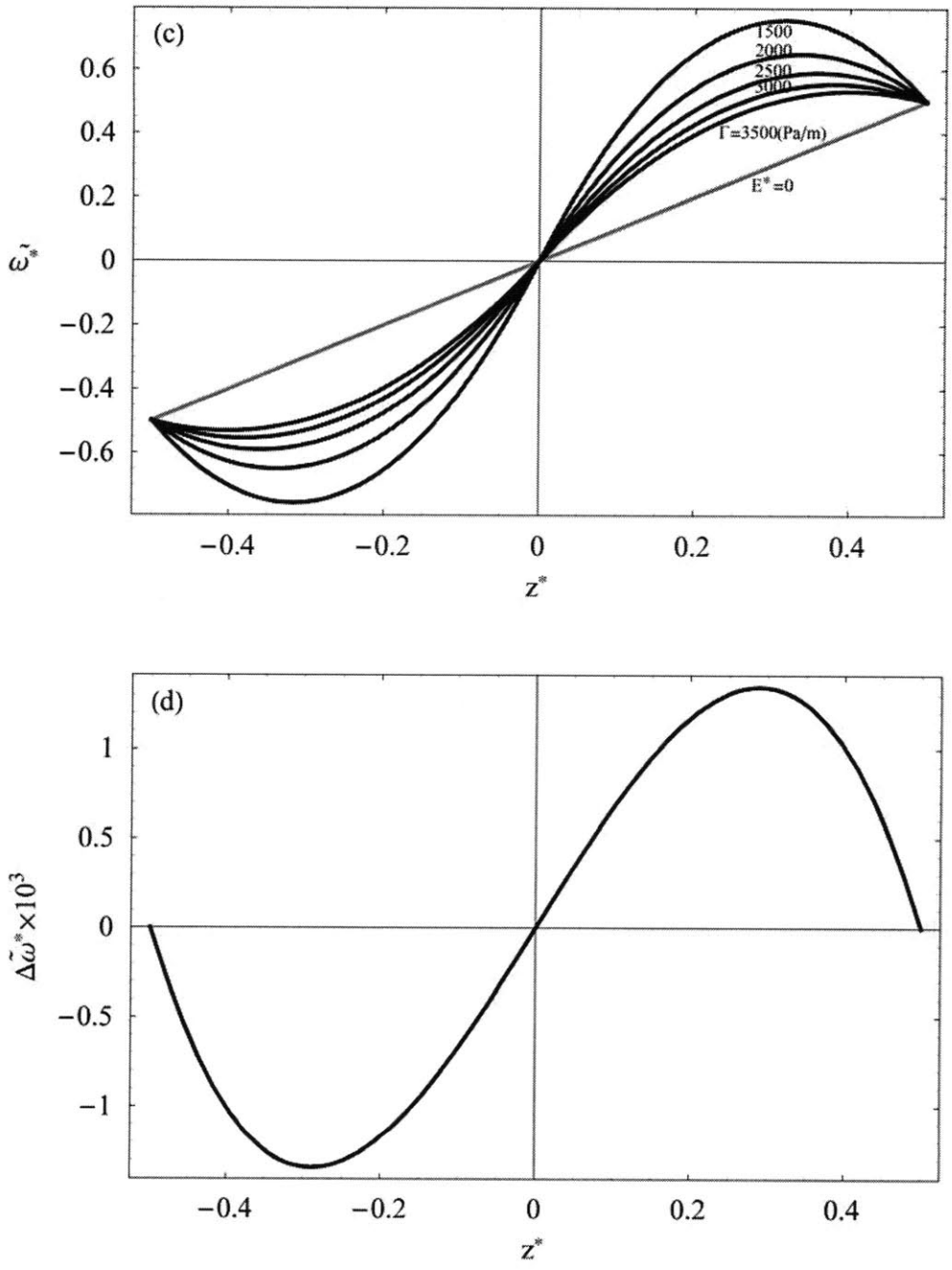

Figure 5.10. (Cont.) The solid gray line in Fig. 5.10(c) denotes the zero electric field solution of $\widetilde{\omega_0^*} = z^*$ as given in Eq. (5.51). (d) The spatial variations of the differences in the normalized spin velocity, $\Delta\widetilde{\omega^*}$ as defined in Eq. (5.52), evaluated at $\Gamma = 1500$, 2000, 2500, 3000, and 3500 (Pa/m) while $\beta = 1$, $\eta_p^* = 1$ and $E^* = 0.6$ are kept constant. Note that all five profiles have merged into one curve at this electric field strength of interest.

variations of the differences between the normalized spin velocity, $\widetilde{\omega^*}$, and the zero electric field

solution, $\widetilde{\omega}_0^* = z^*$, *i.e.*,

$$\Delta\widetilde{\omega}^*\left(z^*, E^* = 0.6, \Gamma^*, \beta = 1, \eta_p^* = 1\right) = \widetilde{\omega}^*\left(z^*, E^* = 0.6, \Gamma^*, \beta = 1, \eta_p^* = 1\right) - \widetilde{\omega}_0^* = \widetilde{\omega}^*\left(z^*, E^* = 0.6, \Gamma^*, \beta = 1, \eta_p^* = 1\right) - z^*, \tag{5.52}$$

evaluated at $\Gamma = 1500$, 2000, 2500, 3000, and 3500 (Pa/m) (or $\Gamma^* = 0.075$, 0.1, 0.125, 0.15, and 0.175, respectively) while $E^* = 0.6 < 1$, $\beta = 1$, and $\eta_p^* = 1$ are maintained constant. Note that as compared to the results shown in Fig. 5.10(c), the $\Delta\widetilde{\omega}^*$ solutions given in Fig. 5.10(d) for $E^* = 0.6 < 1$ are independent of the applied driving pressure gradient and do not approach to zero as the pressure gradient is increased. These $\Delta\widetilde{\omega}^*$ profiles given by Eq. (5.52) have collapsed into one curve with the numerical values of the differences among the $\Delta\widetilde{\omega}^*$ profiles evaluated at their respective pressure gradients being within $O\left(10^{-17}\right)$. Alternatively speaking, the normalized spin velocity profiles, $\widetilde{\omega}^*$, evaluated at the electric field regime of $E^* = 0.6 < 1$ do not depend upon the applied driving pressure gradient and do not approach to the zero electric field solution of $\widetilde{\omega}_0^* = z^*$ (or Eq. (5.51)) when we gradually increase the driving pressure gradient. The discrepancy between the results found in Fig. 5.10(d) and those given in Fig. 5.10(c) is basically due to the different form of the polarizability (α_y and α_z with the micro-particle rotation speed being set to zero) used in the calculations for the $E^* = 0.6 < 1$ case as compared to the calculated results obtained for Fig. 5.10(c), and does not necessarily suggest that the solutions given in Fig. 5.10(d) is incorrect. By comparing Figs. 5.10(c) and 5.10(d) as well as reviewing Figs. 4.5(c) and 4.5(d), we again note that there is a difference in the flow field responses when we employ different forms of polarizabilities (α_y and α_z) in regard of the different regimes of the applied electric field strengths—the model of the polarizabilities (α_y and α_z) and subsequently the equilibrium retarding polarization, Eqs. (3.32) and (3.33), employed in the polarization relaxation equation, Eq. (3.35), may generally have influence on the final negative electrorheological response of the nER2 fluid flows.

Next, we examine the spatial variations of the total spin velocity profile, ω^*, with respect to distinct values of the boundary condition selection parameter, β, in Figs. 5.11(a) and 5.11(b) for

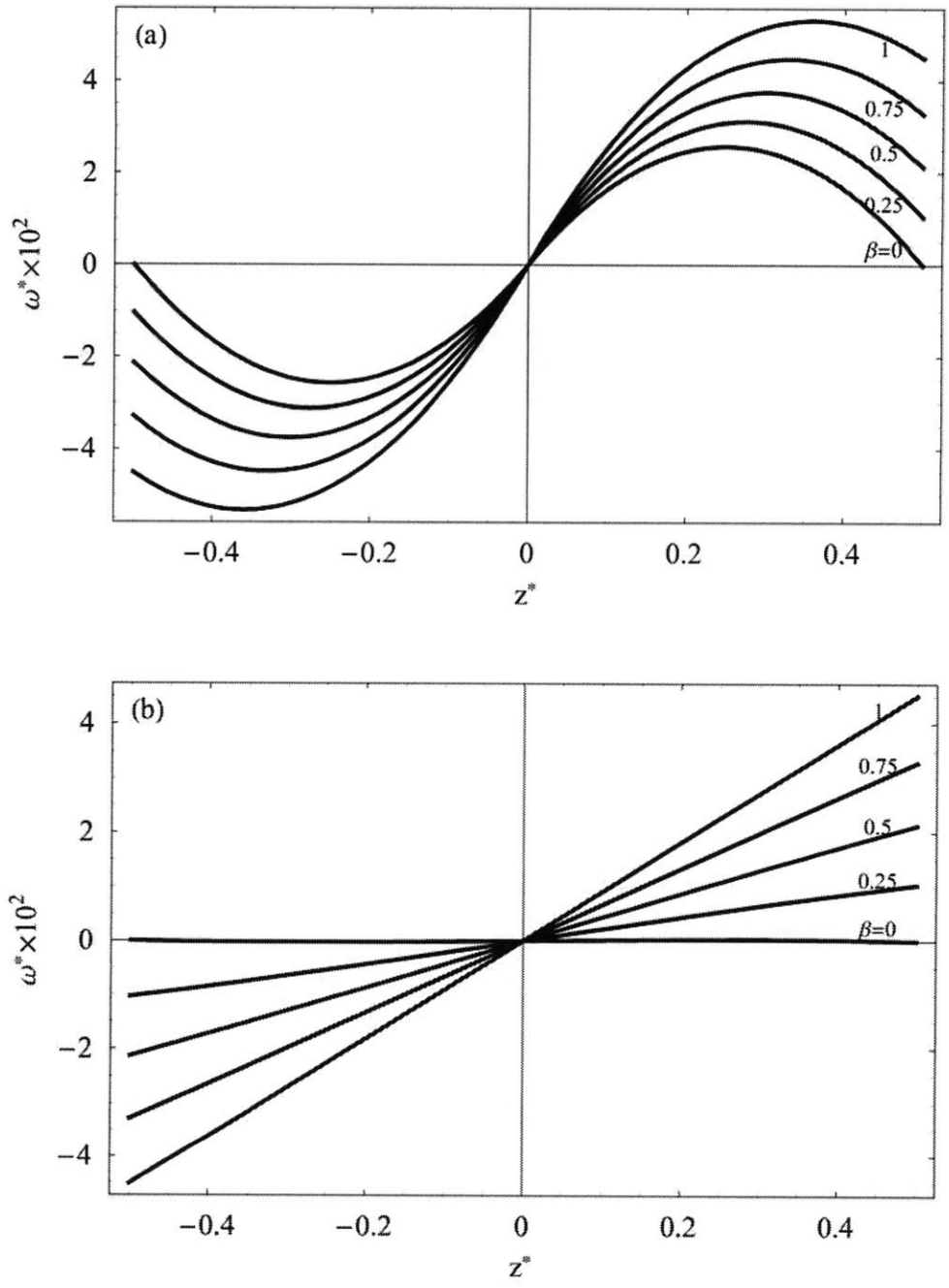

Figure 5.11. The spatial variations of the total spin velocity evaluated at $\beta = 0$, 0.25, 0.5, 0.75, and 1 while $\Gamma^* = 0.125$, $\eta_p^* = 1$, and the electric field strengths of $E^* = 2$ for Fig. 5.11(a) and $E^* = 0.6$ for Fig. 5.11(b) are kept constant.

the DC electric field strengths of $E^* = 2 > 1$ and $E^* = 0.6 < 1$, respectively. In both figures, the spin viscosity, $\eta_p^* = 1$, the Poiseuille driving pressure gradient, $\Gamma = 2500$ (Pa/m) (or

$\Gamma^* = 0.125$), and the respective electric field strengths are maintained constant while the boundary selection parameter is varied from $\beta = 0$, 0.25, 0.5, 0.75, to 1. As can be seen from both Figs. 5.11(a) and 5.11(b), the magnitude of the total spin velocity profiles decreases as the value of β is reduced from one to zero. The directions of rotation of the spin velocity profiles shown in the two figures are also consistent with the imposed Poiseuille vorticity direction, *i.e.*, the total spin velocity being positively valued in the upper half of the flow channel, $0 \le z^* \le 1/2$, and being negatively valued in the lower half of the channel, $-1/2 \le z^* \le 0$. Note however that the strength of the total spin velocity is nearly zero as shown in Fig. 5.11(b) when $\beta = 0$ for the electric field strength of $E^* = 0.6 < 1$ suggesting that there is nearly zero spin velocity within the flow field under low electric field strengths and zero-spin boundary conditions. Additionally, the total spin velocity profiles for the electric field regime of $E^* = 2 > 1$ as shown in Fig. 5.11(a) are much more wiggled or zigzag-shaped as compared to the linear profiles shown in Fig. 5.11(b) for the DC field strength of $E^* = 0.6 < 1$. These results as illustrated in the two plots of Fig. 5.11 suggest that varying the boundary condition selection parameter, β, gives rise to different responses in the total spin velocity field, ω^*, when different polarizabilities (α_y and α_z as in Eq. (4.7)) are employed within the equilibrium polarization (Eq. (3.33)) for the respective (different) regimes of electric field strengths of interest. Consequently, the negative electrorheological responses of the nER2 effect are also dependent on the boundary condition selection parameter, β, and the different polarizabilities utilized for the different regimes of electric field strengths applied since the linear velocity field, u^*, and the 2D Poiseuille volume flow rate, Q, both depend on the solutions of the total spin velocity field, ω^*.

Figure 5.12(a) presents the spatial variations of the dimensionless total spin velocity profiles, ω^*, evaluated at $\eta_p^* = 0.5$, 0.65, 1, 2, and 10 while $E^* = 2 > 1$, $\beta = 1$, and $\Gamma^* = 0.125$ (or $\Gamma = 2500$ (Pa/m)) are kept constant. From the figure, it can be seen that the spin velocity profiles in the upper half of the flow channel, $0 \le z^* \le 1/2$, are positively valued (rotating counter clockwise) and that the profiles in the lower half of the channel, $-1/2 \le z^* \le 0$, are negatively valued (rotating clockwise), which is a result consistent with the direction of rotation of the macroscopically imposed Poiseuille vorticity. The magnitude of the spin velocity profiles, ω^* or

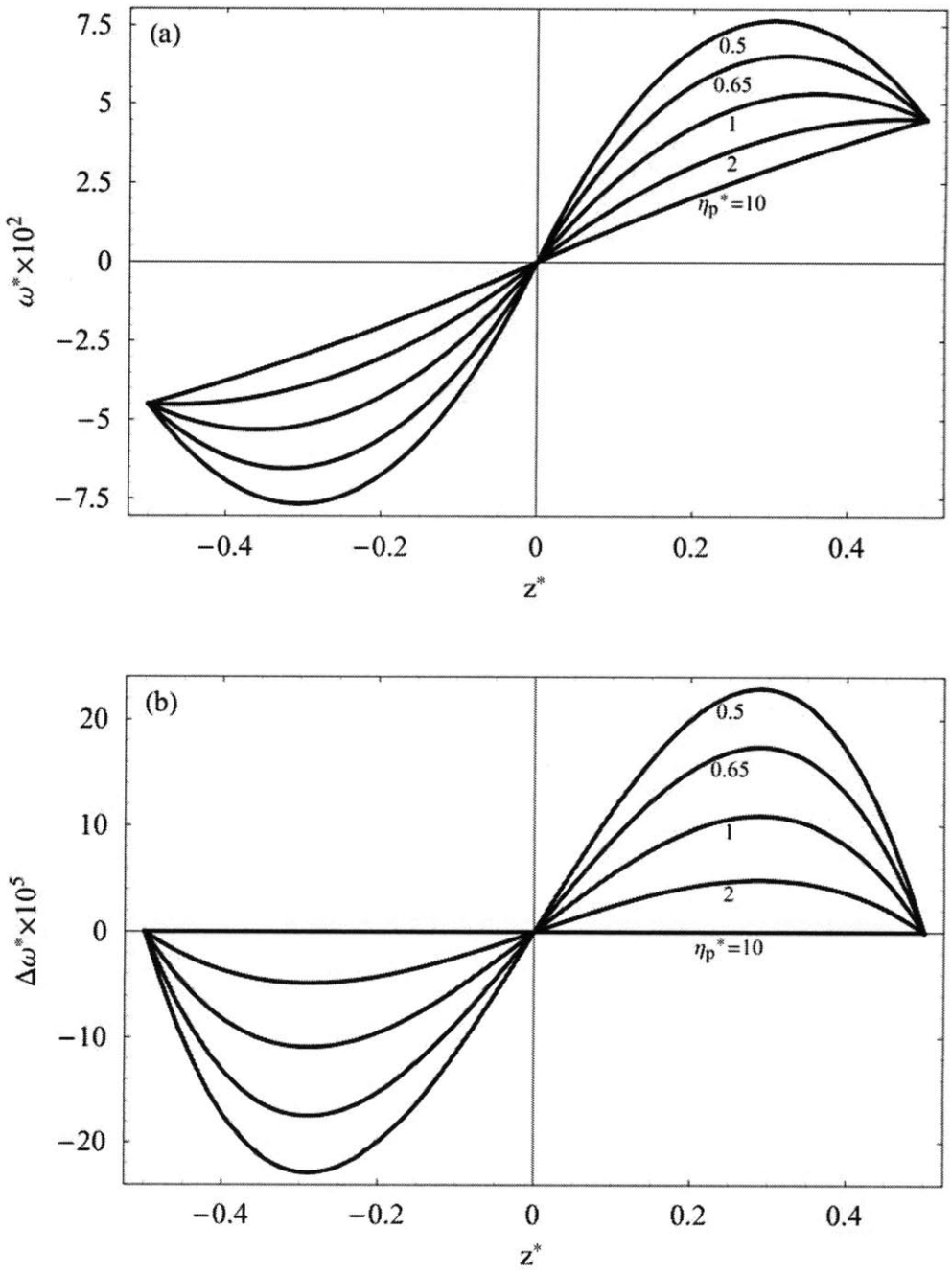

Figure 5.12. (a) Spatial variations of the total spin velocity evaluated at $\eta_p^* = 0.5$, 0.65, 1, 2, and 10 with $E^* = 2$, $\beta = 1$, and $\Gamma^* = 0.125$ kept constant. (b) Spatial variations of the differences in the total spin velocity, $\Delta\omega^*$ as defined in Eq. (5.53), evaluated at $\eta_p^* = 0.5$, 0.65, 1, 2, and 10 with $E^* = 0.6$, $\beta = 1$, and $\Gamma^* = 0.125$ kept constant.

ω_x, increases as we reduce the magnitude or value of the spin viscosity, η_p^* or η'. Alternatively,

increasing the value of the spin viscosity, η_p^*, reduces the magnitude of the spin velocity and flattens or smoothes out the spin velocity profiles as well. Once again, this result agrees with the mathematical nature of the diffusive term, $\partial^2/\partial z^2$ or d^2/dz^2, presented in the governing equation, Eq. (4.27), of the spin velocity field, *i.e.*, the presence of a diffusive term in the governing equation tends to smooth out the concentrated values, or singularities, in our calculation domain. Therefore, the larger the spin viscosity, the stronger the diffusive transport of the ER fluid angular momentum (from the electrical body torque), and the total spin velocity profile, ω^*, becomes smoother or flatter with a smaller magnitude regardless of the electric field strengths of interest. Contrarily, the smaller the spin viscosity, the weaker the diffusive transport of the angular momentum introduced by the external electric field through the electrical body torque of the ER fluid, and the total spin velocity is then more concentrated or enlarged. Note however that there is a limitation to the reduction of the spin viscosity in our present model since as η' is gradually reduced, the spin velocity becomes large enough that it violates the $\tau_{MW}^2\omega^2 \ll 1$ criteria. Thus, our discussions are limited to the parametric range of η_p^*=0.5~10. With the other pertinent parameters kept constant, the spin velocity profile, ω^*, show in Fig. 5.12(a) also gradually approaches the zero electric field solution of $\omega_0^* = \Gamma h \tau_{MW} z^*/2\eta$ as the spin viscosity is increased from $\eta_p^* = 0.5$ to 10. The zero electric field solution, $\omega_0^* = \Gamma h \tau_{MW} z^*/2\eta$, is not further shown in Fig. 5.12(a) since it falls very close to the spin velocity profile evaluated at $\eta_p^* = 10$. As for the electric field strength of $E^* = 0.6 < 1$, the spatial variations of the differences in the total spin velocity field defined by

$$\Delta\omega^*\left(z^*, E^* = 0.6, \Gamma^* = 0.125, \beta = 1, \eta_p^*\right) = \omega^*\left(z^*, E^* = 0.6, \Gamma^* = 0.125, \beta = 1, \eta_p^*\right) - \omega^*\left(z^*, E^* = 0.6, \Gamma^* = 0.125, \beta = 1, \eta_p^* = 10\right), \quad (5.53)$$

are evaluated at $\eta_p^* = 0.5$, 0.65, 1, 2, and 10 while $E^* = 0.6$, $\beta = 1$, and $\Gamma^* = 0.125$ (or $\Gamma = 2500$ (Pa/m)) are kept constant as shown in Fig. 5.12(b). From Fig. 5.12(b), it can be learned that the magnitude of $\Delta\omega^*$ is increased as the magnitude or value of the spin viscosity, η_p^*, is reduced. Thus, as compared to the total spin velocity profile, ω^*, evaluated at $\eta_p^* = 10$, the magnitude of the total spin velocity, ω^*, gradually increases as we gradually reduce the magnitude of the spin

viscosity, η_p^*, in the governing angular momentum equation, Eq. (4.27) or in the subsequent solutions. From examining both Figs. 5.12(a) and 5.12(b), we find that the trends of variation of the magnitude of the total spin velocity profiles with respect to the spin viscosity are generally the same regardless of the electric field strength regime of interest.

Before moving on to the discussions of the linear velocity profiles, we first define a micro-particle Quincke rotation induced linear velocity, namely,

$$u_q^* = u^* - u_0^* = u^* - 6\left(0.5^2 - z^{*2}\right), \tag{5.54}$$

where u^* is the total linear velocity field and $u_0^* = 6\left(0.5^2 - z^{*2}\right)$ is the zero electric field solution (*i.e.*, pure viscous Poiseuille flow) of the total linear velocity solved with respect to the spatial coordinates defined in Fig. 5.8. Notice that an additional factor of "6" is present in the zero electric field solution of $u_0^* = 6\left(0.5^2 - z^{*2}\right)$ because of the fact that we have used V_0 as defined in Eq. (5.29) instead of $h^2\Gamma/2\eta$ as employed in Section 5.2 when non-dimensionalizing the linear velocity field, u_y. Hence, the zero electric field solution presented herein is different from that as seen in Section 5.2 due to the differences arising from both the coordinate system and the non-dimensionalization scheme. Again, since we have non-dimensionalized the linear velocity with V_0, the dimensionless linear velocity, u^*, is also normalized and no further normalization of the solutions is required in our following presentation of results.

Shown in Figs. 5.13(a) and 5.13(b) are the spatial variations of the Quincke rotation induced linear velocity profiles, u_q^*, evaluated respectively at $E^* = 1$, 1.5, 2, 2.5, and 3 (Fig. 5.13(a)) and at $E^* = 0$, 0.2, 0.4, 0.6, 0.8, and 1 (Fig. 5.13(b)) while the rest of the parameters $\beta = 1$, $\eta_p^* = 1$, and $\Gamma^* = 0.125$ (or $\Gamma = 2500$ (Pa/m)) are maintained constant. Note that we have plotted the $E^* = 1$ solution in both figures because the micro-particle rotation speed equals to zero when $E^* = 1$, and thus is equivalent to the case of setting $\Omega = 0$ in the polarizabilities or the equilibrium polarization for the electric field regime of $E^* < 1$. It can be found from both Figs. 5.13(a) and 5.13(b) that the magnitude of the induced linear velocity is enhanced as the applied DC electric field strength is increased. However, the order of magnitude of the u_q^* solutions obtained in the $E^* \geq 1$ regime, as in Fig. 5.13(a), is much greater than that of the u_q^* solutions

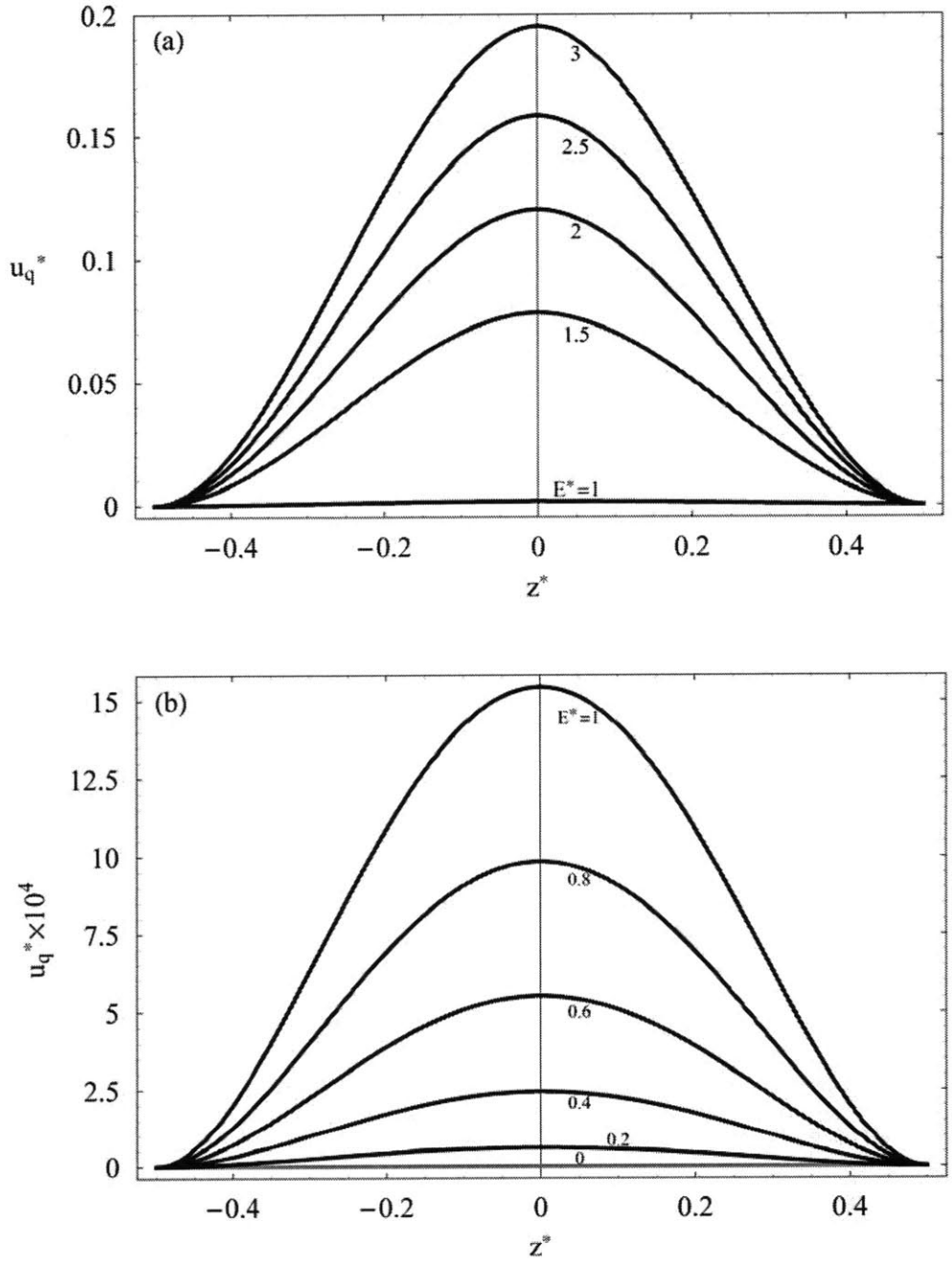

Figure 5.13. Spatial distributions of the induced velocity, u_q^*, evaluated at constant $\Gamma^* = 0.125$, $\beta = 1$, and $\eta_p^* = 1$ for electric field strengths of (a) $E^* = 1$, 1.5, 2, 2.5, and 3 and (b) $E^* = 0$, 0.2, 0.4, 0.6, 0.8, and 1. Note that the zero electric field solution of "zero induced velocity" is noted by the solid gray line shown in Fig. 5.13(b).

found for the electric field regime of $E^* < 1$, as in Fig. 5.13(b). Furthermore, if we gradually reduce the electric field strength from $E^* \geq 1$ to $E^* < 1$, and to $E^* = 0$, we find that the induced

linear velocity also decreases and eventually meets the zero electric field solution of zero induced linear velocity, *i.e.*, $u_q^* = 0$, as denoted by the solid gray line in Fig. 5.13(b). In other words, the total linear velocity profile, u^*, of the negative ER Poiseuille flow approaches the zero electric field solution, *i.e.*, pure viscous Poiseuille flow solution of $u_0^* = 6\left(0.5^2 - z^{*2}\right)$, as the applied DC electric field strength is reduced to zero whereas the total linear velocity is enhanced (based on Eq. (5.54)) as the applied DC field strength is increased. Also from examining the two sets of linear velocity profiles shown in both Figs. 5.13(a) and 5.13(b), we find that the magnitude or the strength of the induced linear velocity, u_q^*, or equivalently the total linear velocity, u^*, is the greatest in the middle of the flow channel, *i.e.*, $z^* = 0$, based on the coordinates defined in Fig. 5.8. This result is consistent with the physical picture (that we have discussed earlier) of the spin velocity rotating counter clockwise (positively valued) in the upper half of the channel and rotating clockwise (negatively valued) in the lower half of the channel such that the ER fluid near the mid-plane of the flow channel experiences counter rotation from both sides and is likely to be pushed forward or accelerated.

In Figs. 5.14(a) and 5.14(b), the spatial variations of the micro-particle Quincke rotation induced linear velocity, u_q^*, are respectively evaluated for the DC electric field regimes of $E^* = 2 > 1$ and $E^* = 0.6 < 1$. For both figures, we vary the applied Poiseuille driving pressure gradient from $\Gamma = 1500$, 2000, 2500, 3000, and to 3500 (Pa/m) (or equivalently, $\Gamma^* = 0.075$, 0.1, 0.125, 0.15, and 0.175) while keeping $\beta = 1$, $\eta_p^* = 1$, and the respective electric field strengths constant. Examining Fig. 5.14(a), it can be found that the induced linear velocity is reduced as the applied Poiseuille driving pressure gradient is increased, and u_q^* gradually approaches the zero electric field solution of zero induced linear velocity, $u_q^* = 0$, as the pressure gradient becomes very large. Alternatively speaking, the total linear velocity field, u^*, of the present negative ER Poiseuille flow gradually approaches the zero electric field solution of $u_0^* = 6\left(0.5^2 - z^{*2}\right)$, *i.e.*, total linear velocity of pure viscous Poiseuille flow, as the applied pressure gradient is increased to a very large value. This result agrees with that given in 5.10(c) for the normalized spin velocity profiles, $\widetilde{\omega}^*$, and once again verifies the physical picture of the

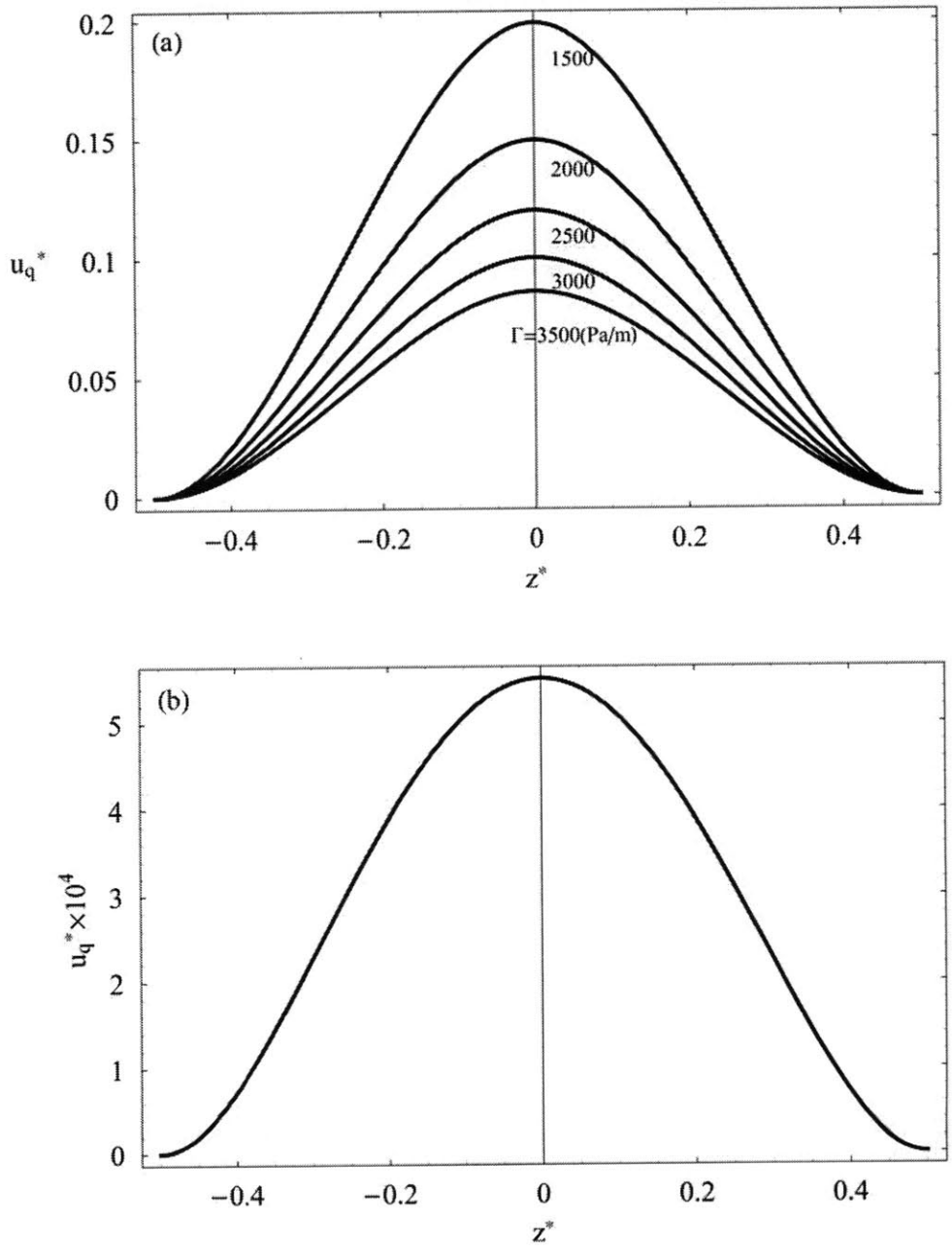

Figure 5.14. Spatial distributions of the induced linear velocity profile evaluated at $\Gamma^* = 1500, 2000, 2500, 3000,$ and 3500 (Pa/m) with constant $\beta = 1$ and $\eta_p^* = 1$ for the electric field strengths of (a) $E^* = 2$ and (b) $E^* = 0.6$. Note that all five profiles shown in Fig. 5.14(b) have collapsed into one curve for the electric field strength of $E^* = 0.6 < 1$.

mechanical (viscous and pressure) driving forces gradually dominate over the electrical body torque input as we gradually increase the pressure driving force while keeping the applied DC

electric field constant for our nER2 fluid flow. As for the electric field regime of $E^* = 0.6 < 1$, we find that all the induced linear velocity profiles, u_q^*, have collapsed or merged into one curve regardless of the magnitude of the driving pressure gradient applied to drive the Poiseuille flow, *i.e.*, the induced velocities shown in Fig. 5.14(b) are independent of the magnitude of the driving pressure gradient, Γ^*, with the differences among the induced velocities evaluated at their respective pressure gradients being within the order of magnitude of $O\left(10^{-15}\right)$. Moreover, the magnitude or strength of the single curve shown in Fig. 5.14(b) for $E^* = 0.6 < 1$ is much less than that of the induced linear velocity profiles as given in Fig. 5.14(a) for $E^* = 2 > 1$. The discrepancy found between the sets of solutions obtained under the respective DC electric field strengths, *i.e.*, $E^* = 2 > 1$ and $E^* = 0.6 < 1$, indicates that the negative electrorheological response of the ER fluid flow will general be dependent upon the forms of the polarizabilities (α_y and α_z) or the equilibrium retarding polarization models employed in the analytical solutions for the respective regimes of the DC electric field strengths applied to the flow.

We then consider the influences of different values of the boundary condition selection parameter, β, on the spatial variations of the Quincke rotation induced linear velocity profile, u_q^*, as shown in Figs. 5.15(a) and 5.15(b) for the respective DC electric field regimes of $E^* = 2 > 1$ and $E^* = 0.6 < 1$. In both plots, the boundary selection parameter, β, is varied from 0, 0.25, 0.5, 0.75, and to 1 while the spin viscosity, $\eta_p^* = 1$, the pressure gradient, $\Gamma = 2500$ (Pa/m) (or $\Gamma^* = 0.125$), and the respective electric field strengths are kept constant. It can be found from Fig. 5.15(a) that as β is reduced from 1 to 0, the induced linear velocity, u_q^*, decreases from a positively valued velocity profile to a negatively valued profile—a reversal of the induced linear velocity field is obtained for the electric field strength of $E^* = 2 > 1$. In other words, the magnitude or strength of the total linear velocity, u^*, is first enhanced (or accelerated) and then suppressed (or decelerated) as the boundary condition selection parameter, β, is reduced from 1 to 0. As for the spatial variations of the induced linear velocity profiles shown in Fig. 5.15(b), we find that the induced linear velocity profiles are generally negatively valued when β is less than one and that u_q^* evaluated at $\beta = 1$ is only slightly positively valued. Therefore, for the DC

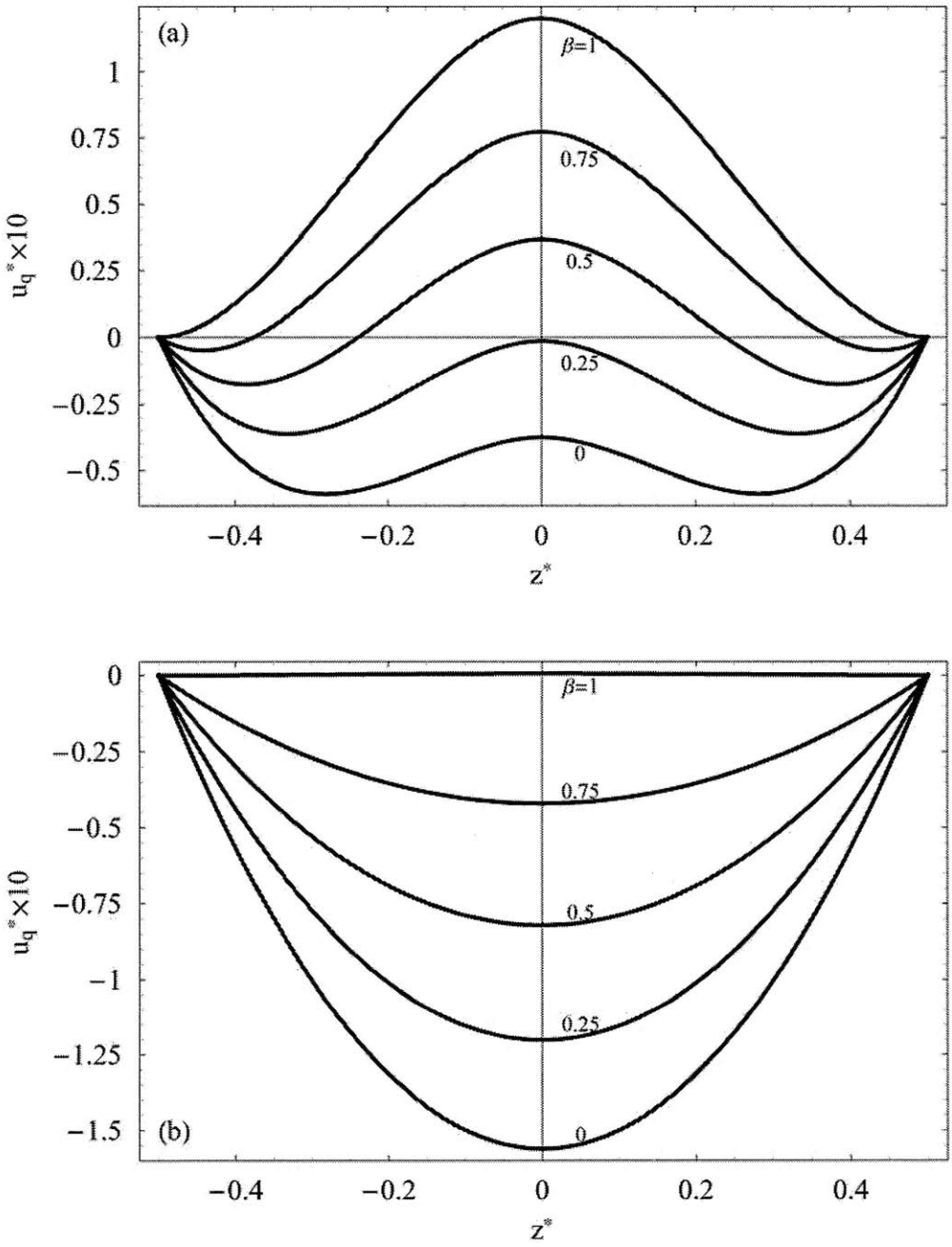

Figure 5.15. Spatial distributions of the induced linear velocity profile, u_q^*, plotted with respect to the boundary condition selection parameter of $\beta = 0$, 0.25, 0.5, 0.75, and 1 while $\eta_p^* = 1$, $\Gamma^* = 0.125$, and the respective DC electric field strengths of $E^* = 2$ in Fig. 5.15(a) and $E^* = 0.6$ in Fig. 5.15(b) are kept constant.

electric field strength of $E^* = 0.6 < 1$, it is learned that the total linear velocity, u^*, is generally

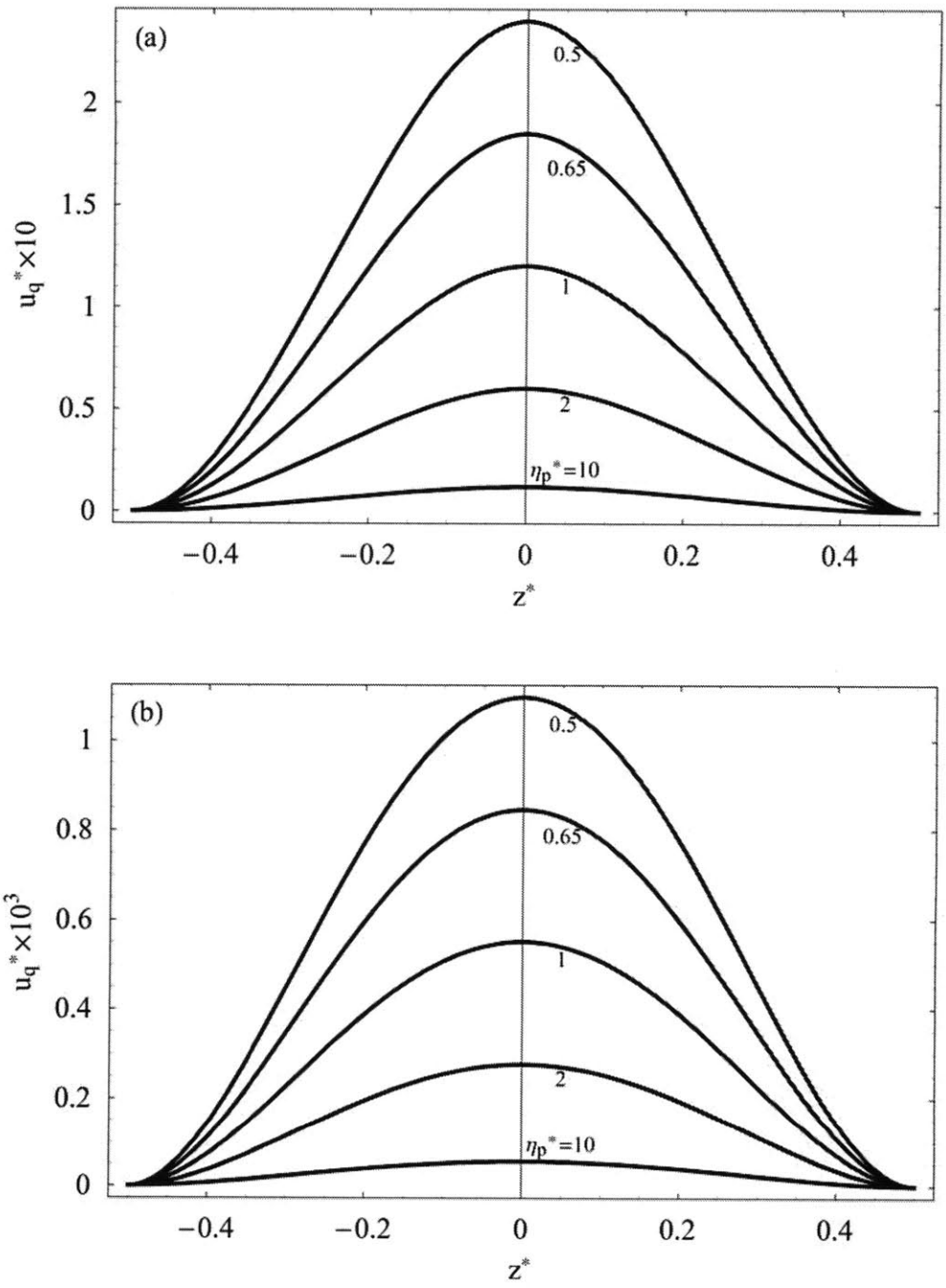

Figure 5.16. Spatial distributions of the induced linear velocity evaluated at $\eta_p^* = 0.5$, 0.65, 1, 2, and 10 with constant $\Gamma^* = 0.125$ and $\beta = 1$ for electric field strengths of (a) $E^* = 2$ and (b) $E^* = 0.6$. As can be seen from the two figures, the induced linear velocity gradually reduces to zero as the spin viscosity is increased.

decelerated (or suppressed) when the value of β is less than one, and that the reduction in the total linear velocity is increased as the value of the boundary selection parameter is decreased.

Comparing the respective results shown in Figs. 5.15(a) and 5.15(b), it can be seen that the shape of the induced linear velocity profiles obtained with the electric field strength of $E^* = 2 > 1$ are much more wiggled or zigzag fashioned than the smooth parabolic profiles obtained with $E^* = 0.6 < 1$. By further comparing the spin velocity results shown in Fig. 5.11 and the induced velocity results given in Fig. 5.15, we learn that both the magnitudes of the total spin velocity and the total linear velocity are decreased as the boundary condition selection parameter is decreased and that the ER fluid flow responses obtained by varying β in the respective regimes of electric field strengths are generally different due to the different forms of polarizabilities (α_y and α_z) employed in the governing equations and subsequently the A, B, and Π_i coefficients found in the analytical solutions for the respective electric field strengths.

Lastly, we study how the spatial variations of the Quincke rotation induced linear velocity, u_q^*, change or behave by varying the spin viscosity from $\eta_p^* = 0.5$, 0.65, 1, 2, and to 1 for the two different electric field strengths of $E^* = 2 > 1$ and $E^* = 0.6 < 1$ in Figs. 5.16(a) and 5.16(b), respectively. In both figures, $\beta = 1$, $\Gamma^* = 0.125$ (or $\Gamma = 2500$ (Pa/m)) and the respective electric field strengths are kept constant. Though the order of magnitudes of the induced velocities found in the two figures are different, the strengths of the induced linear velocities found in both Figs. 5.16(a) and 5.16(b) are increased as the value of the spin viscosity is decreased. Moreover, as we increase the value of the spin viscosity with the other parameters kept constant, we find that the magnitudes of the induced linear velocity profiles, u_q^*, are decreased and eventually approach to the zero electric field solution of zero induced linear velocity, $u_q^* = 0$, that is, the total linear velocity solutions, u^*, approach the zero electric field solution of $u_0^* = 6\left(0.5^2 - z^{*2}\right)$ for pure viscous Poiseuille flow regardless of the electric field strengths of interest as we increase the value of the spin viscosity, η_p^*. These results are consistent with those obtained from examining the total spin velocity profile as discussed previously in Figs. 5.12(a) and 5.12(b).

In order to facilitate the presentation of the 2D Poiseuille volume flow rate results, we now define a micro-particle Quincke rotation induced volume flow rate for the 2D parallel plate Poiseuille geometry shown in Fig. 5.8 as

$$Q_q \equiv Q - Q_0 = Q - \frac{\Gamma h^3}{12\eta}, \tag{5.55}$$

where Q is the total 2D Poiseuille volume flow rate given by Eq. (5.46) or (5.47) and $Q_0 = \Gamma h^3/12\eta$ is the zero electric field solution derived from purely viscous Poiseuille flows. Illustrated in Figs. 5.17(a) and 5.17(b) are the Quincke rotation induced flow rates, Q_q, plotted with respect to the applied pressure gradient, Γ^*, evaluated at $E^* = 1$, 1.5, 2, 2.5, and 3 for Fig. 5.17(a) and at $E^* = 0$, 0.2, 0.4, 0.6, 0.8, and 1 for Fig. 5.17(b). The boundary condition selection parameter, $\beta = 1$, and the spin viscosity, $\eta_p^* = 1$, are kept constants in the two figures of Fig. 5.17. The $E^* = 1$ solution is given in both figures because the micro-particle rotation speed, $\overline{\Omega}$, goes to zero as evaluated by Eq. (5.19), and thus gives the same polarizabilities or equilibrium polarization as the $E^* < 1$ solutions do by setting the micro-particle rotation speed to zero. For both Figs. 5.17(a) and 5.17(b), the induced 2D volume flow rate, Q_q, increases as the applied DC electric field strength increases while the pressure gradient is maintained constant. If contrarily, we reduce the DC electric field strength while keeping the pressure gradient constant, the induced flow rate, Q_q, decreases and eventually becomes zero, *i.e.*, zero induced flow for zero electric field conditions as noted by the solid gray line in Fig. 5.17(b). Equivalently, by keeping the driving pressure gradient constant, the total 2D volume flow rate, Q, increases (decreases) as the applied DC electric field is increased (decreased), and approaches to the zero electric field solution of $Q_0 = \Gamma h^3/12\eta$ when the applied DC electric field goes to zero. On the other hand, if we keep a constant value of the electric field strength and vary the driving pressure gradient, it can be found that the induced flow rate solutions, Q_q, obtained for the electric field regime of $E^* \geq 1$ as shown in Fig. 5.17(a) are less dependent on the pressure gradient as compared to the Q_q solutions obtained for $E^* < 1$ in Fig. 5.17(b). Moreover, the induced volume flow rates, Q_q, obtained in the DC electric field regime of $E^* \geq 1$ are generally two orders of magnitude greater than those found in the $E^* < 1$ regime. Note however that for the $E^* > 1$ solutions found in Fig. 5.17(a), non-zero induced volume flow rates, Q_q, at zero driving pressure gradients are present when the ER fluid flow is subjected to an applied DC electric field. This result suggests that there are non-zero total volume flow rate solutions, Q, present at zero

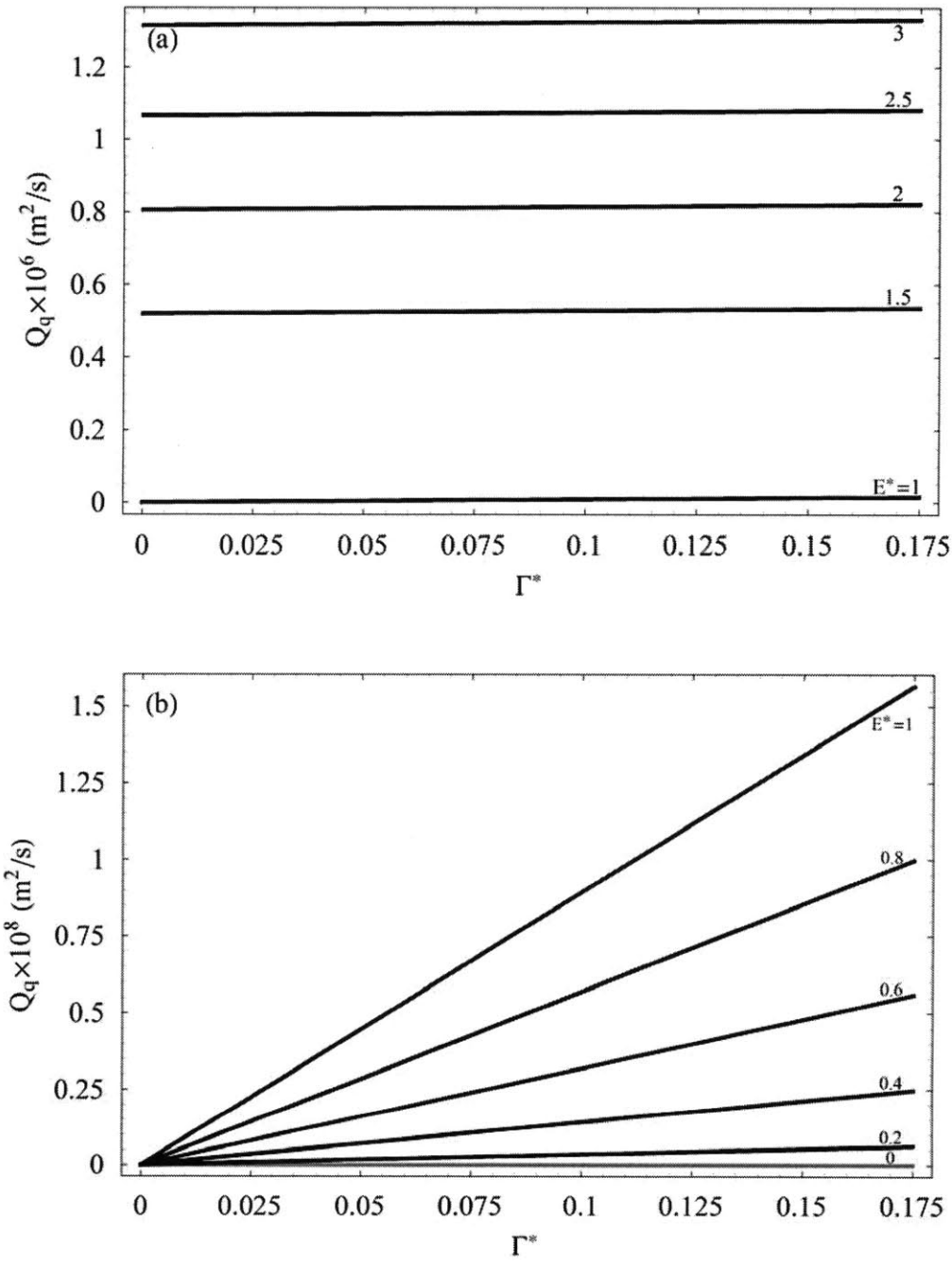

Figure 5.17. The variations of the induced flow rate, Q_q, plotted with respect to the driving pressure gradient, Γ^*, evaluated at constant $\beta = 1$ and $\eta_p^* = 1$ for electric field strengths of (a) $E^* = 1$, 1.5, 2, 2.5, and 3 and (b) $E^* = 0$, 0.2, 0.4, 0.6, 0.8, and 1. The zero electric field solution, *i.e.*, zero induced flow rate, is denoted by the solid gray line shown in Fig. 5.17(b).

driving pressure gradients when the ER fluid flow is subjected to a DC electric field strength of

$E^* > 1$, which is a situation very similar to what we have obtained from zero spin viscosity, $\eta' = 0$, analysis as shown in Fig. 5.7 of Section 5.2. Yet, as already discussed at the end of Section 5.2, both initial flow vorticity and micro-particle Quincke rotation are generally required to produce negative ER responses of the ER fluid flow. To this point, no experimental observations have confirmed negative ER responses when the ER fluid flow is subjected to electric field strengths of $E^* > 1$ without an initial imposed flow vorticity (Lobry & Lemaire, 1999). As for the induced flow rate solutions evaluated in the electric field regime of $E^* \leq 1$ as shown in Fig. 5.17(b), we find that all the induced flow rate solutions become zero as the driving pressure gradient is reduced to zero regardless of the applied DC electric field strength. It seems true that the different forms of polarizabilities (α_y and α_z in Eq. (4.7)) employed in the governing equations and the subsequent A, B, and Π_i coefficients found in the analytical solutions for the respective electric field regimes of $E^* > 1$ and $E^* \leq 1$ give rise to different negative ER responses of the fluid flow.

Figures 5.18(a) and 5.18(b) present the variations of the induced volume flow rate, Q_q, plotted with respect to the driving pressure gradient, Γ^*, for the electric field strengths of $E^* = 2 > 1$ and $E^* = 0.6 < 1$, respectively. For both figures, the induced flow rate solutions are evaluated at $\beta = 0$, 0.25, 0.5, 0.75, and 1 while the spin viscosity, $\eta_p^* = 1$, and the respective electric field strengths are maintained constant. As can be learned from Figs. 5.18(a) and 5.18(b), the induced flow rate, Q_q, decreases as the value of the boundary condition selection parameter, β, is reduced from 1 to 0 when the driving pressure gradient is kept constant. Moreover, the induced flow rate also decreases as the driving pressure gradient is increased for a constant value of the boundary condition selection parameter, β. Specifically, for the Q_q solutions shown in Fig. 5.18(a), it can be seen that all the induced flow rate solutions start as positive values and then decrease as the pressure gradient is increased. However, the rate of reduction (or the magnitude of the Q_q to Γ^* slope) of the induced flow rates increases as the value of β decreases, and for the Q_q solutions evaluated at $\beta = 0$, 0.25, and 0.5, the initially positively valued induced flow rates eventually become negatively valued. Therefore, a reduction or suppression of the total flow rate, Q, is eventually obtained for large enough driving pressure

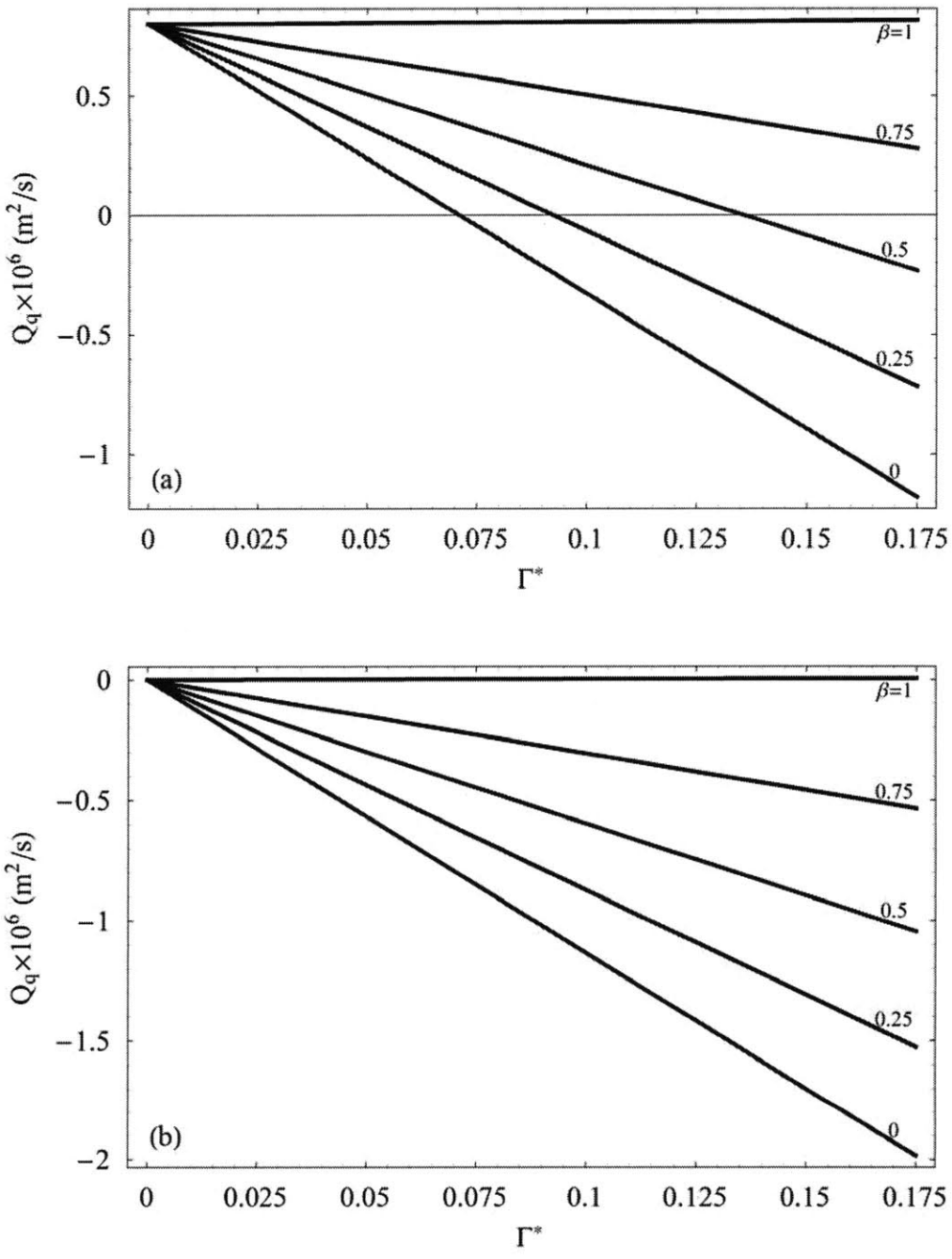

Figure 5.18. Variations of the induced volume flow rate, Q_q, plotted with respect to the driving pressure gradient, Γ^*, evaluated at $\beta = 0$, 0.25, 0.5, 0.75, and 1 while $\eta_p^* = 1$ and the respective DC electric field strengths in (a) $E^* = 2$ and (b) $E^* = 0.6$ are maintained constant.

gradients when the boundary condition selection parameter is small or zero. For the solutions shown in Fig. 5.18(b), we find that all but the $\beta = 1$ solution are negatively valued induced

volume flow rates. Similarly, the rate of reduction (or the magnitude of the Q_q to Γ^* slope) of the induced flow rates with respect to the increasing driving pressure gradient increases as the boundary condition selection parameter decreases for the electric field strength of $E^* = 0.6 < 1$ as shown in Fig. 5.18(b). Reviewing the results shown in both Figs. 5.18(a) and 5.18(b), it can be learned that small or zero boundary condition selection parameters, β, give rise to negative induced volume flow rates, Q_q. In other words, as compared to the zero electric field solution of $Q_0 = \Gamma h^3/12\eta$, the total 2D Poiseuille volume flow rate, Q, given by Eq. (5.46) or (5.47) is reduced or suppressed instead of enhanced when the boundary condition selection parameter is small or simply zero for moderate or large driving pressure gradients applied to the ER fluid flow. This result implies the inconsistency between the experimental observations made by Lemaire *et al.* (2006), *i.e.*, enhancement of flow rate due to nER2 effect, and the theoretical predictions based on our present continuum mechanical field equations in the finite spin viscosity small spin limit when the boundary condition parameter, β, is very small or simply zero, and once again verifies Kaloni's (1992) report of the inconsistency between theory and experiments when the theoretical solutions are obtained with $\beta = 0$ for some flow situations. Nevertheless, the degree of inconsistency between experimental observations (Lemaire *et al.*, 2006) and our present continuum theory when β is small or zero also depends on which DC electric field strength regime of interest and subsequently which form of polarizabilities (α_y and α_z in Eq. (4.7)) or equilibrium retarding polarization is employed in our analyses as indicated by Figs. 5.18(a) and 5.18(b).

Finally, the effects of varying the spin viscosity, η_p^*, on the Quincke rotation induced volume flow rate, Q_q, are studied in Figs. 5.19(a) and 5.19(b) for the respective electric field strengths of $E^* = 2 > 1$ and $E^* = 0.6 < 1$. In both figures, the induced volume flow rate solutions are plotted with respect to the applied pressure gradient, Γ^*, and are evaluated at $\eta_p^* = 0.5$, 0.65, 1, 2, and 10 while the boundary condition selection parameter, $\beta = 1$, and the respective electric field strengths are kept constant. As can be seen from both Figs. 5.19(a) and 5.19(b), positive induced flow rates, Q_q, are generally achieved for the spin viscosity values considered despite the fact that the magnitude of the Q_q solutions shown in Fig. 5.19(a) for $E^* = 2 > 1$ is two orders of

magnitude greater than that of the induced flow rates found in Fig. 5.19(b) for $E^* = 0.6 < 1$. It can also be learned from the two figures that for a given constant driving pressure gradient the induced flow rate is increased as the value of the spin viscosity is reduced. If contrarily, we increase the value of the spin viscosity, the induced flow rate is decreased and eventually approaches the zero electric field solution, *i.e.*, zero induced volume flow rate. Again, we find that the negative ER effect or the enhancement of the Poiseuille ER fluid flow is more significant when the value of the spin viscosity, η_p^*, is small. On the other hand, if the driving pressure gradient is varied while the value of the spin viscosity is kept constant, it can be found that the induced flow rate solutions, Q_q, obtained for the electric field strength of $E^* = 0.6 < 1$ have a stronger dependence on the driving pressure gradient, Γ^*, as compared to those obtained for the field strength of $E^* = 2 > 1$. The rate of increase (or Q_q to Γ^* slope) of the induced volume flow rates with respect to the driving pressure gradient is also greater when the value of spin viscosity is small as compared to that of the Q_q solutions obtained with large spin viscosities as shown in Fig. 5.19(b). Referring back to Fig. 5.19(a), it can also be seen that non-zero induced flow rates at zero driving pressure gradients are present for the electric field strength of $E^* = 2 > 1$, which is a result similar to those found in Figs. 5.17(a) and 5.18(a) as well as in Fig. 5.7 when the spin viscosity is zero. However, as can be learned from the results shown in Fig. 5.19(b) for $E^* = 0.6 < 1$, the induced flow rate is always zero when the driving pressure gradient is zero. This difference found between the two figures is basically due to the different polarizabilities employed in the governing equations as well as the subsequent analytical solutions for the respective regimes of electric field strengths.

Similar to the effective viscosity results studied in Chapter 4, we find that the variations of the induced flow rate, Q_q, versus the applied driving pressure gradient, Γ^*, as shown in Figs. 5.17(a), 5.18(a), and 5.19(a) obtained for the electric field regime of $E^* > 1$ in the finite spin viscosity small spin limit of our present continuum equations share some common features with those of the total flow rate, Q, versus pressure gradient, Γ^*, obtained in the zero spin viscosity limit as shown in Fig. 5.7. Despite the fact that the two sets of results are obtained in the two respective limits, the volume flow rates shown in Figs. 5.7, 5.17(a), 5.18(a), and 5.19(a) increase as the DC electric field strength is increased while the pressure gradient is kept constant, and

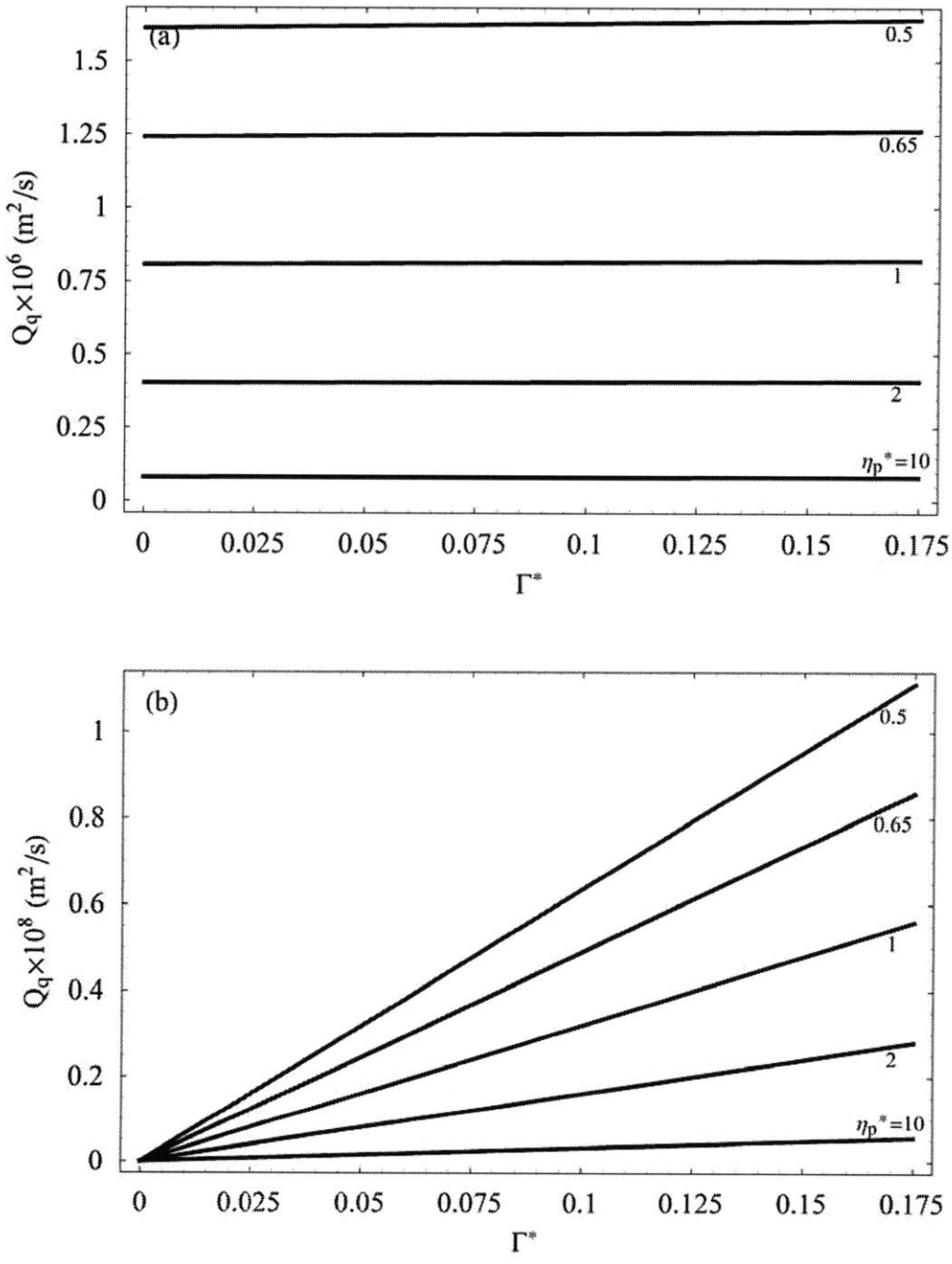

Figure 5.19. Variations of the induced volume flow rate plotted with respect to the driving pressure gradient for electric field strengths of (a) $E^* = 2$ and (b) $E^* = 0.6$. In both figures, the solutions are evaluated at constant $\beta = 1$ and at a varying spin viscosity of $\eta_p^* = 0.5$, 0.65, 1, 2, and 10.

indicate finite volume flow rates at zero driving pressure gradients in the general parametric regime of $E^* > 1$. By further reviewing the results shown in Figs. 5.7, 5.17, 5.18, and 5.19, it can

be learned that the non-linear feature of finite (or non-zero) flow rates at zero driving pressure gradients is only present when we treat the continuum spin velocity, $\overline{\omega}$, and the micro-particle rotation speed, $\overline{\Omega}$, as separate variables with the micro-particle rotation speed being non-zero. In other words, as can be learned from examining Figs. 5.17(b), 5.18(b), and 5.19(b), it is not likely that a finite value of flow rate at zero driving pressure gradients can be obtained (regardless of whether the finite jump in flow rate is physical or not) with the micro-particle rotation speed being set to zero, *i.e.*, $\overline{\Omega}=0$, in the polarizabilities of α_y and α_z (given in Eq. (4.7)) and the continuum spin velocity, $\overline{\omega}$, being the only kinematic variable characterizing the rotational effects on the relaxation process of the negative ER fluid flow.

These results once again suggest that even if the angular momentum equation given by Eq. (4.27) is linearized for finite spin viscosity small spin velocities, it is still possible to capture some of the non-linear features of the polarization relaxation of the ER fluid flow by the finite micro-particle rotation speed built-in the polarizabilities of α_y and α_z given in Eq. (4.7) and the subsequent A, B, and Π_i coefficients found in the analytical solutions. It is likely that treating the micro-particle rotation speed, $\overline{\Omega}$, and the continuum spin velocity, $\overline{\omega}$, as separate kinematic variables at the respective microscopic and macroscopic levels preserves some of the non-linear features or information of the polarization relaxation of the negative ER fluid flow through the finite microscopic particle rotation speed for $E^*>1$ in the finite spin viscosity small spin velocity limit of our present continuum mechanical model, and thus gives rise to the non-linear responses or behavior as shown in Figs. 4.12(a), 4.13(a), and 4.14(a) for the effective viscosity and in Figs. 5.17(a), 5.18(a), and 5.19(a) for the induced volume flow rate. These results also suggest that a proper modeling of the polarization relaxation process consistent with both the macroscopic and microscopic physical pictures is very crucial to analyzing ER fluid flows since the polarization relaxation determines the body torque input to the flow field and the subsequent macroscopic effective ER flow properties.

Chapter 6

Comparison of Results

In this chapter, we compare the theoretical solutions to the spin velocity, linear velocity, effective viscosity, as well as two-dimensional (2D) volume flow rate found in the previous chapters from several different aspects. We first compare the similarities and the differences between the set of solutions obtained in the respective zero spin viscosity limit and the finite spin viscosity small spin velocity limit of the continuum mechanical modeling field equations proposed in this thesis in Section 6.1. We identify and summarize the strengths and limitations of the set of solutions obtained in the respective two limits. Next, in Section 6.2, the continuum solutions to the Couette effective viscosity as derived in Chapter 4 for the respective two limits are compared with the experimental results as reported in Lemaire *et al.* (2008) as well as with the theoretical predictions obtained from the combined single particle dynamics and two-phase effective medium theories as found in the literature (Brenner, 1970; Lobry & Lemaire, 1999; Cebers *et al.*, 2000; Cebers *et al.*, 2002; Lemaire *et al.*, 2006; Pannacci *et al.*, 2007*a*; Lemaire *et al.*, 2008). Lastly, we compare the continuum solutions to the 2D Poiseuille volume flow rate obtained in Chapter 5 for the respective two limits with the experimental results found in Lemaire *et al.* (2006) and the single particle dynamics modeling predictions given in Cebers *et al.* (2002) and Lemaire *et al.* (2006) in Section 6.3. Based on the comparisons made in Sections 6.2 and 6.3, we point out the agreement and the degree of consistency among our present continuum theory, experimental observations found in the literature, and the combined single particle dynamics two-phase effective medium theory.

6.1 Comparison between Solutions Obtained from the Zero Spin Viscosity Limit and the Finite Spin Viscosity Small Spin Velocity Limit

6.1.1 Comparison of the Couette Results Found in Chapter 4

We first consider the continuum Couette spin velocity solutions, ω^* or ω_x, respectively obtained in the zero spin viscosity limit, $\eta' = 0$, and the finite spin viscosity small spin velocity limit, $\eta' \neq 0$, $\tau_{MW}^2 \omega_x^2 \ll 1$. In the zero spin viscosity limit, $\eta' = 0$, it can be found that the spin velocity is a constant value throughout the Couette flow channel and does not vary with respect to the spatial coordinate of z^*. The spin velocity, ω^*, assumes some finite value at the ER fluid-solid interfaces due to the loss of the highest order differential, d^2/dz^2, in the angular momentum equations, and only depends on the applied DC electric field strength, E_0 or E^*, and the Couette driving boundary velocity, U_0 (or shear rate γ^*). Unlike the zero spin viscosity solutions, we find that the continuum spin velocity solutions found in the finite spin viscosity small spin velocity limit depend and vary with respect to the spatial coordinate of z^*—the spin velocity attains its greatest strength in the middle of the Couette flow channel and approaches to the boundary values set by the boundary condition of $\overline{\omega} = 0.5\beta\nabla \times \overline{v}$. Therefore, in addition to the applied DC electric field strength, E^*, and the driving Couette boundary velocity, U_0, the spin velocity solutions solved in the $\eta' \neq 0$, $\tau_{MW}^2 \omega_x^2 \ll 1$ limit are also dependent on the value of the boundary condition selection parameter, β, with $0 \leq \beta \leq 1$, and the magnitude of the spin viscosity, η', which is roughly defined to scale as $\eta' \sim h^2 \eta$ in the present thesis. Note however that the order of magnitudes of the spin velocity solutions found in the $\eta' = 0$ limit is generally greater than that of the spin velocity solutions found in the $\eta' \neq 0$, $\tau_{MW}^2 \omega_x^2 \ll 1$ limit, which is readily understandable. The characteristics or features shared by the spin velocity solutions obtained in both limits are that the magnitude of the spin velocity increases as the electric field strength is increased while the driving shear rate (or boundary velocity) is kept constant, and that the spin velocity solutions reduce to the zero electric field solution, *i.e.*, $\omega_0^* = -\gamma^*/2$ or half of the purely viscous Couette flow vorticity, when the electric field strength is reduced to zero.

Secondly, we examine the total Couette linear velocity fields found in the respective $\eta' = 0$ and $\eta' \neq 0$, $\tau_{MW}^2 \omega_x^2 \ll 1$ limits. From Eq. (4.12), it can be learned that the total linear velocity of Couette flow with internal micro-particle electrorotation in the zero spin viscosity limit is simply the ordinary solution of purely viscous Couette flow, *i.e.*, $u_y = U_0 z/h$. This solution does not depend on the applied DC electric field strength but on the Couette boundary driving velocity, U_0, only and subsequently determines the characteristic shear rate of the flow field. As for the total linear velocity, u_y or u^*, of the Couette ER fluid flow in the $\eta' \neq 0$, $\tau_{MW}^2 \omega_x^2 \ll 1$ limit, it can be found by examining the Quincke rotation induced linear velocity solutions, u_q^*, shown in Figs. 4.8-4.11 that the linear velocity field depends on the applied DC electric field, the driving shear rate (or boundary velocity), the boundary condition selection parameter, and the magnitude of the spin viscosity. The total linear flow velocity is generally accelerated in the upper half of the Couette flow channel and decelerated in the lower half of the channel. The magnitude of the induced linear flow can be increased by increasing the applied DC electric field or reducing the magnitude of the spin viscosity. Furthermore, the induced linear velocity, u_q^*, approaches to the zero electric field solution, *i.e.*, zero induced flow, when the DC field is reduced to zero with the shear rate kept constant, the driving shear rate is increased with the DC electric field strength kept constant, or when the magnitude of the spin viscosity becomes very large. In this zero induced linear flow case, the total linear velocity again becomes the purely viscous Couette flow solution of $u_y = U_0 z/h$.

Comparing the effective viscosity solutions, η_{eff} or η^*, found respectively in Fig. 4.3 for $\eta' = 0$ conditions and in Figs. 4.11-4.13 for $\eta' \neq 0$, $\tau_{MW}^2 \omega_x^2 \ll 1$ conditions, we find that the effective viscosity solutions obtained in the respective two limits behave similarly for DC electric field strengths greater than $E^* = 1$—the effective viscosities are reduced as the electric field strength is increased while the shear rate is kept constant, and the reduction in the effective viscosity is decreased as the applied shear rate (or boundary driving velocity) becomes large. Nonetheless, note that for DC electric field strengths less than or equal to one, *i.e.*, $E^* \leq 1$, the effective viscosity solutions obtained in the $\eta' \neq 0$, $\tau_{MW}^2 \omega_x^2 \ll 1$ limit generally do not depend on the driving shear rate or boundary velocity, which is a result considerably different from the

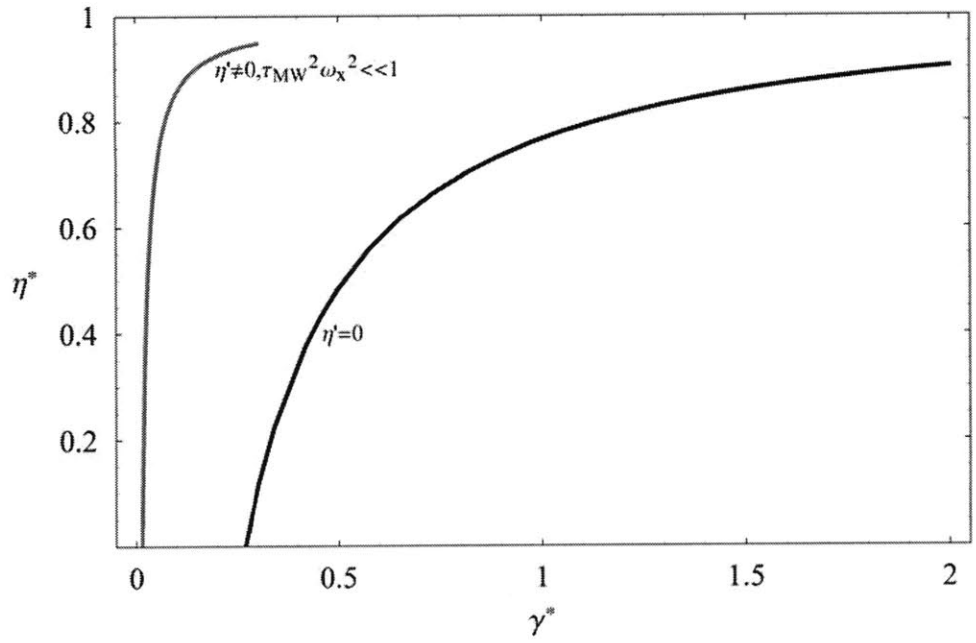

Figure 6.1. Comparison of the two Couette effective viscosity solutions respectively obtained in the zero spin viscosity, $\eta' = 0$, and finite spin viscosity small spin velocity, $\eta' \neq 0$, $\tau_{MW}^2 \omega_x^2 \ll 1$, limits. For both curves, we have employed a DC electric field strength of $E^* = 2$. Also, we have used $\beta = 1$ and $\eta_p^* = 1$ for the $\eta' \neq 0$, $\tau_{MW}^2 \omega_x^2 \ll 1$ solution.

shear rate dependent solutions found in Fig. 4.3 for $E^* \leq 1$. This discrepancy is likely caused by the different forms of polarizabilities (α_y and α_z in Eq. (4.7)) and the subsequent equilibrium retarding polarization (Eqs. (3.32) and (3.33)) employed in the governing equations and the resulting solutions since the expressions of the micro-particle rotation speed, $\overline{\Omega}$, that enter Eq. (4.7) or (3.33) are different for the DC electric field strengths of $E^* > 1$ and $E^* \leq 1$, respectively. Referring back to the total linear velocity field discussed in the previous paragraph, it can be learned by examining the expressions of Eqs. (4.23) and (4.24) that the electrical dependence of the effective viscosity in the zero spin viscosity limit generally comes from the spin velocity solution, ω^*, instead of the total linear velocity (or its vorticity) since the linear velocity in the zero spin viscosity limit is invariant of the DC electric field strength as can be seen in Eq. (4.12). However, this is not the case for the effective viscosity obtained in the $\eta' \neq 0$, $\tau_{MW}^2 \omega_x^2 \ll 1$ limit as can be learned from the functional forms of Eqs. (4.44) and (4.45). In the $\eta' \neq 0$, $\tau_{MW}^2 \omega_x^2 \ll 1$ limit, we find that both the spin velocity field and the induced (or total) linear velocity field are

dependent on the applied DC electric field strength and the Couette driving boundary velocity (or shear rate), and thus the electrical dependence of the effective viscosity in this limit is contributed by both the spin velocity and the linear velocity (or more specifically, the derivative of the linear velocity).

Finally, using the material properties and physical constants given in Table 4.1, we plot the effective viscosity solutions respectively obtained from the zero spin viscosity and finite spin viscosity small spin velocity limits together in Fig. 6.1 to show the respective parametric regimes in which they are valid or suitably applied. In Fig. 6.1, we plot the effective viscosity solution, η^*, obtained in the $\eta' = 0$ limit with respect to the applied shear rate, γ^*, at $E^* = 2$ as noted by the solid black curve, whereas the effective viscosity solution obtained in the $\eta' \neq 0$, $\tau_{MW}^2 \omega_x^2 \ll 1$ is plotted with respect to the shear rate evaluated at $E^* = 2$, $\beta = 1$, and $\eta_p^* = 1$ as noted by the solid gray curve. By examining the figure, it can be found that both of the effective viscosity solutions start at small or negative (not shown) values at very small shear rates, then increase as the shear rate, γ^*, is increased, and finally level out and approach to one as the shear rate becomes very large. It can also be found that the $\eta' \neq 0$, $\tau_{MW}^2 \omega_x^2 \ll 1$ solution predicts an additional leveled out or plateau region at small shear rates, which is a feature that cannot be captured by the zero spin viscosity, $\eta' = 0$, analysis. Notice that this leveled out or plateau region predicted by the $\eta' \neq 0$, $\tau_{MW}^2 \omega_x^2 \ll 1$ solution in Fig. 6.1 is similar to the low viscosity plateaus theoretically predicted and experimentally observed in the work of Lemaire *et al.* (2008). However, our theoretical basis is rooted in a continuum anti-symmetric/couple stress analysis in the $\eta' \neq 0$, $\tau_{MW}^2 \omega_x^2 \ll 1$ limit, which is completely different from the particle-liquid phase separation arguments and particle rotation stability analysis in their work. We shall come back to this comparison in Section 6.2.

6.1.2 Comparison of the Poiseuille Results Found in Chapter 5

We now examine the Poiseuille total spin velocity profiles shown in Figs. 5.3-5.4 and in Figs. 5.9-5.12 obtained in the respective zero spin viscosity, $\eta' = 0$, and finite spin viscosity small spin velocity, $\eta' \neq 0$, $\tau_{MW}^2 \omega_x^2 \ll 1$, limits. Identifying the common features of the two sets of solutions, it can be found that the magnitude of the total spin velocity profiles increases as the

applied DC electric field strength, E^*, is increased while keeping the driving pressure gradient, Γ^*, constant regardless of the limit from which they are obtained. Moreover, the total (dimensionless and normalized) spin velocity profiles approach to the zero electric field solution of half the vorticity of purely viscous Poiseuille flows as the applied DC electric field strength is reduced while the driving pressure gradient is kept constant or as the driving pressure gradient is increased to a large value while the DC field strength is maintained constant. On the other hand, due to the lack of the viscous diffusion term in the angular momentum equation in the zero spin viscosity limit, the governing angular momentum equation eventually reduces to an algebraic cubic equation, and a finite jump in the total spin velocity profile at the center position of the Poiseuille flow channel is produced in order the satisfy the stable micro-particle rotation requirement imposed by the macroscopic vorticity directions. This finite jump in the spin velocity profile is generally permitted since $\eta' = 0$ in the angular momentum equation, which is an analogous situation to the case of inviscid flows for which the viscosity is zero in the linear momentum equation. Nevertheless, the finite jump in the spin velocity profile as shown in Figs. 5.3-5.4 is not found in the spin velocity profiles obtained in the $\eta' \neq 0$, $\tau_{MW}^2 \omega_x^2 \ll 1$, limit as shown in Figs. 5.9-5.12 due to finite spin viscosities, *i.e.*, $\eta' \neq 0$, and the finite couple stress or diffusion transport of angular momentum in the flow system. Additional to the dependences of the spatial coordinate, z^*, the DC electric field strength, E^*, and driving pressure gradient, Γ^*, the $\eta' \neq 0$, $\tau_{MW}^2 \omega_x^2 \ll 1$ spin velocity solutions also depend upon a boundary condition selection parameter, β, and the magnitude of the spin viscosity, η', which is very much different from the zero spin viscosity solutions. Lastly, the order of magnitude of the $\eta' \neq 0$, $\tau_{MW}^2 \omega_x^2 \ll 1$ spin velocity solutions is generally less than that of the zero spin viscosity solutions due to the small spin velocity condition that we have applied during the course of solution.

Comparing the total linear velocity profiles obtained in the $\eta' = 0$ limit to the induced linear velocity profiles found for the $\eta' \neq 0$, $\tau_{MW}^2 \omega_x^2 \ll 1$ limit, it can be found that the general difference between these two sets of solutions is the cusp structure observed near the middle plane of the Poiseuille flow channel for the zero spin viscosity solutions when the applied DC electric field strength is increased with a constant driving pressure gradient or when the driving pressure gradient is reduced with the DC electric field strength kept constant. This cusp structure

is basically related to the finite jump that is produced in the total spin velocity profile in order to satisfy the stable micro-particle rotation direction in the zero spin viscosity limit. As can be seen in the induced linear velocity profiles shown in Figs. 5.13-5.16 for the finite spin viscosity small spin case, the cusp structure is generally less severe or eventually smoothed out due to the additional diffusional transport mechanism introduced by a finite spin viscosity. This result is consistent with the mathematical nature of the additional diffusion term, *i.e.*, d^2/dz^2 (which tends to smooth out singular or concentrated physical values within the ER flow field), as presented in the governing angular momentum equation of Eq. (4.27), and is not described or captured by the zero spin viscosity analysis. Due to the additional dependence on the boundary condition selection parameter, β, in the finite spin viscosity small spin velocity solutions, we find that reduction (or suppression) in total linear velocity or equivalently a reversal of direction in the induced linear flow field is predicted when $\beta = 0$, *i.e.*, zero spin boundary conditions at the solid-ER fluid boundaries, even when a DC electric field strength greater than the critical electric field strength for Quincke rotation is applied to the fluid flow. This result offers a new case of flow conditions or situations that support the observation of experimental results being inconsistent with theoretical continuum anti-symmetric/couple stress analyses with zero spin boundary conditions as discussed in Kaloni (1992). Despite all the above differences between the two sets of solutions obtained in their respective limits, the magnitudes of both sets of the linear velocity solutions increase as the applied DC electric field strength is increased while the driving pressure gradient is kept constant, and decrease as the driving pressure gradient is increased when subjected to a constant DC electric field. The total linear velocities obtained in the $\eta' = 0$ and in the $\eta' \neq 0$, $\tau_{MW}^2 \omega_x^2 \ll 1$ limits both approach the zero electric field solution of the ordinary parabolic profile of the purely viscous Poiseuille flow (or zero induced flow velocity) as the applied DC electric field strength is reduced while keeping the driving pressure gradient constant or the driving pressure gradient is increased to a very large value while the applied DC field strength is kept constant.

Examining the total 2D flow rates shown in Fig. 5.7 and the induced 2D flow rates found in Figs. 5.17-5.19, it can be learned that there are in general, non-zero "total" volume flow rates at zero driving pressure gradients for the two sets of flow rate solutions found in the respective zero spin viscosity and finite spin viscosity small spin velocity limits when the applied DC electric

field is greater than one, *i.e.*, $E^* > 1$. However, the order of magnitude of the non-zero flow rate at zero pressure gradients found in the $\eta' \neq 0$, $\tau_{MW}^2 \omega_x^2 \ll 1$ limit is generally less than that of the non-zero flow rate obtained in the $\eta' = 0$ limit. On the other hand, it can be found that the induced volume flow rates shown in Figs. 5.17(b), 5.18(b), and 5.19(b) become zero when the driving pressure gradient reduces to zero for electric field strengths of $E^* < 1$. In other words, the 2D Poiseuille total volume flow rate solutions obtained in the limit of $\eta' \neq 0$, $\tau_{MW}^2 \omega_x^2 \ll 1$ are zero when the applied driving pressure gradient is zero in the DC electric field strength regime of $E^* < 1$ since the total volume flow rate, Q, is related to the induced volume rate, Q_q, by

$$Q = Q_q + Q_0 = Q_q + \frac{\Gamma h^3}{12\eta}. \tag{6.1}$$

A similar situation can also be found from the total flow rate solutions given in Fig. 5.7—the total volume flow rates obtained in the zero spin viscosity limit, $\eta' = 0$, also become zero when the driving pressure gradient is reduced to zero at low DC electric field strengths (*i.e.*, $E^* \leq 0.8$). Again, this particular difference of zero or non-zero volume flow rates found at zero driving pressure gradients is generally due to the form or polarizabilities, *i.e.*, α_y and α_z in Eq. (4.7), and the subsequent equilibrium retarding polarization, $\overline{P_{eq}}$ given by Eqs. (3.32) and (3.33), employed in the polarization relaxation equation, Eq. (3.35), when solving the governing equations of motion in the respective two electric field strength regimes of interest. Additional to the above common features, the 2D flow rate solutions respectively obtained in the zero spin viscosity and finite spin viscosity small spin velocity limits are also similar in several ways such as (i) with a given constant driving pressure gradient, the flow rate solutions increase as the applied DC electric field increases and (ii) for a given DC electric field strength, the flow rate solutions increase as the driving pressure gradient increases. Note however that the increase or rate of increase with respect to the increasing pressure gradient of the induced flow rates found in the $\eta' \neq 0$, $\tau_{MW}^2 \omega_x^2 \ll 1$ limit is generally not very significant as can be seen in Fig. 5.17(a).

Lastly, similar to the development of the Couette flow case, we present the total volume flow rate solutions, Q, obtained respectively in the zero spin viscosity, $\eta' = 0$, and finite spin viscosity small spin velocity, $\eta' \neq 0$, $\tau_{MW}^2 \omega_x^2 \ll 1$, limits together in Fig. 6.2 to show the respective parametric regimes in which they are valid or suitably applied. In Fig. 6.2, we have

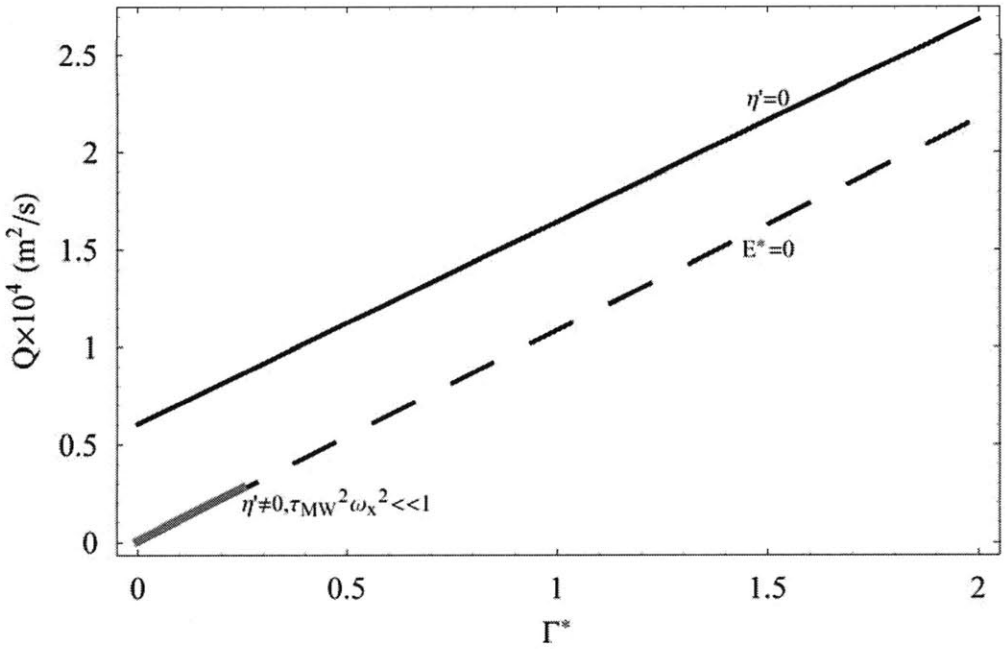

Figure 6.2. Comparison of the two total volume flow rate solutions obtained in the zero spin viscosity, $\eta' = 0$, and the finite spin viscosity small spin velocity, $\eta' \neq 0$, $\tau_{MW}^2 \omega_x^2 \ll 1$, limits, respectively. The solid black line represents the $\eta' = 0$ solution evaluated at $E^* = 2$, whereas the solid gray line represents the $\eta' \neq 0$, $\tau_{MW}^2 \omega_x^2 \ll 1$ solution evaluated at $E^* = 2$, $\beta = 1$, and $\eta_p^* = 1$. The dash-dash line denotes the zero electric field solution, *i.e.*, the total 2D flow rate of purely viscous Poiseuille flows, $Q_0 = \Gamma h^3 / 12\eta$.

plotted the total volume flow rate solutions, Q, with respect to the driving pressure gradient, Γ^*; the back solid (long) line represents the $\eta' = 0$ solution evaluated at an electric field strength of $E^* = 2$, whereas the gray solid (short) line represents the $\eta' \neq 0$, $\tau_{MW}^2 \omega_x^2 \ll 1$ evaluated at $E^* = 2$, $\beta = 1$, and $\eta_p^* = 1$. The dash-dash line shown in Fig. 6.2 denotes the zero electric field solution of the purely viscous 2D Poiseuille volume flow rate, *i.e.*, $Q = \Gamma h^3 / 12\eta$. From this figure, it can be learned that the zero spin viscosity solution generally applies to the whole regime of pressure gradient of interest, but the finite spin viscosity small spin velocity solution only applies to a small range of driving pressure gradients due to the limitation of $\tau_{MW}^2 \omega_x^2 \ll 1$ on the linear solutions we have obtained. Also seen in Fig. 6.2, the $\eta' \neq 0$, $\tau_{MW}^2 \omega_x^2 \ll 1$ solution falls closely to the zero electric field solution and increases as the driving pressure gradient increases. On the other hand, the zero spin viscosity solution starts from a non-zero total flow rate at zero

driving pressure gradient and increases as the driving pressure gradient is increased (with the trend of variation being almost parallel to that of the zero electric field solution) while the applied DC electric field strength is maintained at $E^* = 2$. Hence, it is evidently seen that the zero spin viscosity, $\eta' = 0$, solution cannot capture the more physically reasonable picture of the total flow rate being reduced to almost zero when the driving pressure gradient is reduced to zero. As we further compare Fig. 6.2 to the experimental and theoretical flow rate results reported in Lemaire *et al.* (2006), it can be found that our zero spin viscosity solutions obtained from our proposed continuum mechanical modeling field equations predict similar trends of variation as to those predicted by the combined single particle dynamics two-phase effective medium model employed in Lemaire *et al.* (2006). Yet, only our finite spin viscosity small spin velocity solutions are more capable of capturing the more physical picture of zero or almost zero flow rates at small or zero pressure gradients, which is a result consistent with the experimental observations done by Lemaire *et al.* (2006). Both zero spin viscosity analysis and the combined single particle dynamics two-phase effective medium theory predict non-zero flow rates at zero driving pressure gradients. This issue will be further addressed in Section 6.3.

6.1.3 The Eigen or Characteristic Parameter A for Finite Spin Viscosity Small Spin Velocity Solutions

Before closing this section, it is insightful to point out a non-dimensional parameter which characterizes the negative ER fluid flow phenomena in the finite spin viscosity small spin velocity limit presented herein. By reviewing Sections 4.4.1 and 5.4.1, it can be learned that the non-dimensional parameter, namely, A as defined in Eqs. (4.34) and (5.26), appears repeatedly in the analytical solutions obtained in the finite spin viscosity small spin velocity limit. We can further factor out the channel height of h in Eq. (4.34) or (5.26) and have

$$A = h\sqrt{\frac{\tau_{MW}}{\eta'}\left(n\alpha_z E_0^2 + \frac{4\zeta}{\tau_{MW}} - \frac{4\zeta^2}{\eta_e \tau_{MW}}\right)} = \frac{h}{\ell}, \tag{6.2}$$

where

$$\ell = 1\Big/\sqrt{\frac{\tau_{MW}}{\eta'}\left(n\alpha_z E_0^2 + \frac{4\zeta}{\tau_{MW}} - \frac{4\zeta^2}{\eta_e \tau_{MW}}\right)}, \tag{6.3}$$

which generally represents a length scale, ℓ, characterized by the balance between the forcing or

driving mechanism, *i.e.*, the electrical body torque input, the internal angular momentum conversion between the spin and linear velocity fields, and the diffusional transport of internal angular momentum. By examining Eq. (6.3), we find that the greater the applied DC electric field strength is, the smaller this length scale, ℓ, becomes, and the greater the spin viscosity is, the greater ℓ becomes. The parameter A then becomes a ratio of the characteristic length imposed by the geometry (h) to the characteristic length due to the angular momentum balance or conversion (ℓ) within the ER flow field. Reviewing the solutions and results given in Chapters 4 and 5, it can be learned that in general, the smaller this characteristic length, ℓ, is, the greater the parameter A as well as the negative ER response become. Contrarily, the greater the length scale ℓ is, the smaller the parameter A and the negative ER response become. In the zero spin viscosity limit, *i.e.*, $\eta' = 0$, ℓ is simply zero, which most likely implies that the electrical torque input and the angular momentum conversion occur at a very local length scale—the particulate limit of our proposed continuum mechanical modeling field equations (as discussed at the end of Section 5.2). This result explains why the present continuum mechanical formulation in the zero spin viscosity limit predicts similar negative electrorheological responses of the Couette effective viscosity and of the 2D Poiseuille volume flow rate as compared to those obtained from the combined analysis of single particle dynamics and two-phase effective medium theories as found in current literature (Brenner, 1970; Lobry & Lemaire, 1999; Cebers *et al.*, 2000; Cebers *et al.*, 2002; Lemaire *et al.*, 2006; Pannacci *et al.*, 2007*a*; Lemaire *et al.*, 2008). In single particle dynamics, the electrical torque input and the angular momentum conversion basically occurs in the microscopic particle scale (before taking macroscopic averages), which is equivalent to the previously described physical picture of the characteristic length scale, ℓ, being very small or zero in the zero spin viscosity limit for our present continuum mechanical formulation with finite spin viscosities. Note however that the A parameter generally cannot be derived from the zero spin viscosity analysis.

6.2 Comparison of Couette Effective Viscosity Results Found in Chapter 4 with Those Found in Current Literature

In this section, we compare the Couette effective viscosity results obtained by our proposed continuum mechanical modeling field equations to the theoretical and experimental results

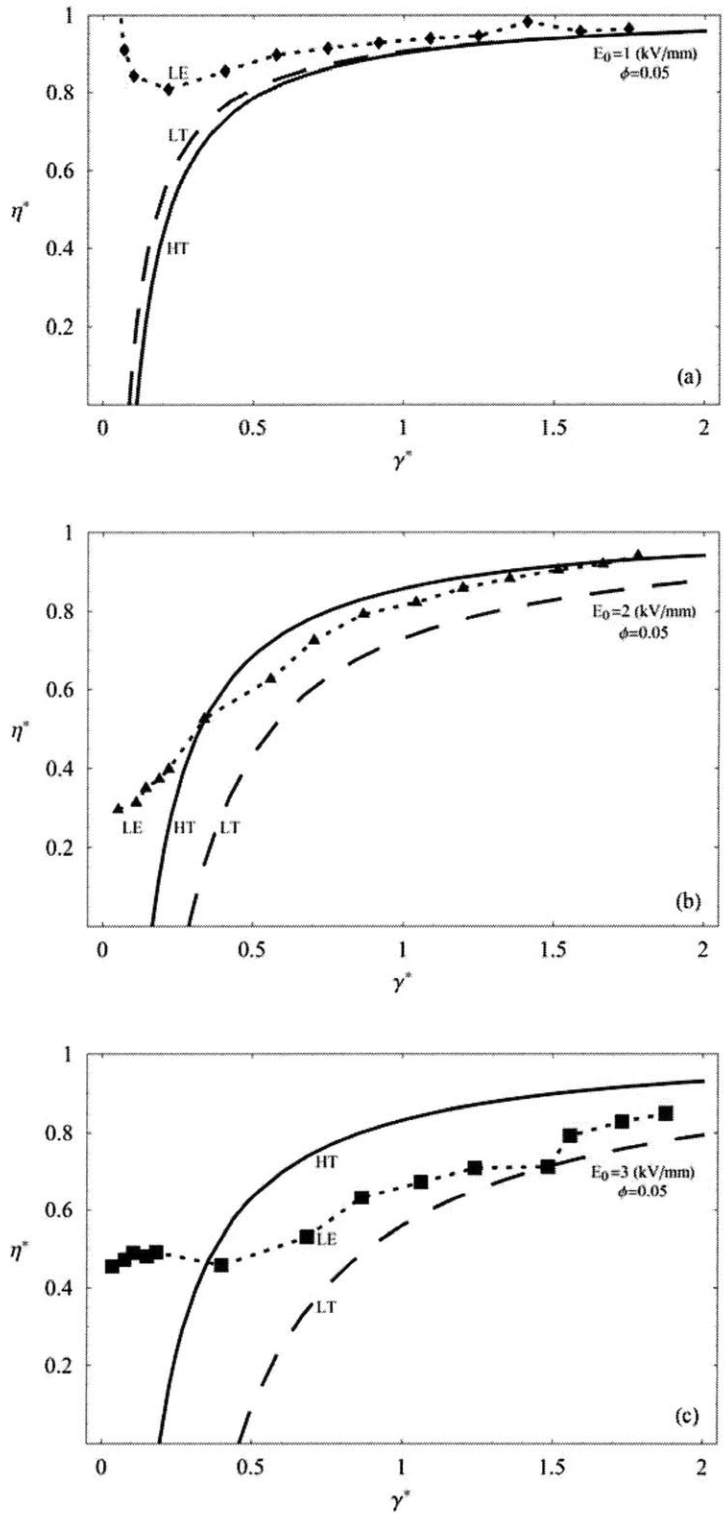

Figure 6.3. Captions on facing page top.

reported in Figs. 7a and 7b of Lemaire *et al.* (2008). In the following figures and discussions, we

Figure 6.3. Comparison of the Couette effective viscosity results among the present continuum zero spin viscosity modeling predictions (HT, solid curve), the experimental measurements (LE, dotted curve) reported in Fig. 7a of Lemaire *et al.* (2008), and the combined single particle dynamics two-phase volume averaged effective medium theory predictions (LT, dashed-dashed curve) employed in Fig. 7a of Lemaire *et al.* (2008). In this figure, the ER fluid solid volume fraction is $\phi = 0.05$, and the solutions or measurements are obtained at DC electric field strengths of (a) $E_0 = 1$ (kV/mm), (b) $E_0 = 2$ (kV/mm), and (c) $E_0 = 3$ (kV/mm). No fitting parameters or procedures are used in evaluating the zero spin viscosity HT solutions.

shall denote the theoretical results predicted by the present continuum mechanical formulation as HT (abbreviating Huang Theory), the theoretical results predicted by the combined single particle dynamics and effective medium formulation as LT (abbreviating Lemaire Theory), and the experimental results measured by Lemaire *et al.* (2008) as LE (abbreviating Lemaire Experiments). Also, we shall plot the HT results with solid curves, the LT results with dashed-dashed curves, and the LE results with dotted curves in the following figures. Due to the different regimes of application as indicated in Fig. 6.1, we shall first present the comparison of solutions obtained in the zero spin viscosity limit for the moderate to high shear rate regime, and then present that of the solutions obtained in the finite spin viscosity small spin velocity limit for the low shear rate regime.

By substituting the same material properties and system parameters, *e.g.*, a carrier liquid conductivity of $\sigma_1 = 1.5\times10^{-8}$ (S/m) and an average micro-particle diameter of 56.5 (μm), etc., employed in Lemaire *et al.* (2008) into our zero spin viscosity solutions presented in Chapter 4, *i.e.*, Eqs. (4.23) and (4.24), we simultaneously plot the three sets of results (HT, LT, and LE) of the Couette effective viscosity, η^*, with respect to the applied shear rate, γ^*, in Figs. 6.3(a), 6.3(b), and 6.3(c) evaluated or measured respectively at $E_0 = 1$, 2, and 3 (kV/mm) for the micro-particle solid volume fraction of 5%, $\phi = 0.05$. Similarly, we plot the three HT, LT, and LE results of the Couette effective viscosity, η^*, with respect to the applied shear rate, γ^*, in Figs. 6.4(a), 6.4(b), and 6.4(c) evaluated or measured respectively at $E_0 = 1$, 2, and 3 (kV/mm) for the micro-particle solid volume fraction of 10%, $\phi = 0.1$. Note that the critical electric field is evaluated to be $E_c \approx 0.83$ (kV/mm) when using the same material properties and system parameters as in Lemaire *et al.* (2008), and that no other fitting parameters are employed when evaluating our present continuum zero spin viscosity, HT, solutions.

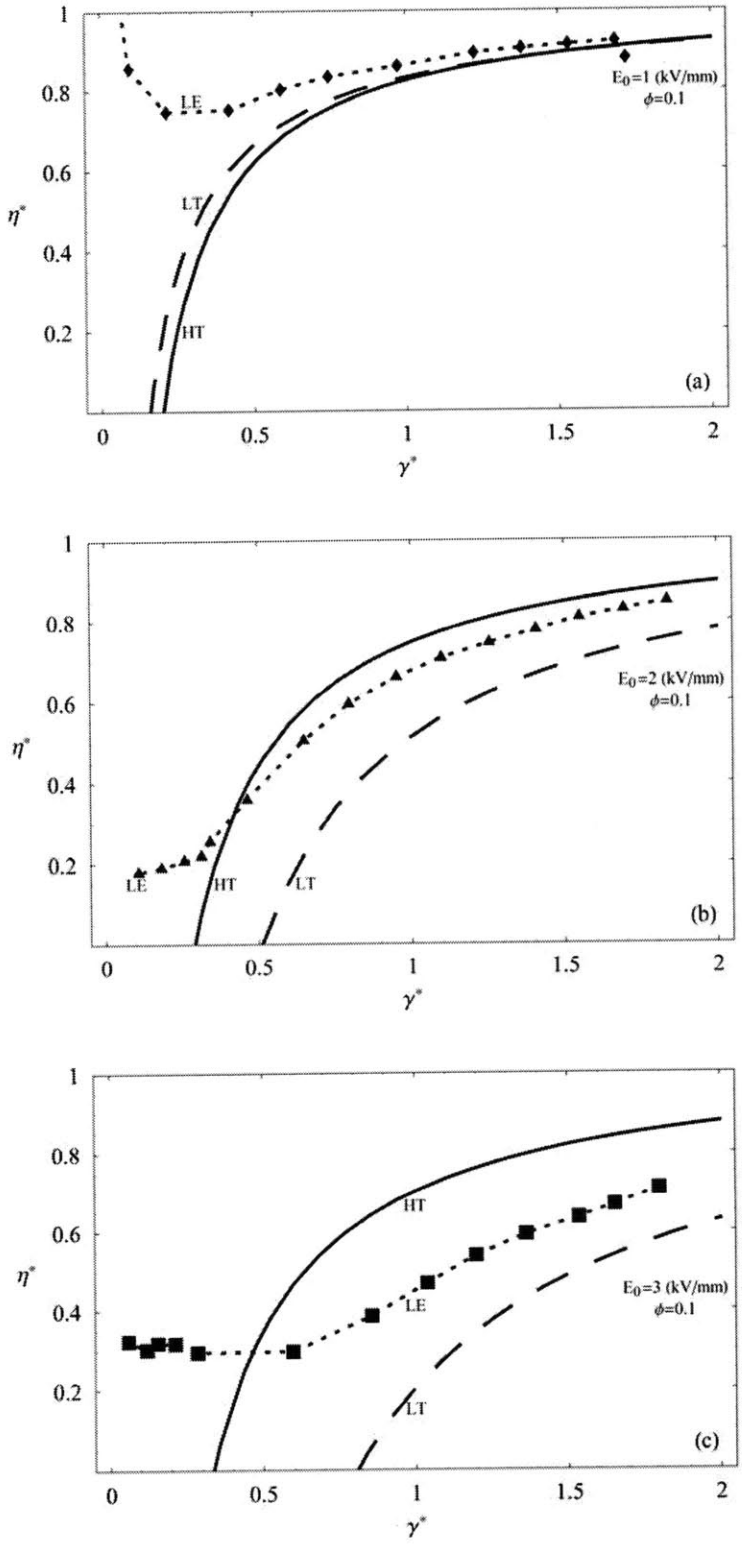

Figure 6.4. Captions on facing page top.

From the two sets of figures as respectively shown in Figs. 6.3 and 6.4, it can be seen that the

Figure 6.4. Comparison of the Couette effective viscosity results among the present continuum zero spin viscosity modeling predictions (HT, solid curve), the experimental measurements (LE, dotted curve) reported in Fig. 7b of Lemaire *et al.* (2008), and the combined single particle dynamics two-phase volume averaged effective medium theory predictions (LT, dashed-dashed curve) employed in Fig. 7b of Lemaire *et al.* (2008). In this figure, the ER fluid solid volume fraction is $\phi = 0.1$, and the solutions or measurements are obtained at DC electric field strengths of (a) $E_0 = 1$ (kV/mm), (b) $E_0 = 2$ (kV/mm), and (c) $E_0 = 3$ (kV/mm). No fitting parameters or procedures are used in evaluating the zero spin viscosity HT solutions.

experimental effective viscosity data obtained by Lemaire *et al.* (2008), curve LE, fall closely to both of the LT and HT theoretical predictions at moderate to high shear rates when the DC electric field strength is at $E_0 = 1$ (kV/mm) in Figs. 6.3(a) and 6.4(a). As the electric field strength is increased to $E_0 = 2$ (kV/mm) as shown in Figs. 6.3(b) and 6.4(b), the continuum predictions of HT come closer to the Lemaire measurements (Lemaire *et al.*, 2008), LE, while the single particle dynamics theory represented by LT over estimates the reduction in effective viscosity as compared to LE. Finally, we find in Figs. 6.3(c) and 6.4(c) that the continuum theory, HT, under estimates whereas the single particle dynamics, LT, over estimates the reduction in the Couette effective viscosity as compared to the experimental measurements, LE, found in Lemaire *et al.* (2008) when the DC electric field strength is $E_0 = 3$ (kV/mm). Generally speaking, it can be found that in the zero spin viscosity limit, our continuum model predicted effective viscosity, η^*, varies in a similar trend with respect to γ^* and/or E^* as compared with the theoretical predictions from the single particle dynamics based two-phase volume averaged model (Lemaire *et al.*, 2008). However, unlike Lemaire *et al.*'s (2008) theoretical model which always over estimates the reduction in effective viscosity (as compared to their experimental data), our proposed continuum mechanical model under estimates the reduction in the effective viscosity, η^*, at high DC electric field strengths, but likely falls closer to the experimental rheometer data of Lemaire *et al.* (2008) at low to moderate electric field strengths, *i.e.*, $E^* = E_0/E_c \approx 1.2\sim2.4$.

On the other hand, we simultaneously plot the Couette effective viscosity results obtained from the LE experimental measurements (Lemaire *et al.*, 2008), the combined single particle dynamics and effective medium theory predictions, LT, and the present continuum mechanical solutions in the $\eta' \neq 0$, $\tau_{MW}^2 \omega_x^2 \ll 1$ limit, *i.e.*, Eqs. (4.44) and (4.45), denoted by HT with respect

to the shear rate, $\gamma^* = 0 \sim 0.2$, in Figs. 6.5 and 6.6 for the respective micro-particle solid volume fractions of 5%, or $\phi = 0.05$, and of 10%, or $\phi = 0.1$. In Figs. 6.5 and 6.6, the HT solutions are evaluated at DC electric field strengths of $E_0 = 1$, 2, and 3 (kV/mm), the LE data (Lemaire *et al.*, 2008) are measured at $E_0 = 1$, 2, and 3 (kV/mm), and the LT predictions are invariant of the applied DC electric field strengths and depend only upon the micro-particle solid volume fraction, ϕ (Lemaire *et al.*, 2008). Note that in the evaluation of the present continuum mechanical solutions, HT, shown in Figs. 6.5 and 6.6, we have substituted the same material properties and system parameters as employed in Lemaire *et al.* (2008) into Eqs. (4.44) and (4.45) and evaluated the effective viscosity solutions at $E_0 = 1$, 2, and 3 (kV/mm) with $\beta = 1$ and $\eta' = h^2\eta \approx h^2\eta_0(1+2.5\phi)$ $(N \cdot s)$, where h is the gap or spacing between the two electrodes, η_0 is the carrier liquid viscosity, and ϕ is the micro-particle solid volume fraction. The numerical values employed for the spin viscosity, η', and the boundary condition selection parameter, β, are based on physical arguments as discussed in Chapters 4 and 5 and no *ad hoc* fitting is performed. By comparing the three sets of results, *i.e.*, HT, LT, and LE, in the low shear rate regime, $\gamma^* = 0 \sim 0.2$, it can be found that both our continuum mechanical predictions and the combined single particle dynamics two-phase effective medium analyses (Lemaire *et al.*, 2008) predict similar plateau curves in the low shear rate, low effective viscosity regime. However, our proposed continuum mechanical model in the $\eta' \neq 0$, $\tau_{MW}^2\omega_x^2 \ll 1$ limit, HT, predicts a positively valued leveled out or nearly plateau structure and likely falls closer to the experimental rheometric data of LE (Lemaire *et al.*, 2008) as compared to the negatively valued low shear rate plateau predicted by the single particle dynamics model, LT (Lemaire *et al.*, 2008). Notice that the plateau predicted by LT is based on the theoretical formulation of allowing the suspended micro-particles to rotate with the axis of rotation lying in the general *x-y* plane instead of only in the *x*-direction with the coordinate system employed in the Lemaire *et al.* (2008) analysis being the same as those defined in Figs. 2.1 and 4.1 of this thesis. Lemaire *et al.* (2008) also suggested that an experimentally observed particle-liquid phase separation along the longitudinal axis of the cylindrical Couette flow rheometer used in their experiments was responsible for their experimental measured plateaus, LE, and advocated the existence of the class of solutions with the suspended micro-particles rotating with the axis of rotation lying in the general *x-y* plane.

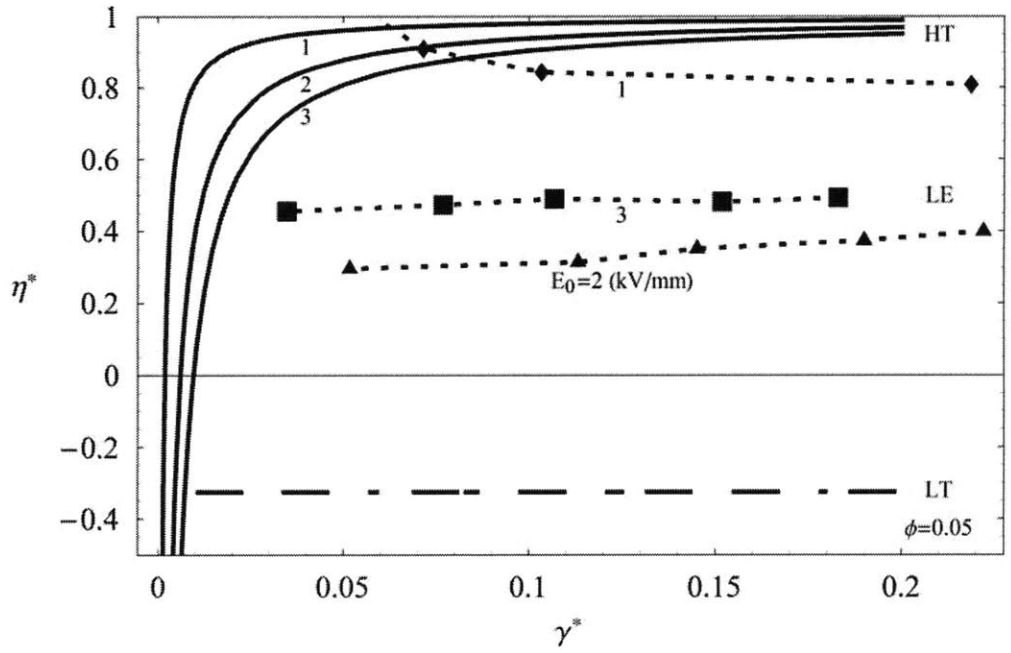

Figure 6.5. Comparison of the Couette effective viscosity results in the low shear rate regime among the present continuum finite spin viscosity small spin velocity modeling predictions (HT, solid curve), the experimental measurements (LE, dotted curve) reported in Fig. 7a of Lemaire *et al.* (2008), and the combined single particle dynamics two-phase volume averaged effective medium theory predictions (LT, dashed-dashed curve) employed in Fig. 7a of Lemaire *et al.* (2008). In this figure, the ER fluid solid volume fraction is $\phi = 0.05$, and the solutions or measurements are obtained at DC electric field strengths of $E_0 = 1$ (diamond), 2 (triangle), and 3 (box) (kV/mm). Note that the LT theoretical prediction of the effective viscosity is invariant of the applied DC electric field strength, and that the numerical values for the boundary condition selection parameter, $\beta = 1$, and the spin viscosity, $\eta' = h^2\eta$, employed in the finite spin viscosity HT analysis are chosen by physical arguments discussed in Chapters 4 and 5. No *ad hoc* fitting parameters or procedures are used in evaluating the finite spin viscosity HT solutions.

Nevertheless, we should point out that the class of solutions with the suspended micro-particles rotating with the axis of rotation lying in the general x-y plane only exists when the background flow vorticity in the z-direction of the cylindrical Couette flow rheometer shown in Lemaire *et al.* (2008) (or in the x-direction as defined by the coordinate system shown in Figs. 2.1 and 4.1 of the present thesis) is zero, and that the longitudinal (cylindrical z-direction) particle-liquid phase separation reported in Lemaire *et al.* (2008) is likely a moderate to high shear rate, *i.e.*, $\gamma^* \sim 0.5 - 0.6$ (Pannacci *et al.*, 2007*a*), and long term or duration—at least 5 minutes after the cylindrical rheometer starts to rotate—experimental observation (Pannacci *et al.*, 2007*a*; Lemaire

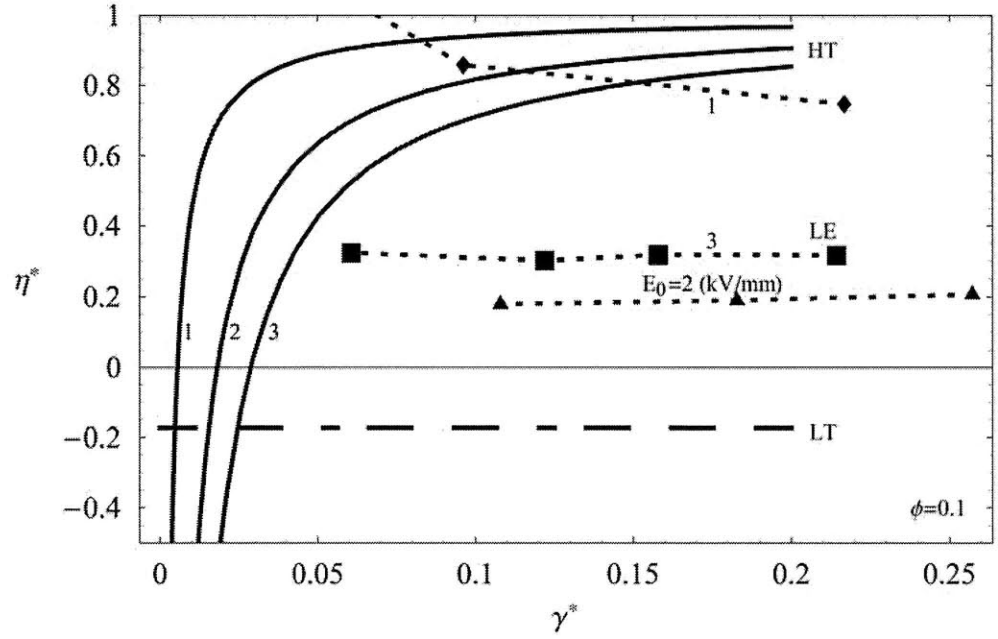

Figure 6.6. Comparison of the Couette effective viscosity results in the low shear rate regime among the present continuum finite spin viscosity small spin velocity modeling predictions (HT, solid curve), the experimental measurements (LE, dotted curve) reported in Fig. 7b of Lemaire *et al.* (2008), and the combined single particle dynamics two-phase volume averaged effective medium theory predictions (LT, dashed-dashed curve) employed in Fig. 7b of Lemaire *et al.* (2008). In this figure, the ER fluid solid volume fraction is $\phi = 0.1$, and the solutions or measurements are obtained at DC electric field strengths of $E_0 = 1$ (diamond), 2 (triangle), and 3 (box) (kV/mm). Note that the LT theoretical prediction of the effective viscosity is invariant of the applied DC electric field strength, and that the numerical values for the boundary condition selection parameter, $\beta = 1$, and the spin viscosity, $\eta' = h^2\eta$, employed in the finite spin viscosity HT analysis are chosen by physical arguments discussed in Chapters 4 and 5. No *ad hoc* fitting parameters or procedures are used in evaluating the finite spin viscosity HT solutions.

et al., 2008). Therefore, the assumptions in their theoretical formulation are likely to be inconsistent or contradictory to their actual experimental conditions.

As for the present analysis (HT) of the continuum mechanical modeling field equations in the finite spin viscosity small spin velocity limit, we have, instead of using a two-phase volumetric averaged model, utilized the continuum anti-symmetric/couple stress theories to describe the negative ER fluid flow phenomenon with the elementary microscopic ER fluid parcel being defined as consisting of a representative amount or ensemble of carrier liquid molecules and rotating micro-particles under the framework of the continuum hypothesis. This approach is

likely more capable of capturing the low shear rate macroscopic ER fluid flow dynamics resulting from the averaged effects of the two competing microscopic physical mechanisms of micro-particle chaining (dipole-dipole attraction) and the chained micro-particles being "ripped out of the chains" by spontaneous micro-particle Quincke rotation (Pannacci *et al.*, 2007*a*).

Despite the very different physical arguments and modeling theories employed in the two respective models of HT and LT, the result of the above comparison is encouraging since it suggests that our $\eta' \neq 0$, $\tau_{MW}^2 \omega_x^2 \ll 1$ solutions are capable of capturing a positively valued low shear rate nearly plateau behavior and may offer some additional insights or possible physical explanations in interpreting the experimentally observed low shear rate, low viscosity plateau in the viscosity versus shear rate plots found in current literature (Lemaire et *al.*, 2008).

6.3 Comparison of 2D Poiseuille Volume Flow Rate Results Found in Chapter 5 with Those Found in Current Literature

This section compares the 2D Poiseuille volume flow rate solutions predicted by the present continuum mechanical modeling field equations of this thesis to the experimental measurements and the single particle dynamics theoretical predictions given in Figs. 5 and 6 of Lemaire *et al.* (2006). A detailed theoretical development of the single particle dynamics based two-phase volume averaged effective medium theory in modeling the 2D Poiseuille volume flow rate response employed in Lemaire *et al.* (2006) is presented in Cebers *et al.* (2002). Again, we denote the present continuum mechanical theoretical predictions as HT (abbreviating Huang Theory), the single particle dynamics based theoretical predictions as LT (abbreviating Lemaire Theory), and the experimental measurements done by Lemaire *et al.* (2006) as LE (abbreviating Lemaire Experiments) in the following discussions. As for the figures presented in the following, we plot the HT solutions in solid curves, the LT solutions in dashed-dashed curves, and the LE data (Lemaire *et al.*, 2006) in dotted curves. Referring to the different regimes of application of the respective $\eta' = 0$ and $\eta' \neq 0, \tau_{MW}^2 \omega_x^2 \ll 1$ limits of the HT solutions as shown in Fig. 6.2, we shall first present the comparison results for the zero spin viscosity 2D Poiseuille volume flow rate solutions for moderate to high applied pressure gradients, and then present the results for the finite spin viscosity small spin velocity solutions for low applied pressure gradients.

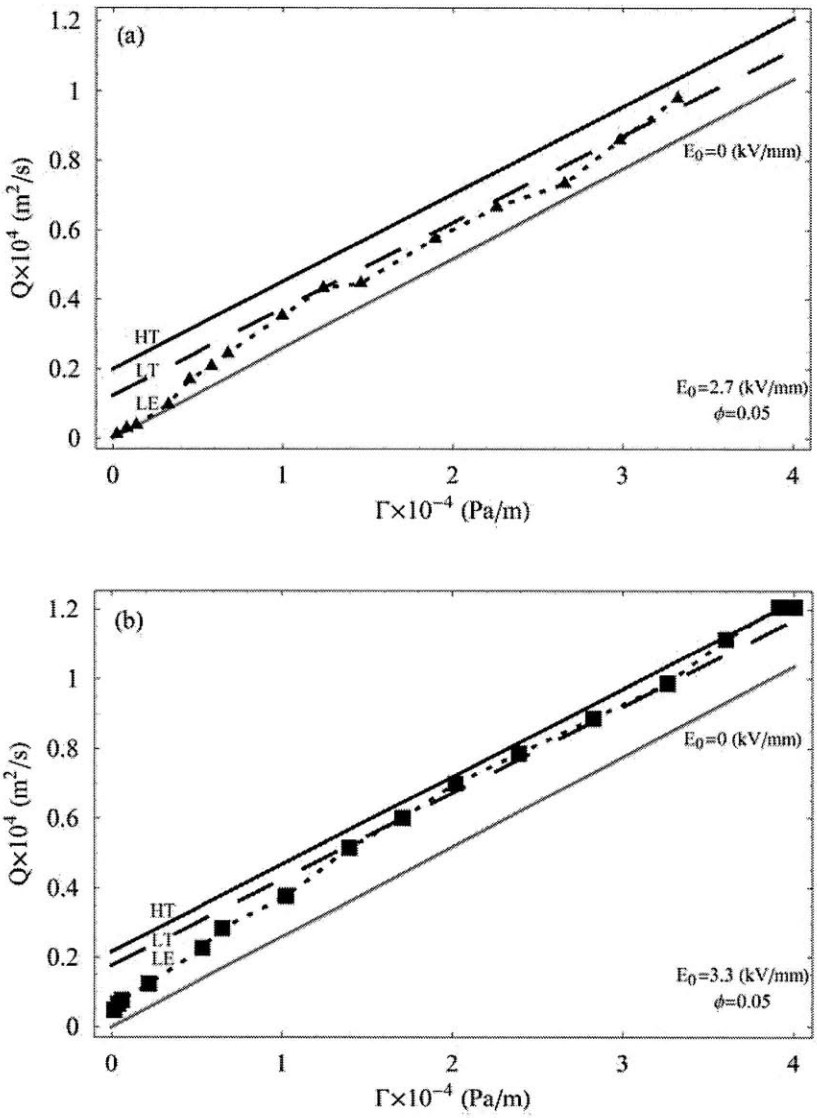

Figure 6.7. Comparison of the 2D Poiseuille volume flow rate results among the present zero spin viscosity HT (solid curve) predictions, the experimental measurements, LE (dotted curve), found in Fig. 5 of Lemaire *et al.* (2006), and the single particle dynamics based predictions (dashed-dashed curve) found in Fig. 5 of Lemaire *et al.* (2006). In this figure, the gray solid lines denote the zero electric field Poiseuille volume flow rate and the ER fluid solid volume fraction is $\phi = 0.05$. The HT and LT solutions and the LE measurements are obtained at DC electric field strength of $E_0 = 2.7$ (kV/mm) in Fig. 6.7(a) and of $E_0 = 3.3$ (kV/mm) in Fig. 6.7(b). No fitting parameters or procedures are used in the evaluation of the HT results.

Substituting the same material properties and system parameters, *e.g.*, $h = 750$ (μm), $d = 71.5$ (μm), and $\sigma_1 = 4\times10^{-8}$ (S/m), as employed in Lemaire *et al.* (2006) into the zero spin

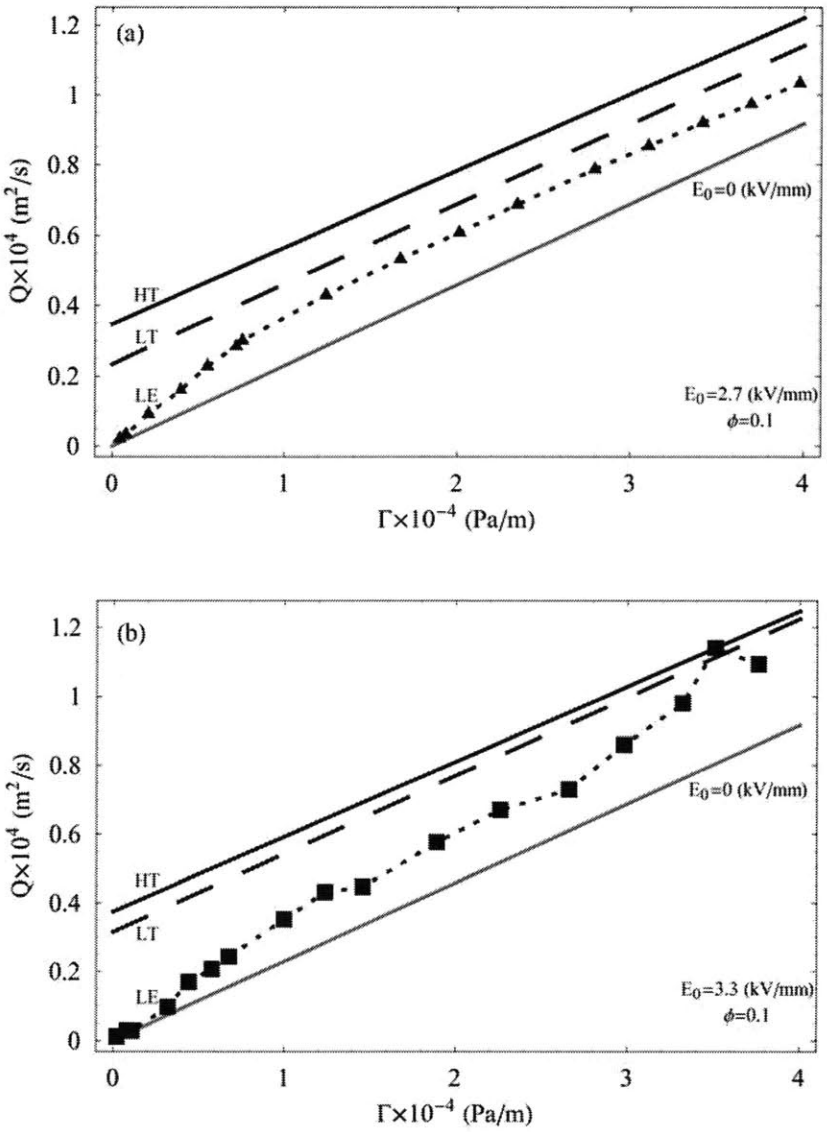

Figure 6.8. Comparison of the 2D Poiseuille volume flow rate results among the present zero spin viscosity HT (solid curve) predictions, the experimental measurements, LE (dotted curve), found in Fig. 6 of Lemaire *et al.* (2006), and the single particle dynamics based predictions (dashed-dashed curve) found in Fig. 6 of Lemaire *et al.* (2006). In this figure, the gray solid lines denote the zero electric field Poiseuille volume flow rate and the ER fluid solid volume fraction is $\phi = 0.1$. The HT and LT solutions and the LE measurements are obtained at DC electric field strength of $E_0 = 2.7$ (kV/mm) in Fig. 6.8(a) and of $E_0 = 3.3$ (kV/mm) in Fig. 6.8(b). No fitting parameters or procedures are used in the evaluation of the HT results.

viscosity HT solutions, Eq. (5.17) or (5.18), we simultaneously plot the HT, LT, and LE results of the 2D Poiseuille total volume flow rate, Q, with respect to the driving pressure gradient, Γ,

in Figs. 6.7(a) and 6.7(b) for the respective applied DC electric field strengths of $E_0 = 2.7$ and 3.3 (kV/mm) with a micro-particle solid volume fraction of $\phi = 0.05$. Similarly, for an ER fluid suspension with a micro-particle solid volume fraction of $\phi = 0.1$, we simultaneously plot the HT, LT, and LE results of the 2D Poiseuille flow rate, Q, with respect to the driving pressure gradient, Γ, in Figs. 6.8(a) and 6.8(b) for the respective applied DC electric field strengths of $E_0 = 2.7$ and 3.3 (kV/mm). In these figures, the critical electric field is evaluated to be $E_c \approx 1.3$ (kV/mm) when using the same material properties and system parameters as in Lemaire *et al.* (2006) and the solid gray lines shown in both Figs. 6.7 and 6.8 denote the zero electric field flow rate solutions of purely viscous Poiseuille flows. Also notice that the LE and LT results are given in Figs. 5 and 6 of Lemaire *et al.* (2006), and that no other fitting parameters are employed when evaluating the zero spin viscosity HT solutions.

Examining Figs. 6.7 and 6.8, we find that the theoretical predictions of HT and LT fall closer to the experimental measurements done by Lemaire *et al.* (2006), *i.e.*, LE, for micro-particle solid volume fraction of $\phi = 0.05$ (Fig. 6.7) as compared to the comparisons shown in Fig. 6.8 for $\phi = 0.1$. In general, the theoretical results obtained from our proposed continuum model in the zero spin viscosity limit, HT, slightly over estimate the volume flow rate as compared to the experimental data shown in Figs. 5 and 6 of Lemaire *et al.* (2006), or LE. The flow rate results predicted by the single particle dynamics two-phase volume averaged model employed in Lemaire *et al.* (2006), LT, generally fall closer to the same set of experimental data, LE, given in their work as compare to our present theoretical treatment, HT. Note however that the theoretical predictions from both the present continuum model, HT, and the single particle dynamics based model, LT, give similar variations of the 2D volume flow rate with respect to the applied electric field strength and pressure gradient—the volume flow rate increases as the applied electric field increases. Nonetheless, the two HT and LT models predict non-zero total volume flow rates at zero driving pressure gradients which is a result inconsistent with the experimental observations found in Lemaire *et al.* (2006), *i.e.*, LE.

Finally, we compare our $\eta' \neq 0$, $\tau_{MW}^2 \omega_x^2 \ll 1$ solutions (HT) to the experimental (LE) and theoretical (LT) results given in Lemaire *et al.* (2006). Substituting the same material properties and physical parameters employed in Lemaire *et al.* (2006) into the total volume flow rate solutions given by Eq. (5.46) or (5.47), we simultaneously plot the HT, LT, and LE results of the

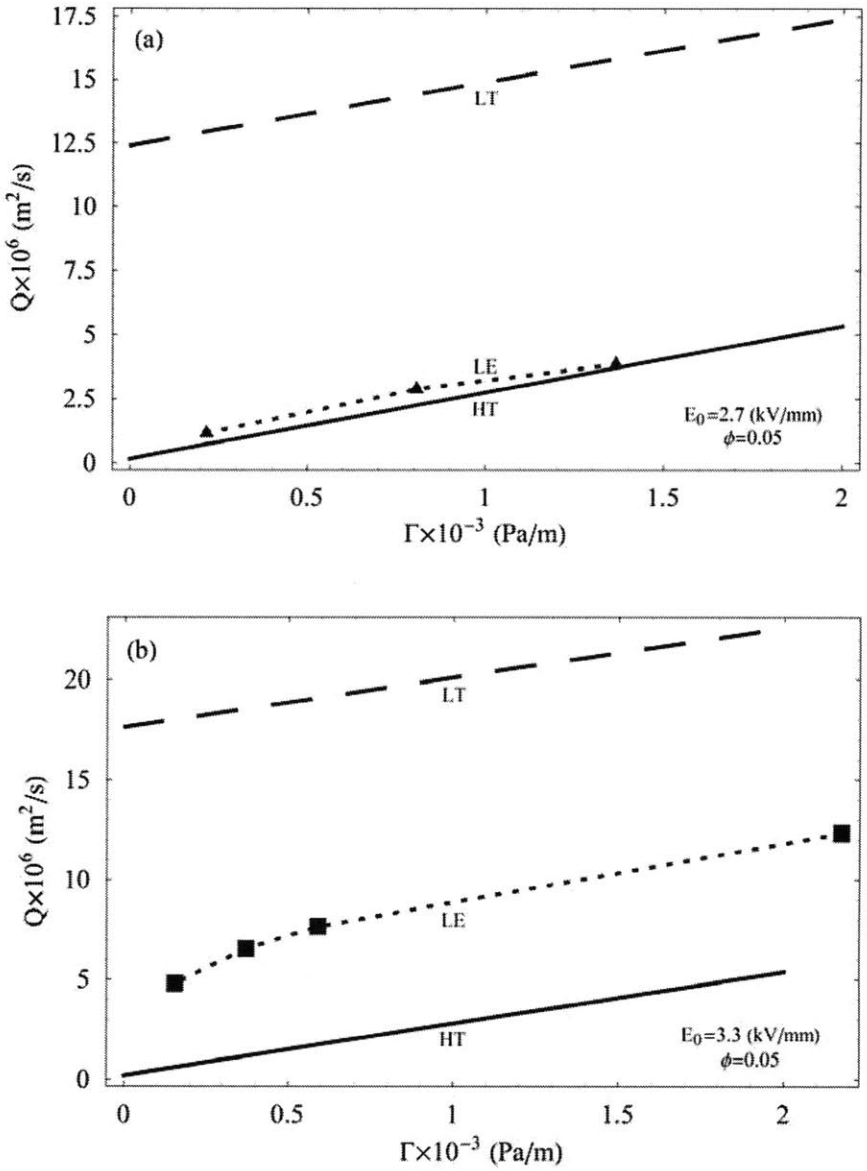

Figure 6.9. Comparison of the 2D Poiseuille volume flow rate results in the low pressure gradient regime among the present finite spin viscosity small spin velocity HT (solid curve) predictions, the experimental measurements, LE (dotted curve), found in Fig. 5 of Lemaire *et al.* (2006), and the single particle dynamics based predictions (dashed-dashed curve) found in Fig. 5 of Lemaire *et al.* (2006). In this figure, the ER fluid solid volume fraction is $\phi = 0.05$. The HT and LT solutions and the LE measurements are obtained at DC electric field strength of $E_0 = 2.7 \ (kV/mm)$ in Fig. 6.9(a) and of $E_0 = 3.3 \ (kV/mm)$ in Fig. 6.9(b). In the evaluations of the HT predictions, $\beta = 1$ and $\eta' = h^2\eta$ are chosen by physical arguments discussed in Chapters 4 and 5. No *ad hoc* fitting parameters or procedures are used in the evaluation of the HT results.

2D Poiseuille volume flow rate, Q, with respect to the driving pressure gradient, Γ, in the low

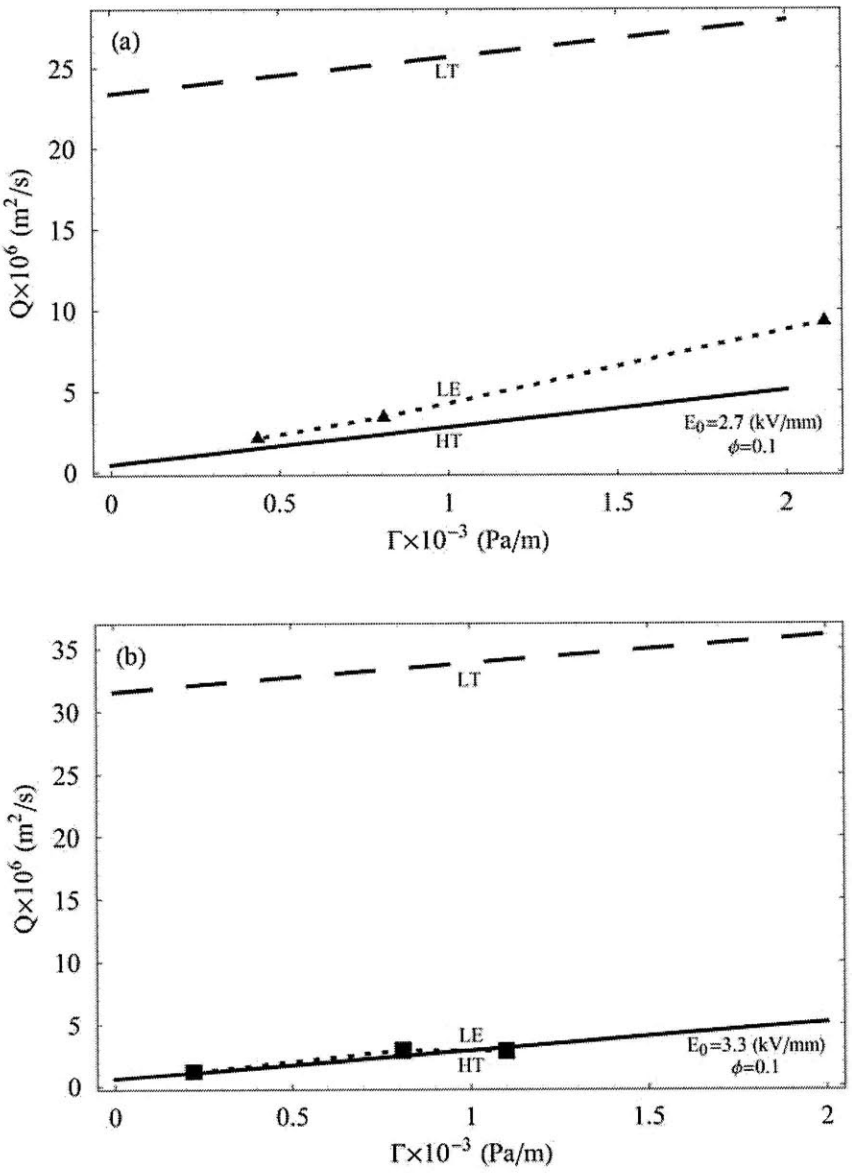

Figure 6.10. Comparison of the 2D Poiseuille volume flow rate results in the low pressure gradient regime among the present finite spin viscosity small spin velocity HT (solid curve) predictions, the experimental measurements, LE (dotted curve), found in Fig. 6 of Lemaire *et al.* (2006), and the single particle dynamics based predictions (dashed-dashed curve) found in Fig. 6 of Lemaire *et al.* (2006). In this figure, the ER fluid solid volume fraction is $\phi = 0.1$. The HT and LT solutions and the LE measurements are obtained at DC electric field strength of $E_0 = 2.7$ (kV/mm) in Fig. 6.10(a) and of $E_0 = 3.3$ (kV/mm) in Fig. 6.10(b). In the evaluations of the HT predictions, $\beta = 1$ and $\eta' = h^2\eta$ are chosen by physical arguments discussed in Chapters 4 and 5. No *ad hoc* fitting parameters or procedures are used in the evaluation of the HT results.

pressure gradient regime of $\Gamma = 0 \sim 2000$ (Pa/m) in Figs. 6.9(a) and 6.9(b) at the respective DC

electric field strengths of $E_0 = 2.7$ and 3.3 (kV/mm) with $\beta = 1$, $\eta' = h^2\eta \approx h^2\eta_0(1+2.5\phi)$ $(N \cdot s)$, and micro-particle solid volume fraction of $\phi = 0.05$. As for the case with micro-particle solid volume fraction of $\phi = 0.1$, the same is done in Figs. 6.10(a) and 6.10(b) at the respective DC electric field strengths of $E_0 = 2.7$ and 3.3 (kV/mm) with $\beta = 1$, $\eta' = h^2\eta \approx h^2\eta_0(1+2.5\phi)$ $(N \cdot s)$. Note that the theoretical and experimental results denoted respectively by LT and LE are from Figs. 5 and 6 of Lemaire *et al.* (2006), and that the choice of numerical values of the boundary condition selection parameter, $\beta = 1$, and the spin viscosity, $\eta' = h^2\eta$, is based on the physical arguments previously discussed in Chapters 4 and 5. No other *ad hoc* fitting parameters or procedures are used in our HT modeling.

By carefully examining Figs. 6.9 and 6.10, it can be found that the present HT $\eta' \neq 0$, $\tau_{MW}^2\omega_x^2 \ll 1$ solutions fall much closer to the experimental measurements, LE, reported by Lemaire *et al.* (2006) and are closer to the physical reality of zero (or nearly zero) volume flow rates at zero driving pressure gradients as compared to the single particle dynamics based two-phase volume averaged effective medium analysis, LT, employed in Lemaire *et al.* (2006). Since Lobry and Lemaire (1999) have reported that up to this point, no negative ER response due to micro-particle Quincke rotation, *i.e.*, nER2, has been experimentally observed without an initial macroscopically imposed flow vorticity, it is not likely physical to have a finite flow rate at zero driving pressure gradients as predicted by the single particle dynamics based two-phase volume averaged effective medium analysis, LT, and the zero spin viscosity, $\eta' = 0$, analysis under the continuum mechanical framework presented in this thesis. However, in the $\eta' \neq 0$, $\tau_{MW}^2\omega_x^2 \ll 1$ limit, theoretical predictions obtained from our continuum mechanical modeling field equations are capable of capturing the low pressure gradient behavior, namely, zero or nearly zero volume flow rates at zero pressure gradients and bring the theoretical modeling of the present nER2 phenomenon more closer to physical reality. This result predicted by our $\eta' \neq 0$, $\tau_{MW}^2\omega_x^2 \ll 1$ solutions is indeed very encouraging since both our present zero spin viscosity analysis and the single particle dynamics model employed in literature (Lemaire *et al.*, 2006) cannot capture this low driving pressure gradient, low volume flow rate behavior and thus offers the possibility of taking one more step closer to accurately predicting the 2D Poiseuille total volume flow rates using continuum anti-symmetric/couple stress theories with finite spin viscosities.

6.4 Comparison of 2D Poiseuille Flow Velocity Profile Results Found in Chapter 5 with Those Found in Current Literature

We close this chapter by comparing the 2D Poiseuille velocity profiles predicted by the continuum mechanical modeling field equations presented in this thesis with the experimental ultrasound velocimetry velocity profile measurements reported in a very recent paper by Peters *et al.* (2010). We shall first compare the continuum theory velocity profiles obtained in the zero spin viscosity limit with the experimental measurements found in Fig. 9 of Peters *et al.* (2010), and then compare the velocity profiles predicted in the finite spin viscosity small spin velocity limit of our continuum mechanical equations with the measurements shown in Fig. 9 of Peters *et al.* (2010). The relevant material properties and experimental conditions employed in the experiments of Peters *et al.* (2010) are a micro-particle (PMMA particles) diameter of $d = 6$ (μm), a carrier liquid viscosity of $\eta_0 = 0.0165$ $(Pa \cdot s)$, a liquid phase electrical conductivity of $\sigma_1 = 5.4 \times 10^{-8}$ (S/m), and a particle-liquid suspension made with a micro-particle solid volume fraction of 5%, *i.e.*, $\phi = 0.05$. The resulting critical electric field strength found in Peters *et al.* (2010) is around $E_c = 1.8$ (kV/mm).

By substituting the above material and system parameters as well as a channel height (or spacing between the two electrodes) of $h = 1.15$ (mm) into Eqs. (5.15) and (5.16), we plot the zero spin viscosity total linear velocity profiles predicted by our present continuum model at electric field strengths of $E_0 = 0$, 1.8483, 2, 2.1, 2.2, and 2.275 (kV/mm) with a pressure gradient of $\Gamma = 5974.6$ (Pa/m) and compare these results with the ultrasound velocimetry measurements reported in Fig. 9 of Peters *et al.* (2010) as shown in Fig. 6.11. In Fig. 6.11, the gray solid curve represents the zero electric field solution, *i.e.*, purely viscous Poiseuille flow, of the velocity profile, whereas the black solid curves represent the zero spin viscosity velocity profiles respectively evaluated at $E_0 = 1.8483$, 2, 2.1, 2.2, and 2.275 (kV/mm) with $\Gamma = 5974.6$ (Pa/m). The dots shown in Fig. 6.11 are the ultrasound velocity profiles as found in Fig. 9 of Peters *et al.* (2010) measured at $E_0 = 0$ (gray box), 1.8 (gray triangle), 2 (black star), 2.1 (black diamond), 2.2 (black triangle), and 2.275 (black box) (kV/mm). Notice that we have shifted the

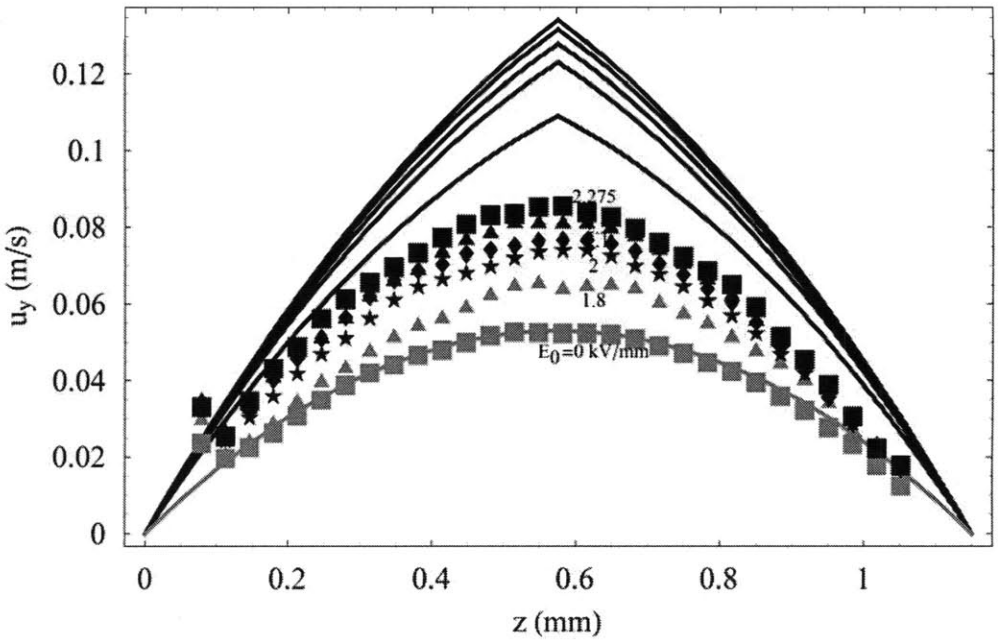

Figure 6.11. Comparison of the electrorotation assisted 2D Poiseuille flow velocity profiles between the ultrasound velocimetry experimental measurements as reported in Peters *et al.* (2010) and the theoretical predictions obtained from the continuum mechanical modeling field equations in the zero spin viscosity limit as presented in the present thesis.

spatial z-coordinate system from $-0.575 \le z \le 0.575$ (mm) as found in Fig. 9 of Peters *et al.* (2010) to $0 \le z \le 1.15$ (mm) as shown in our current Fig. 6.11 so as to satisfy the coordinate system employed in our zero spin viscosity analysis given in Chapter 5. When plotting Fig. 6.11, we have also discarded the ultrasound data points near the electrode or wall boundaries as reported in Fig. 9 of Peters *et al.* (2010) due to ultrasound signal reflection and saturation reasons (Chaves *et al.*, 2006, 2007; Peters *et al.*, 2010).

From the comparison shown in Fig. 6.11, it can be learned that the zero spin viscosity solutions to the 2D Poiseuille velocity profiles predicted by the present continuum modeling field equations do not agree very well with the ultrasound velocimetry measurements (Peters *et al.*, 2010)—particularly due to the cusp structure in the predicted velocity profiles at the mid-plane of the flow channel resulting from a zero spin viscosity analysis. However, the zero spin viscosity velocity profiles capture the right order of magnitude of the velocity profiles and the increase of linear velocity with respect to the increase of the applied electric field strength as compared to the experimental measurements reported by Peters *et al.* (2010). Again, we find that

the zero spin viscosity results over estimates the magnitude of the linear velocity profiles as compared to the experimental measurements found in current literature, which is consistent with the previous comparisons of the 2D Poiseuille volume flow rate as discussed in Section 6.3.

Before proceeding to comparing the Poiseuille velocity profiles obtained in the finite spin viscosity small spin velocity limit with the experimental results found in Peters *et al.* (2010), we discuss the validity of the respective numerical values of the channel height, h, pressure gradient, Γ, and electric field strength, E_0 (particularly near 1.8 (kV/mm)), used in our calculations of our present continuum mechanical solutions in the zero spin viscosity limit, *i.e.*, Eqs. (5.15) and (5.16). Firstly, although the designed value of the channel height is $h=1$ (mm) as given in Peters *et al.* (2010), we have used a channel height of $h=1.15$ (mm) in the evaluation of our zero spin viscosity solutions for Fig. 6.11. We employ this $h=1.15$ (mm) value instead of the designed $h=1$ (mm) value based on the direct measurements of the positions of the Poiseuille flow channel wall boundaries as shown in Figs. 8 and 9 of Peters *et al.* (2010). Next, due to the installation of the ultrasound probe that measures the flow velocity in the Poiseuille flow channel, a differential pressure sensor that measures the pressure drop or pressure gradient in the flow channel cannot be further installed to the experimental apparatus of Peters *et al.* (2010). Thus, in their work (Peters *et al.*, 2010), the true experimental values of the pressure gradient were not directly and simultaneously measured along with the ultrasound velocimetry and volume flow rate measurements. From the zero electric field velocity profile measurements and the hydraulic resistance of the Poiseuille flow test channel (not the whole flow circuit) reported in Peters *et al.* (2010), we can back out a pressure drop of $\Delta p=1508$ (Pa) and subsequently calculate a pressure gradient of $\Delta p/L=1508/0.22=6854.5$ (Pa/m) for the experimental measurements found in Figs. 8 and 9 of Peters *et al.* (2010). Note however that we have used a pressure gradient of $\Gamma=5974.6$ (Pa/m) in our evaluations of Eqs. (5.15) and (5.16) as shown in Fig. 6.11 so as to achieve good agreement between the purely viscous Poiseuille flow velocity profile and the ultrasound velocimetry measurements done by Peters *et al.* (2010) at zero electric field. This discrepancy between the two values is within 15% and is likely due to end effects or entry losses of a finite dimension Poiseuille flow channel. Lastly, we have used an applied electric field strength of $E_0=1.8483$ (kV/mm) in the theoretical evaluation of our zero spin viscosity solutions, which were compared to the ultrasound velocity profiles measured

around $E_0 = 1.8\,(kV/mm)$ by Peters *et al.* (2010) as shown in Fig. 6.11, so as to examine the improvement of theory made by our proposed "rotating coffee cup model" for the polarization relaxation of the ER fluid as discussed in Chapter 3 of this thesis. The difference between the values of $E_0 = 1.8483$ and 1.8 (kV/mm) is within 3% and the uncertainty in the electric field strength measurement of $E_0 = 1.8\,(kV/mm)$ is likely easily accounted for by measurement error or contact resistance between the high voltage probe and the electrodes of the flow apparatus used in the experiments of Peters *et al.* (2010). Based on the above discussions, it can be learned that the numerical values of the channel height, h, pressure gradient, Γ, and electric field strength, E_0 (near 1.8 (kV/mm)), we have substituted into our continuum mechanical theory in the zero spin viscosity limit are generally reasonable and valid for the purposes of our comparison. Hence, we shall employ a channel height of $h = 1.15$ (mm), a pressure gradient of $\Gamma = 5974.6$ (Pa/m), and an applied electric field strength of $E_0 = 1.8483$ (kV/mm) (to be compared with the ultrasound results measured by Peters *et al.* (2010) at $E_0 = 1.8\,(kV/mm)$) in the theoretical calculations of our continuum mechanical results obtained in the finite spin viscosity small spin velocity limit for the comparison between our present theory and the experimental measurements found in current literature as presented in the following.

Substituting the relevant experimental parameters of $d = 6$ (μm), $\eta_0 = 0.0165$ $(Pa \cdot s)$, $\sigma_1 = 5.4 \times 10^{-8}$ (S/m), $\phi = 0.05$, and $E_c = 1.8$ (kV/mm) as given in Peters *et al.* (2010) as well as a channel height of $h = 1.15$ (mm) and a pressure gradient of $\Gamma = 5974.6$ (Pa/m) into Eqs. (5.33), (5.35), and (5.38)-(5.45), we evaluate the finite spin viscosity small spin velocity, *i.e.*, $\eta' \neq 0$, $\tau_{MW}^2 \omega_x^2 \ll 1$, Poiseuille velocity profile solutions obtained from our present continuum mechanical model at electric field strengths of $E_0 = 0$, 1.8483, 2, 2.1, 2.2, and 2.275 (kV/mm) with $\beta = 1$ and $\eta' \approx 0.012 h^2 \eta = 0.012 h^2 \eta_0 (1 + 2.5\phi)$ $(N \cdot s)$ and simultaneously plot our $\eta' \neq 0$, $\tau_{MW}^2 \omega_x^2 \ll 1$ theoretical predictions with the experimental velocity profile measurements found in Fig. 9 of Peters *et al.* (2010) in Fig. 6.12. In Fig. 6.12, similar to Fig. 6.11, the gray solid curve represents the zero electric field solution, *i.e.*, purely viscous Poiseuille flow, of the velocity profile, whereas the black solid curves represent the $\eta' \neq 0$, $\tau_{MW}^2 \omega_x^2 \ll 1$ Poiseuille velocity profiles respectively evaluated at $E_0 = 1.8483$, 2, 2.1, 2.2, and 2.275 (kV/mm) with $\Gamma = 5974.6$

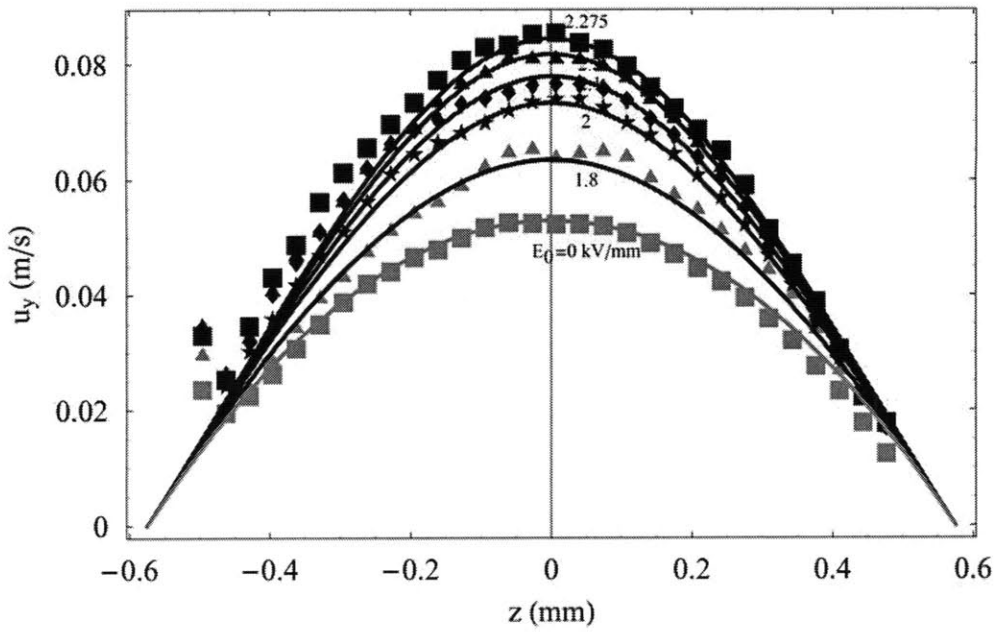

Figure 6.12. Comparison of the electrorotation assisted 2D Poiseuille flow velocity profiles between the ultrasound velocimetry experimental measurements as reported in Peters *et al.* (2010) and the theoretical predictions obtained from the continuum mechanical modeling field equations in the finite spin viscosity small spin velocity limit as presented in the present thesis.

(Pa/m), $\beta = 1$, and $\eta' \approx 0.012h^2\eta = 0.012h^2\eta_0\left(1+2.5\phi\right)$ $(N\cdot s)$. The dots shown in Fig. 6.12 are the ultrasound velocity profiles as found in Fig. 9 of Peters *et al.* (2010) measured at $E_0 = 0$ (gray box), 1.8 (gray triangle), 2 (black star), 2.1 (black diamond), 2.2 (black triangle), and 2.275 (black box) (kV/mm). Again when plotting Fig. 6.12, we have discarded the ultrasound data points near the electrode or wall boundaries as reported in Fig. 9 of Peters *et al.* (2010) due to ultrasound signal reflection and saturation reasons (Chaves *et al.*, 2006, 2007; Peters *et al.*, 2010). There is no need to shift the coordinate system in Fig. 6.12 as we did for Fig. 6.11 since the spatial z-coordinate system shown in Fig. 9 of Peters *et al.* (2010) is defined in the same manner as that shown in Fig. 5.8 (and Fig. 6.12) used for solving our finite spin viscosity small spin velocity solutions, *i.e.*, $-0.575 \le z \le 0.575$ (mm).

From the comparison shown in Fig. 6.12, it can be found that the finite spin viscosity small spin velocity solutions to the Poiseuille velocity profile obtained from our present continuum mechanical modeling field equations agree very well with the experimental ultrasound velocimetry results as reported in Fig. 9 of Peters *et al.* (2010). This rare degree of agreement

between theory and experiment is not only surprising, but also encouraging since this result once again suggests that our continuum mechanical theory applied in the finite spin viscosity small spin velocity limit as presented in this thesis is more capable of capturing the physical reality of the Quincke rotation induced negative ER flow phenomenon as compared to the continuum zero spin viscosity solutions. Although the application of the $\eta' \neq 0$, $\tau_{MW}^2 \omega_x^2 \ll 1$ solutions introduces two additional degrees of fitting freedom, namely the boundary condition selection parameter, β, and the spin viscosity, η', we did *not* actually fit the numeric value of β and set the boundary condition selection parameter as $\beta = 1$ based on the results discussed in the previous Chapters of 4 and 5 as well as in the paper of Kaloni (1992). This situation leaves the spin viscosity, η', as the only degree of freedom to be determined in the finite spin viscosity small spin velocity Poiseuille velocity profile solutions. From the work of Zaitsev and Shliomis (1969) and the book by Rosensweig (1997) as well as our discussions given in Sections 4.4.2 and 5.4.2, we know that the magnitude of the spin viscosity, η', generally scales as the suspension viscosity, η, times the square of a characteristic angular momentum diffusion length, l_D. Although in both Zaitsev and Shliomis (1969) and Rosensweig (1997), the characteristic angular momentum diffusion length, l_D, has been set to equal the average particle-to-particle distance, which scales as the micro-particle diameter, d, that is, $l_D \sim d$ and subsequently $\eta' \sim d^2\eta$, we have instead set the characteristic angular momentum diffusion length, l_D, to scale as the height of the Poiseuille flow channel, h, *i.e.*, $l_D \sim h$ and subsequently $\eta' \sim h^2\eta$, throughout the present thesis since we are considering a fully developed steady state internal fluid flow with the ER fluid continuum being composed of an enormous amount of continuum ER fluid parcels which consist of a representative amount or ensemble of rotating micro-particles and carrier liquid molecules. Acknowledging both literature (Zaitsev & Shliomis, 1969; Rosensweig, 1997) and the comparison results discussed in Sections 6.2 and 6.3, a general fitting range for the value of the spin viscosity can be given as

$$d^2\eta \leq \eta' \leq h^2\eta, \tag{6.4}$$

which in terms of the numerical values from the experimental conditions described in Peters *et al.* (2010) can be re-written as

$$6.7\times10^{-13} \le \eta' \le 2.5\times10^{-8} \ (N\cdot s). \tag{6.5}$$

Nonetheless, as can be found from the comparison shown in Fig. 6.12, best fit is achieved between our finite spin viscosity small spin velocity theory and the experimental measurements of Peters *et al.* (2010) when the value of the spin viscosity is around

$$\eta' \approx 0.012h^2\eta = 0.012h^2\eta_0\left(1+2.5\phi\right) = 2.96\times10^{-10} \ (N\cdot s), \tag{6.6}$$

which is a value that not only falls within the range given by Eqs. (6.4) and (6.5), but also agrees with the best fit values of the spin viscosity (between theory and experiment) reported for ferrofluid spin-up flows in cylindrical geometries as discussed in Elborai (2006) and He (2006). Therefore, our choice of the value of the spin viscosity and subsequently the good agreement between our present continuum theory and the experimental measurements of Peters *et al.* (2010) shown in Fig. 6.12 are, rigorously speaking, not merely *ad hoc* or arbitrary fitting results, but still supported by physical arguments as well as previous experimental measurements as found in current literature. Note however that care must still be exercised when applying the finite spin viscosity small spin velocity solutions to predicting the negative ER (nER2) responses characterized by the 2D Poiseuille flow velocity profile. This is because with the pressure gradient of $\Gamma = 5974.6 \ (Pa/m)$ employed in evaluating the continuum solutions shown in Fig. 6.12, the value of the resulting dimensionless spin velocity, *i.e.*, $\omega^* = \tau_{MW}\omega_x$, is roughly around $\tau_{MW}\omega_x \approx 0.7$ (or $\tau_{MW}^2\omega_x^2 \approx 0.49$), which is a situation that requires relaxing the small spin limit constraint on or extending the range of application of the analytical continuum solutions, Eqs. (5.33), (5.35), and (5.38)-(5.45), as presented in Section 5.4.

Although it may be argued that the velocity profiles obtained from the combined single particle dynamics two-phase volume averaged effective medium theory as shown in Fig. 9 of Peters *et al.* (2010) are also in good agreement with their ultrasound experimental measurements, the success of the single particle dynamics based theory as described in Peters *et al.* (2010) is basically due to a combined effort of theoretical modeling, experimental rheometric data utilization, and numerical solution methods, whereas the success of applying the present continuum mechanical modeling field equations in the finite spin viscosity small spin velocity limit is merely based on a "plug-and-play" effort of substituting the required material properties or system parameters (with minimal fitting of the spin viscosity based on information available in the literature) and plotting the resulting electrorotation assisted 2D Poiseuille flow velocity

profiles. Hence, the continuum theory in the finite spin viscosity small spin velocity limit as presented in this thesis not only improves the zero spin viscosity continuum modeling, but also is easier and more straightforward in terms of practical implementation and engineering analysis. The implications and assumptions inherent in a "finite spin viscosity (additional dissipation mechanisms) rotating coffee cup (treating the continuum spin velocity and the averaged micro-particle rotation speed as two different variables in the ER fluid polarization relaxation)" modeling approach may also suggest further physical insights and ideas to the research fields of negative ER effects induced by micro-particle Quincke rotation as well as ferrofluid spin-up flows in magnetorheology.

Chapter 7

Concluding Remarks, Contributions, and Future Work

7.1 Summary of Thesis and Concluding Remarks

The negative electrorheological responses (nER2) of two dimensional Couette and Poiseuille flows with internal, spontaneous micro-particle electrorotation, or Quincke rotation, are modeled and analyzed through a "fully continuum mechanical modeling field equations" formulation in this thesis. Combining the theories of particle electromechanics and continuum anti-symmetric/couple stresses, general governing equations are developed and presented to describe the physical aspects of mass conservation, linear momentum balance, angular momentum balance, and electro-quasi-static (EQS) field of this novel negative electrorheological fluid flow phenomenon. A "rotating coffee cup model" is also developed to derive the retarding polarization relaxation equation along with its accompanying equilibrium retarding polarization in order to characterize the non-equilibrium motion effects of the continuum spin velocity, $\bar{\omega}$, continuum linear velocity, $\bar{v}$, and micro-particle rotation speed, $\overline{\Omega}$, on the polarization responses as well as the electrical body torque inputs of the negative ER fluid flow. Using the general assumptions of steady, incompressible, fully developed, and two dimensional flows, we reduce and simplify the full general governing equations in the zero spin viscosity, $\eta' = 0$, and the finite spin viscosity small spin velocity, $\eta' \neq 0$, $\tau_{MW}^2 \omega_x^2 \ll 1$, limits for both Couette and Poiseuille flow geometries.

In the zero spin viscosity limit, $\eta' = 0$, the two sets of simplified governing equations for the respective Couette and Poiseuille flow geometries are further reduced into two respective algebraic, cubic equations of the ER fluid flow spin velocity, ω^*. Symmetry, "free-to-spin," and stable micro-particle rotation conditions are then applied to the two cubic spin velocity equations to choose, select, or pick out the real valued solution or combination of solutions consistent with the physical assumptions and phenomena of interest. Expressions for the spin velocity, ω^*, and effective viscosity, η^*, of Couette flow as well as the spin velocity field, ω^*, linear velocity field, u^*, and the 2D volume flow rate, Q, of Poiseuille flow are further derived in terms of the applied DC electric field strength, E^*, shear rate, γ^* (for Couette flow), driving pressure gradient, Γ^* (for Poiseuille flow), or spatial coordinate, z^*, by respectively substituting the most physically suitable and meaningful solution or combination of solutions to the spin velocity, ω^*, into the linear momentum equation with the no-slip boundary conditions on the velocity field being applied at the spatial boundaries.

As for the limit of finite spin viscosity small spin velocity, *i.e.*, $\eta' \neq 0$, $\tau_{MW}^2 \omega_x^2 \ll 1$, the governing equations are further simplified into two sets of linearized coupled ordinary differential equations for the Couette and Poiseuille flow geometries, respectively. Combining the physical arguments of symmetry and stable micro-particle rotation, we solve the linearized coupled equations by applying the no-slip boundary condition to the linear velocity field, $\bar{v}$, and the boundary condition of $\bar{\omega} = 0.5\beta\nabla \times \bar{v}$ with β being the boundary condition selection parameter to the spin velocity field, $\bar{\omega}$. Analytical solutions of the spin velocity, ω^*, linear velocity, u^*, and effective viscosity, η^*, to Couette flow as well as solutions of the spin velocity, ω^*, linear velocity, u^*, and two dimensional volume flow rate, Q, to Poiseuille flow are obtained and expressed in terms of the applied DC electric field strength, E^*, boundary condition selection parameter, β, spin viscosity, η' or η_p^*, and driving shear rate, γ^* (for Couette flow), or pressure gradient, Γ^* (for Poiseuille flow).

After obtaining the solutions in the respective zero spin viscosity and finite spin viscosity small spin velocity limits, a series of parametric studies are then performed on these solutions via varying the pertinent physical parameters involved in several parametric regimes of interest so as

to illustrate the negative electrorheological behavior and fluid flow response due to internal micro-particle electrorotation. The principle results and findings of this thesis are given in the following:

Zero Spin Viscosity Results

(i) With internal micro-particle electrorotation, the spin velocity, ω^*, increases as either the applied electric field strength, E^*, or the shear rate, γ^*, is increased for Couette flow. Contrarily, the spin velocity reduces back to the zero electric field solution ($E^*=0$, no micro-particle electrorotation), *i.e.*, $\omega_0^*=-\gamma^*/2$, or half of the flow vorticity of purely viscous Couette flow, as the applied electric field strength is decreased. In the limit of zero spin viscosities, the linear Couette velocity profile, $u_y(z)=U_0 z/h$, remains invariant regardless of the applied electric field strength.

(ii) The effective viscosity, η^*, is found to decrease as the applied DC electric field strength increases for Couette flow with internal micro-particle electrorotation. However, as the driving shear rate becomes large, the amount of reduction in the effective viscosity is reduced regardless of the applied electric field strength. For a decreasing electric field strength, the effective viscosity goes back to the zero electric field solution, $\eta^*=1$, *i.e.*, the zero field viscosity of the ER fluid (or particle-liquid mixture), $\eta \approx \eta_0(1+2.5\phi)$, as given by the Einstein relation.

(iii) With a constant driving pressure gradient, Γ^*, the magnitude of the normalized Poiseuille spin velocity, $\widetilde{\omega}^*$, as well as the jump or discontinuity in the spin velocity profile increases as the applied electric field, E^*, increases whereas the spin velocity reduces back to the zero field solution, $\widetilde{\omega}_0^*=\left(z^*-0.5\right)$, and the discontinuity in the spin velocity profile diminishes as E^* is reduced. The normalized spin velocity solution also approaches back to the zero electric field solution, or half the vorticity of purely viscous Poiseuille flow, when the driving pressure gradient becomes very large while the DC electric field strength is kept constant.

(iv) With a constant driving pressure gradient, Γ^*, the magnitude of the dimensionless (and normalized) Poiseuille linear velocity, u^*, as well as the sharpness of the cusp in the velocity

profile increases as the applied electric field, E^*, increases. On the contrary, the velocity profile reduces back to the zero field solution, $u_0^* = z^*\left(1-z^*\right)$, and the cusp in the velocity profile becomes blunt as E^* is reduced. The linear total velocity, u^*, also approaches back to the zero electric field solution when the driving pressure gradient is increased with the applied DC electric field strength being kept constant.

(v) The two dimensional Poiseuille volume flow rate, Q, increases as the applied DC electric field strength increases whereas the electrorotation enhanced flow rate solution reduces back to the zero electric field solution, $Q_0 = \Gamma h^3/12\eta$, as the applied electric field is decreased. At zero driving pressure gradients, the electrorotation enhanced volume flow rate assumes some finite value because of the fact that we have employed the spin velocity solution that satisfies the symmetry, real valued, stable micro-particle rotation, and free-to-spin conditions in the evaluation of Q in the zero spin viscosity limit.

(vi) Comparing the results of effective viscosity and volume flow rate obtained in the present thesis with the theoretical and experimental results found in current literature (Lemaire *et al.*, 2006, 2008), it can be found that both the single particle dynamics based two-phase volume averaged model and our present continuum mechanical modeling field equations in the zero spin viscosity limit qualitatively predict the same trends of variation for the effective viscosity with respect to the electric field strength and average shear rate, and for the volume flow rate with respect to the field strength and driving pressure gradient. Using the same material properties and system parameters as found in current literature (Lemaire *et al.*, 2006, 2008), the Couette effective viscosity solutions predicted by our proposed continuum mechanical model generally fall closer to the experimental observations as reported in current literature (Lemaire *et al.*, 2008).

Finite Spin Viscosity Small Spin Velocity Results

(i) The magnitude of the Couette total spin velocity profile, ω^*, generally increases as the applied DC electric field strength, E^*, is increased while the shear rate, γ^*, spin viscosity, η_p^*, and boundary condition parameter, β, are kept constant, or when the spin viscosity, η_p^*, is reduced while the electric field strength, E^*, the shear rate, γ^*, and boundary condition

parameter, β, are kept constant. By reducing the applied electric field strength (with other parameters kept constant) or increasing the spin viscosity, the magnitude of the spin velocity profile reduces back to the zero electric field solution of half the vorticity of purely viscous Couette flow, *i.e.*, $\omega_0^* = -\gamma^*/2$. The normalized spin viscosity, $\widetilde{\omega^*}$, also approaches the zero electric field value as the driving shear rate or Couette boundary driving velocity is increased while the other parameters are maintained constant. As for the variations of the spin velocity profile with respect to the boundary condition selection parameter, β, the exact value of the spin velocity slightly decreases as the value of β is reduced for general electric field strengths greater than one, *i.e.*, $E^* > 1$. On the other hand, for electric field strengths less than one, $E^* < 1$, the exact values of the spin velocity increases as the value of β is reduced. This result is generally due to the different forms of polarizabilities (Eq. (4.7), which depends on the micro-particle rotation speed given in Eq. (2.57)) or equilibrium polarization (Eq. (3.32) and (3.33)) employed in the governing equations and the subsequent analytical solutions for the respective regimes of the applied electric field strengths.

(ii) The magnitude of the micro-particle Quincke rotation induced linear velocity, u_q^*, is increased as the applied electric field strength, E^*, is increased (with other parameters kept constant) or as the spin viscosity, η_p^*, is decreased while the other parameters are maintained constant. The induced linear velocity approaches to the zero electric field solution of "zero induced linear velocity" as the applied electric field is decreased, as the driving shear rate is increased (for the electric field regime of $E^* > 1$), and the spin viscosity is increased while their respective complementary parameters are held constant. Increasing or reducing the boundary condition selection parameter, β, generally has very little influence on the variations of the induced linear velocity profile in the electric field strength regime of $E^* > 1$. However, the magnitude of the induced linear velocity increases as the value of β decreases when the ER fluid flow is subjected to a DC electric field strength of $E^* < 1$. Again, this result is due to the different forms of polarizabilities (Eq. (4.7), which depends on the micro-particle rotation speed given in Eq. (2.57)) employed in the governing equations and the subsequent analytical solutions for the respective regimes of the applied electric field strengths.

(iii)For the electric field strength regime of $E^* > 1$, it can be found that the variations of the Couette effective viscosity solutions with respect to the applied shear rate obtained in the $\eta' \neq 0$, $\tau_{MW}^2 \omega_x^2 \ll 1$ limit behave similarly to those found in the zero spin viscosity limit, $\eta' = 0$, *i.e.*, the exact value of the effective viscosity decreases as the applied electric field strength increases (with γ^*, β, and η_p^* kept constant), and the reduction in the effective viscosity decreases and approaches to the zero electric field solution as the driving shear rate increases regardless of the electric field strength applied. Moreover, with γ^*, β, and $E^* > 1$ being kept constant, the exact value of the Couette effective viscosity decreases as the spin viscosity is reduced, and the reduction in the effective viscosity is decreased and approaches to the zero electric field solution as the driving shear rate becomes very large regardless of the value of the spin viscosity. The reduction in the effective viscosity is also decreased as the value of the boundary condition selection parameter, β, is reduced while the other parameters are kept constant. On the other hand, for the electric field strength regime of $E^* \leq 1$, we find that the Couette effective viscosity solutions are generally independent or invariant of the driving shear rate or boundary velocity. The exact value of effective viscosity generally decreases as the applied DC electric field is increased, as the boundary condition selection parameter is increased, and as the spin viscosity is decreased while their respective complementary parameters are held constant. Note that for the electric field regime of $E^* \leq 1$, effective viscosities greater than one, *i.e.*, positive ER effect, instead of effective viscosities less than one, *i.e.*, negative ER effect, are predicted for boundary condition selection parameters generally less than one. Yet, this prediction is not likely a valid explanation or interpretation of the viscosity increase due to particle chaining and structure formation as observed at low shear rates and low electric field strengths in Lemaire *et al.* (2008), and is generally inconsistent with the experimentally observed negative ER phenomenon considered herein.

(iv)Regardless of the electric field strength regimes of interest, the total spin velocity profiles, ω^*, obtained for the Poiseuille geometry generally increases as the applied electric field strength is increased, as the spin viscosity is decreased, or as the boundary condition selection parameter is increased while their respective complementary parameters are maintained constant. The total spin velocity profile approaches to the zero electric field

solution of half the vorticity of purely viscous Poiseuille flow as the electric field strength is reduced or as the spin viscosity is increased. The normalized spin velocity profile also reduces to the zero electric field value as the driving pressure gradient increases while the applied DC electric field (in the regime of $E^* > 1$) and the rest of the parameters are kept constant.

(v) The micro-particle Quincke rotation induced linear velocity of Poiseuille flow, u_q^*, generally increases as the applied electric field strength is increased while the pressure gradient, the spin viscosity, and the boundary condition selection parameter is held constant. The induced velocity also increases as the spin viscosity is reduced with the rest of the parameters being constant. By reducing the electric field strength or increasing the value of the spin viscosity while keeping their respective complementary parameters constant, the induced linear velocity approaches the zero electric field solution of zero induced linear velocity, or equivalently the total linear velocity of purely viscous Poiseuille flow. The dimensionless as well as normalized induced velocity also approaches its zero electric field value as the driving pressure gradient is increased to a large value while the electric field strength (for the regime of $E^* > 1$), the spin viscosity, and the boundary condition selection parameter is kept constant. As we decrease the value of the boundary condition selection parameter, β, it can be found that reversal of the induced linear velocity, or a decrease in the total linear velocity, is obtained for both electric field strength regimes, *i.e.*, $E^* > 1$ and $E^* \leq 1$, of interest. This result again suggests an inconsistency between the experimentally observed phenomena (Lemaire *et al.*, 2006) and the theoretical predictions obtained by the continuum anti-symmetric/couple stress theory with a zero or nearly zero spin boundary condition on the spin velocity field.

(vi) Following the previous discussion on the induced linear velocity field, a negatively valued induced volume flow rate, Q_q, or decreased total volume flow rate, Q, is generally obtained regardless of the electric field strength of interest when the value of the boundary condition selection parameter, β, is reduced, which is a result inconsistent with the experimental observations reported in Lemaire *et al.* (2006). Meanwhile, the variations of the induced volume flow rate, Q_q, with respect to the driving pressure gradient generally increases as the applied electric field strength is increased (with $\beta = 1$ and η_p^* held constant) or as the value

of the spin viscosity is reduced while the rest of the parameters are maintained constant. Note however that for the induced flow rate solutions obtained in the electric field strength regime of $E^* > 1$ with $\beta = 1$, the dependence on the driving pressure gradient is in general not very strong, that is, the induced flow rate increases only slightly as the driving pressure gradient is increased in the electric field strength regime of $E^* > 1$ while the rest of the complementary parameters being held constant.

(vii) Substituting the same material properties and system parameters as employed in Lemaire *et al.* (2006, 2008) into our continuum mechanical solutions obtained in the finite spin viscosity small spin velocity limit, the Couette effective viscosity and 2D Poiseuille volume flow rate results predicted by our present continuum model are compared to the theoretical and experimental results reported in current literature (Lemaire *et al.*, 2006, 2008). The comparisons indicate that both the Couette and Poiseuille solutions predicted by our present continuum model in the $\eta' \neq 0$, $\tau_{MW}^2 \omega_x^2 \ll 1$ limit are likely capable of capturing the experimentally observed negative ER behavior, *i.e.*, the respective low viscosity plateau and zero-flow rate at zero driving pressure gradients, as well as fall relatively closer to the experimental data (Lemaire *et al.*, 2006, 2008) in the respective low shear rate and low pressure gradient regimes as compared to the solutions obtained from single particle dynamics two-phase effective medium modeling (Lemaire *et al.*, 2006, 2008) and our present continuum model in the zero spin viscosity limit.

(viii) Using the same material properties and system parameters, we compared the electrorotation assisted 2D Poiseuille flow velocity profiles predicted by the present continuum mechanical modeling field equations in the finite spin viscosity small spin velocity limit with the experimental ultrasound velocimetry measurements as reported in Peters *et al.* (2010) and found that our present finite spin viscosity continuum theory is in good agreement with the experimental measurements obtained by Peters *et al.* (2010). Additional to the respective comparisons of Couette effective viscosity and Poiseuille volume flow rate, this good agreement in the Poiseuille velocity profile between our present theory and the experimental measurements as found in current literature suggests that the implications and assumptions inherent in a "finite spin viscosity (additional dissipation mechanisms) rotating coffee cup (treating the continuum spin velocity and the averaged micro-particle rotation speed as two different variables in the ER fluid polarization

relaxation)" modeling approach may likely bring further physical insights and ideas to the research fields of negative ER effects induced by micro-particle Quincke rotation as well as ferrofluid spin-up flows in magnetorheology.

7.2 Contributions of Thesis

The contributions made by the present thesis to the current negative ER literature are summarized as follows:

(i) In this thesis, we have developed and presented a "continuum mechanical modeling field equations" formulation to analyze and study the nER2 effect. The present treatment should likely be the first to investigate the nER2 phenomenon from a more field theory based continuum mechanical perspective as compared to the single particle dynamics based two-phase effective medium theory employed in current literature (Brenner, 1970; Lobry & Lemaire, 1999; Cebers *et al.*, 2000; Cebers *et al.*, 2002; Lemaire *et al.*, 2006; Pannacci *et al.*, 2007*a*; Lemaire *et al.*, 2008).

(ii) Additional to our continuum analysis in the zero spin viscosity limit, we have presented a first analysis to investigate finite spin viscosity effects on the negative electrorheological fluid flow phenomenon in both Couette and Poiseuille geometries in the small spin velocity limit.

(iii) As compared to previous literature (Cebers, 1980; Shliomis, 1972, 2002), a "rotating coffee cup model" is firstly proposed in this thesis to account for the non-equilibrium motion effects of the continuum spin velocity, $\overline{\omega}$, the continuum linear velocity, $\overline{v}$, and the micro-particle rotation speed, $\overline{\Omega}$, on the (retarding) polarization relaxation process of the negative ER fluid flow.

(iv) From the finite spin viscosity small spin velocity analysis, we have identified a dimensionless parameter, A as given in Eq. (6.2), which characterizes the ratio of the length scale of the flow geometry, h, to a length scale (ℓ in Eq. (6.3)) determined by the balance between the electrical body torque input and the angular momentum conversion between the linear and spin velocity fields. In the zero spin viscosity limit, *i.e.*, $\eta' = 0$, ℓ goes to zero, which likely implies that the balance between the electrical body torque input and the angular momentum conversion between the linear and spin velocity fields occurs at a very local or

concentrated microscopic scale—the particulate limit of the present continuum mechanical modeling field equations. This result supports the observation that the theoretical solutions predicted by our present continuum model in the zero spin viscosity limit generally varies in a similar manner as compared to those obtained from "single particle dynamics" two-phase effective medium theories.

(v) In this thesis, we offer a new (if not arbitrarily dismissed in the past) perspective of treating the continuum spin velocity and the (averaged) micro-particle rotation speed as separate physical variables. This perspective is equivalent to the question of whether should we treat the spin viscosity and the micro-particle rotation speed as exactly the same (or exactly different) physical variables. With the implementation of the polarization relaxation equation along with its accompanying equilibrium polarization as derived from the "rotating coffee cup model," we treat the spin velocity and the micro-particle rotation speed as different variables and find that the linear governing equations derived in the finite spin viscosity small spin velocity limit are capable of capturing the non-linear negative ER behavior or features similar to those obtained by the zero spin viscosity analysis. Moreover, by treating the spin velocity and the micro-particle rotation speed as different variables, the $\eta' \neq 0$, $\tau_{MW}^2 \omega_x^2 \ll 1$ solutions are also capable of capturing the experimentally observed (Lemaire *et al.*, 2006, 2008) negative ER behavior in the low shear rate or low pressure gradient regimes, which likely suggests that the spin velocity may not be physically exactly the same as the (averaged) micro-particle rotation speed.

(vi) By varying the boundary condition selection parameter, β, we find that our theoretical predictions obtained in the finite spin viscosity small spin velocity limit is generally inconsistent with the experimental observations reported in Lemaire *et al.* (2006, 2008) when $\beta = 0$, *i.e.*, zero spin conditions on the solid-ER fluid boundary. This result offers additional support to Kaloni's (1992) report of theoretical predictions and experimental observations being inconsistent when the zero spin boundary condition, $\beta = 0$, is applied to micro-polar flow fields governed by equations of motion based upon continuum mechanical anti-symmetric/couple stress theories.

7.3 Directions for Future Work

Future work includes a more advanced modeling of the polarization relaxation processes in the negative electrorheological fluid flow, the full non-linear analysis of finite spin viscosity effects on the angular momentum balances within the ER flow field without the restriction of $\tau_{MW}^2 \omega_x^2 \ll 1$, and the search of possible applications of our proposed continuum mechanical modeling field equations theory for this novel negative electrorhological phenomenon, *i.e.*, nER2 effect. Potential applications of the theory presented in this thesis may include design of electrically actuated dampers, clutches, and smart materials (Espin *et al.*, 2005; Esmonde *et al.*, 2009) as well as in modeling or analyzing the electrorheological or magnetorheological responses of physiological and human blood flows (Happel & Brenner, 1983; Larson, 1998; Lukaszewicz, 1999; Haik *et al.*, 2001; Khashan & Haik, 2006).

Appendix

Experimental Considerations

This appendix presents the synthesis, electrical impedance characterization, and rheological viscosity characterization of an electrorheological fluid, namely, a mixture of polyethylene micro-particles and Silicone oil DC 200/Shell DIALA® AX oil liquid, as preparations for the negative electrorheological flow experiments analyzed by our present continuum mechanical model in the previous chapters. We shall also consider the construction of a Poiseuille flow electrorotation testing apparatus and subsequently the electrorotation modified Poiseuille flow rate experiment to demonstrate the experimental methods and procedures in obtaining flow rate measurements via the constructed electrorotation testing apparatus. The purpose of this appendix is to bridge the gap between theoretical analysis and actual experimental measurements since even for similar experiments, the material properties and ER flow responses are generally quite case specific depending on which combination of materials are selected or chosen to synthesize the ER fluid employed in the experiments. For example, two kinds of ER fluid were considered in the experiments done by Boissy *et al.* (1995) to examine the negative ER effect of the first kind (nER1), they are: (i) a mixture of poly(methyl methacrylate) (PMMA) particles and Ugilec T/mineral oil TF 50 (Elf-Atochem) liquid and (ii) a mixture of polyethylene (PE) particles and silicone oil liquid. However, the nER1 effects observed using the PMMA/Ugilec T/TF 50 suspension are generally more significant as compared to the nER1 results obtained from the PE/silicone oil suspension. Perhaps this is likely the reason why later experiments designed and performed to examine the negative ER effect of the second kind (nER2) are generally based on a

PMMA/Ugilec/Dielec suspension (Lobry & Lemaire, 1999; Cebers *et al.*, 2000; Cebers *et al.*, 2002; Lemaire *et al.*, 2006; Pannacci *et al.*, 2007*a*; Lemaire *et al.*, 2008). Note however that Ugilec® (tetrachlorobenzyltoluenes) is a known carcinogen and has been restricted for use in the United States. Thus an alternative as well as environment friendly particle-liquid mixture or blend is required if nER2 experiments were to be performed and studied herein. We offer this possible alternative as the mixture of PE micro-particles and Silicone oil DC 200/Shell DIALA® AX oil liquid and present its synthesis process, electrical and rheological material property characterization measurements, and finally electrorotation modified flow rate experiments. Hopefully, the experimental measurements presented in this appendix promote more environment friendly ER fluids as better candidates for future negative ER fluid flow studies.

In the following sections, we first start with the material selection and the preparation for synthesizing the electrorheological fluid proposed in the present work. After the material and the relative composition of the blend is determined or identified, both the electrical, *i.e.*, dielectric constant and electric conductivity, and the rheological, *i.e.*, viscosity, properties of the ER fluid blend are to be measured and characterized. The construction of the Poiseuille flow channel and the whole electrorotation testing apparatus are then outlined and summarized. We close this appendix by presenting the measurements obtained from the electrorotation modified Poiseuille flow rate experiments performed on the constructed apparatus and the synthesized ER fluid.

A.1 Synthesis and Preparation of Electrorheological Fluid

A.1.1 Criteria of Material Selection for Electrorheological Fluid Synthesis

Although micro-particle Quincke rotation can be observed in both aqueous (Jones, 1984) and non-aqueous particle-liquid suspensions, the negative ER effects discussed in this thesis are generally observed in or designed to operate on transformer oil-particle suspension systems due to the higher dielectric breakdown strengths that can be offered by such non-aqueous liquids when subjected to strong high voltage electric fields. In order to prepare for the negative electrorheological experiments considered in the previous chapters, the synthesis of the non-aqueous liquid-solid particle mixture (or ER fluid) needs to satisfy the following criteria:

(i) The density of the liquid phase should be roughly the same as that of the solid micro-particles so that the suspended particles become neutrally buoyant and are less likely to

sediment through time. For this reason, a blend of two types of oil liquids is generally required since it is less likely to find "one" specific oil that is dense enough to match the density of the insulating dielectric, usually plastic, particles.

(ii) The chemical substance used cannot be extremely toxic. In the past, transformer oils and other dielectric liquids found in high power electrical applications contained polychlorinated biphenyl (PCBs), which is a carcinogen that has been banned in the United States for over three decades. Previous experiments on negative electrorheological flow with internal micro-particle Quincke rotation (Lobry & Lemaire, 1999; Cebers *et al.*, 2000; Cebers *et al.*, 2002; Lemaire *et al.*, 2006; Pannacci *et al.*, 2007*a*; Lemaire *et al.*, 2008) were done using a blend of transformer oil, Ugilec® (tetrachlorobenzyltoluenes), and poly(methyl methacrylate) (or PMMA with a mass density around ~ 1.18 (g/mL)) micro-particles. However, Ugilec® is also extremely toxic and is regulated or banned in the United States. Considering the density matching requirement, and the toxicity of the liquid to be used in the experiments, we find that the selection of the liquid limits the dielectric (plastic) particles being used and vice versa.

(iii) Chemical compatibility of the suspending oil and the suspended solid plastic particles is necessary. Since we are mixing at least two different oils so that the density of the liquid mixture matches that of the added insulating dielectric plastic particles, the two different oils need to be miscible so that a homogeneous oil solution can be obtained, and the oils need to be chemically compatible with the solid plastic particles so that the particles will not dissolve into the liquid phase while they are undergoing Quincke rotation. The chemical compatibility is important because some plastic materials can be dissolved by several common lab hydrocarbons such as toluene (methylbenzene).

(iv) The electrical conductivity modifier must be soluble in the blend of transformer oils. In order to boost up the liquid conductivity of the transformer oil blend (dielectrically insulating) so that the charge relaxation time of the liquid phase is much less than that of the solid phase, a conductivity modifier needs to be added to the liquid phase. This is generally done by adding docusate sodium salt (an organic salt or surfactant, also called Aerosol OT or AOT) into the liquid blend. Note, however, that AOT is generally not soluble in silicone oils (Pannacci, 2006), which is a type of oil now used to replace transformer oils containing PCBs, and is also an oil that possesses a relatively high mass

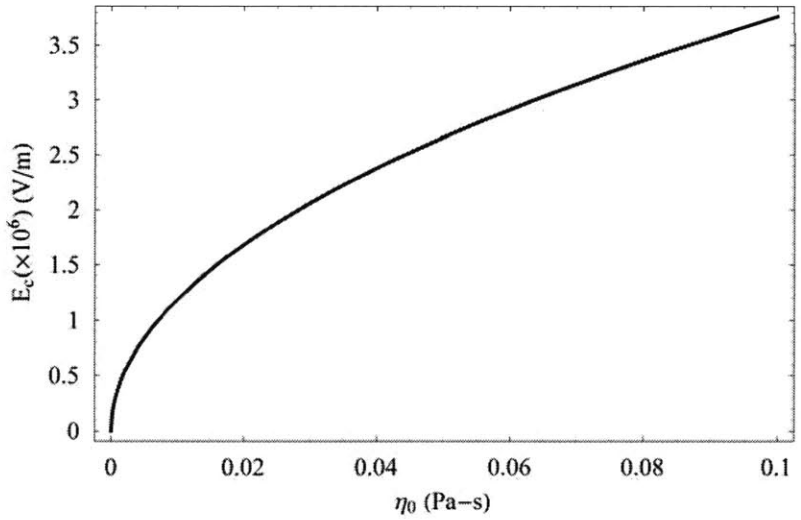

Figure A.1. The critical electric field strength for the onset of micro-particle Quincke rotation plotted with respect to the carrier liquid viscosity. E_c is evaluated by substituting material parameters given in Table A.9 into Eq. (1.1).

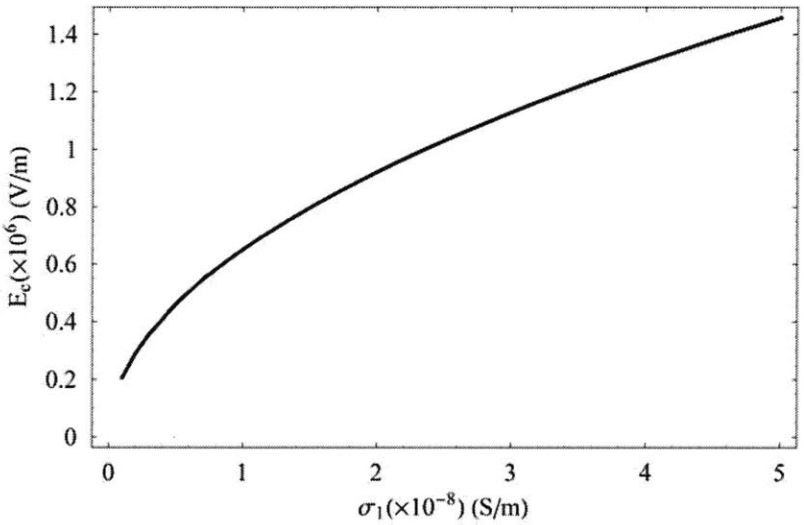

Figure A.2. The critical electric field strength for the onset of micro-particle Quincke rotation plotted with respect to the carrier liquid electrical conductivity. E_c is evaluated by substituting material parameters given in Table A.9 into Eq. (1.1).

density as compared to most transformer oils and solid plastics. Here, we consider silicone oil as a potential candidate to perform the Quincke rotation and negative electrorheological flow experiments.

(v) The viscosity of the liquid phase needs to be low enough so that the critical electric field strength for the onset of micro-particle Quincke rotation is controlled around the order of

magnitudes of $\sim O\left(10^5 \sim 10^6\right)$ (V/m) but not too high as compared with the range of voltage achievable by the high voltage amplifier. The critical electric field strength for the onset of Quincke rotation is plotted with respect to the viscosity of the suspending liquid as shown in Fig. A.1. The desired viscosity for our negative ER experiments should be around $\sim O\left(10^{-2}\right)$ $(Pa \cdot s)$ considering typical values of oil viscosities.

(vi) Finally, we also plot the critical electric field strength for the onset of Quincke rotation with respect to the electrical conductivity of the liquid phase as shown in Fig. A.2. From the figure, we find that the higher the liquid electric conductivity, the higher the critical electric field strength. Moreover, previous negative ER experiments (Lobry & Lemaire, 1999; Cebers *et al.*, 2000; Cebers *et al.*, 2002; Lemaire *et al.*, 2006; Pannacci *et al.*, 2007*a*; Lemaire *et al.*, 2008) done in transformer oil/Ugilec®/PMMA particle systems have shown that the actual critical electric field strength for the onset of micro-particle electrorotation is higher than the theoretically predicted value. This is due to the particle chain formation when the electric field is initially applied—a higher electric field strength as compared to the theoretical value is required so that the electrical torque on the micro-particles is strong enough to overcome the initial chaining process (or simply "rip off" the particles from the chains). Nevertheless, some researchers (Shulman & Nosov, 1996) have also suggested that the liquid electrical conductivity cannot be too low (yet, still high compared to the insulating micro-particles) in order to observe significant Quincke rotation responses. Therefore, with the technical requirements and literature review, we choose a liquid electrical conductivity around $\sim O\left(10^{-8}\right)$ (S/m) for this work.

A.1.2 The Preparation and Synthesis of the Electrorheological Fluid

With all the above requirements considered, the type of dielectric insulating solid micro-particles used in the experiments presented in this thesis was chosen to be polyethylene (PE) micro-particles (Aldrich, ultra-high molecular density, surface modified, 53-75 (μm) particle size powder) with a mass density around 0.94 (g/mL) at 25°C (Sigma-Aldrich material data sheet, 2008), a dielectric constant of 2.25-2.28 (between 100 Hz and 3 GHz) (Von Hippel, 1954; Shugg, 1995), and an electric conductivity around 10^{-16} (S/m) (Adamec and Calderwood, 1981;

Material	Mass density	Dielectric constant	Conductivity	Viscosity
PE micro-particles	0.94 (g/mL) @ 25°C	2.25-2.28*	10^{-16} (S/m)	----
Shell DIALA® AX Oil	0.886 (g/mL) @ 15°C	2.2-2.3	----	~20 (cSt)
Silicone Oil DC 200	1.0 (g/mL) @ 20°C	2.5-2.6	----	~10($mPa \cdot s$)@25°C

Table A.1. Summary of the micro-particle and carrier liquid (blend of two oils) selected for the proposed ER fluid flow experiments. *Measurement frequency ranging from 100 Hz to 3 GHz (Von Hippel, 1954; Shugg, 1995).

Shugg, 1995). The liquid phase was designed to be a mixture of two oils, namely, the Shell DIALA® Oil AX with a mass density of 0.886 (g/mL) at 15°C, a dielectric constant of 2.2-2.3, a dielectric breakdown voltage of at least 28 (kV), and a liquid kinematic viscosity around 20 (cSt) (Shell material data sheet, 2005), and the Silicone oil DC 200 (polydimethylsiloxane; Aldrich, neat (25°C)) with a mass density around 1 (g/mL) at 20°C (Sigma-Aldrich material data sheet, 2009), a liquid viscosity around 10 ($mPa \cdot s$) at 25°C (Sigma-Aldrich material data sheet, 2009), and a dielectric constant around 2.5-2.6 (Wu *et al.*, 1996*a*, *b*; Wu & Conrad, 1997; Wu *et al.*, 1998). All the above material properties are summarized in Table A.1.

Using the following relation, namely,

$$\rho_{PE} = \rho_{AX} f_r + \rho_{DC} (1 - f_r), \tag{A.1}$$

where ρ_{PE} is the mass density of the polyethylene micro-particles, ρ_{AX} is the mass density of the Shell DIALA® Oil AX, ρ_{DC} is the mass density of the Silicone oil DC 200, and f_r is the volume fraction of the DIALA® oil, we blended the two oils with a volume fraction ratio of DIALA® : DC 200 = 0.526 : 0.474 so as to match the liquid density to the density of the solid PE micro-particles. The two oils were miscible forming a transparent clear lightly yellow colored solution and the PE material and micro-particles were not dissolved in the oil blend.

Arbitrary concentrations of docusate sodium salt or AOT (Sigma, SigmaUltra, ≥99%, $C_{20}H_{37}NaO_7S$, $M_w = 444.56$) was respectively added into pure DIALA® oil, pure Silicone oil DC 200, and pure blend of the two oils (all without particles). We found that AOT can be completely dissolved in pure DIALA® oil and the pure blend of the two oils for the AOT concentrations of interest. However, we again confirm that AOT cannot be dissolved in silicone oil as previously reported by Pannacci (2006). Since addition of AOT also changes the total volume of a given oil blend solution, the PE micro-particles were added into the mixture after the blend of DIALA® oil, silicone oil, and AOT salt was prepared. We shall determine the

concentration of AOT salt added to the pure oil mixture in Section A.2.1 so that the desired liquid phase conductivity, σ_1, can be obtained. The final solid volume fraction of the PE micro-particles in our synthesized ER fluid was about 5%.

Before the PE micro-particles can be added into the DIALA® oil/silicone oil/AOT salt blend, dehydration of the micro-particles is required so that the conductivities of the respective solid and liquid phases are not considerably affected by the presence of moisture in the ER fluid. In our preparation of the solid phase, polyethylene micro-particle powder was spread out on a rectangular aluminum baking pan forming a not too thick sheet of powder above the surface of the pan. The particles were heated to 132°C (below the melting point of PE around 144°C) for six hours and then taken out of the oven at around 80°C. The PE micro-particles were added to the DIALA® oil, pure Silicone oil DC 200, and AOT salt blend within three hours after being taken out of the oven.

Due to the mixture nature of the ER fluid we have prepared, both the fluid electrical and rheological properties need to be characterized in order to find the dielectric constant, ε_1, electric conductivity, σ_1, and viscosity, η_0, of the liquid phase (mixture of AOT salt, DIALA® oil, and silicone oil) so that the theoretical value of the critical electric field strength, E_c, can be calculated. Measurements of the viscosity of the liquid-particle suspension, η, *i.e.*, mixture of PE micro-particles, AOT salt, DIALA® oil, and silicone oil, are also required so as to serve as the viscosity reference datum at zero electric field strengths. The characterization of the ER fluid electrical and rheological properties are given in the following section.

A.2 Characterization of Electrorheological Fluid Electrical and Rheological Properties

A.2.1 Impedance Measurements of the Suspending Liquid Phase of the Electrorheological Fluid

As discussed in Section A.1.1, the dielectric constant, or equivalently the dielectric permittivity, ε_1, and the electrical conductivity, σ_1, of the suspending liquid phase, *i.e.*, the blend of Shell DIALA® AX oil, Silicone oil DC 200, and AOT salt play important roles in determining the critical electric field strength, E_c, for the onset of micro-particle Quincke rotation. However, adding AOT salt into the mixture of the two oils changes both the dielectric constant and the electric conductivity of the whole blend, and neither of these electrical

properties, especially conductivity, σ_1, has been characterized as a function of the concentration of the AOT salt added for the specific mixture of the pair of oils employed herein. Therefore, a crucial step in the preparation and characterization of our ER fluid is to measure both the dielectric permittivity and the electric conductivity of the liquid phase so as to find a suitable value of conductivity or concentration of AOT salt that induces a significant micro-particle Quincke rotation effect in the final suspension without drastically boosting the required critical electric field strength (see Fig. A.2) required to induce Quincke rotation.

We measured the electrical conductivity, σ_1, as a function of the concentration of AOT salt added for the liquid blend of the Shell DIALA® AX oil and Silicone oil DC 200 by a high-accuracy, calibration technique developed by Schiefelbein (1996) and Schiefelbein *et al.* (1996). The technique utilizes a coaxial cylindrical electrode that is immersed into the subject liquid solution and that is connected to an impedance meter or analyzer giving the desired data readouts. Measurements of the impedances respectively obtained at distinct electrode immersion depths are taken, and the electrical conductivity of the liquid can be calculated by taking the differences in conductivity of the distinct measurements, dG, and dividing the conductivity differences with the corresponding differences in the electrode immersion depths, $d\xi$, *i.e.*,

$$\sigma_1 = \frac{\ln(b/a)}{2\pi}\frac{dG}{d\xi}, \tag{A.2}$$

where G represents the measured conductance, ξ represents the electrode immersion depth, b is the inner diameter of the outer ring of the coaxial cylinder electrode, and a is the outer diameter of the middle rod of the coaxial cylindrical electrode. The dielectric permittivity, ε_1, (or the dielectric constant) of the liquid blend can also be calculated from the impedance measurements via a similar procedure through the following relation,

$$\varepsilon_1 = \varepsilon_{air} + \frac{\ln(b/a)}{2\pi}\frac{dC}{d\xi}, \tag{A.3}$$

where ε_{air} is the permittivity of air and C is the measured capacitance. Note that the coaxial cylindrical electrode technique was originally designed to measure the liquid conductivities of electrolytes and molten oxides (Schiefelbein, 1996; Schiefelbein *et al.*, 1996), and thus this is perhaps the first time that this technique is applied to measuring the liquid impedances of insulating dielectric oils.

(a)

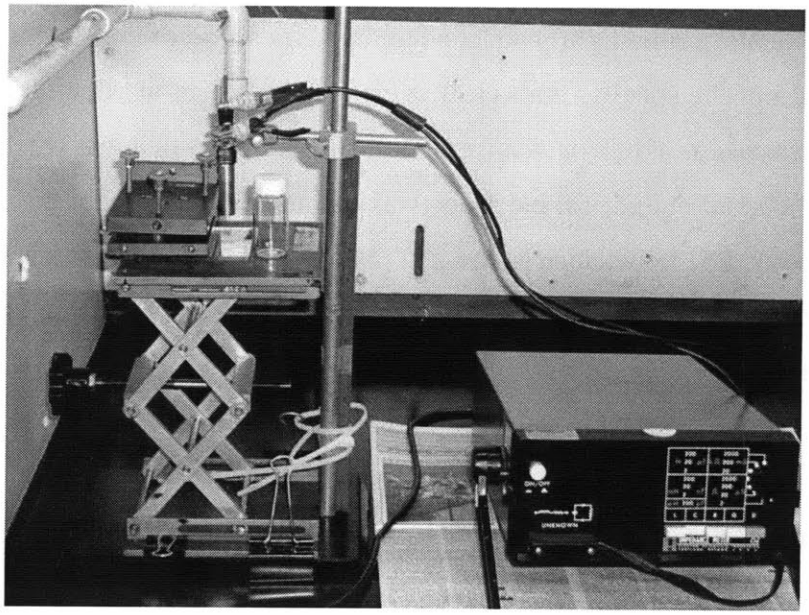

(b)

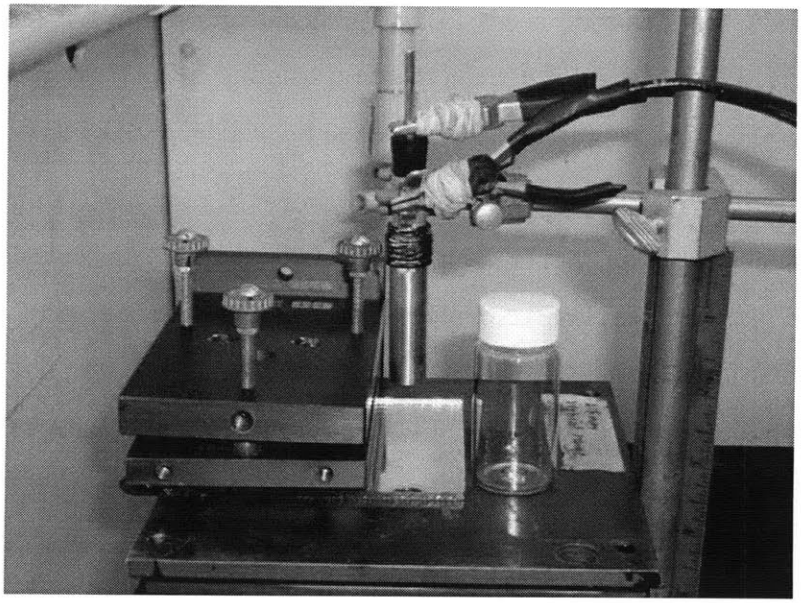

Figure A.3. The coaxial cylindrical electrode and liquid impedance measuring equipment. (a) Global over view of the experimental setup. (b) Zoom-in view of the coaxial cylinder electrode and test leads.

An impedance testing apparatus was built for the impedance measurements of the liquid phase as shown in Fig. A.3 with Fig. A.3(a) showing a global view of the equipment and Fig. A.3(b) showing the zoom in features of the coaxial cylindrical electrode. As can be seen in Fig. A.3, a standard chemistry laboratory stand was used to hold the coaxial cylindrical electrode, a glass vial (roughly 25 (mL) in volume) was used to contain samples of the liquid blend, a mechanical jack was used to adjust the relative elevation or height of the glass vial among

distinct measurements, a ruler tightly attached to the vertical rod of the chemical laboratory stand was used to read out the specific numerical values of the height at which a specific impedance measurement was taken, a mirror was used for constantly evaluating whether the concentric geometry of the coaxial cylindrical electrode was maintained throughout the measurements, and an impedance meter, ESI Impedance Meter 252 (Electro Scientific Industries, Portland, OR), was used to read out the numerical values of the capacitance and conductance all measured at 1 kHz. The coaxial cylindrical electrode was machined at the Central Machine Shop of MIT.

Oil samples were contained in the glass vials as shown in Fig. A.3(b). The initial oil sample volume was 15 (mL). For a given AOT salt concentration, the initial oil sample volume cannot be too large to conserve AOT material, and yet cannot be too small due to the resolution of the electronic scale (A&D Engineering Top loading electronic balance) 0.01 (g). To avoid fringing field interactions between the tip of the coaxial cylindrical electrode and the free liquid surface inside the electrode, the electrode needs to be immersed into liquid for at least 0.75 (in) ~1.9 (cm) (Schiefelbein, 1996). To avoid the electrode tip fringing fields from hitting the glass wall at the bottom of the glass vial, the electrode tip needs to be at a distance of $2(b-a)$~1.6 (cm) away from the bottom of the vial (Schiefelbein, 1996). However, for the initial volume of 15 (mL), the liquid height inside the vial was not enough to provide the two length scales required above, and some overlap of the two lengths were present causing the measurement results to be a bit unstable in the first liquid conductivity test. The oil sample volume was increased to 20.5 (mL) to provide the safety distance in our second and third liquid conductivity tests. To minimize all possible fringing field and unstable effects during the measurement, three immersion depths were employed for each of the oil samples. For 15 (mL) samples, they are: one slightly above the immersion level limit defined by the boundary of the bottom of the vial, one around this limit, and one slightly below. For 20.5 (mL) samples, they are: one slightly above the immersion level limit defined by the bottom boundary, one slightly below the immersion level limit defined by the upper liquid free surface, and one around the middle distance between these two boundary limits. The capacitance and conductance measurements were respectively taken at the three immersion depths, and the final results were taken to be the averaged value of the results obtained at the three immersion depths for each of the oil samples. By almost touching or touching the free liquid surface in the vial with the tip of electrode, a numerical value for the free surface liquid level of each of the oil samples was also taken to serve as the reference datum for

	Literature	Measured
Shell DIALA® Oil AX	2.2-2.3	2.25
Silicone Oil DC 200	2.5-2.6	2.67

Table A.2. Comparison of the dielectric constants of the two pure liquid oils used in the present study between the given literature values and the measured experimental data by the coaxial cylindrical electrode method (Schiefelbein, 1996). The value of 2.5-2.6 shown in the table is the literature value specifically for Dow Corning 200 Silicone Oil (Wu *et al.*, 1996*a*, *b*; Wu & Conrad, 1997; Wu *et al.*, 1998). Our measurements were taken at 1 kHz and between 17-27°C.

the subsequent three immersion depths. The coaxial cylindrical electrode was rinsed with DIALA® : DC 200 = 0.526 : 0.474 pure base oil solution ([AOT] = 0 (M)) between subsequent measurements of different oil samples. Also, notice that the immersion depths of the electrode as observed from the outside, ξ_{out}, is different from that, ξ, within the coaxial cylindrical electrode due to the volume exclusion effects resulting from the presence of the electrode immersed in the liquid samples. Schiefelbein (1996) has offered a general relation to correct for this volume exclusion effect on the immersion depth measurements. For our particular electrode setup with the outer diameter of the outer ring of the coaxial cylinder electrode being 1.27 (cm), the inner diameter of the outer ring of the coaxial cylinder electrode, $b = 1.11$ (cm), the outer diameter of the middle rod of the coaxial cylindrical electrode, $a = 0.32$ (cm), and the inner radius of the glass vial shown in Fig. A.3(b) being 1.26 (cm), a simple correction relation can be obtained as

$$\xi \approx 1.083\xi_{out}, \tag{A.4}$$

by substituting all the required information into the correction relation, Eq. (E.0-6), derived in Appendix E of Schiefelbein (1996).

Before measuring the conductivity of the oil blend as a function of AOT concentration, we first measured the respective dielectric constants (or permittivities) of pure Shell DIALA® oil AX and pure Silicone oil DC 200 and compared the measured results with the known values found in vendor material data sheets and current literature serving as a confidence or validation test of the equipment. The measured results are shown and compared with the given values found in literature in Table A.2. As can be found from the table, the data obtained from the impedance measurement apparatus agree closely with those found in the literature. Note that rigorously speaking, a short circuit measurement of the coaxial cylindrical electrode should be performed to obtain the impedances of the metal electrode and the test leads of the impedance meter by

[AOT] (M)	$\log_{10}[AOT]$	$\sigma_1\ (S/m)$	$\log_{10}\sigma_1$
0.0915	-1.03858	3.06E-08	-7.51428
0.123	-0.91009	5.41E-08	-7.2668
0.165	-0.78252	7.87E-08	-7.10403
0.306	-0.51428	2.53E-07	-6.59688

Table A.3. Summary of results from our first carrier liquid electric conductivity test. The measurements were taken by the coaxial cylindrical electrode method at 1 kHz around 27°C.

immersing the electrode into highly conducting liquid metals (Schiefelbein, 1996). The impedances of the electrode and test leads are to be subtracted from the measured impedance of the subject liquids. Despite the satisfactory results shown in Table A.2, we did not perform the short circuit test as mentioned in Schiefelbein (1996) in this work. Nevertheless, we chose a highly conducting electronic grade copper (as compared with the highly insulating oils being measured) as the material for the coaxial cylindrical electrode and carefully maintained the relative positions of the test leads of the impedance meter between subsequent measurements (the capacitance measured by the impedance meter is maintained at 2.8-2.9 pF at 1 kHz and around 21-27°C when the electrode is totally drawn out of the liquid and exposed in air) so as to minimize the error introduced without performing the short circuit measurements. The electrode polarization effects or double layer impedances (Bard and Faulkner, 2001; Morgan and Green, 2003; Ma, 2007) were not considered in the post processing of our measurements.

A first conductivity measurement was done by performing a conductivity sweep of oil blends with AOT salt concentrations ranging across two decades (from $O\left(10^{-3}\right)$ to $O\left(10^{-1}\right)$ molars) with the base oil being the DIALA® : DC 200 = 0.526 : 0.474 mixture; no PE micro-particles were included. The tested oil sample volumes contained inside the glass vials were all controlled at 15 (mL). The aim of this first conductivity test was to find out the AOT salt concentration that gives liquid electrical conductivities closest to the desired value of $\sim 10^{-8}\ (S/m)$. Due to the highly insulating liquids being measured and the resolution of the ESI Impedance Meter 252 employed herein, we were only able to obtain electrical conductivity data for oil samples with AOT salt concentrations greater than [AOT] = 0.09 M. These results are summarized in Table A.3, and the log-log plot of the liquid phase conductivity versus the AOT salt concentration is given in Fig. A.4. By examining Table A.3, it is found that the measured liquid conductivity

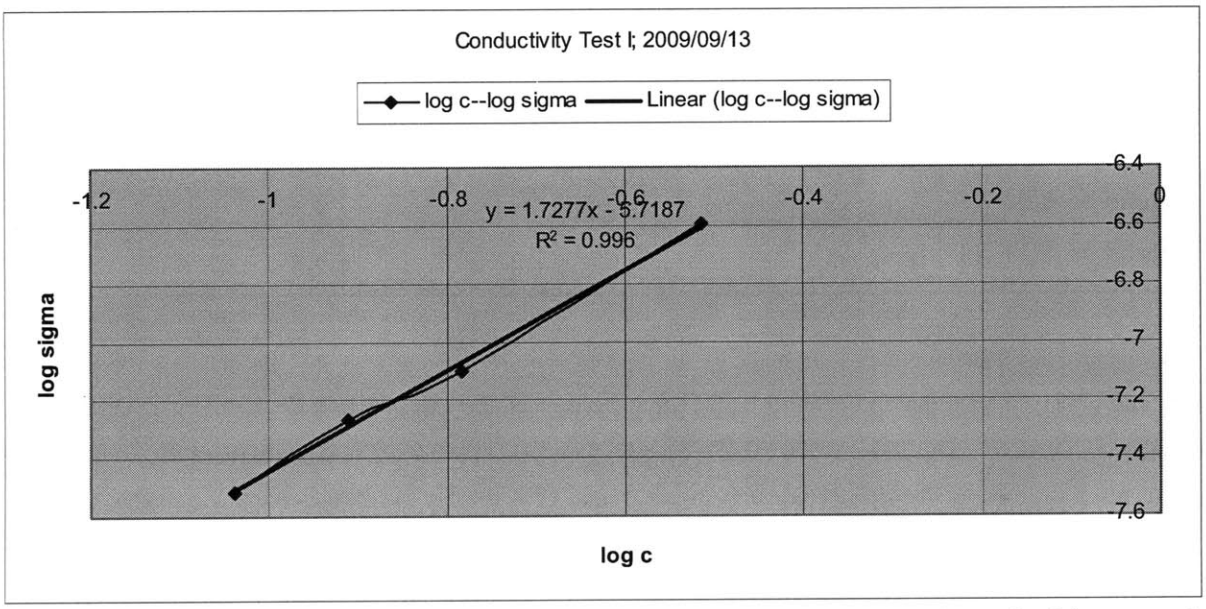

Figure A.4. The log-log plot of the measured carrier liquid (oil blend + AOT salt) electric conductivity versus the AOT salt concentration added to the oil blend.

closest to the desired value of $\sim 10^{-8}$ (S/m) is $\sigma_1 = 3.06\times 10^{-8}$ (S/m) with the corresponding AOT salt concentration being [AOT] = 0.0915 (M) whereas the highest liquid conductivity of all the samples prepared was found to be $\sigma_1 = 2.53\times 10^{-7}$ (S/m) with the corresponding AOT salt concentration being [AOT] = 0.306 (M). The order of magnitude of the sample with a liquid conductivity of $\sigma_1 = 2.53\times 10^{-7}$ (S/m) with the corresponding AOT salt concentration of [AOT] = 0.306 (M) is consistent with an even earlier measurement done by a parallel plate electrode fixture (not presented herein). Moreover, from examining Fig. A.4, we find the log-log plot of the liquid conductivity versus the AOT salt concentration is essentially linear, which is a result consistent with those obtained from mixtures of Dielec, Ugilec®, and AOT salts as found in Pannacci (2006). The figure also shows a linear fitting equation, *i.e.*,

$$\log_{10}\sigma_1 = 1.7277\log_{10}[AOT] - 5.7187, \tag{A.5}$$

that relates the liquid conductivity, σ_1, as a function of AOT salt concentration, [AOT]. Using Eq. (A.5), we find that in order to achieve a liquid conductivity of $\sigma_1 = 1.48\times 10^{-8}$ (S/m), the corresponding AOT salt concentration for a prepared sample of the oil mixture should be [AOT] = 0.06 (M). A second liquid conductivity test was then performed to verify this finding.

	[AOT] (M)	σ_1 (S/m)	Dielectric constant
Base oil blend	0	----	2.5
Oil blend & AOT #1	0.03182	N/A	2.3-2.6
Oil blend & AOT #2	0.06254	N/A	2.5-2.7
Oil blend & AOT #3	0.09053	3.36E-08	2.5

Table A.4. Results from the second and third liquid conductivity and dielectric constant (permittivity) measurements. The measurements were made by the coaxial cylinder electrode method and the data were taken at 1 kHz and 17-21°C. Note that in our third liquid conductivity test, the carrier liquid conductivity of Oil blend & AOT #3, *i.e.*, DIALA® : DC 200 = 0.526 : 0.474 base oil with [AOT] = 0.09053 (M), was measured to be 1.93E-08. This result is probably due to the cold temperature around 17°C the day the measurement was made.

In our second liquid conductivity test, we prepared four oil samples with respective AOT concentrations of [AOT] = 0, 0.03182, 0.06254, and 0.09053 (M) with the oil mixture sample volumes (before the addition of AOT) being ~20.5 (mL). We increased the sample volume so as to minimize the possible fringing field interactions between the tip of the coaxial cylindrical electrode and the free liquid surface inside the coaxial cylinder geometry (Schiefelbein, 1996) as found in the not quite stable measurement results from our first liquid conductivity test. A second reason for increasing the oil sample volume was to increase the contact area between the electrodes and the liquid phase so as to possibly push down the lower limit set by the instruments employed when measuring the conductances of the oil samples prepared. Unfortunately, none of the conductances were successfully obtained for oil samples with AOT salt concentrations less than [AOT] = 0.09053 (M)—we have reached the limits of the equipment. The liquid conductivity of the oil sample with the AOT salt concentration of [AOT] = 0.09053 (M) was obtained to be $\sigma_1 = 3.36\times10^{-8}$ (S/m), which is within 8% as compared with the $\sigma_1 = 3.06\times10^{-8}$ (S/m) at [AOT] = 0.0915 (M) found from our first test. The results of our second liquid conductivity test are summarized in Table A.4. From the table, we find both the oil samples with a zero AOT concentration and [AOT] = 0.09053 (M) have roughly the same dielectric constant being 2.5. However, for oil samples with [AOT] = 0.03182 and 0.06254 (M), the result of the dielectric constant fluctuates between 2.3-2.6 and 2.5-2.7, respectively. Finally, a third liquid conductivity test was performed to again verify the conductivity and dielectric constant (permittivity) measurements found in the first and second tests for the pure Shell DIALA® oil

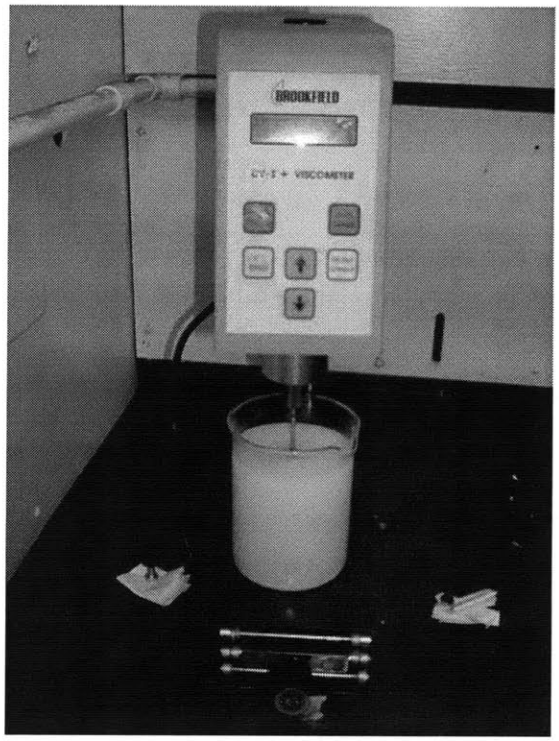

Figure A.5. The experimental setup for measuring the viscosity of the proposed ER fluid and other related liquid samples. The basic components of the experimental setup are a standard 600 (*mL*) beaker and a Brookfield Model DV-1+ viscometer along with an accompanying Brookfield Model LV-1 spindle (Brookfield Engineering Laboratories, Middleboro, MA).

AX, pure Silicone oil DC 200, the DIALA® : DC 200 = 0.526 : 0.474 base oil mixture with zero AOT concentration, and the DIALA® : DC 200 = 0.526 : 0.474 base oil with [AOT] = 0.09053 (M) with all oil sample volumes being 20.5 (mL). The results of the third test generally agree with those obtained from the first and second tests except for the DIALA® : DC 200 = 0.526 : 0.474 base oil with [AOT] = 0.09053 (M) sample. For this concentration, the liquid conductivity was measured to be $\sigma_l = 1.93 \times 10^{-8}$ (S/m) ($\sigma_l = 3.06 \times 10^{-8}$ (S/m) in the first test and $\sigma_l = 3.36 \times 10^{-8}$ (S/m) in the second test). This is probably due to the low temperature, 17°C, on the day of measurement as compared to the 21-27°C for the previous measurements.

From all the obtained results of our three liquid conductivity tests, the liquid phase conductivity for the ER fluid used in the following experiments was determined to be $\sigma_l = 3.36 \times 10^{-8}$ (S/m) with the corresponding oil and salt blend being DIALA® : DC 200 = 0.526 : 0.474 base oil with [AOT] = 0.09053 (M).

Liquid/oil	Standard value	Measured value
Shell DIALA® AX	15.5 ($mPa \cdot s$) at 23°C	15.9 ($mPa \cdot s$)
Silicone oil DC 561	50.6 ($mPa \cdot s$) at 23°C	41.3 ($mPa \cdot s$)
Silicone oil DC 200	~10 ($mPa \cdot s$) at 25°C	10.4 ($mPa \cdot s$)

Table A.5. Summary of the measured and standard viscosity values of the liquids employed in the calibration test of the viscometer. The standard values of the liquid viscosities were obtained from manufacturer material data sheets (Shell material data sheet, 2005; Sigma-Aldrich material data sheet, 2009) and literature (Elborai, 2006; Khushrushahi, 2010). The measured viscosities were all obtained at a spindle rotation speed of 60 rpm.

A.2.2 Viscosity Measurements of the Electrorheological Fluid

Viscosity measurements of the liquids and ER fluid considered in this appendix were done by a Brookfield Model DV-1+ viscometer (Brookfield Engineering Laboratories, Middleboro, MA) as shown in Fig. A.5. The type of spindle chosen for measuring all the oil or liquid samples was the Brookfield Model LV-1 (spindle code: S61). All measurements were done without the presence of the spindle guard.

The procedure of measuring the liquid viscosity is relatively straightforward. We first filled a standard 600 (mL) beaker with liquid samples of volumes ranging roughly from 520 to 550 (mL). The size of the beaker and the amount of liquid used were chosen so as to minimize the boundary or size effects of the beaker on the end results of the viscosity measurements. We attached the Brookfield LV-1 spindle to the Brookfield DV-1+ viscometer after the DV-1+ viscometer has finished its auto-calibration. The LV-1 spindle was then totally immersed into the liquid samples till the liquid surface reaches the notch position as indicated on the LV-1 spindle rod. After switching on the motor to drive the spindle, viscosity and torque measurement readouts were recorded at their respective assigned spindle rotation speeds. All measurements were performed within a room temperature range of 21~25°C.

Calibration tests were first performed to verify the correctness of the viscometer viscosity and torque readouts. Three viscosity standards were employed, *i.e.*, the Shell DIALA® AX oil, Silicone oil DC 561, and Silicone oil DC 200. Respective measurements were taken at three spindle rotation speeds, namely, 50, 60, and 100 rpm. A common result irrespective of the liquid sample tested during the measurements was that viscosity values tend to be a little bit higher when measured at a spindle rotation speed of 100 rpm as compared to those obtained at 50 or 60

Base pure oil blend	@ 50 rpm	@ 60 rpm
Shell DIALA® AX : Silicone oil DC 200 = 0.526 : 0.474	----	10.95 ($mPa \cdot s$)

Table A.6. Summary of viscosity results of the base pure oil blend respectively measured at spindle rotation velocities of 50 and 60 rpm.

Liquid phase of ER fluid (viscosity: η_0)	@ 50 rpm	@ 60 rpm
DIALA®/DC 200 = 0.526/0.474 & [AOT] = 0.09053 (M)	13.2 ($mPa \cdot s$)	13 ($mPa \cdot s$)

Table A.7. Summary of measured viscosity results for the liquid phase of the proposed ER fluid. Measurements were performed at spindle rotation speeds of 50 and 60 rpm, respectively.

Final ER fluid blend (viscosity: η)	@ 50 rpm	@ 60 rpm
Theoretical calculation by Einstein relation $\eta \approx \eta_0 (1+2.5\phi)$	14.9 ($mPa \cdot s$)	14.7 ($mPa \cdot s$)
DIALA®/DC 200 = 0.526/0.474 & [AOT] = 0.09053 (M) & 5% solid volume fraction of PE micro-particles	15.4 ($mPa \cdot s$)	15.5 ($mPa \cdot s$)

Table A.8. Comparison between the theoretically predicted and experimentally measured values of the proposed ER fluid viscosity, η, *i.e.*, the zero electric field viscosity of the ER fluid.

rpm. Since the viscosity values measured at 50 or 60 rpm agree better with the viscosity standards obtained from material data sheets (Shell material data sheet, 2005; Sigma-Aldrich material data sheet, 2009) or literature (Elborai, 2006; Khushrushahi, 2010), we shall only consider and present the viscosity measurements performed at spindle rotations speeds of 50 or 60 rpm. Shown in Table A.5 are the viscosity values of the viscosity standards and the viscosity measurement results obtained from our calibration tests. As can be seen from the table, our measurements closely agree with the viscosity standards of the Shell DIALA® AX oil and Silicone oil DC 200. However, the test result for Silicone oil DC 561 is lower by roughly 20% from the viscosity standard possibly due to the aging process or inhomogeneity of the viscosity standard Silicone oil DC 561. With the results of this calibration test, we have gained confidence in our viscosity measurements and are now ready to measure the viscosities of our proposed ER fluid and other related liquid samples considered herein.

The final formula of the proposed electrorheological fluid blend:		
Shell DIALA® AX : Silicone oil DC 200 = 0.526 : 0.474 & Aerosol OT salts at 0.09053 (M) concentration & 5% solid volume fraction of polyethylene micro-particles (53~75 microns)		
Properties of the ER fluid liquid phase:		
DIALA® AX/DC 200 = 0.526/0.474 & [AOT] = 0.09053 (M)		
Viscosity, η_0	Conductivity, σ_1	Permittivity, ε_1
~13.1 $(mPa \cdot s)$	3.36×10^{-8} (S/m)	2.21×10^{-11} $(C^2/N \cdot m^2)$
Properties of the ER fluid solid phase (Adamec & Calderwood, 1981; Shugg, 1995):		
5% solid volume fraction of polyethylene micro-particles (53~75 microns)		
Viscosity	Conductivity, σ_2	Permittivity, ε_2
----	~10^{-16} (S/m)	2.02×10^{-11} $(C^2/N \cdot m^2)$

Table A.9. Summary of the final formula and material properties of the proposed ER fluid considered in this appendix.

We next performed viscosity measurements on three liquid samples, they are: (i) the base oil blend of Shell DIALA® AX/Silicone oil DC 200 with the ratio of the oil mixture being Shell DIALA® AX : Silicone oil DC 200 = 0.526 : 0.474, (ii) the liquid blend of AOT salt and Shell DIALA® AX/Silicone oil DC 200 with the oil mixture ratio being 0.526/0.474 and the AOT concentration being [AOT] = 0.09053 (M), and (iii) the electrorheological fluid (or particle-liquid suspension) of Shell DIALA® AX/Silicone oil DC 200 = 0.526/0.474 with additives of [AOT] = 0.09053 (M) and 5% solid volume fraction of polyethylene (PE) micro-particles. The test results of the above three liquid samples (i), (ii), and (iii) are presented in Tables A.6, A.7, and A.8, respectively.

As can be learned from comparing Tables A.6 and A.7, the viscosity of the liquid increases as we add AOT salts into the pure oil mixture of Shell DIALA® AX : Silicone oil DC 200 = 0.526 : 0.474. Moreover, by further adding solid PE micro-particles into the blend of AOT salt ([AOT] = 0.09053 (M)) and Shell DIALA® AX/Silicone oil DC 200 = 0.526/0.474, it can be found by comparing Tables A.7 and A.8 that the ER fluid (particle-liquid suspension) viscosity, η, increases roughly according to the Einstein relation, *i.e.*, $\eta \approx \eta_0(1+2.5\phi)$, where η_0 is the

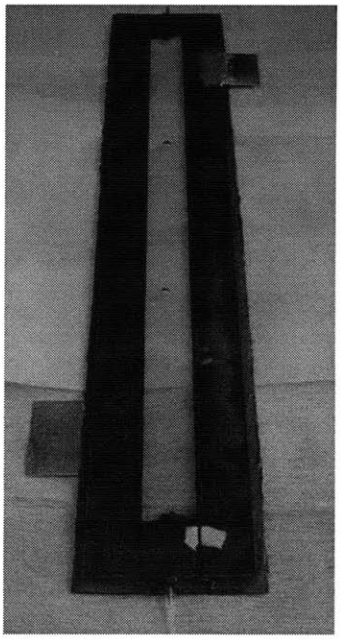

Figure A.6. The Poiseuille electrorheological fluid flow and electrorotation testing channel.

viscosity of the blend of AOT salt ([AOT] = 0.09053 (M)) and Shell DIALA® AX/Silicone oil DC 200 = 0.526/0.474 and $\phi = 5\%$ is the solid volume fraction of the PE micro-particles.

Finally, with the electrical and rheological properties obtained in Sections A.2.1 and A.2.2, we determine the theoretical value of the critical electric field strength for the onset of single micro-particle Quincke rotation, *i.e.*, E_c, for our proposed electrorheological fluid, namely, Shell DIALA® AX : Silicone oil DC 200 = 0.526 : 0.474 added with Aerosol OT salts at 0.09053 (M) concentration and 5% solid volume fraction of polyethylene micro-particles, by substituting the material properties shown in Table A.9 into Eq. (1.1), that is,

$$E_c \equiv \left(1+\frac{\sigma_2}{2\sigma_1}\right)\sqrt{\frac{8\eta_0\sigma_1}{3\varepsilon_1\sigma_2(\tau_2-\tau_1)}} \approx 1.62\times10^6 \ (V/m). \tag{A.6}$$

A.3 The Poiseuille Flow Electrorotation Testing Apparatus

The experimental design of our Poiseuille flow electrorotation testing apparatus generally follows those presented in Lemaire *et al.* (2006) and Pannacci (2006). Here, we briefly summarize the procedure and important steps of constructing the testing apparatus. Shown in Fig. A.6 is a rectangular Poiseuille flow cell. This is where we stress the electrorheological fluid

flow with a high voltage electric field and is the primary component of the testing apparatus. The pair of electrodes of the Poiseuille test cell, *i.e.*, the upper and lower parallel plates, was made using transparent indium tin oxide (ITO) coated glass (30 *Ohms/sq.*), Bayview Optics, Dover-Foxcroft, ME) as shown in Fig. A.6. The raw ITO glasses were machined (by Bayview Optics) into roughly 35.6 (*cm*) long and 6.93 (*cm*) wide rectangular electrodes with the glass thickness being 1.1 (*mm*). Two one eighth inch (1/8" or 3.2 (*mm*)) through holes were drilled onto one of the pair of ITO glasses serving as the upper plate electrode of the Poiseuille flow channel while the other piece of glass without through holes becomes the lower plate electrode of the channel. The transparent ITO glass electrodes were chosen because of the need to carefully distinguish whether the observed negative ER effect is nER1 or nER2, *i.e.*, it is desirable to know whether the ER fluid flow within the channel is a sediment phase-separated flow or a homogeneous suspension. Moreover, judging from the observed micro structure of the ER fluid flow, *i.e.*, chained particles or a homogeneous suspension, we can also determine whether the stressed high voltage electric field has reached the experimental value of the critical electric field for the onset of micro-particle Quincke rotation, which usually is a value greater than the theoretical predicted E_c as given by Eq. (1.1). ITO coated transparent plastics were also considered during the process of development. However, the surface resistivity of ITO coated plastics is found to be higher than that of the ITO coated glasses.

The pair of ITO glasses shown in Fig. A.6 were spaced apart by insulating electrical grade Teflon® PTFE films. We bonded the ITO glasses and the PTFE films together by an oil resistant Permatex Ultra-blue RTV gasket maker. The ITO coated side of the glass electrodes was bonded to copper foils by silver filled conducting epoxy such that the copper foils can be further connected to the external high voltage power supply. The ER fluid enters and exits the channel space (indicated by the rectangular transparent region shown in Fig. A.6) through PTFE microbore tubings which have inner diameter of 0.022 (*in.*) and outer diameter of 0.042 (*in.*). The channel space in which the ER fluid flows as indicated by the rectangular transparent region in the figure was made to be 30 (*cm*) long by 2 (*cm*) wide, and the thickness of the channel, h (or spacing between the two electrodes), is to be carefully controlled to roughly 1.1 (*mm*). With a channel height of $h = 1.1$ (*mm*), the required high voltage drop in order to produce the theoretical electric field strength as calculated in Eq. (A.6) is at least 1.8 (*kV*). The schematic

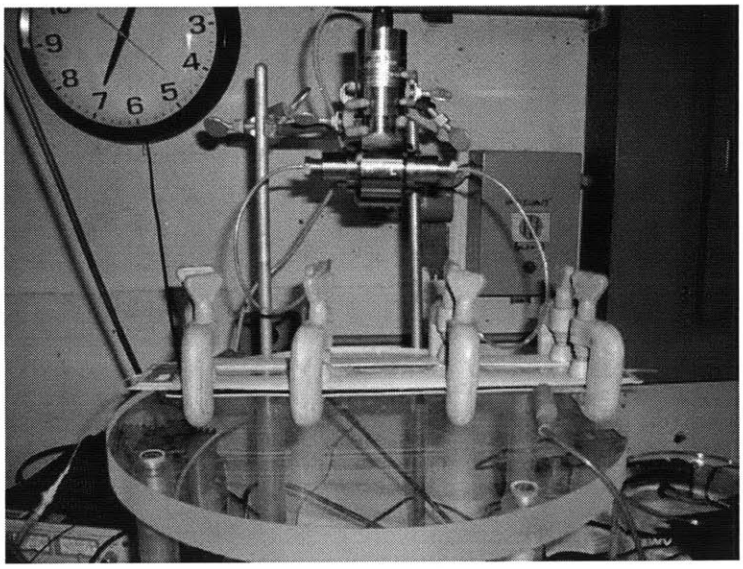

Figure A.7. Zoom-in view of the Poiseuille flow channel testing section of the whole completed electrorotation testing apparatus. The dimension of channel height, h, of Poiseuille flow channel is restrained by plastic C-clamps as shown holding the test cell in the figure.

diagram and the designed dimensions of the Poiseuille flow test cell as shown in Fig. A.6 are given at the end of this appendix.

Lastly, we present the final constructed Poiseuille flow electrorotation testing apparatus. Figure A.7 shows a zoom-in view of the final Poiseuille test cell (thin rectangular object in the middle of the figure). Due to the flexibility of the bonding Permatex Ultra-blue RTV gasket maker adhesive between the ITO glass and the PTFE films as previously described, the dimension of the channel height, $h = 1.1$ (mm), may vary when hydrodynamic pressure builds up due to the ER fluid flow within the flow channel, and thus may change the high voltage electric field stressed across the channel. Therefore, the original Poiseuille test cell as shown in Fig. A.6 was further carefully clamped and restrained to the dimension of $h = 1.1$ (mm) by use of plastic C-clamps (Carr Lane Mfg. Co., St. Louis, MO) so as to maintain constant channel geometry and the subsequent electric field strengths applied. Plastic tubings with outer diameter of 1/8" $(in.)$ were used to connect the two 1/8" $(in.)$ through holes in the upper ITO glass electrode and a differential pressure sensor (model 216-D-XF-LB, GP:50 Co., Grand Island, NY) such that the pressure drop along the stream wise direction can be measured and recorded. One of the microbore tubings of the Poiseuille test cell was connected to a fluid reservoir upstream while the other serves as an outlet to a beaker receiving the ER fluid discharge.

The whole global view of the electrorotation testing apparatus setup is illustrated in Fig. A.8. As can be seen from the figure, the upstream of the Poiseuille test cell was connected to a four liter carboy made of high density polyethylene serving as the ER fluid reservoir. We controlled the fluid pressure head or vertical distance between the ER fluid liquid surface in the reservoir and the horizontal position of the Poiseuille test cell by adjustable jacks that are positioned beneath the reservoir. Since the ER fluid flow is designed as an open loop circuit, *i.e.*, fluid does not recirculate between upstream and downstream, the loss of pressure head within the reservoir was compensated by inert nitrogen gas coming from the compressed nitrogen gas cylinder (Airgas, Salem, NH) as shown on the left of the figure. The amount and the outlet pressure of the nitrogen gas released into the fluid reservoir were regulated by an electro-pneumatic proportional valve (model: ED02, Bosch Rexroth Corp.: Pneumatics, Lexington, KY) as shown right above the carboy in Fig. A.8. A computer program is required to monitor the change in pressure drop in the flow channel and send control signals to the electro-pneumatic valve so that a suitable amount of nitrogen gas is released into the reservoir to compensate for the loss of pressure head in the reservoir and to maintain a constant pressure drop within the Poiseuille flow channel downstream. A closed loop or recirculating design of the ER fluid flow was not considered because of the particle-liquid suspension nature of the ER fluid—the size of the micro-particles suspended in our proposed ER fluid are generally too large to smoothly flow within commercial pneumatic or gear pumps without jamming the equipment. As for the receiving end or downstream of our ER fluid flow, a 2 liter glass beaker was used to receive the ER fluid discharge from the Poiseuille flow channel. The top loading electronic balance (A&D Engineering Inc., San Jose, CA) beneath the 2 liter glass beaker was employed to measure the change in the amount of liquid mass in the beaker with respect to time. The actual values of the voltage stressed and the current passing through the Poiseuille test cell were to be measured by a Fluke multimeter (accompanied with Fluke high voltage probe) and a Keithley 614 electrometer. Direct current (DC) power was supplied to the differential pressure sensor and the electro-pneumatic valve by an HP 0-40 V dual channel power supply. The DC high voltage power supply was manufactured by Hipotronics. In the following, we summarize some further experimental aspects not discussed or considered in detail in our present treatment:

(i) De-gassing of insulating liquid oils: de-gassing is a procedure performed on insulating oils before their application to high power or high voltage equipment. The reason for this

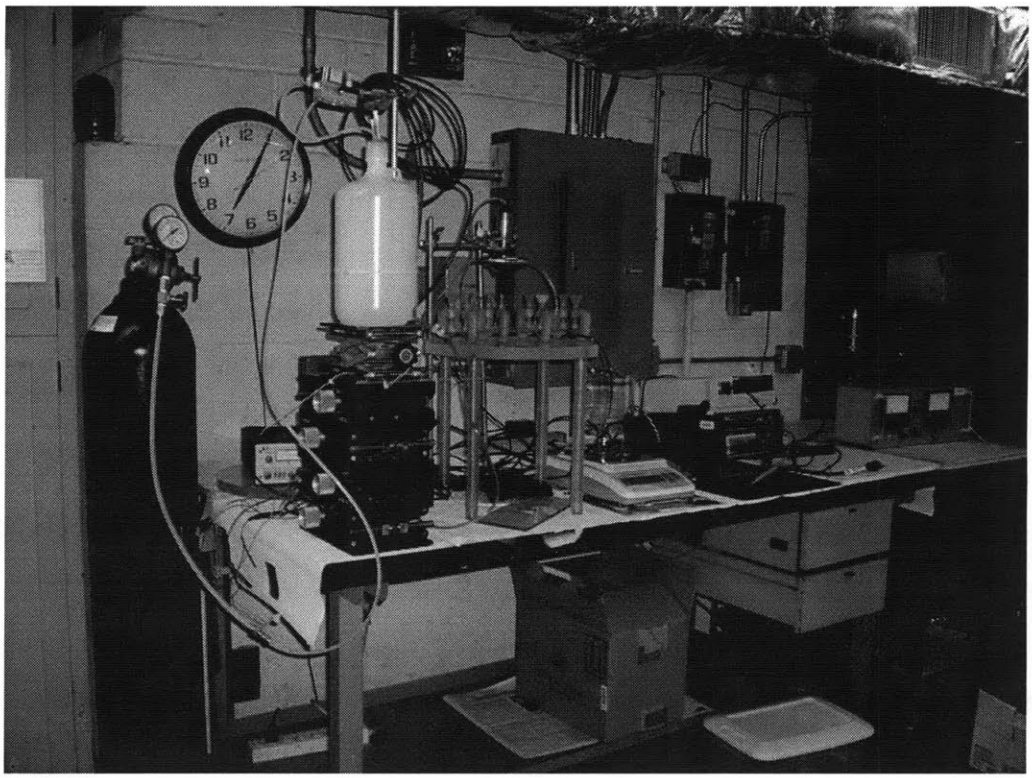

Figure A.8. Global view of the whole completed Poiseuille flow electrorotation testing apparatus and equipment.

procedure is to remove micro or nano gas bubbles trapped within the insulating oils so that the presence of the micro/nano bubbles does not locally distort the electric field distribution within the liquids (Crowley, 1999). However, since we are actually mixing two types of insulating oil as well as AOT salt and polyethylene micro-particles all together, it is almost impossible to perform a de-gassing procedure on the liquid phase. The trapped micro or nano air bubbles may then serve as additional insulating sites or spots within the liquid phase, which may be equivalently considered as additional insulating micro-particles suspended within the liquid phase, and may change the actual fraction of insulating volume as compared to the fraction of slightly conducting liquid volume. The presence of micro/nano air bubbles also lowers the dielectric breakdown strength of the liquid.

(ii) Moisture control of the electrorheological fluid: although we have performed a moisture control on the solid micro-particles before adding them into the liquid phase, moisture control is again a somewhat case specific procedure depending on the material combination employed for synthesizing the ER fluids as well as practical experimental experiences. In spite of the data available in the literature (Boissy et al., 1995; Wu & Conrad, 1997), it is

less likely to find a general measure or rule-of-the-thumb that may indicate or show whether our dehydration procedure is complete or incomplete. Moreover, moisture may still diffuse into the ER fluid and change the conductivity of the whole suspension as time progresses. All these variables add further complexities to the ER fluid system and may cause potential high voltage breakdown phenomena to occur in the synthesized ER fluid—a phenomenon which may damage our Poiseuille test cell and other experimental equipment. Therefore, it is still likely an open question of finding a suitable way to control the moisture within the ER fluid and to eliminate the possibility of high voltage breakdown.

(iii) Despite the theoretically estimated value of the critical electric field strength for the onset of Quincke rotation as given in Eq. (A.6), the actual experimental critical electric field is usually much greater than the theoretical value (Lemaire *et al.*, 2006; Pannacci *et al.*, 2007*a*) due to chaining of micro-particles at high field low shear rate conditions. Hence, it is usually favorable to lower the theoretically estimated critical electric field, based on the measured electrical and rheological properties of the solid and liquid phases, to roughly 7×10^5 (V/m); a critical electric field of 1.62×10^6 (V/m) as calculated by Eq. (A.6) is generally still too high. Also, the association and dissociation processes of salts within non-polar liquids are field dependent (Onsager, 1934; Castellanos, 1998), and thus the liquid phase conductivity becomes a function of the applied electric field, *i.e.*, $\sigma_1 = \sigma_1(E_0)$. The theory of Quincke rotation discussed in this thesis does not account for such field dependences of the liquid phase conductivity.

(iv) High voltage safety: when working with voltage strengths greater than 600 (V), workers are always required to work in pairs. It is also necessary to have suitable grounding equipment or facilities, such as discharge rods and metallic fiber woven stripes, designed and integrated to the primary experimental apparatus. Lockout procedures of energized equipment must also be practiced so as to ensure the safety of both workers and non-essential personnel.

A.4 The Electrorotation Modified Poiseuille Flow Rate Experiment

A.4.1 Some Revisions to the Experimental Design and Conditions of the Experiments

Before proceeding onto the details of the micro-particle electrorotation modified Poiseuille flow rate experiment, some revisions were made to the original experimental design and

conditions as discussed in the previous sections of this appendix. These revisions are summarized as follows:

(i) The two 1/8"-through hole junctions connecting the upper ITO glass electrode to the flexible PVC tubing (to the differential pressure sensor) originally made by the Permatex Ultra-blue RTV gasket making adhesive were not gas tight, and thus the fluid within the Poiseuille flow channel may leak through the junctions resulting in erroneous differential pressure sensor measurements. To solve this problem, we replaced the original RTV gasket junctions with Upchurch® NanoPorts (Upchurch Scientific, Inc., Oak Harbor, WA) (Greener *et al.*, 2008) model N-333 along with P-663 adapters, which connect the PVC tubing with the N-333 NanoPorts. With the combined N-333 and P-663 NanoPorts module, robust and gas tight junctions were made to connect the 1/8"-through hole junctions on the upper ITO glass electrode to the flexible PVC tubings (to the differential pressure sensor) so that no suspension fluid within the Poiseuille flow channel leaks out through the junctions and that the differential pressure measurements taken by the differential pressure sensor are more stabilized.

(ii) In our original design, the suspension fluid leaks through the tiny gaps or pockets trapped in-between the bonding surfaces of the ITO glass electrodes and the PTFE film spacers (to keep the two electrodes apart) from the Poiseuille flow test cell. This problem was solved by replacing the PTFE film spacers with the Permatex Ultra-blue RTV gasket making adhesive so that tiny gaps or pockets are eliminated from the bonding surfaces of the ITO glass electrodes and the RTV gaskets as was done in Pannacci (2006). All the corners or edges of the new Poiseuille flow test cell were then completely sealed with the Permatex Ultra-blue RTV gasket making adhesive to eliminate all possible leakage of ER fluid from the Poiseuille flow test cell. The channel height of the new Poiseuille flow test cell was maintained at $h \approx 1.1\ (mm)$.

(iii)The originally proposed formula for the ER fluid suspension as discussed in Sections A.1 and A.2 suffers from micro-particle sedimentation (despite our efforts of matching the densities of the solid and liquid phases); the PE micro-particles sediment in the blend of AOT/DIALA/SILICONE oil and electrorotation flow rate experiments cannot be conducted. We modified the ER fluid suspension by replacing the PE particles with glucose powder

(Sigma-Aldrich) in the original oil blend such that the suspension phase or state of the ER fluid can be maintained long enough for flow rate measurement purposes.

A.4.2 The Experimental Procedure

As described in the previous Section A.3, the upstream of the ITO glass Poiseuille flow test cell was connected to a 4 liter carboy serving as an ER fluid reservoir. We varied the gravitational pressure head by adjusting the vertical height of the carboy reservoir to generate different pressure gradients in the Poiseuille flow test cell driving the fluid flow. The pressure gradient within the Poiseuille flow test cell was measured by a GP:50 differential pressure sensor (model 216-D-XF-LB, GP:50 Co., Grand Island, NY), which was excited with 24-25 Vdc voltage by the HP 0-40 V dual channel DC power supply. Measurement signals generated by the differential pressure sensor were collected by a data acquisition system consisting of a National Instruments NI USB-6221 BNC data acquisition (DAQ) card and a DELL Optiplex 760 desktop PC installed with LabVIEW 2009. A simple LabVIEW program, as shown in Fig. A.9, was coded so that a virtual instrument was developed to monitor the pressure gradient measured by the differential pressure sensor as well as take average over the pressure gradient measurements recorded over a specific period of time. Confidence tests were performed on the differential pressure sensor and the data acquisition system (including LabVIEW coding) by hydrostatic pressure tests. During our hydrostatic pressure tests, two 1/8" OD PVC tubings both filled with a certain amount of Shell DIALA AX oil were connected to the GP:50 differential pressure sensor. We then varied the vertical distance between the two liquid surfaces within the two respective PVC tubings to generate different values of hydrostatic pressure head. By measuring the vertical distances between the two liquid surfaces in the respective PVC tubings and converting these measurements of hydrostatic pressure differences into proper units, we can compare the pressure difference measurements obtained by measuring the vertical distances between the two liquid surfaces with the pressure differences measured by the LabVIEW DAQ system. Both the LabVIEW DAQ system and the GP:50 differential pressure sensor were verified to give reliable measurements.

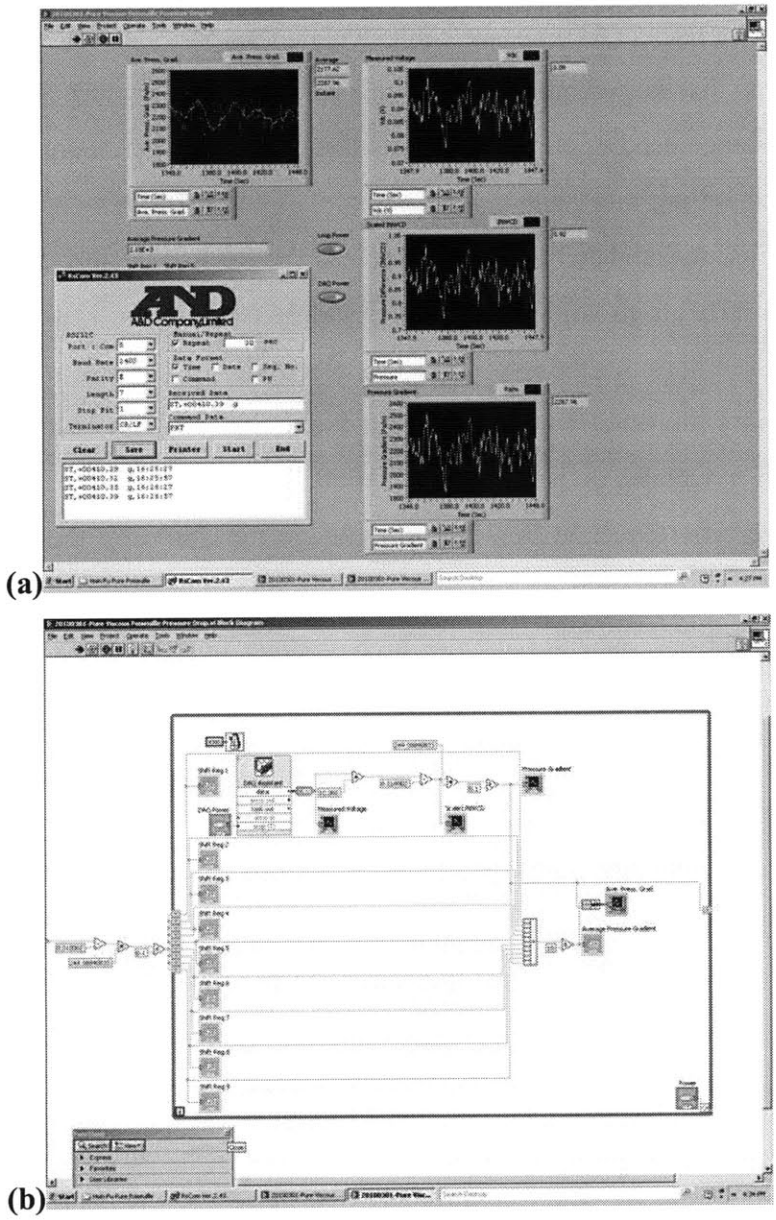

Figure A.9. Simple LabVIEW program used for monitoring the driving pressure gradient within the Poiseuille flow channel. (a) Front panel. (b) Block diagram.

A WinCT software (A&D Engineering Inc., San Jose, CA), including RSKEY and RSCOM programs, was also installed into our desktop PC to record the liquid mass measurements obtained by the A&D top loading electronic balance through an RS-232C interface. The software records the liquid mass within the 2 liter beaker on top of the electronic balance at the fluid receiving end of the electrorotation testing apparatus as well as records the time at which each mass measurement was taken. Therefore, by measuring and recording the increase of fluid mass

within the beaker with respect to time, we can calculate the mass flow rate (of volume flow rate) of the ER fluid being discharged out of the ITO glass Poiseuille flow test channel. The sensitivity of the electronic balance used in our experiments had a minimum measureable unit mass of 0.01 g and a maximum sampling rate (with respect to time) of one measurement every 0.2 seconds.

As shown in Figs. A.8 and A.10(a), we energized the Poiseuille flow electrorotation test cell with a Hipotronics R10B high voltage DC power supply (Hipotronics, Inc., Brewster, NY). The actual voltage stressed between the two ITO glass electrodes of the test cell were measured by a Fluke 45 dual display multimeter connected to a Fluke 80k-40 high voltage probe (Fluke Co., Everett, WA) with a voltage division ratio of 1000:1 as shown in Fig. A.10(b). The voltage measurements were cross checked between the voltage measured by the Fluke meter and that found from the voltage indicator on the high voltage power supply. During our experimental measurements, the current indicator on the high voltage power supply showed that there is indeed current ($\sim 0.1\ mA$) passing through the Poiseuille flow electrorotation test cell when the test cell is stressed by high voltage.

Before energizing the test cell and taking actual measurements of mass or volume flow rates, we need to make sure that there are indeed particles present within the test cell and that the fluid inside the test cell is indeed a suspension. This can be easily done by looking through the ITO glass electrodes of the Poiseuille flow test cell and see if the fluid inside the test cell is transparent or relatively fuzzy (opaque for high concentrations of particles). Since the flow being discharged out of the Poiseuille flow test cell was observed to be dripping flow during all our measurements, the liquid surface level in the 4 liter carboy ER fluid reservoir basically doesn't change within the duration of each measurement, and thus there is no need to compensate the loss of pressure head (due to the loss of liquid) within the fluid reservoir by additional nitrogen gas input into the carboy reservoir (Peters *et al.*, 2010). After energizing the Poiseuille flow electrorotation test cell, we measured the mass flow rate of the fluid suspension, or ER fluid, being discharged out of test cell with respect to the driving pressure gradient (setup by gravitational pressure head) at applied DC electric field strengths of $E_0 = 0.018$, 0.7, 1.43, and 2.06 (kV/mm). Using an infrared thermometer, the temperature of the test cell was measured to be within 22-24°C throughout all our flow rate measurements.

A.4.3 Results and Discussions

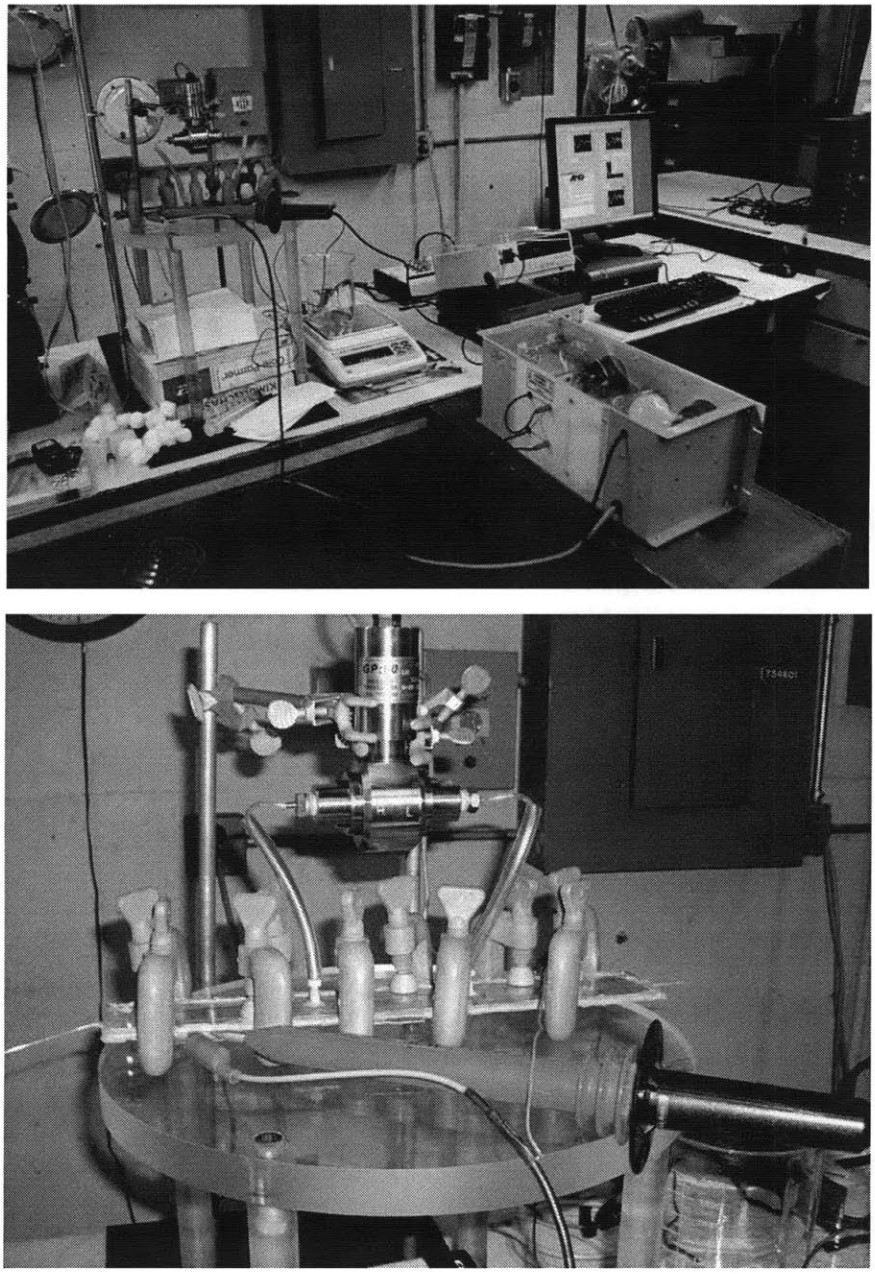

Figure A.10. (a) Experimental setup of the Poiseuille flow electrorotation testing apparatus when the apparatus is energized with high voltage by the Hipotronics R10B high voltage DC power supply. (b) A Fluke 80k-40 high voltage probe (connected to a Fluke 45 dual display multimeter) with a voltage division ratio of 1000:1 is used to measure the actual voltage stressed within the ITO glass Poiseuille flow test cell.

Shown in Fig. A.11 are the mass flow rates of the ER fluid suspension being discharged out of the Poiseuille flow electrorotation test cell measured with respect to the driving pressure gradient at applied DC electric field strengths of $E_0 = 0.018$ (box), 0.7 (star), 1.43 (triangle), and

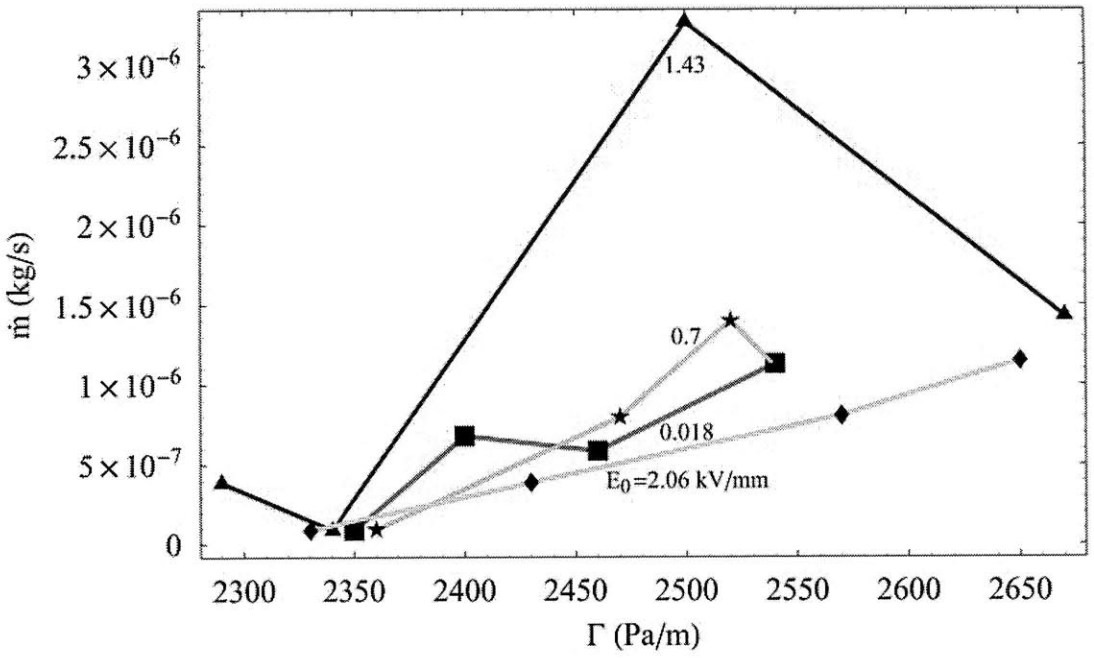

Figure A.11. Mass flow rate of the suspension fluid (or ER fluid) measured with respect to the driving pressure gradient at applied DC electric field strengths of $E_0 = 0.018$ (box), 0.7 (star), 1.43 (triangle), and 2.06 (diamond) (kV/mm). Each data point shown in the figure is the averaged result of 2-3 measurements.

2.06 (diamond) (kV/mm). Each data point shown in Fig. A.11 is the average result of 2-3 measurements. As can be seen from Fig. A.11, measurements of the mass flow rate of the suspension fluid generally increased as the driving pressure gradient was increased while the applied electric field strength was maintained at a certain value. On the other hand, by keeping the driving pressure gradient within a specific range, we found that the mass flow rate of the suspension very slightly increased as the applied electric field strength was raised to $E_0 = 0.7$ (star) (kV/mm) as compared to the flow rate measured at $E_0 = 0.018$ (box) (kV/mm). As we continued to raise the field strength to $E_0 = 1.43$ (triangle) (kV/mm), an apparent increase in the mass flow rate of the suspension was measured. Finally, the mass flow rates of the suspension dropped to relatively low values as compared to the other measurements when we increased the DC electric field strength to $E_0 = 2.06$ (diamond) (kV/mm). These measurement results as shown in Fig. A.11 were generally likely to be qualitatively consistent with the experimental measurements reported in Cebers *et al.* (2002), Lemaire *et al.* (2006), and Pannacci (2006) as

well as the theoretical predictions given by the present thesis. The sudden drop in mass flow rate of the suspension measured at $E_0 = 2.06$ (diamond) (kV/mm) was possibly likely due to the loss of applied electric field strength resulting from dielectric breakdown of small air pockets or bubbles trapped within the RTV gasket making adhesives (spacing the ITO electrodes apart) since sparks were observed in the RTV region of the electrorotation test cell when the applied electric field strength was raised to near $E_0 = 2.27$ (kV/mm). Nonetheless, no apparent drop in the applied electric field strength or voltage strength was measured by the Fluke meter during the flow rate measurements conducted at $E_0 = 2.06$ (diamond) (kV/mm).

Also found from Fig. A.11 was the respective parametric ranges of the driving pressure gradients and the measured mass flow rates were quite limited. This limitation was likely due to several reasons. The first reason was that the hydraulic resistance of the whole flow circuit of the electrorotation testing apparatus (Poiseuille flow test cell and connections to the carboy reservoir) is likely to be too large leading to the only result of dripping flow observed throughout our flow rate experiments. Secondly, since our driving pressure gradient within the ITO glass Poiseuille flow test cell was generated by gravitational pressure heads, the vertical linear distance available for adjusting the gravitational pressure head was limited by the linear height or distance from the table surface to the floor ceiling in the lab space. This reason may also lead to the result of a very low mass flow rate due to a dripping flow. Lastly, due to the very small inner diameter (0.022 *in.*, or 0.56 *mm*) of the micro tubing employed for our fluid outlet of the ITO glass Poiseuille flow electrorotation test cell, surface tension effects were likely to be significant and thus were likely responsible for a limited dripping flow mass flow rate and undesired variations in the differential pressure measurements taken by the pressure sensor. To eliminate or minimize the effects of the above three factors in our experiments, re-design and reconstruction of the electrorotation testing apparatus is likely needed and thus requires further future experimental efforts in improving the hardware as well as the resulting measurement results. Despite the limitations imposed by the hardware, the measurement results shown in Fig. A.11 surprisingly agreed with the common intuition of "a stronger driving pressure gradient gives rise to a greater mass flow rate" as well as with our experimental expectations of what we would observe in an electrorotation modified fluid flow.

One final comment to the experiments discussed in this Appendix is the need of identifying a better blend of suspension fluid or ER fluid in which the suspended micro-particles will not

sediment. If micro-particle sedimentation occurs relatively quickly, a greater part of the suspended micro-particles will sediment in the fluid reservoir well before entering the high voltage electrorotation testing section, *i.e.*, the ITO glass Poiseuille flow test cell, and thus rendering the electrorotation modified flow rate measurements less meaningful while jamming the flow circuit of the experimental equipment. The measurement results shown in Fig. A.11 was due to the modified suspension blend of replacing the PE particles with glucose. We have also attempted to use the original ER fluid of PE micro-particles suspended within the mixture of AOT/DIALA/SILICONE oil for our electrorotation modified flow rate experiments. However, the PE micro-particles sediment relatively quickly (despite our efforts of matching the densities of the solid and liquid phases) in the fluid reservoir and were not able to enter the Poiseuille flow test cell for further high voltage testing measurements.

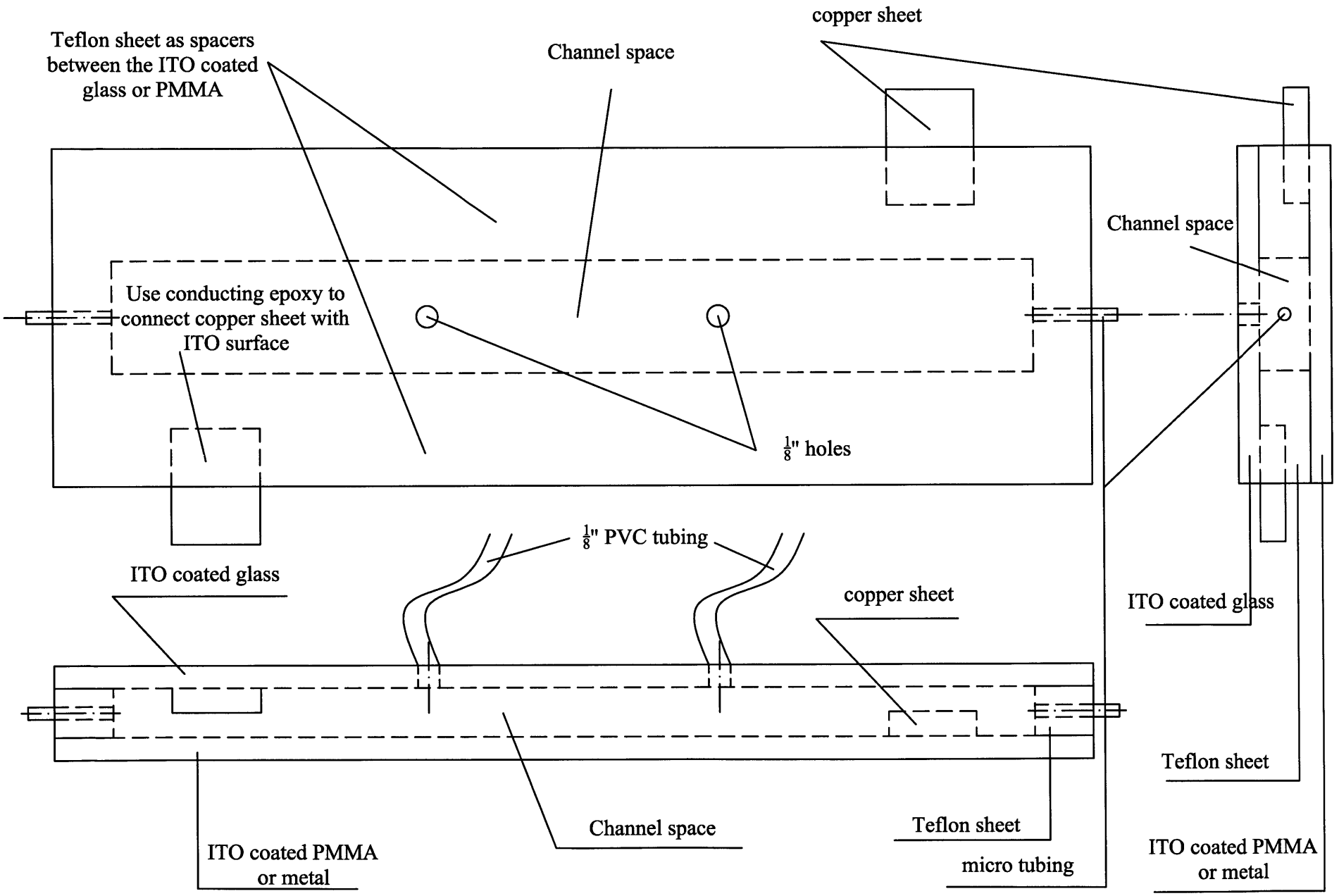
Teflon sheet as spacers between the ITO coated glass or PMMA
Channel space
copper sheet
Channel space
Use conducting epoxy to connect copper sheet with ITO surface
1/8" holes
1/8" PVC tubing
ITO coated glass
copper sheet
ITO coated glass
Teflon sheet
Channel space
Teflon sheet
micro tubing
ITO coated PMMA or metal
ITO coated PMMA or metal

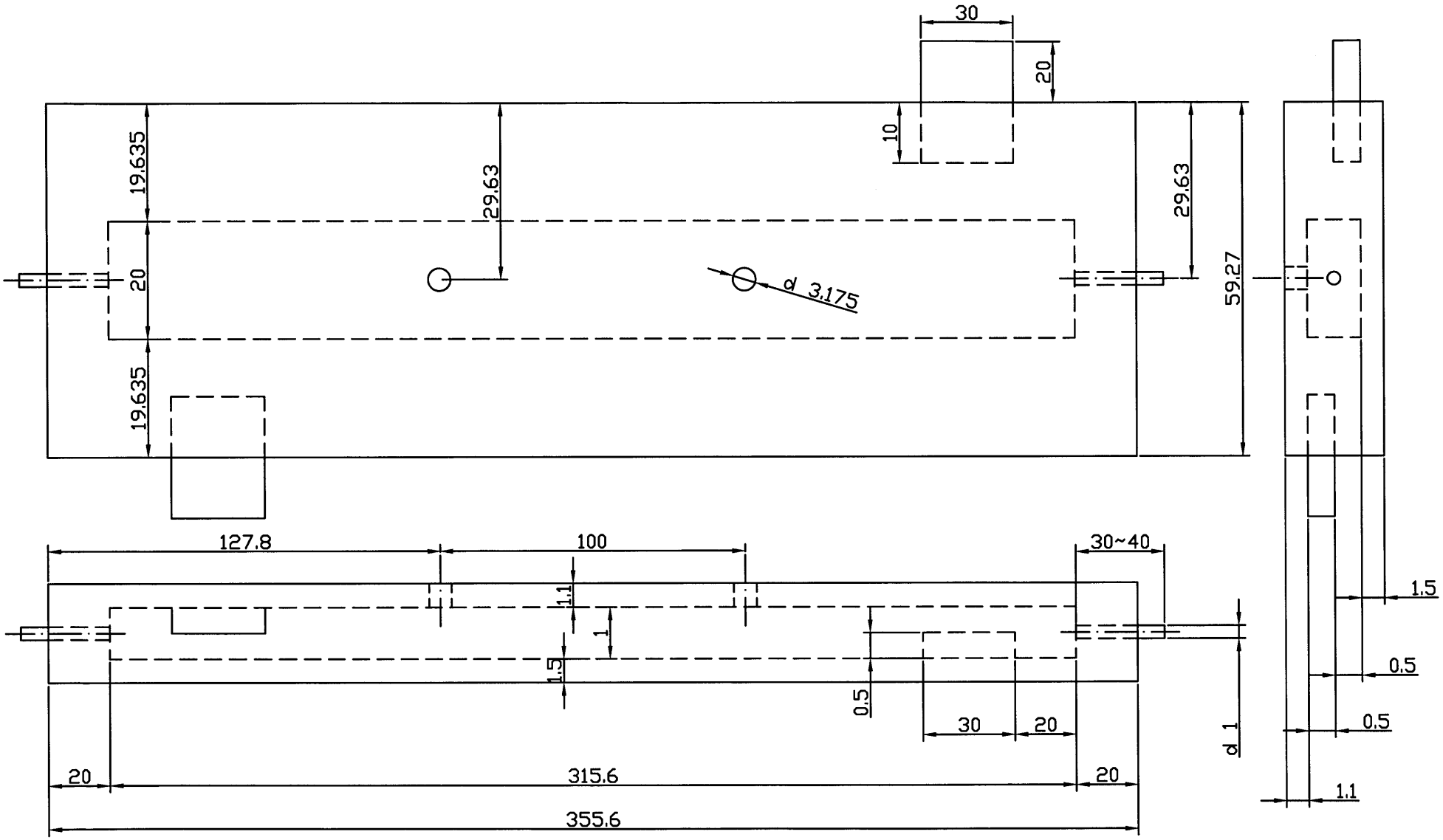
30
20
10
19.635
20
19.635
29.63
29.63
59.27
d 3.175
127.8
100
30~40
1.1
1
1.5
0.5
30
20
20
315.6
20
355.6
d 1
1.5
0.5
0.5
1.1

Bibliography

Adamec, V. and J.H. Calderwood 1981. On the determination of electrical conductivity in polyethylene. *J. Phys. D: Appl. Phys.* 14, 1487-1494.

Arfken, G.B. 1970. *Mathematical Methods for Physicists*, 2nd edn. San Diego, CA: Academic Press.

Bard, A.J. and L.R. Faulkner 2001. *Electrochemical Methods: Fundamentals and Applications*, 2nd edn. New York, NY: John Wiley.

Boissy, C., P. Atten, and J.N. Foulc 1995. On a negative electrorheological effect. *J. Electrost.* 35, 13-20.

Brand, L. 1947. *Vector and Tensor Analysis.* New York, NY: John Wiley.

Brenner, H. 1970. Rheology of two-phase systems. *Annu. Rev. Fluid Mech.* 2, 137-176.

Brenner, H. 1984. Antisymmetric stresses induced by the rigid-body rotation of dipolar suspensions. *Int. J. Eng. Sci.* 22(6), 645-682.

Castellanos, A. 1998. *Electrohydrodynamics.* New York, NY: Springer.

Cebers, A.O. 1980. Internal rotation in the hydrodynamics of weakly conducting dielectric suspensions. *Mekhanika Zhidkosti i Gaza* 2, 86-93. (in Russian; see also Cebers, A.O. 1980. *Fluid Dyn.* 15, 245-251)

Cebers, A., E. Lemaire, and L. Lobry 2000. Internal rotations in dielectric suspensions. *Magnetohydrodyn.* 36, 347-364.

Cebers, A., E. Lemaire, and L. Lobry 2002. Flow modification induced by Quincke rotation in a capillary. *Int. J. Mod. Phys. B* 16, 2063-2069.

Chaves, A., C. Rinaldi, S. Elborai, X. He, and M. Zahn 2006. Bulk flow in ferrofluids in a uniform rotating magnetic field. *Phys. Rev. Lett.* 96, 194501.

Chaves, A., F. Gutman, and C. Rinaldi 2007. Torque and bulk flow of ferrofluid in an annular gap subjected to a rotating magnetic field. *Trans. ASME-J. Fluid. Eng.* 129, 412-422.

Chaves, A., M. Zahn, and C. Rinaldi 2008. Spin-up flow of ferrofluids: asymptotic theory and experimental measurements. *Phys. Fluid.* 20, 053102.

Chhabra, R.P. and J.F. Richardson 1999. *Non-newtonian Flow in the Process Industries: Fundamentals and Engineering Applications.* Boston, MA: Butterworth-Heinemann.

Condiff, D.W. and J.S. Dahler 1964. Fluid mechanical aspects of anti-symmetric stress. *Phys. Fluid.* 7, 842-854.

Crowley, J.M. 1999. *Fundamentals of Applied Electrostatics.* Morgan Hill, CA: Laplacian Press.

Dahler, J.S. and L.E. Scriven 1961. Angular momentum of continua. *Nat.* 192, 36-37.

Dahler, J.S. and L.E. Scriven 1963. Theory of structured continua. I. General consideration of angular momentum and polarization. *Proc. Roy. Soc. A* 275, 504-527.

Deen, W.M. 1998. *Analysis of Transport Phenomena.* New York, NY: Oxford University Press.

Eringen, A.C. 1964. Simple microfluids. *Int. J. Eng. Sci.* 2, 205-217.

Eringen, A.C. 1966. Theory of micropolar fluids. *J. Math. Mech.* 16, 1-16.

Elborai, S.M. 2006. *Ferrofluid surface and volume flows in uniform rotating magnetic fields*, Ph.D. Dissertation, Department of Electrical Engineering and Computer Science, Massachusetts Institute of Technology, Cambridge, MA.

Esmonde, H., H. See, and M.V. Swain 2009. Modeling of ER squeeze films at low amplitude oscillations. *J. Non-Newtonian Fluid Mech.* 161, 101-108.

Espin, M.J., A.V. Delgado, and L. Rejon 2005. Electrorheological properties of hematite/silicone oil suspensions under DC fields. *J. Non-Newtonian Fluid Mech.* 125, 1-10.

Feng, S., A.L. Graham, J.R. Abbott, and H. Brenner 2006. Anti-symmetric stresses in suspensions: vortex viscosity and energy dissipation. *J. Fluid Mech.* 563, 97-122.

Foulc, J.N., P. Atten, and N. Felici 1994. Macroscopic model of interaction between particles in an electrorheological fluid. *J. Electrost.* 33, 103-112.

Fox, R.W. and A.T. McDonald 1998. *Introduction to Fluid Mechanics*, 5th edn. New York, NY: John Wiley.

Fredrickson, A.G. 1964. *Principles and Applications of Rheology*, Englewood Cliffs, NJ: Prentice-Hall.

Greener, J., W. Li, D. Voicu, and E. Kumacheva 2008 (October 8). Chips & tips: Reusable, robust NanoPort connections to PDMS chips. Retrieved April 25, 2010, from Lab on a Chip (RSC Publishing) website: http://www.rsc.org/Publishing/Journals/lc/Chips_and_Tips/nanoport_connections.asp

Griffiths, D.J. 1999. *Introduction to Electrodynamics*, 3rd edn. Upper Saddle River, NJ: Prentice –Hall.

Haik, Y., V. Pai, and C.J. Chen 2001. Apparent viscosity of human blood in high static magnetic field. *J. Magn. Magn. Mater.* 225, 180.

Halsey, T.C. 1992. Electrorheological fluids. *Science* 258, 761-766.

Happel, J. and H. Brenner 1983. *Low Reynolds Number Hydrodynamics: with Special Applications to Particulate Media.* Hingham, MA: Kluwer.

Haus, H.A. and J.R. Melcher 1989. *Electromagnetic Fields and Energy*. Englewood Cliffs, NJ: Prentice-Hall.

He, X. 2006. *Ferrohydrodynamic flows in uniform and non-uniform rotating magnetic fields.* Ph.D. Dissertation, Department of Electrical Engineering and Computer Science, Massachusetts Institute of Technology, Cambridge, MA.

Jackson, J.D. 1999. *Classical Electrodynamics*, 3rd edn. New York, NY: John Wiley.

Jones, T.B. 1984. Quincke rotation of spheres. *IEEE Trans. Ind. Appl.* IA-20, 845-849.

Jones, T.B. 1995. Electromechanics of Particles. New York, NY: Cambridge University Press.

Kaloni, P.N. 1992. Some remarks on the boundary conditions for magnetic fluids. *Int. J. Eng. Sci.* 30(10), 1451-1457.

Khashan, S.A. and Y. Haik 2006. Numerical simulation of biomagnetic fluid downstream an eccentric stenotic orifice. *Phys. Fluids* 18, 113601.

Khushrushahi, S. 2010. Internal laboratory notes. Laboratory for Electromagnetic and Electronic Systems, Research Laboratory of Electronics, Department of Electrical Engineering and Computer Science, Massachusetts Institute of Technology, Cambridge, MA. (see also: *Ferrofluid spin-up flows from uniform and non-uniform rotating magnetic fields*. Ph.D. Dissertation.)

Klingenberg, D.J. and C.F. Zukoski IV 1990. Studies of the steady-shear behavior of electro-rheological suspensions. *Langmuir* 6, 15-24.

Kundu, P.K. and I.M. Cohen 2004. *Fluid Mechanics*, 4th edn. San Diego, CA: Elsevier Academic Press.

Lamb, H. 1945. *Hydrodynamics*, 6th reprint edn. Mineola, NY: Dover Publications.

Larson, R.G. 1999. *The Structure and Rheology of Complex Fluids*. New York, NY: Oxford University Press.

Lemaire, E., L. Lobry, and N. Pannacci 2006. Flow rate increased by electrorotation in a capillary. *J. Electrost.* 64, 586-590.

Lemaire, E., L. Lobry, N. Pannacci, and F. Peters 2008. Viscosity of an electro-rheological suspension with internal rotations. *J. Rheol.* 52, 769-783.

Lobry, L. and E. Lemaire 1999. Viscosity decrease induced by a DC electric field in a suspension. *J. Electrost.* 47, 61-69.

Lukaszewicz, G. 1999. *Micropolar Fluids: Theory and Applications*. Boston, MA: Birkhäuser.

Ma, H. 2007. *Electrochemical Impedance Spectroscopy using Adjustable Nanometer-gap Electrodes*. Ph.D. Dissertation, Department of Electrical Engineering and Computer Science, Massachusetts Institute of Technology, Cambridge, MA.

Melcher, J.R. and G.I. Taylor 1969. Electrohydrodynamics: a review of the role of interfacial shear stresses. *Annu. Rev. Fluid Mech.* 1,111-146.

Melcher, J.R. 1974. Electric fields and moving media. *IEEE Trans. Educ.* E-17, 100-110.

Melcher, J.R. 1981. *Continuum Electromechanics*. Cambridge, MA: The MIT Press.

Morgan, H. and N.G. Green 2003. *AC Electrokinetics: Colloids and Nanoparticles*. Baldock, Hertfordshire: Research Studies Press.

Moskowitz, R. and R.E. Rosensweig 1967. Nonmechanical torque-driven flow of a ferromagnetic fluid by an electromagnetic field. *Appl. Phys. Lett.* 11, 301-303.

Onsager, L. 1934. Deviations from Ohm's law in weak electrolytes. *J. Chem. Phys.* 2, 599-615.

Pannacci, N. 2006. *Rotation de Quincke dans des Suspensions*. Doctoral Thesis, CNRS—Universite de Nice, Sophia Antipolis. (in French).

Pannacci, N., E. Lemaire, and L. Lobry 2007*a*. Rheology and structure of a suspension of particles subjected to Quincke rotation. *Rheol. Acta* 46, 899-904.

Pannacci, N., L. Lobry, and E. Lemaire 2007*b*. How insulating particles increase the conductivity of a suspension. *Phys. Rev. Lett.* 99, 094503.

Peters, F., L. Lobry, and E. Lemaire 2010. Pressure-driven flow of a micro-polar fluid: Measurement of the velocity profile. *J. Rheol.* 54(2), 311-325.

Probstein, R.F. 1994. *Physicochemical Hydrodynamics—An Introduction*, 2nd edn. New York, NY: John Wiley.

Quincke, G. 1896. Ueber rotationen im constanten electrischen felde. *Ann. Phys. Chem.* 59, 417-486. (in German).

Reitz, J.R., F.J. Milford, and R.W. Christy 1992. *Foundations of Electromagnetic Theory*, 4th edn. Reading, MA: Addison-Wesley.

Rinaldi, C. 2002. *Continuum modeling of polarizable systems*. Ph.D. Dissertation, Department of Chemical Engineering, Massachusetts Institute of Technology, Cambridge, MA.

Rinaldi, C. and M. Zahn 2002. Effects of spin viscosity on ferrofluid flow profiles in alternating and rotating magnetic fields. *Phys. Fluids 14(8)*, 2847-2870.

Rinaldi, C., F. Gutman, X. He, A.D. Rosenthal, and M. Zahn 2005. Torque measurements on ferrofluid cylinders in rotating magnetic fields. *J. Magn. Magn. Mater.* 289, 307-310.

Rosensweig, R.E., J. Popplewell, and R.J. Johnston 1990. Magnetic fluid motion in rotating field. *J. Magn. Magn. Mater.* 85, 171-180.

Rosensweig R.E. 1997. *Ferrohydrodynamics*, reprint ed., Mineola, NY: Dover Publications.

Rosensweig, R.E. 2002. Basic equations for magnetic fluids with internal rotations. in *Ferrofluids: Magnetically Controllable Fluids and Their Applications (Lecture Notes in Physics: 594)*, S. Odenbach (ed.). Berlin, Heidelberg: Springer-Verlag, 61-84.

Sauer, F.A. and R.W. Schlögl 1985. Torques exerted on cylinders and spheres by external electromagnetic fields. A contribution to the theory of field induced rotation. in *Interactions between electromagnetic fields and cells*, A. Chiabrera, C. Nicolini, and H.P. Schwan (eds.). New York, NY: Plenum, 203-251.

Schiefelbein, S.L. 1996. *A New Technique to Measure the Electrical Properties of Molten Oxides.* Ph.D. Dissertation, Department of Material Science and Engineering, Massachusetts Institute of Technology, Cambridge, MA.

Schiefelbein, S.L., N.A. Fried, K.G. Rhoads, and D.R. Sadoway 1996. A high-accuracy, calibration-free technique for measuring the electrical conductivity of liquids. *Rev. Sci. Instr.* 69(9), 3308-3313.

Schumacher, K.R., I. Sellien, G.S. Knoke, T. Cader, and B.A. Finlayson 2003. Experiment and simulation of laminar and turbulent ferrofluid pipe flow in an oscillating magnetic field. *Phys. Rev. E* 67, 026308.

Shliomis, M.I. 1972. Effective viscosity of magnetic suspensions. *Sov. Phys. JETP* 34, 1291-1294.

Shliomis, M.I. 1974. Certain gyromagnetic effect in a liquid paramagnet. *Sov. Phys. JEPT* 39, 701-704.

Shliomis, M.I. 1975. Nonlinear effects in suspension of ferromagnetic particles under action of a rotating magnetic field. *Sov. Phys. Dokl.* 19, 686-687.

Shliomis, M.I. 2002. Ferrohydrodynamics: retrospective and issues. in *Ferrofluids: Magnetically Controllable Fluids and Their Applications (Lecture Notes in Physics: 594)*, S. Odenbach (ed.). Berlin, Heidelberg: Springer-Verlag, 85-111.

Shugg, W.T. 1995. *Handbook of Electrical and Electronic Insulating Materials*, 2nd edn. New York, NY: IEEE.

Shulman, Z.P. and V. Nosov 1996. Rotation of the axisimmetric dielectric bodies (DEB) in electrorheological suspensions (ERS). *Int. J. Mod. Phys. B* 10(23-24), 2903-2915.

Shell DIALA® Oil AX: Electrical insulating oil (material data sheet) 2005 (April). Retrieved April 25, 2010, from Shell website: http://www.shellusserver.com/products/pdf/DialaAX.pdf

Sigma-Aldrich Polyethylene (material data sheet) 2008 (December 11). Retrieved April 25, 2010, from Sigma-Aldrich website: http://www.sigmaaldrich.com/catalog/ProductDetail.do?lang=en&N4=434272|ALDRICH&N5=SEARCH_CONCAT_PNO|BRAND_KEY&F=SPEC#test

Sigma-Aldrich Silicone Oil DC200 (material data sheet) 2009 (January 6). Retrieved April 25, 2010, from Sigma-Aldrich website: http://www.sigmaaldrich.com/catalog/ProductDetail.do?N4=85411|ALDRICH&N5=Product No.|BRAND_KEY&F=SPEC

Von Hippel, A.R. (ed.) 1954. *Dielectric Materials and Applications.* Cambridge, MA: The MIT Press.

Winslow, W.M. 1949. Induced fibration of suspensions. *J. Appl. Phys.* 20, 1137-1140.

Wu, C.W., Y. Chen, X. Tang, and H. Conrad 1996*a*. Conductivity and force between particles in a model electrorheological fluid: I. Conductivity. *Int. J. Mod. Phys. B* 10(23-24), 3315-3325.

Wu, C.W., Y. Chen, X. Tang, and H. Conrad 1996*b*. Conductivity and force between particles in a model electrorheological fluid: II. Interaction force. *Int. J. Mod. Phys. B* 10(23-24), 3327-3334.

Wu, C.W. and H. Conrad 1997. Negative electrorheological effect and electrical properties of a Teflon/silicone oil suspension. *J. Rheol.* 41, 267-281.

Wu, C.W., Y. Chen, and H. Conrad 1998. Electrorheology of a zeolite/silicone oil suspension with DC and AC fields. *J. Phys. D: Appl. Phys.* 31, 960-963.

Xiao, J.J., J.P. Huang, and K.W. Yu 2008. Dynamic polarizability of rotating particles in electrorheological fluids. *J. Phys. Chem. B* 112, 6767-6771.

Zahn, M. 2003. *Electromagnetic Field Theory: A Problem Solving Approach.* Malabar, FL: Krieger Publishing Company.

Zahn, M. and L.L. Pioch 1998. Magnetizable fluid behavior with effective positive, zero, or negative dynamic viscosity. *Indian J. Eng. Mater. Sci.* 5, 400-410.

Zahn, M. and L.L. Pioch 1999. Ferrofluid flows in AC and traveling wave magnetic fields with effective positive, zero or negative dynamic viscosity. *J. Magn. Magn. Mater.* 201, 144-148.

Zaitsev, V.M. and M.I. Shliomis 1969. Entrainment of ferromagnetic suspension by a rotating field. *J. Appl. Mech. Tech. Phys.* 10(5), 696-700.